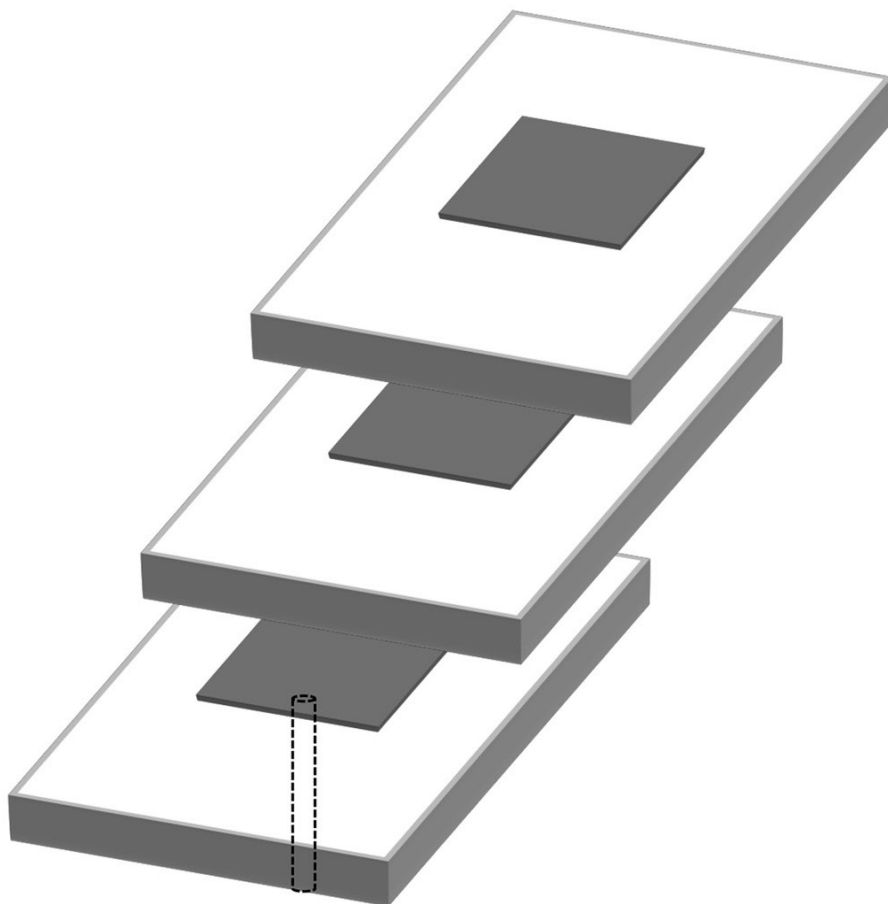


STACKED ANTENNAS

Design, Analysis and Applications



**Ankita A. Malhotra
and Ananjan Basu**



CRC Press
Taylor & Francis Group

Stacked Antennas

The text focuses primarily on details related to the design concepts of stacked microstrip antennas, performance characteristics, and complete static analysis based on different approaches. It will further provide readers with an in-depth understanding of static analysis approaches for analyzing and understanding the performance of multi-layered stacked antennas. The book covers important topics such as conformal mapping, the transmission-line equivalent model-based approach, and the microstrip patch antenna model. The book also discusses reconfigurable stacked microstrip antennas, stacked microstrip antenna arrays, and a wide range of potential applications of stacked microstrip antennas.

This book:

- Presents systematic and simplified design steps of stacked antennas, the factors involved, and various design examples and explains static analysis of multi-layered stacked antennas in an easy-to-understand manner.
- Discusses topics such as conformal mapping, the transmission-line equivalent model-based approach, and the microstrip patch antenna model and reconfigurable stacked microstrip antennas and their applications, along with briefly discussing the design concepts of stacked microstrip antenna arrays.
- Covers simulation, design concepts, and measurement techniques for stacked microstrip antennas.
- Illustrates microstrip stacked antenna parameters, including bandwidth, polarization, radiation pattern, gain, directivity, and efficiency.
- Focuses on covering a wide range of potential applications of stacked microstrip antennas.

It is primarily written for senior undergraduates, graduate students, and academic researchers in fields including electrical engineering, electronics, and communications engineering.



Taylor & Francis

Taylor & Francis Group

<http://taylorandfrancis.com>

Stacked Antennas

Design, Analysis and Applications

Ankita A. Malhotra and Ananjan Basu



CRC Press

Taylor & Francis Group

Boca Raton London New York

CRC Press is an imprint of the
Taylor & Francis Group, an **informa** business

Designed cover image: Ankita A. Malhotra

MATLAB® and Simulink® are trademarks of The MathWorks, Inc. and are used with permission. The MathWorks does not warrant the accuracy of the text or exercises in this book. This book's use or discussion of MATLAB® or Simulink® software or related products does not constitute endorsement or sponsorship by The MathWorks of a particular pedagogical approach or particular use of the MATLAB® and Simulink® software.

First edition published 2025

by CRC Press

2385 NW Executive Center Drive, Suite 320, Boca Raton FL 33431

and by CRC Press

4 Park Square, Milton Park, Abingdon, Oxon, OX14 4RN

CRC Press is an imprint of Taylor & Francis Group, LLC

© 2025 Ankita A. Malhotra and Ananjan Basu

Reasonable efforts have been made to publish reliable data and information, but the author and publisher cannot assume responsibility for the validity of all materials or the consequences of their use. The authors and publishers have attempted to trace the copyright holders of all material reproduced in this publication and apologize to copyright holders if permission to publish in this form has not been obtained. If any copyright material has not been acknowledged please write and let us know so we may rectify in any future reprint.

Except as permitted under U.S. Copyright Law, no part of this book may be reprinted, reproduced, transmitted, or utilized in any form by any electronic, mechanical, or other means, now known or hereafter invented, including photocopying, microfilming, and recording, or in any information storage or retrieval system, without written permission from the publishers.

For permission to photocopy or use material electronically from this work, access www.copyright.com or contact the Copyright Clearance Center, Inc. (CCC), 222 Rosewood Drive, Danvers, MA 01923, 978-750-8400. For works that are not available on CCC please contact mpkbookspermissions@tandf.co.uk

Trademark notice: Product or corporate names may be trademarks or registered trademarks and are used only for identification and explanation without intent to infringe.

ISBN: 978-1-032-66722-5 (hbk)

ISBN: 978-1-032-94479-1 (pbk)

ISBN: 978-1-003-56527-7 (ebk)

DOI: 10.1201/9781003565277

Typeset in Sabon

by Deanta Global Publishing Services, Chennai, India

Dedication

We would like to dedicate this book to our loving families who inspired and supported us through everything.



Taylor & Francis

Taylor & Francis Group

<http://taylorandfrancis.com>

Contents

<i>Preface</i>	viii
<i>Introduction</i>	x
<i>About the authors</i>	xii
<i>Abbreviations</i>	xiii
1 Introduction to stacked microstrip antennas	1
2 Design concepts of stacked microstrip antennas	16
3 Methods for static analysis of stacked microstrip antennas	59
4 Reconfigurable stacked microstrip antennas	94
5 Stacked microstrip antenna arrays	117
6 Advantages, limitations, and applications of stacked microstrip antennas	137
7 Stacked microstrip antennas for microwave imaging	157
<i>Index</i>	201

Preface

Our book is designed to cover all the design and analysis aspects of printed stacked microstrip antennas. The details of the design techniques and various approaches for the analysis of multi-layered stacked microstrip antennas are discussed.

The proposed book is driven by the continuous need for broadband printed antennas in the wireless communication industry. Inspiration to write this book stems from authors' research work on broadband printed antennas. The authors faced challenges in gathering information on the design techniques, specifically the analysis approaches of broadband stacked microstrip antennas. While the full-wave approaches become complex for multi-layered structures, static analysis methods are not yet available for generalized analysis of these stacked structures. As a result, the authors developed an almost generalized static analysis approach based on the transmission-line model for these stacked microstrip antennas, which is extensively covered in the book. Additionally, other reported static analysis methods for such stacked antennas are also addressed, making this book a comprehensive resource on such planar stacked antennas.

The book delves into the various applications of stacked microstrip antennas, showcasing their practical utility. Additionally, it explores the design techniques of reconfigurable stacked microstrip antennas and antenna arrays. It further delves into the microwave imaging application of stacked microstrip antennas, providing detailed insights into imaging algorithms, concepts, and results.

The authors believe it will benefit a lot of researchers and students working in the field of antennas.

MATLAB® is a registered trademark of The MathWorks, Inc. For product information, please contact:

The MathWorks, Inc.

3 Apple Hill Drive

Natick, MA 01760-2098 USA

Tel: 508 647 7000

Fax: 508-647-7001

E-mail: info@mathworks.com

Web: www.mathworks.com

Introduction

The proposed book will explore the design principles and analysis of stacked microstrip antennas, exploring their potential applications. These antennas are created by stacking multiple layers of patches over a printed microstrip antenna. This stacking process leads to electromagnetic coupling among the patches, resulting in enhanced bandwidth and the ability to operate across multiple frequency bands. As a result, stacked antennas offer the advantages of being compact, broadband, and featuring a printed geometry, allowing for seamless integration with other printed circuits. The book provides detailed insights into the design techniques and steps for creating stacked antennas. It also includes several design examples, detailing the characteristics of the designs, the fabrication process for these intricate structures, and the simulated and measured parameters of the antennas.

The book, along with covering design techniques and examples, also provides a thorough analysis of multi-layered stacked antennas, incorporating various existing approaches and a new method developed by the authors. The analysis methods offer valuable insights into the structural, modelling, and electromagnetic coupling effects among the layers of these antennas, ultimately affecting their overall performance. This analysis also provides guidance for designing stacked antennas tailored to specific requirements. Additionally, the book discusses quick and efficient static analysis models as an alternative to more complex full-wave analysis. It explores analytical approaches such as the conformal mapping approach, the TLM-based analysis approach, and the cavity-model approach for stacked antennas.

The book further covers the design of reconfigurable stacked antennas, presenting various design techniques for different types of reconfigurability. These antennas offer the combined benefits of being broadband and electronically tuneable in terms of frequency, radiation pattern, and polarization. Frequency-reconfigurable broadband stacked antennas are commonly used in base station antennas, while pattern and polarization reconfigurable stacked antennas are valuable in wireless communications among multiple users and satellite communication systems.

The book also throws light on design examples of stacked antenna arrays and their potential applications. Arrays are needed for gain enhancement

and improved directivity. This is useful in the case of data communication to dedicated users. Further, phased arrays can help in achieving pattern reconfigurability. The book focuses on design techniques of stacked microstrip antenna arrays, which combine improved bandwidth with improved gain and directivity.

The book also includes a detailed discussion of several advantages and limitations of the stacked microstrip antennas. Further, there are several applications of stacked microstrip antennas in this era of wireless communication. The book covers details of all the potential applications of stacked antennas, in general. The discussion is further extended to stacked microstrip antenna applications for microwave imaging. The microstrip stacked antennas, being broadband, compact, and with a mostly unidirectional radiation pattern, can be effectively used as transceivers in a microwave imaging system. Experimental results of microwave imaging of multiple metallic targets kept in the antenna's far field are reported for the case of stacked microstrip antennas as transceivers. The SAR algorithm, applied for image reconstruction of the targets, is included. Irregular shaped targets can be effectively detected and their shapes are also recovered in the image reconstruction process. Moreover, no absorbers are needed near the proposed microwave imaging set-up, as these stacked microstrip antennas are unidirectional, thus avoiding backside clutter.

Overall, the book has a wide scope for those working in the field of broadband antennas and looking for an in-depth understanding of widely used printed broadband stacked antennas and their potential applications including details of microwave imaging.

Aim: The book aims to provide complete information and understanding of miniaturized broadband stacked microstrip antennas in general and details of possible applications, specific advantages, and limitations.

Scope: The book has a broad scope, covering a wide range of topics that focus on the intricate design techniques and analysis methods for generalized stacked antennas, as well as their various practical applications. It will delve into diverse design approaches and analysis methods for multi-layer stacked antenna structures, exploring the extended potential of these antennas by introducing reconfigurability in their designs and also covering the utility of these antennas in planar arrays. The book will also provide in-depth insights into microwave imaging using stacked antennas as transceivers and the associated image reconstruction algorithms.

About the authors

Ankita A. Malhotra received her BTech in electronics and communications engineering from Kumaun Engineering College, Uttarakhand, in 2009 and her MTech in microwaves from G. B. Pant University of Agriculture and Technology, Pantnagar, in 2011. She received her PhD in RF and microwave domain from the Indian Institute of Technology, Delhi, in 2017. She has worked as an Assistant Professor in the Electronics and Telecommunications Department of SVKM's D J Sanghvi College of Engineering, Mumbai, since November 2023. She worked as an Assistant Professor at the Electronics and Telecommunications Department of Rajiv Gandhi Institute of Technology, Mumbai, from 2017 to 2023. She also worked as RF consultant at Vahaant Technologies Noida and SPEZL Pvt. Ltd. Mumbai. Her research interests include reconfigurable broadband antennas, microwave imaging, computational electromagnetics, and MIMO phased array antennas. She was a recipient of the Top-up scholarship award by Bharti Airtel during her PhD and has authored/co-authored in more than 12 reputed journal and conference publications. She is an active reviewer at many reputed journals and conferences including *IEEE Transactions on Antennas and Propagation*, *IEEE Antennas and Wireless Propagation Letters*, *IET Image Processing*, and *International Journal of Microwave and Wireless Technologies*.

Ananjan Basu was born 12 August 1969. He received a BTech degree in electrical engineering and an MTech degree in communication and radar engineering from the Indian Institute of Technology Delhi (IIT Delhi), in 1991 and 1993, respectively, and a PhD in electrical engineering from the University of California at Los Angeles (UCLA), in 1998. He has been with the Centre for Applied Research in Electronics, IIT Delhi, as an Assistant Professor (2000–2005), Associate Professor (2005–2012), and Professor (since 2012). His specialization is in microwave and millimetre-wave component design and characterization. He is currently the Head of the Centre for Applied Research in Electronics, IIT Delhi. He is a senior member of IEEE and editor of *IETE Journal*. His research interests include microwave and millimetre-wave component design, microwave imaging, wideband and reconfigurable antennas, and guided wave analysis.

Abbreviations

2D	Two-dimensional
3D	Three-dimensional
4G	Fourth generation
5G	Fifth generation
6G	Sixth generation
ADS	Advanced design system
CAD	Computer-aided design
CMA	Conformal mapping approach
CST	Computer simulation technology
CP	Circular polarization
EM	Electro-magnetic
EF	Electric field
GHz	Gigahertz
GPS	Global positioning system
HFSS	High-frequency structure simulator
IE3D	Integrated electromagnetic environment design and development
IoT	Internet of Things
ISM	Industrial, scientific, and medical
LHCP	Left-hand circularly polarized
MIMO	Multiple-input multiple-output
MEMS	Micro-electromechanical system
MD	Magneto-dielectric
MF	Magnetic field
PIN	Positive-intrinsic-negative
RHCP	Right-hand circularly polarized
SAR	Specific absorption rate
SRR	Split ring resonator
SIW	Substrate integrated waveguide
S11	Reflection coefficient
S21	Transmission coefficient
T/R	Transceiver
TLM	Transmission line model

UWB	Ultra wideband
VNA	Vector network analyzer
WLAN	Wireless local area network
WiFi	Wireless fidelity
XPD	Cross polarization density

Introduction to stacked microstrip antennas

I.1 INTRODUCTION

Stacked antennas consist of multiple resonating elements stacked in a single antenna structure, with only one element being fed by the source while the other elements are coupled to the driven element. There are printed stacked antennas as well as non-printed ones such as the dipole stacked antenna and the yagi-uda stacked antenna. This book will primarily focus on the design strategies and analysis methods of printed/planar stacked microstrip antennas. Printed microstrip antennas are low-profile planar structures that are easily integrated with other printed circuits. However, these antennas typically have low bandwidth, which can be addressed through various methods. One approach is to use a thick dielectric substrate to reduce the energy stored in the substrate and maximize the radiated energy. Additionally, aperture coupling can be employed to enhance the bandwidth of microstrip antennas. Despite these methods, achieving very wide bandwidth remains a challenge. By stacking multiple resonators in the printed antenna structure, it is possible to achieve wide bandwidth without compromising the inherent advantages of these antennas. This chapter will provide an introduction to the fundamental concepts related to types of stacked antennas and various design techniques.

I.2 DESIGN CONSIDERATION OF STACKED MICROSTRIP ANTENNAS

Printed stacked microstrip antennas are commonly utilized across various applications to achieve optimal system performance, including broad bandwidth and high gain. A thorough understanding of the proper design and configuration of stacked antennas provides valuable insight into their design approach, enabling them to operate at a specific central frequency while maintaining the required bandwidth within the operational range. The choice of substrates significantly impacts the overall performance and efficiency of stacked antennas, making it a crucial parameter to consider.

This chapter will delve into the influence of different substrate types, including their dielectric constants and heights. Additionally, essential antenna parameters such as gain, directivity, bandwidth, efficiency, and polarization will be briefly discussed in the context of stacked antennas. Furthermore, the chapter will focus on the specific details of various types of stacked antennas and their respective applications. In particular, the following section will provide a detailed exploration of different types of printed stacked microstrip antennas, including aperture-coupled, proximity-coupled, and microstrip/probe-fed stacked antennas.

1.3 TYPES OF STACKED MICROSTRIP ANTENNAS

1.3.1 Aperture-coupled stacked antennas

In aperture-coupled antennas, an aperture or slot indirectly excites the driven patch via the feed line. This structure involves at least two dielectric substrates, one with a feed at the bottom and a slot at the upper side, and the other with a patch on it. The energy is coupled from the feed to the patch through the slot, causing it to resonate at its operating frequency. Adding more layers over the driven patch in the aperture-coupled antenna turns it into an aperture-coupled stacked antenna. These stacked antennas offer a wider impedance bandwidth and improved gain compared to simple aperture-coupled antennas. Examples of such aperture-coupled stacked antennas are discussed below. The geometry of an aperture-coupled stacked antenna with an additional parasitic patch is shown in Figure 1.1.

As shown in Figure 1.1, there is an aperture on one side and feed on the other side of the substrate, which couples electromagnetic energy to the driven patch and excites it. On the top of driven patch, there is a parasitic patch which is further excited through the coupling of energy from the driven patch. Multiple resonances exist due to multiple resonators, and these close resonances result in broad bandwidth of the given antenna. In the aperture-coupled antennas, the slot width is optimized to ensure good coupling to the driven patch, and for the case of a stacked antenna, proper coupling among the stacked layers is obtained. Further feed line width can be optimized to match the antenna with a $50\ \Omega$ microstrip line. As demonstrated in [1], the input impedance depicted on the Smith chart shows three coupled resonances, due to the two patches and that of the aperture, thus resulting in wider bandwidth, compared to simple aperture-coupled antenna design. A bandwidth (SWR < 2:1) of 57% is computed while 52% was measured with a centre frequency of 8.95 GHz in this case [1].

A circularly polarized aperture-coupled stacked antenna design is demonstrated in [2], with two stacked patches fed through two orthogonal slots. The feed is given to the aperture-coupled antenna through a hybrid coupler such that two output ports at 90° phase shift are used as two orthogonal

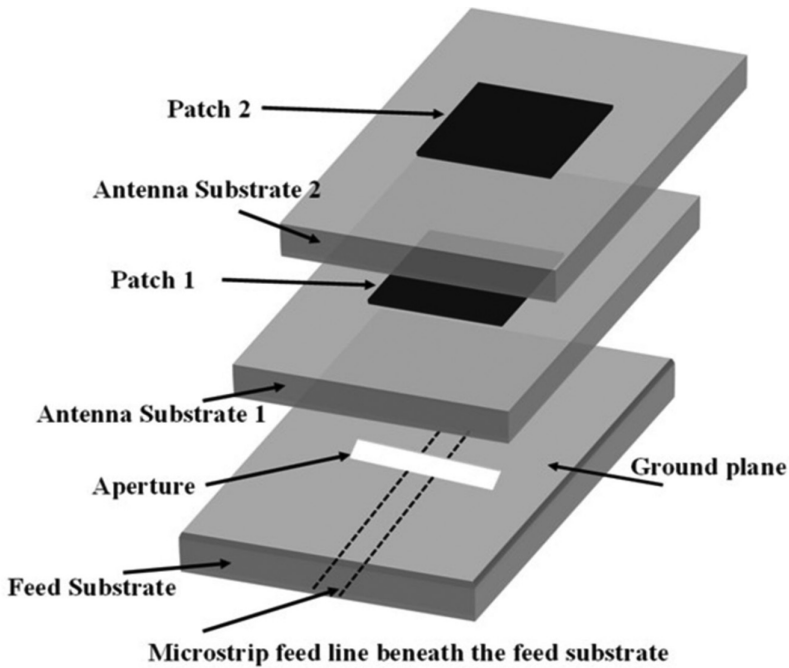


Figure 1.1 Geometry of aperture-coupled stacked patch antenna.

feed lines, feeding the antenna through two slots. As shown in Figure 1.2 the two I-shaped slots are placed beneath the two consecutive edges of the square patch, such that orthogonal currents flow through two stacked patches through electromagnetic coupling. This yields a circularly polarized aperture-coupled stacked antenna design. The improved impedance bandwidth response is evident from Figure 1.3(a) with wide axial ratio bandwidth too depicted in Figure 1.3(b). The stacking of another layer over the driven patch further enhances the overall antenna gain as visible from Figure 1.3(c).

1.3.2 Microstrip and probe-fed stacked patch antennas

A microstrip patch antenna with one or more parasitic patches, stacked above the driven patch, is known as a microstrip stacked antenna. Microstrip stacked antennas offer a wider bandwidth compared to basic microstrip antenna designs due to the presence of multiple resonant layers stacked on top of each other. Similar to microstrip antennas, these antennas have a planar ground plane beneath the resonant layers and exhibit unidirectional radiation properties. This characteristic provides them with an advantage

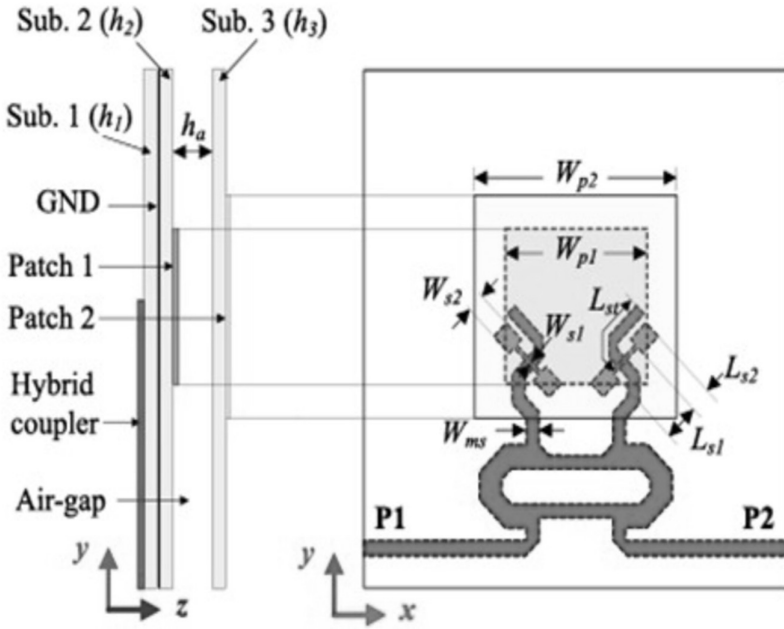


Figure 1.2 Geometry of dual-CP aperture-coupled stacked patch antenna. (Source: Son Xuat Ta, Vancuongnguyen, Bang-Tam Nguyen and Chien Dao-Ngoc, “Wideband Dual-Circularly Polarized Antennas Using Aperture-Coupled Stacked Patches and Single-Section Hybrid Coupler”, IEEE Access, Vol. 10, pp: 21883–21891, Feb 2022 [2].)

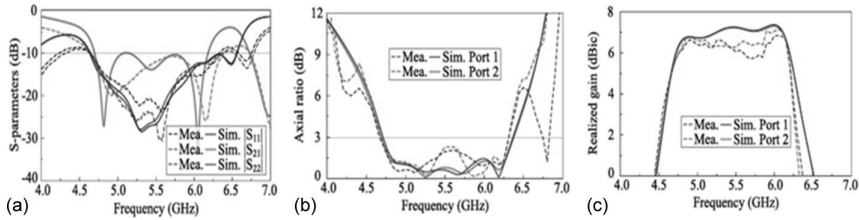


Figure 1.3 (a) S-parameters, (b) AR bandwidth, and (c) gain of the proposed antenna. (Source: Son Xuat Ta, Vancuongnguyen, Bang-Tam Nguyen and Chien Dao-Ngoc, “Wideband Dual-Circularly Polarized Antennas Using Aperture-Coupled Stacked Patches and Single-Section Hybrid Coupler”, IEEE Access, Vol. 10, pp: 21883–21891, Feb 2022 [2].)

over aperture-coupled stacked antennas in scenarios where backside radiation is undesirable, such as applications where electromagnetic coupling is a significant constraint.

As shown in Figure 1.4 a printed microstrip antenna with planar ground plane is stacked vertically with multiple resonators. The resonators consist

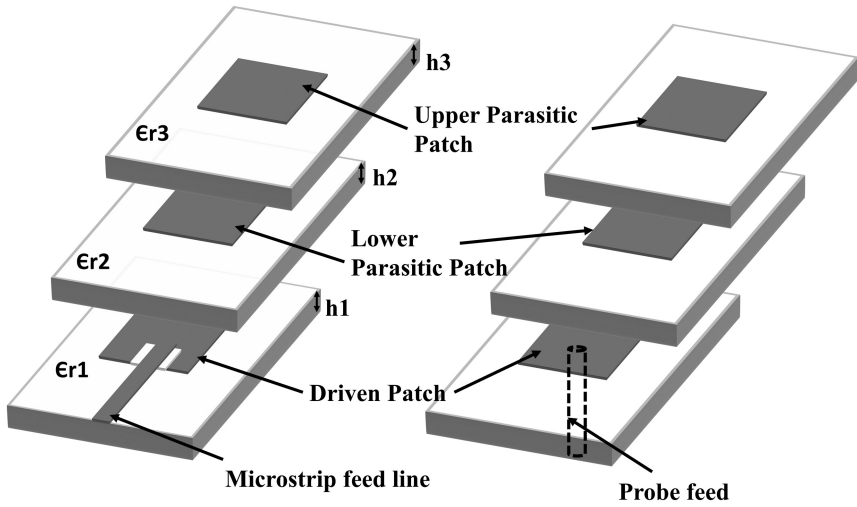


Figure 1.4 Microstrip-fed and probe-fed microstrip stacked antenna design.

of metallic patches etched onto one side of the substrates. These resonators become electromagnetically coupled with the driven patch when the driven patch is excited through the feed. This excitation leads to multiple resonances due to the stacked patches, resulting in a multiband antenna response or a broadband response if the resonances are closely spaced. The response of a multi-layered stacked microstrip antenna can be fine-tuned to achieve a sufficiently broadband response by adjusting the multiple resonances obtained.

1.3.3 Proximity-coupled stacked antennas

The proximity-coupled stacked antenna utilizes multiple resonant layers stacked one above the other, which generate multiple resonances when excited through the proximity-coupled feed. In this design, shown in Figure 1.5, the driven patch is electromagnetically coupled with the feed line, which in turn couples the energy with the stacked parasitic patches. By carefully selecting substrate materials and patch dimensions, a bandwidth of over 20% can be achieved with this antenna design [3]. The antenna structure includes one driven patch fed by a proximity-coupled microstrip feed line printed on the lower-most substrate, along with a parasitic patch placed above the driven patch. The specific substrate heights and dielectric constants chosen for the multiple layers can vary based on the desired performance of the antenna. The details related to these antenna design parameters, crucial for achieving optimal performance, are discussed in the next section.

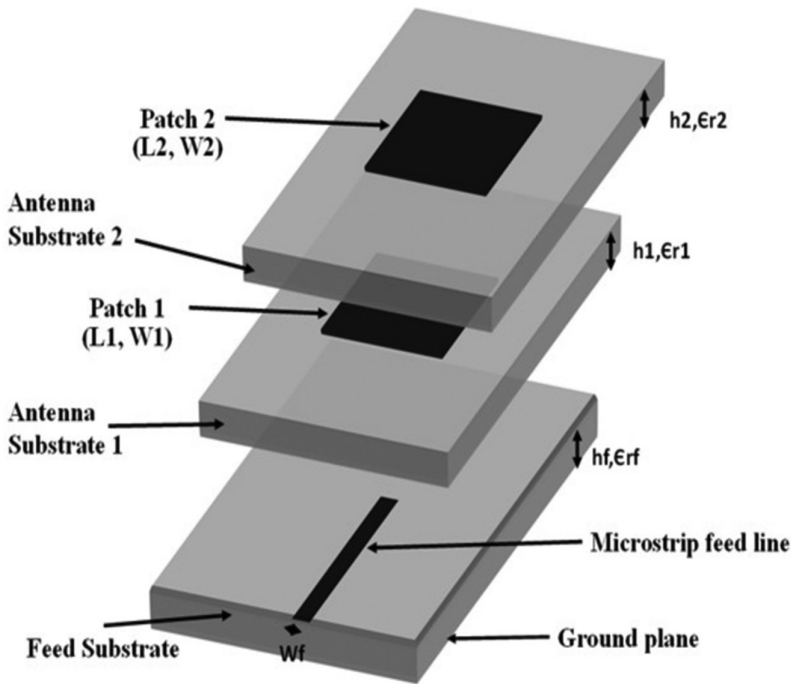


Figure 1.5 Stacked proximity-coupled patch antenna structure.

1.4 DESIGN PARAMETERS OF STACKED MICROSTRIP ANTENNAS

The design of stacked microstrip antennas is based on several key parameters aimed at achieving a broadband antenna response. With multiple stacked layers involved, each design parameter significantly influences the antenna's performance. Factors such as the choice of substrates, dimensions and shapes of resonant patches, number of stacked layers, and their relative placement all significantly impact the overall response of the printed stacked antenna. Optimal results can be achieved by carefully selecting and fine-tuning these parameters according to the chosen antenna geometry. These crucial parameters will be briefly discussed in the following sections.

1.4.1 Choice of substrates

The selection of substrates significantly impacts the performance of stacked antennas. The electrostatic fields stored within the substrates and the electromagnetic coupling among the layers are greatly influenced by the choice of substrates. It is crucial to carefully consider the dielectric material and substrate height in order to achieve the desired antenna performance. A

lower dielectric constant material enhances the radiation properties, gain, and bandwidth of the antenna, but it also leads to an increase in antenna dimensions, as indicated by Equations (1.1)–(1.5) [4]. When designing a compact antenna using a lower dielectric constant material, the overall antenna gain is reduced. On the other hand, employing a higher dielectric constant substrate allows for a compact antenna design (as per Equations 1.1–1.5), but it comes with reduced bandwidth and some gain reduction. Therefore, selecting an optimal substrate that reduces antenna dimensions with minimal compromise on radiation properties is crucial for a printed antenna.

$$W = \frac{c}{2fr} \sqrt{\frac{2}{\epsilon_r + 1}} \quad (1.1)$$

$$\epsilon_{re} = \frac{\epsilon_r + 1}{2} + \frac{\epsilon_r - 1}{2} \left(1 + \frac{12h}{w} \right)^{-0.5} \quad (1.2)$$

$$L_{eff} = \frac{c}{2fr\sqrt{\epsilon_{re}}} \quad (1.3)$$

$$\Delta l = 0.412 * h * \frac{(\epsilon_{re} + 0.3) \left(\frac{w}{h} + 0.264 \right)}{(\epsilon_{re} - 0.258) \left(\frac{w}{h} + 0.8 \right)} \quad (1.4)$$

$$L = L_{eff} - 2\Delta l \quad (1.5)$$

It's crucial to consider the thickness of the dielectric substrate when designing a microstrip antenna, as it has a significant impact on the antenna's performance. The use of a thicker dielectric material enhances the overall bandwidth and gain of the antenna, which is especially beneficial for inherently narrowband antenna designs. However, thicker substrates can lead to surface wave propagation within the substrate, causing unwanted effects such as edge diffractions and the generation of side lobes in the antenna's radiation pattern.

On the other hand, using thinner dielectric substrates can help minimize surface wave propagation, but this can result in increased dielectric losses and reduced antenna gain. Therefore, selecting the optimum substrate height is a critical parameter in designing a microstrip stacked antenna to achieve the desired antenna response while minimizing surface wave effects. Careful selection of the substrate material and its thickness is essential for ensuring overall good antenna performance. The surface waves are discussed in detail in Chapter 2.

1.4.2 Patch shapes and dimensions

The design of microstrip stacked antennas involves stacking resonant patches one above the other. The dimensions of these patches are crucial for achieving the required antenna resonance. The dimensions of the driven patch are calculated according to the desired resonant frequency for the antenna's operation, as explained in Chapter 2. Similarly, the dimensions of the stacked patches are approximately calculated using a similar procedure described in Chapter 2, but consider the effective dielectric constant of the substrates between the parasitic patch and the ground. The dimensions of the stacked patches are calculated to make them resonate near the resonant frequency of the driven patch, resulting in closely spaced multiple resonances that yield an overall broadband antenna response. In addition to the patch dimensions of the stacked microstrip antenna, the chosen shape of the patches is also an important parameter that affects the antenna's overall response. Calculations are available to determine the dimensions of a rectangular patch or a circular patch, which are the simplest resonant structures. If the shape is further modified or meandered using slots, some optimization of patch dimensions is necessary to improve impedance matching. Changes in the antenna's shape and structure, such as meandering slots, curves at the edges, and edge cuts, result in variations in the antenna's input impedance, which helps achieve the required impedance matching. Certain patch shapes, such as E-shaped and H-shaped patches and U-shaped slots [5–9], have been shown to improve impedance matching over a wide bandwidth, thereby contributing to achieving a broadband antenna response.

1.4.3 Number of stacked layers

The performance of stacked antennas is influenced by the electromagnetic coupling between the layers. The number of stacked layers in the antenna design affects the resonances obtained and the total energy coupled to each layer. In theory, each coupled resonating parasitic patch generates a resonance based on its dimensions. However, the amount of energy coupled to each stacked layer decreases beyond the driven patch. Increasing the stacking of parasitic patches can impact the obtained resonances only if a sufficient amount of electromagnetic energy is coupled to each layer. Typically, two to three stacked parasitic patches can receive sufficient coupled energy and contribute to the antenna's resonant response.

1.4.4 Relative placement of stacked patches

The arrangement of stacked parasitic patches plays a crucial role in enhancing electromagnetic coupling among multiple layers and achieving broadband impedance matching. The precise positioning of these stacked layers

in relation to the driven patch and each other is vital in determining how electromagnetic fields will interact within the layers, ultimately influencing the antenna's input impedance. To maximize the energy coupled to the parasitic patches, it is recommended to position them above the region with the highest radiated fields, as determined by the design and excitation of the driven patch. Achieving the optimal placement of the stacked patches will necessitate some degree of optimization to enhance overall performance.

1.5 MICROSTRIP STACKED ANTENNA CHARACTERISTICS

In this section, we will discuss the key antenna parameters that determine the overall performance of the antenna. Parameters such as bandwidth, gain, directivity, polarization, and efficiency define the antenna's response. We will also delve into these performance parameters in the context of stacked antennas, along with the design parameters upon which they depend.

1.5.1 Bandwidth

The design of stacked antennas allows for the creation of either multiband or broadband antennas, depending on the selection and arrangement of stacked resonant patches. Stacked microstrip antennas address the limited bandwidth of basic microstrip antennas by enabling broadband impedance matching through the electromagnetic coupling of multiple layers. This coupling stimulates the parasitic patches and leads to multiple resonances in the stacked antenna's response, resulting in a multiband antenna response. When these resonances closely align in the frequency domain, they produce a broadband antenna response, achieved when the antenna structure attains broadband impedance matching at the input. The physical dimensions of stacked patches, as well as their placement in relation to each other and the driven patch, directly influence the overall input impedance. Modifying these factors allows for adjustments to the frequency response of stacked antennas in line with specific requirements.

1.5.2 Polarization

The concept of polarization in antennas concerns the electric field vector's orientation as the wave travels away from the source. The current distribution along the driven patch, determined by the feeding mechanism, impacts the electric and magnetic field distribution around the antenna's structure. The interaction of these fields with the antenna, results in a specific polarization of the radiated E-field vector. In stacked antennas, the combined current and field distribution across multiple resonant patches determines

the antenna's polarization. In this scenario, the driven patch significantly influences the antenna's current distribution pattern. The parasitic patches are influenced by the radiated fields of the driven patch, leading to a similar current distribution pattern. Typically, the current distribution across the driven patch depends on the feed location for the case of microstrip lined or probe-fed stacked patch antennas. It is dependent on the slot's size and relative position to the driven patch for the aperture-coupled stacked antenna and the relative position of the driven patch to the feed line in the case of proximity-coupled stacked antenna.

1.5.3 Radiation pattern

The radiation pattern refers to the spatial distribution of radiated energy around an antenna's structure. Microstrip antennas with a planar ground plane emit energy in the broadside direction and display unidirectional radiation patterns. Antennas with defected ground planes or meandering/slots emit energy bi-directionally in the broadside direction. In the case of structures with defected ground or slots in the ground, the slots also emit energy, resulting in a bi-directional radiation pattern. Stacked microstrip antennas consist of multiple resonators stacked above the basic microstrip patch antenna. These antennas have a planar ground plane (unlike aperture-coupled or proximity-coupled stacked antennas), resulting in unidirectional radiation patterns in the broadside direction. This feature of stacked microstrip antennas is particularly useful in applications such as remote sensing, cognitive radio, and military applications. Additionally, the radiation pattern of stacked antennas also depends on the relative placement of stacked parasitic patches to the driven element. In some cases, multiple patches are placed in the parasitic layer, thereby modifying the radiation pattern of the antenna in the broadside direction.

1.5.4 Gain

Antenna gain is a parameter used to quantify the radiation intensity in a specific direction compared to the radiation intensity of an isotropic radiator in the same direction while receiving the same total power. It is a measure of the antenna's performance for a given input power and is a crucial parameter to optimize for any specific application. The expression of antenna gain is given by Equation (1.6) [4] and antenna Q factor is given by Equation (1.7) [10]. In Equation (1.7) the quality factor of the antenna is given as the ratio of the stored reactive field to the power dissipated in radiation. The reactive stored power is the maximum of energy stored either in the magnetic field (W_M) or electric field (W_E). As the Q value is inversely proportional to radiated power, lower antenna Q values are obtained for increased radiated power. The radiated power of an

antenna in turn depends on radiation resistance according to Equation (1.8). The expression of radiation resistance is inversely proportional to substrate height and directly proportional to substrate permittivity, as given in Chapter 3.

$$Gain = 4\pi \frac{\text{radiation intensity in a particular direction}}{\text{total input (accepted) power}} \quad (1.6)$$

$$Q = 2\omega \frac{\max(W_M, W_E)}{\text{Power dissipated in radiation}(P_{\text{rad}})} \quad (1.7)$$

$$P_{\text{rad}} = \frac{1}{2} (I_o)^2 R_{\text{rad}} \quad (1.8)$$

Additionally, “realized gain” is also a parameter used, which is similar to “gain” except that “accepted power” is replaced by “power available from source”. Basically, this takes into account the power lost due to impedance mismatch between antenna and source. It is easy to measure this directly, and the conventional gain (which is a little higher) can be easily calculated if $|S_{11}|$ is known.

In the stacked patch antennas, multiple resonators are stacked vertically one above the other and are electromagnetically coupled. The overall energy radiated in the broadside direction is increased, by the lowering of the antenna’s quality factor. This lowering of the Q value happens due to an increase in overall dielectric substrate height and therefore increase of power dissipated in the form of radiation. This lowering of the Q value increases the antenna’s overall gain. The proper placement of stacked layers also plays an important role in achieving improved overall gain of the antenna by enhancing the coupled electromagnetic energy.

1.5.5 Directivity

The directivity of an antenna refers to its spatial distribution of radiated energy. It measures the maximum radiated energy in a specific direction relative to the total radiated energy in all directions. In the case of printed stacked antennas, the vertically arranged resonators focus the radiated energy towards the broadside direction, thereby enhancing directivity in that direction. Additionally, as the gain of the stacked antenna increases, its directivity also improves, particularly in the direction of the stacked radiators.

$$D = 4\pi \frac{\text{Maximum radiation intensity in a particular direction}}{\text{Total radiated power}} \quad (1.9)$$

1.5.6 Efficiency

The efficiency of an antenna is the ratio of the total radiated power to the total input power supplied to the antenna, given by Equation (1.10) [4]. Antenna efficiency accounts for antenna losses and is also expressed as the ratio of gain to directivity, given by Equation (1.11) [4]. When calculating antenna efficiency, it's important to account for antenna losses, such as conduction and dielectric losses. In the case of stacked microstrip antennas, the use of multiple substrates in the design increases the overall substrate thickness. The overall permittivity of the antenna is determined as the effective permittivity of these multiple substrates. If the effective permittivity of the antenna decreases while the effective substrate thickness increases, it will result in a decrease in the antenna's Q value and an improvement in the antenna's radiation efficiency. However, selecting an optimal driven-patch substrate is crucial to minimize surface waves, which can otherwise reduce the antenna's radiation efficiency. The details of surface waves are discussed in Chapter 2.

$$P_{\text{rad}} = e_{cd} P_{\text{in}} \quad (1.10)$$

$$\text{Also } \text{Gain}(\theta, \varphi) = e_{cd} \cdot \text{Directivity}(\theta, \varphi) \quad (1.11)$$

where e_{cd} is the antenna efficiency accounting for conductor and dielectric losses.

1.6 MULTIBAND AND BROADBAND APPLICATIONS OF STACKED MICROSTRIP ANTENNAS

Stacked microstrip antennas find their utility in many of the new generation applications owing to their broad bandwidth and in some cases multiband response along with high gain and low-profile structure. Multiband antennas are mostly useful in communication applications, where different multiple operating frequency bands are useful for the system [11, 12].

An important feature of most stacked patch antennas is the unbroken ground plane leading to unidirectional radiation (i.e. no back-lobe). This feature is useful in system design where circuitry can be placed directly behind the ground plane with no danger of interference. This is the primary distinguishing feature between this class of antennas, and the other two classes of broadband printed antennas – the printed monopole with numerous variations and the Vivaldi and related antennas [13–15]. It is well-known that printed monopoles can give extremely large bandwidths; however, they are not unidirectional and there is no provision to place circuits nearby without additional shielding. Also printed monopoles have limitations for array applications – a 2D array on a single substrate is very difficult. For wideband systems where such shielding or array is not

required, printed monopoles are suitable, but if complex circuitry has to be closely packed behind the antenna (or an antenna array, possibly a phased array) then stacked antennas are appropriate.

Stacked microstrip antennas with unidirectional radiation patterns can be very useful for target scanning applications in remote sensing and military applications [16, 17]. These broadband compact antennas are also a useful candidate in 5G communication systems. Many stacked microstrip antennas have been proposed for base station applications in 4G, 5G, and 6G bands [18–20]. Printed stacked antennas are commonly used for satellite communication where high gain is the major requirement [21, 22]. Further textile-based printed stacked antennas are in demand for biomedical applications as they are planar in their structure (along with wide bandwidth and higher gain) and can be easily worn on different body parts for the study of various biomedical parameters. Such textile-based stacked antennas are proposed in [23, 24] for the analysis of vital human parameters. For applications where electromagnetic coupling among the circuit components is not acceptable, these printed planar antennas are most useful. Also, in applications like antenna mounting on automobiles, where a large metallic plane acts as a ground, such antennas are easy to install [25]. Other common applications of printed stacked antennas are WLAN, GPS, WiFi, ISM band, and other wireless communication bands. The detailed applications of printed stacked antennas are discussed in Chapter 6.

1.7 SUMMARY

This chapter summarizes all the basic concepts related to stacked microstrip antennas. The chapter covers the design and performance parameters of these printed stacked antennas, which is essential for readers to understand in brief, the performance of stacked antennas, and the major parameters on which the various performance characteristics depend. The applications of such stacked microstrip antennas are also discussed in brief.

REFERENCES

1. S. D. Tugonski and R. B. Waterhouse, “An Aperture Coupled Stacked Patch Antenna with 50% Bandwidth”, IEEE Antennas and Propagation Society International Symposium, July 1996.
2. Son Xuat Ta, Vancuongnguyen, Bang-Tam Nguyen, and Chien Dao-Ngoc, “Wideband dual-circularly polarized antennas using aperture-coupled stacked patches and single-section hybrid coupler”, *IEEE Access*, Vol. 10, pp:21883–21891, Feb. 2022.
3. Wayne S. T. Rowe, and Rod B. Waterhouse, “Investigation into the performance of proximitycoupled stacked patches”, *IEEE Trans. on Antennas and Propag.*, Vol. 54, No. 6, pp:1693–1698, June 2006.

4. C. A. Balanis, “*Antenna Theory: Analysis and Design*” Wiley Publications, 2001.
5. B. L. Ooi and Q. Shen, “A Novel Stacked E-Shaped Patch Antenna”, IEEE Antennas and Propagation Society International Symposium, July 2001.
6. Yanshan Gou, Shiwen Yang, Quanjiang Zhu, and Zaiping Nie, “A compact dual-polarized double -shaped patch antenna with high isolation”, *IEEE Trans. Antennas and Propag.*, Vol. 61, No. 8, pp:4339–4353, August 2013.
7. Kwok L. Chung, “A wideband circularly polarized H-shaped patch antenna”, *IEEE Trans. on Antennas and Propag.*, Vol. 58, No. 10, pp:3379–3383, October 2010.
8. Joysmita Chatterjee, Akhilesh Mohan, and Vivek Dixit, “Broadband circularly polarized H-shaped patch antenna using reactive impedance surface”, *IEEE Antennas and Wirel. Propag. Lett.*, Vol. 17, No. 4, pp:625–628, April 2018.
9. Y. L. Chow, Z. N. Chen, K. F. Lee, and K. M. Luk, “A Design Theory on Broadband Patch Antennas with Slot”, 2014 International Conference on Computational Intelligence and Communication Networks, November 2014.
10. R. E. Collin and S. Rothschild, “Evaluation of antenna Q”, *IEEE Trans. on Antennas and Propag.*, Vol. 12, pp:23–27, January 1964.
11. Jianxing Li, Hongyu Shi, Hang Li, and Anxue Zhang, “Quad-band probe-fed stacked annular patch antenna for GNSS applications”, *IEEE Antennas Wirel. Propag. Lett.*, Vol. 13, pp:372–375, 2014.
12. Ningning Yan, Kaixue Ma, Haobin Zhang, and Pengcheng Jia, “Communication an SISL triple-band multimode stacked-patch antenna with L-strips for multiband applications”, *IEEE Trans. on Antennas and Propag.*, Vol. 67, No. 2, pp:1284–1288, Feb. 2019.
13. Andi Ding, Theng Huat Gan, and Zhongxiang Shen, “Design of a compact and wideband printed monopole antenna with stable omnidirectional radiation patterns”, *IEEE Antennas and Wirel. Propag. Lett.*, Vol. 23, No. 5, pp:1483–1487, May 2024.
14. Trivesh Kumar, and A. R. Harish, “Broadband circularly polarized printed slot-monopole antenna”, *IEEE Antennas and Wirel. Propag. Lett.*, Vol. 12, pp:1531–1534, 2013.
15. Ke Zhang, Rong Tan, Zhi Hao Jiang, Wei Hong, Yong Huang, and Lin Tang, “A compact, ultrawideband dual-polarized vivaldi antenna with radar cross section reduction”, *IEEE Antennas and Wirel. Propag. Lett.*, Vol. 21, No. 7, pp:1323–1327, July 2022.
16. Shengying Liu, Kaibo Jiang, Guobing Xu, Xumin Ding, Kunag Zhang, Jiahui Fu, and Qunwu, “A dual-band shared aperture antenna array in Ku/Ka-bands for beam scanning applications”, *IEEE Access*, Vol. 7, pp:78794–78802, June 2019.
17. Md. Rokunuzzaman, Md. Samsuzzaman, Student Member, IEEE, and Mohammad Tariqul Islam, “Unidirectional wideband 3-D antenna for human head-imaging application”, *IEEE Antennas and Wirel. Propag. Lett.*, Vol. 16, pp:169–172, 2017.
18. Philip Ayiku Dzagbletey, and Young-Bae Jung, “An omnidirectional multilayer metasurface antenna for 2G, 3G, 4G and 5G applications”, *IEEE Antennas and Wirel. Propag. Lett.*, Vol. 17, No. 5, pp:780–783, May 2018.

19. Jaebaek Jung, Woojun Lee, Gyuha Lee, Songcheol Hong, and Jungsuek Oh, "Ultra-thinned metasurface-embedded smartphone antenna-in-package for millimeter-wave 5G/6G coverage enhancement", *IEEE Trans. on Antennas and Propag.*, Vol. 71, No. 10, pp:7766–7781, October 2023.
20. Shahanawaz Amal, and Padmanava Sen, "Microstrip-ministered proximity-coupled stacked dual-port antenna for 6G applications," *IEEE Access*, Vol. 12, pp:2817–2829, January 2024.
21. Marco Simone, Matteo Bruno Lodi, Santi Concetto Pavone, Nicola Curreli, Giuseppe Mazzarella, and Alessandro Fanti, "Optimized design and multiphysics analysis of a Ka-band stacked antenna for CubeSat applications", *IEEE Journal on Multiscale and Multiphysics Computational Techniques*, Vol. 6, pp:143–157, 2021.
22. Hao Xu, Zhijiao Chen, Haiwen Liu, Le Chang, Taotao Huang, Sheng Ye, Lina Zhang, and Chao Du, "Single-fed dual-circularly polarized stacked dielectric resonator antenna for K/Ka-band UAV satellite communications", *IEEE Trans. Veh. Technol.*, Vol. 71, No. 4, pp:4449–4453, April 2022.
23. Muhammad M. Tahseen, and Ahmed A. Kishk, "Flexible and portable textile-reflectarray backed by frequency selective surface", *IEEE Antennas and Wirel. Propag. Lett.*, Vol. 17, No. 1, pp:46–49, January 2018.
24. Samuel Ver Hoeye, Miguel Fernández, Leticia Alonso, Carlos Vázquez Antuña Pascal Ghekiere, and Javier Ardura Casas, "A novel surface-independent textile fully woven UHF RFID tag", *IEEE Transac. Antennas and Propag.*, Vol. 70, No. 11, pp:10156–10165, November 2022.
25. Ankita Katyal, and Ananjan Basu, "Compact and broadband stacked microstrip patch antenna for target scanning applications", *IEEE Antennas and Wirel. Propag. Lett.*, Vol. 16, pp:381–384, 2017.

Design concepts of stacked microstrip antennas

2.1 INTRODUCTION

Planar/printed stacked microstrip patch antennas play a vital role in today's wireless communication and have a wide range of applications, including remote sensing and biomedical imaging. The design of these antennas requires thorough analysis to ensure optimal performance. This chapter will provide a detailed discussion of all the design aspects of stacked patch antennas. It will cover the concept of multiple resonances in stacked antennas, which is attributed to the presence of multiple stacked resonators, and can contribute to a broad bandwidth. The electromagnetic coupling among the layers is a fundamental phenomenon that activates the stacked parasitic layers, facilitates broadband impedance matching, and contributes to the achievement of broadband and multiband antenna designs. Additionally, the chapter will explore topics such as the choice of driven patch substrate, the impact of surface waves, and methods to minimize their effect to maximize the coupled energy to the stacked layers. Finally, the chapter will present various design case studies including measured results of different antenna parameters.

2.2 CONCEPT OF MULTIPLE RESONANCES

The basic printed microstrip patch antenna is a resonant structure with a narrow bandwidth. To slightly increase the resonance bandwidth, aperture-coupled or proximity-coupled feed can be chosen. Additionally, using a thicker dielectric substrate can also lead to some increase in bandwidth, although this change is relatively small. If a printed antenna needs to be made multiband or broadband, a stacked configuration is an optimal solution. Multiple stacked patches are placed above the planar microstrip antenna to achieve this. The electromagnetic coupling among the multiple stacked layers ensures broadband or multiband impedance matching

of the stacked antenna. When the electromagnetic energy from the driven patch is coupled with the parasitic patches, they resonate along with the driven patch, resulting in multiple resonances of the antenna. The resonant frequency of each stacked layer depends on patch dimensions, shape, and the dielectric properties of the chosen substrates. Design equations of microstrip antennas can be used to calculate the stacked patch dimensions [1], which are chosen to resonate at frequencies near the resonant frequency of the driven patch. Optimizing the parasitic patch dimensions and substrate parameters achieves proper coupling among the resonances, leading to an overall broadband antenna response.

2.3 SURFACE WAVES

In Chapter 1, we discussed how surface waves propagate beneath the driven patch layer and within the substrate. These waves are confined within the substrate, but at the substrate's edge, they diffract and radiate energy outside in unintended directions, leading to side lobes in the radiation pattern. This unwanted energy trapped within the substrate reduces the antenna's efficiency and affects the radiation pattern. It's essential to minimize these surface waves during antenna design. In stacked antenna designs, multiple substrates are arranged in a stacked configuration with multiple resonating patches printed over them. Surface waves mostly exist within the substrate beneath the driven patch. To minimize these waves, the choice of the lowermost substrate in the stacked antenna design is crucial. Thicker substrates in microstrip antennas store more energy due to the capacitive effect, allowing more surface waves to be confined within them. Consequently, choosing a thinner substrate at the driven patch layer offers a better reduction in surface waves. However, thick dielectric substrates are preferred for enhancing the bandwidth by lowering the Q value of the antenna. Therefore, selecting the proper substrate height at the lower layer beneath the driven patch is crucial for the stacked microstrip antenna's performance.

The surface waves can be avoided if the substrate height beneath the driven patch follows the criteria given in Equation (2.1) [2].

$$\frac{h}{\lambda} < \frac{0.3}{2\pi\sqrt{\epsilon_r}} \quad (2.1)$$

where h is substrate height, λ is the free-space wavelength at operating frequency, and ϵ_r is the dielectric constant of the substrate. Further, as the dielectric constant is inversely proportional to the height in the above equation, the dielectric constant will be higher for thinner substrate.

Note that the substrate thickness used for the stacked elements can be thicker as they are of a limited extent and do not produce surface waves.

2.4 SURFACE CURRENTS

When the printed microstrip antenna gets excited through the feed, surface currents propagate through the metal patch and the associated fields fringe out from the patch end and terminate at the ground. The propagation of surface currents is the deciding factor for the modes existing in the antenna structure. The dominant mode of propagation in microstrip antenna is TM_{mn} mode. The longitudinal or unidirectional current flow is associated with TM_{0n} or TM_{n0} (assuming the microstrip patch is placed in the x - y plane) modes of propagation, while the surface current having both transverse and longitudinal vectors is associated with TM_{mn} mode of propagation. The surface currents can thus give information about the polarization of the radiated waves, according to the propagating modes.

2.5 DESIGN METHODOLOGY OF STACKED MICROSTRIP ANTENNAS

As previously discussed, microstrip patch antennas offer the benefits of a planar, compact, and simple architecture. It is important to maintain these attractive features while implementing techniques to enhance their bandwidth. For a single-layer patch antenna, an increase in the bandwidth can be achieved by using a thicker substrate to lower the antenna's Q value, resulting in a wider bandwidth. However, there is a trade-off between losses due to surface waves (caused by a thicker dielectric substrate layer) and reducing the antenna's efficiency to achieve the desired bandwidth. Therefore, the stacked patch antenna configuration is considered to be an optimal solution. The design of microstrip stacked antennas starts with the design of a basic microstrip patch antenna, which is then extended to the stacked configuration using parasitic patches etched over multiple substrates. The design equations of the microstrip patch antenna are used to calculate the dimensions of the driven patch of the stacked antenna. The physical patch parameters are calculated using transmission-line equations given by Equations (1.1)–(1.5). The patch antenna is initially designed by following the above equations. When fed with an impedance-matched transmission line, the patch antenna resonates at its resonant frequency. Furthermore, when the designed microstrip patch antenna is extended to a stacked configuration, impedance matching needs to be done for the overall stacked antenna design (not for the driven patch only, as was the case with the basic microstrip antenna). For the designed stacked antenna structure, the coupling among the multiple resonators may yield broadband/multiband impedance matching, which can be further optimized to achieve the desired bandwidth or a multiband response. The choice of substrates, both above and below the driven patch, is crucial for achieving broadband impedance matching. Thicker

substrates with low dielectric constants give broader bandwidth by lowering the Q value of the antenna.

As discussed in Section 2.3, the dielectric substrate used beneath the driven patch has constraints on its physical parameters to avoid surface currents. However, for upper-layer substrates, thicker and lower dielectric constant material can be used to obtain broadband impedance matching by lowering the dielectric losses and increasing the radiated power (by lowering the antenna's Q value). This further increases the antenna gain as the electrical size of the patch at the resonance will increase with the lower dielectric constant material. However, the use of thick substrates increases the overall antenna volume; therefore there is a design trade-off that needs to be considered according to the system requirements.

Further, the shape and dimensions of parasitic patches are the deciding factors for the other generated resonances (except the driven patch resonance), resulting in the multiband/broadband response of the stacked antenna. The dimensions of parasitic patches can be approximately calculated using the same transmission-line equations (1.1)–(1.5) and can be further optimized to achieve broadband impedance matching. Moreover, the selection of the shape of the parasitic patches and their placement with respect to the driven patch are important for obtaining broadband response.

Next, the design methodology of a patch antenna fed by a coaxial probe is discussed in this section. The patch dimensions can be calculated using the same set of formulae as for the microstrip-fed patch antenna. The probe inductance in this case gets quite significant when the substrate thickness is increased, which needs to be compensated. For coaxial fed patch antenna, its input impedance and feed inductance are given by [3]:

$$Z_{in} = Z_R + jX_L \quad (2.2)$$

$$X_L = \frac{\eta}{\pi} \tan(0.5kh_1) \ln\left(\frac{2.25}{kd}\right) \quad (2.3)$$

A design methodology for broadband multi-layered stacked antenna structures is proposed in [3], where this inductance can be compensated through the equivalent capacitance. The analytical formulae for the calculation of estimated resonant frequencies, for multiple stacked resonators, specifically for the case of two stacked patches are listed below [3]. The case of the probe-fed two-layered stacked antenna is considered, as shown in Figure 2.1.

To calculate the resonant frequencies, voltage across the layers is considered. The total voltage across the stacked antenna is taken as the sum of voltages across the individual substrate layers. For the present case, it is given by Equations (2.4) and (2.5):

$$V_o = V_{o1} + V_{o2} + V_{o3} + V_{o4} \quad (2.4)$$

$$V_o = (h_1 + h_2 + h_3 + h_4) E_z \quad (2.5)$$

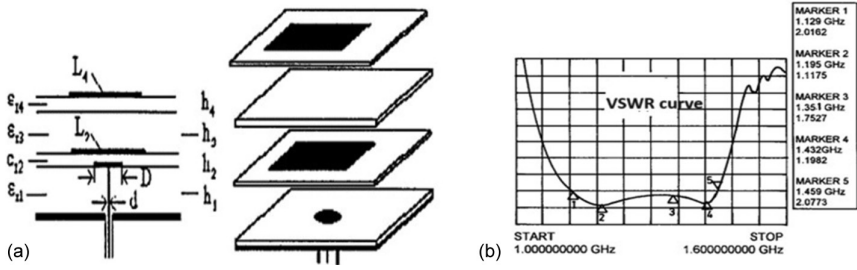


Figure 2.1 (a) Geometry of two-layered probe-fed stacked microstrip antenna, (b) VSWR curve reflecting broadband response. Reproduced with permission from IEEE [3].

Further,

$$D_z = \epsilon_o \epsilon_{re} E_z \quad (2.6)$$

where D_z and ϵ_{re} are the effective flux density and effective dielectric constants, respectively.

According to electromagnetic boundary conditions:

$$D_z = D_{z1} = D_{z2} = D_{z3} = D_{z4} \quad (2.7)$$

$$D_{zi} = \epsilon_o \epsilon_{ri} E_{zi} \quad (2.8)$$

$$V_{oi} = h_i E_{zi} \quad (2.9)$$

Substituting Equation (2.9) in Equation (2.4), we get:

$$V_o = \sum_{i=1}^4 h_i E_{zi} \quad (2.10)$$

Also

$$V_o = \frac{D_z}{\epsilon_o} \sum_{i=1}^4 \frac{h_i}{\epsilon_{ri}} \quad (2.11)$$

Again from Equations (2.2) and (2.3), we get:

$$V_o = \frac{D_z}{\epsilon_o \epsilon_{re}} \sum_{i=1}^4 h_i \quad (2.12)$$

Now from Equations (2.11) and (2.12), we get effective permittivity as:

$$\epsilon_{re} = \frac{\sum_{i=1}^4 h_i}{\sum_{i=1}^4 \frac{h_i}{\epsilon_{ri}}} \quad (2.13)$$

The effective permittivity of the second substrate is given by:

$$\epsilon_{e2} = \frac{\epsilon_{re} + 1}{2} + \frac{\epsilon_{re} - 1}{2} \left[1 + \frac{10.0 \sum_{i=1}^2 h_i}{L_2} \right]^{-1/2} \quad (2.14)$$

and resonant frequency can be expressed as Equation (2.15) according to the modified transmission-line model [4].

$$F_{r2} = \frac{C_o}{2L_2 \sqrt{\epsilon_{e2}}} \cdot \frac{1 - \zeta_2}{1 + \zeta_2 \ln \left(\frac{1.123 L_2 \sqrt{\epsilon_{e2}}}{\sum_{i=1}^2 h_i} \right)} \quad (2.15)$$

Here C_o is the velocity of light in free space,

$$\text{While } \zeta_2 = \frac{2 \sum_{i=1}^2 h_i}{\pi T_2 \epsilon_{e2} L_2} \quad (2.16)$$

$$T_2 = \frac{\sum_{i=1}^2 h_i}{L_2} \left[\frac{L_2}{\sum_{i=1}^2 h_i} + 1.393 + 0.667 \ln \left(\frac{L_2}{\sum_{i=1}^2 h_i} + 1.444 \right) \right] \quad \text{And (2.17)}$$

Similarly the resonant frequency of the upper patch can calculated based on Equations (2.18)–(2.20).

$$\epsilon_{e4} = \frac{\epsilon_{re} + 1}{2} + \frac{\epsilon_{re} - 1}{2} \left[1 + \frac{10.0 \sum_{i=1}^4 h_i}{L_4} \right]^{-1/2} \quad (2.18)$$

$$F_{r4} = \frac{C_o}{2(L_4 + \Delta L_4) \sqrt{\epsilon_{e4}}} \quad (2.19)$$

where

$$\Delta L_4 = 0.412 \sum_{i=1}^4 b_i \left[\frac{\epsilon_{e4} + 0.3}{\epsilon_{e4} - 0.258} \right] \cdot \frac{\frac{L_4}{\sum_{i=1}^4 b_i} + 0.264}{\frac{L_4}{\sum_{i=1}^4 b_i} + 0.8} \quad (2.20)$$

The above set of equations can be used to predict the resonant frequencies of stacked patches and get an approximate stacked antenna design for the desired response.

2.6 STACKED MICROSTRIP ANTENNA DESIGN EXAMPLES

2.6.1 Rectangular microstrip-fed stacked antenna design

A broadband stacked antenna operating in the C-band region is presented in [5]. The proposed stacked antenna features three layers, including one driven patch and two parasitic patches etched onto dielectric substrates with varying dielectric constants and substrate heights. The design incorporates specific criteria to minimize the impact of surface waves, with the driven patch substrate being thinner and having a higher dielectric constant compared to the upper substrates. The upper substrates, on the other hand, have a lower dielectric constant and are thicker to maximize the impedance bandwidth. This stacked configuration aims to improve electromagnetic coupling among the layers, resulting in broadened impedance matching and enhanced overall antenna gain. Qualitative analysis is required at every stage of the antenna design process to ensure the desired antenna response in all aspects. To begin with, a basic microstrip patch antenna with only a driven patch is designed using transmission-line equations at a centre frequency of 6 GHz. The substrate height is set according to specific guidelines to suppress surface waves. The antenna, with a substrate height of 0.508 mm and a dielectric constant of 3.6, is fed using a shifted feed line to achieve some degree of input impedance matching in the absence of a quarter wave transformer. As a result, the patch antenna resonates towards 5 GHz due to the diagonal flow of current caused by the shifted feed line, leading to an increased electrical length of the antenna.

2.6.1.1 Effect of parasitic substrate and patch parameters

The antenna is stacked with a parasitic patch etched over a substrate with a lower dielectric constant, to broaden the antenna bandwidth. The

parasitic patch dimensions are estimated using equations for microstrip patch antenna dimensions. The parasitic patch dimensions are calculated such that it resonates at the frequency near the driven patch resonance. These closely spaced resonances, when optimized properly, can give broadband response. To achieve such closely spaced resonances, the height of substrate between the two patches should follow Equation (2.21) [6]. According to [6], the antenna having distance between the lower patch and parasitic patch (height of second substrate layer) within the limit of Equation (2.21), has two resonant frequencies. When both the resonances are close enough, they give a broadband response. For this case, the electric field between the patches consists mainly of the E_z component, and the magnetic field consists of the H_y component. Thus, the antenna resonates in TM_{10} mode as the usual microstrip patch antenna and contributes to two resonances corresponding to both the patches. The antenna now behaves as a simple microstrip antenna with a thicker substrate and a single effective ϵ_r , which contributes to an increase in gain and bandwidth. On increasing the height between patches approximately to 0.5λ , the E_z and H_y components between patches decrease, and thus the current on the parasitic patch decreases, while the E_x component increases. The E_x component forms a standing wave and the antenna behaves as a resonator. In this case, fields near the patches are out of phase with respect to each other, which in the boresight direction add in phase, thus increasing the overall gain of the antenna, but with narrow bandwidth. The effect of different substrate heights (h_2) is studied and shown in Figure 2.2(a) and chosen $h_2 = 70$ mil (1.78 cm).

$$h_2 < 0.1\lambda. \quad (2.21)$$

2.6.1.2 Effect of placement of parasitic patch and feed parasitics

Further, the modification in the design is studied with the addition of a step transformer between the feed line and the driven patch, to compensate

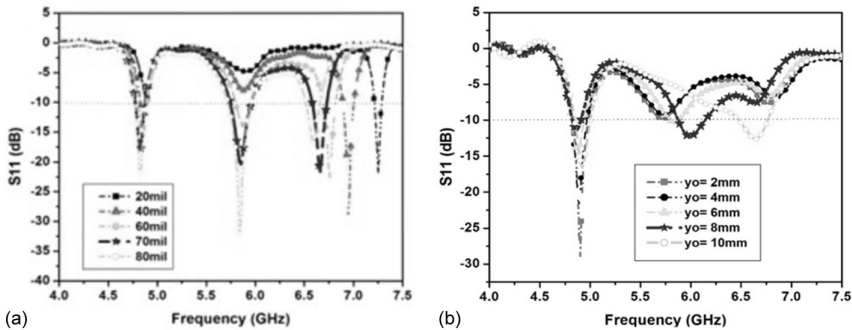


Figure 2.2 S11 response of two-layered stacked antenna (a) for different h_2 and offset $y_0 = 6$ mm, (b) for different offset y_0 and $h_2 = 70$ mil.

for the feed parasitics. Moreover, an offset (y_o) of the parasitic patch with respect to the driven patch is created and studied in terms of changes in the antenna performance as shown in Figure 2.2(b). These changes are shown to improve the coupling among the layers, along with improved impedance matching, when optimized properly. The stages of design modifications are shown in Figure 2.3. Also, the changes in the Smith chart response for different design stages are shown in Figure 2.4.

The step transformer adds the step parasitics to the feed line and helps in improved impedance matching by cancelling the unwanted parasitic effects at the feed line and the patch junction. The initial width of step transformer is taken to be 2mm. The equivalent circuit parameters representing added parasitics are shown in Figure 2.5, and the calculation of these parasitics is discussed in detail in Chapter 3. These extra parasitics affect the higher frequencies and improve the overall resonance as can be seen from the Smith chart. The coupling is further improved when the parasitic patch is displaced at some optimum offset with respect to the lower patch, as depicted in Figure 2.4(c). When the parasitic patch has the maximum area above the

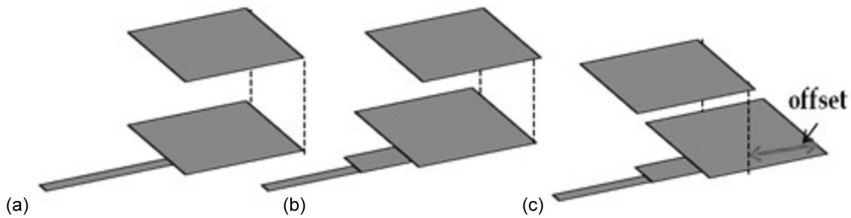


Figure 2.3 Stages of two-layered stacked antenna design, (a) parasitic patch aligned with driven patch, (b) parasitic patch aligned with driven patch and with step transformer, (c) parasitic patch at offset (y_o) with respect to driven patch and having step transformer.

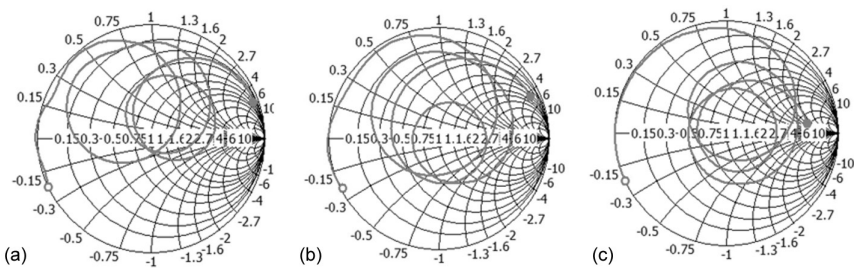


Figure 2.4 Smith chart response of two-layered stacked antenna, (a) parasitic patch aligned with driven patch, (b) parasitic patch aligned with driven patch and with step transformer, (c) parasitic patch at offset (y_o) with respect to driven patch and having step transformer. Reproduced with permission of IEEE [5].

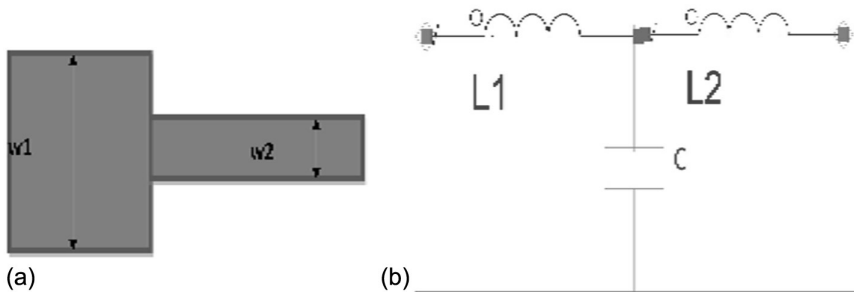


Figure 2.5 (a) Step discontinuity, (b) its equivalent circuit.

feed and the edge of the patch, there is enhanced electromagnetic coupling among the two layers and hence improved impedance matching. A better response is obtained for an offset of 8 mm, in this case.

2.6.1.3 Effect of second parasitic patch and substrate parameters

The stacked antenna design is further modified by adding one more parasitic layer above the first one. Stacking of the additional resonant parasitic patch, with proper placement, provides further improvement in impedance matching and wider bandwidth. The substrate parameters of the second parasitic patch are also crucial for the antenna's performance and thus should be chosen to enhance the overall antenna's performance. A thicker substrate compared to the driven patch substrate is selected such that it helps achieve wider bandwidth but within the constraints given by Equation (2.21). The dielectric constant is ($\epsilon_{r2} = 2.2$), the same as the first parasitic patch substrate, but the height chosen is higher (obtained after optimization) for overall improved antenna response. The antenna response for different heights of the upper-most substrate (h_3) is shown in Figure 2.6, which shows that $h_3 = 100$ mil (2.54 mm) gives the best impedance matching compared to lower values of h_3 . Figure 2.7 depicts the response of the stacked antenna with three layers: one driven patch and two parasitic patches, along with further optimization study of the antenna's performance based on the width of the transformer section connected to the feed line. The width of the step transformer is chosen to be 1.8 mm in this case, having 36Ω impedance.

The obtained antenna design gives broadband response for optimized patch dimensions, substrate parameters, parasitic patch offset, and the width of the transformer between the feed and driven patch. The current flowing through the third patch is very low as it is loosely coupled with the driven patch, so it does not contribute much to introducing any extra resonance but helps in improving the overall impedance matching and coupling.

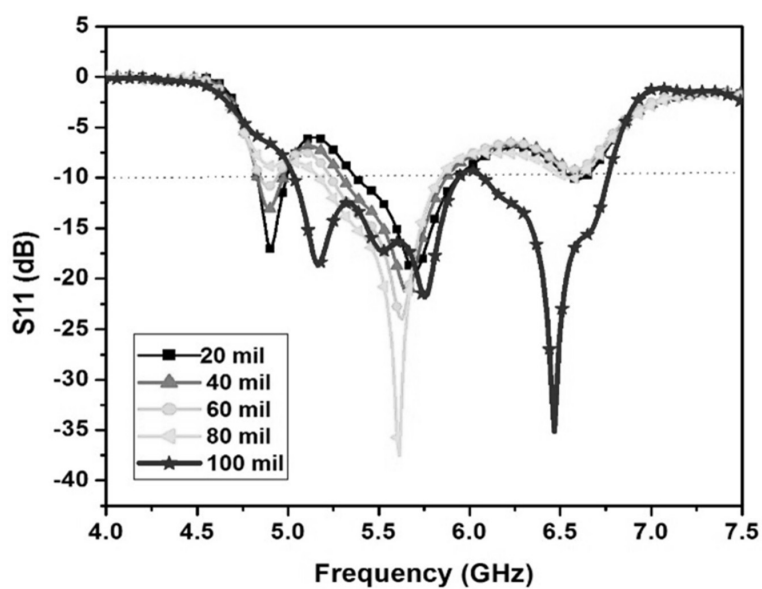


Figure 2.6 S11 response of three-layered stacked antenna for different substrate heights (h_3).

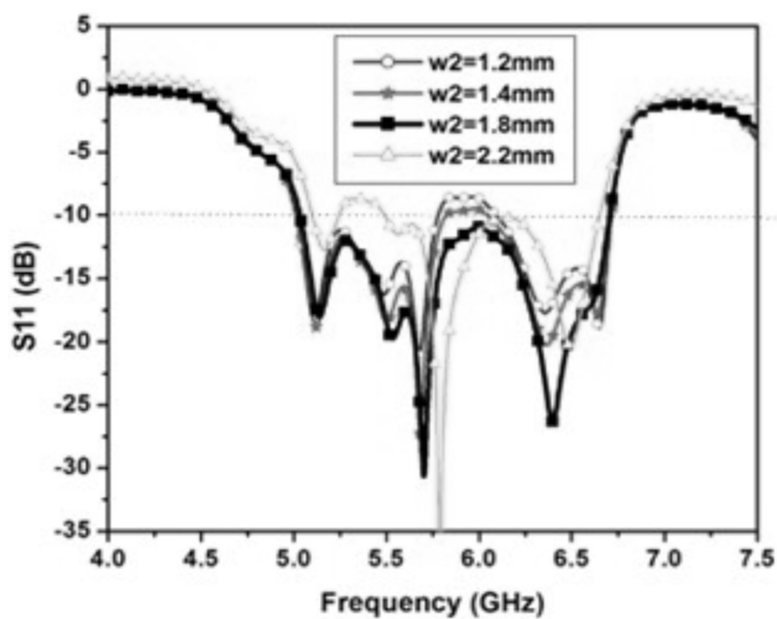


Figure 2.7 S11 response of three-layered stacked antenna for different step transformer widths.

2.6.1.4 Effect of the slot at the driven patch

Inserting a slot in the driven patch increases its electrical length and affects the antenna's resonance. Here a slot is etched near the antenna's edge, which further enhances impedance bandwidth. The resultant S_{11} response is shown in Figure 2.8. The corresponding surface current distribution is shown in Figure 2.9. The surface current graph shows the diagonal flow of current (due to shifted feed), which is dominant at lower frequencies. This indicates high cross-polarization at the lower frequencies. Moreover, the surface current distribution gives information about in-phase currents in stacked patches, generating an even mode within the band of operation. Out-of-phase currents are flowing through the stacked patches at the cut-off frequency of 6.7 GHz, causing the generation of odd mode.

The orthogonal current at the driven patch induces a similar current flow through parasitic patches via electromagnetic coupling between the layers. This results in the generation of two orthogonal modes propagating through the antenna, leading to increased cross-polar radiation. To minimize the impact of cross-polarization in applications where it is not needed, the antenna design should be further modified. This can be achieved by directing the diagonally flowing current, caused by a shifted feed, towards the longitudinal direction by meandering the patch through the proper

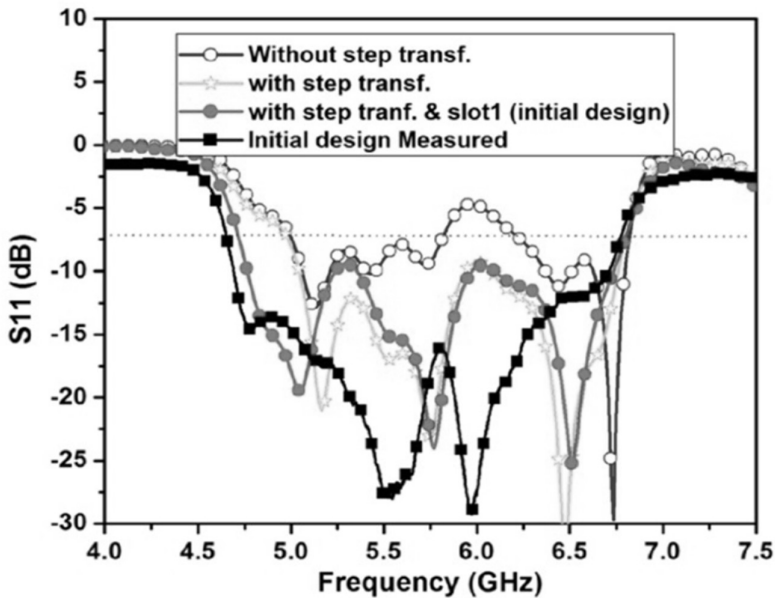


Figure 2.8 Comparison of antenna response at different stages. Reproduced with permission of IEEE [5].

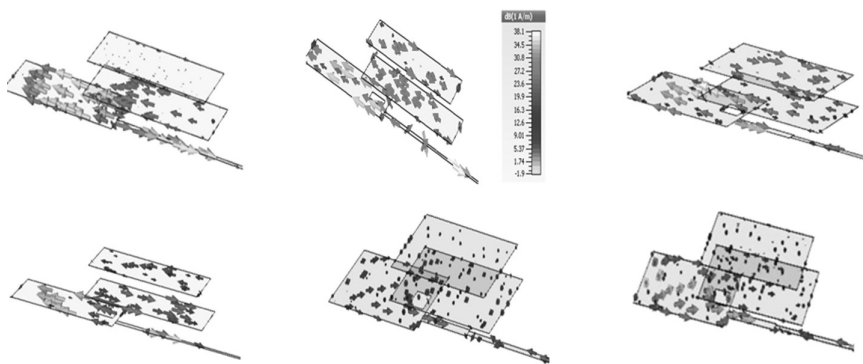


Figure 2.9 Current distribution of the initial stacked antenna design at different frequencies.

Table 2.1 Design parameters of final antenna design [5]

Parameter	Value (mm)	Parameter	Value (mm)
W	35	l_{p2}	12.3
L	35	X_s (feed shift)	1.4
w_1	15	S_{w1} (slot 1 width)	2
l_1	11.8	S_{l1} (slot 1 length)	4
w_{p1}	18	W_2	1.8
l_{p1}	13.3	W_3	1.1
y_o (offset)	6	S_{w2} (slot 2 width)	5.5
w_{p2}	18	S_{l2} (slot 2 length)	1

insertion of slots in the driven patch. In the current antenna design, a slot is etched in the driven patch, aligned with the feed direction, to direct the current longitudinally and reduce the cross-polarization effect. The addition of this slot enhances the antenna’s overall bandwidth and significantly reduces cross-polarization, particularly at lower frequencies. The complete antenna parameters are listed in Table 2.1.

The current distribution of the antenna after both slots are placed in the driven patch is shown in Figure 2.10, which clearly shows the longitudinal flow.

2.6.1.5 Properties of designed stacked antenna

The design of the proposed stacked antenna after all the modifications and optimizations is as given in Figure 2.11. The antenna, after the insertion of two slots, shows a much-improved cross-polar power ratio even with a shifted feed. The attained bandwidth of the proposed stacked antenna is 35%, with a peak gain of 8.2 dBi, a peak efficiency of 95%, and an average

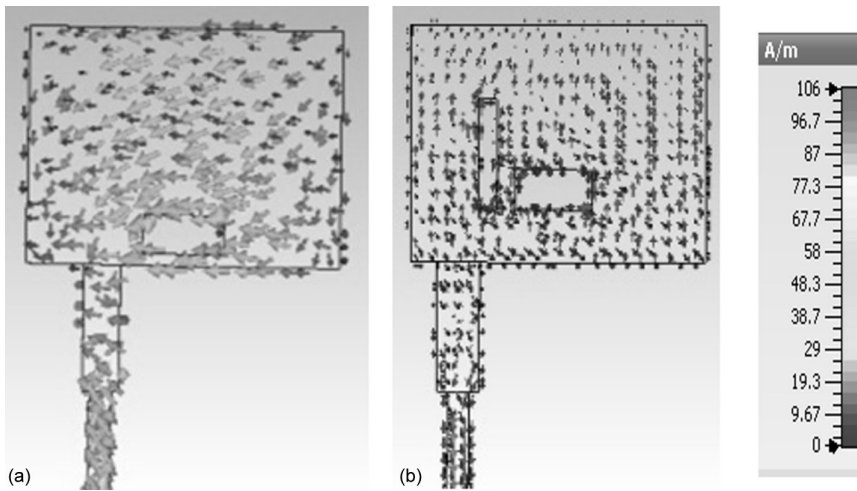


Figure 2.10 Surface current distribution of (a) initial antenna and (b) improved antenna at 5 GHz. Reproduced with permission from IEEE [5].

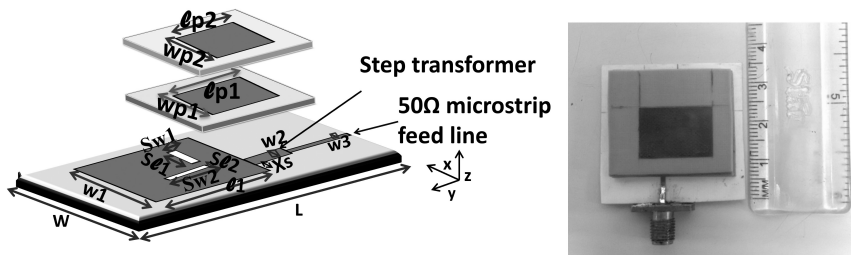


Figure 2.11 (a) Improved/proposed stacked antenna geometry, (b) fabricated antenna. Reproduced with permission from IEEE [5].

efficiency of 80%. These results are shown in Figure 2.12 and Figure 2.13 respectively. The improvement in achieved reduction of cross-polar levels is shown in Figure 2.14. The radiation patterns also show reduced cross-polarization, depicted in Figure 2.15. Since the ground plane of the stacked antenna is uniform and un-broken, the front-to-back ratio is high and also the radiation patterns are stable throughout the operating frequency band. This characteristic of planar stacked antennas is very useful in certain applications, where stable unidirectional antenna radiation is essential. Further, such antennas' performance is independent of the ground plane size and can be integrated with other circuits very easily having common ground. Moreover, for applications where the antenna needs to be placed above a large metallic body like a car or airplane, the performance of these antennas remains unaltered. The same has been verified for the proposed antenna, and

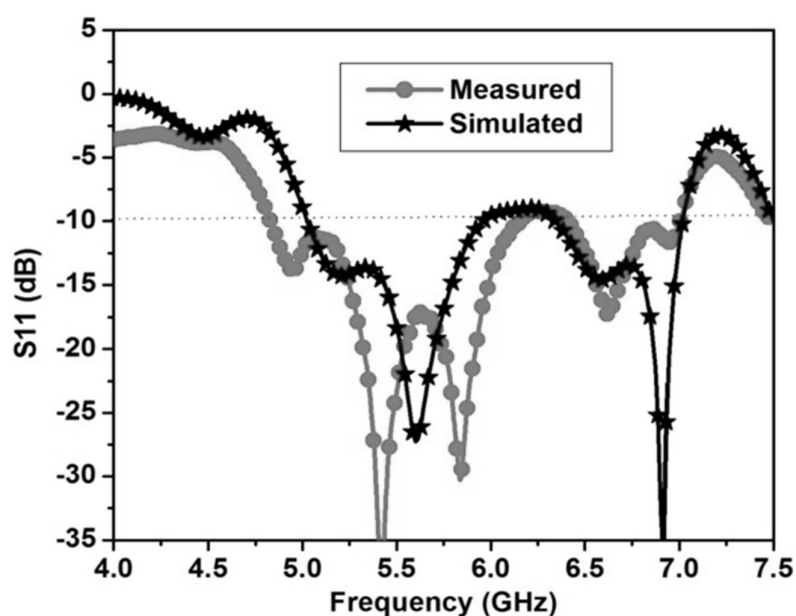


Figure 2.12 S11 response of improved/proposed stacked antenna design. Reproduced with permission from IEEE [5].

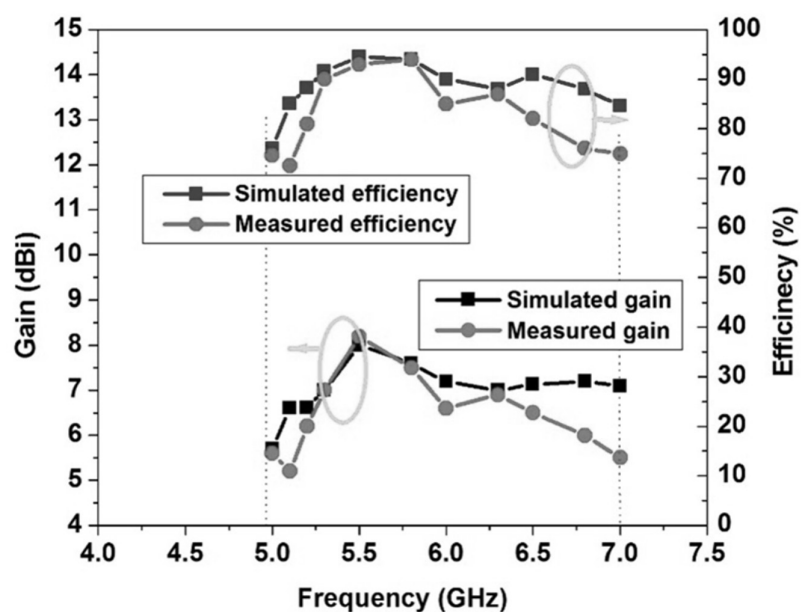


Figure 2.13 Measured vs simulated gain and efficiency graph. Reproduced with permission from IEEE [5].

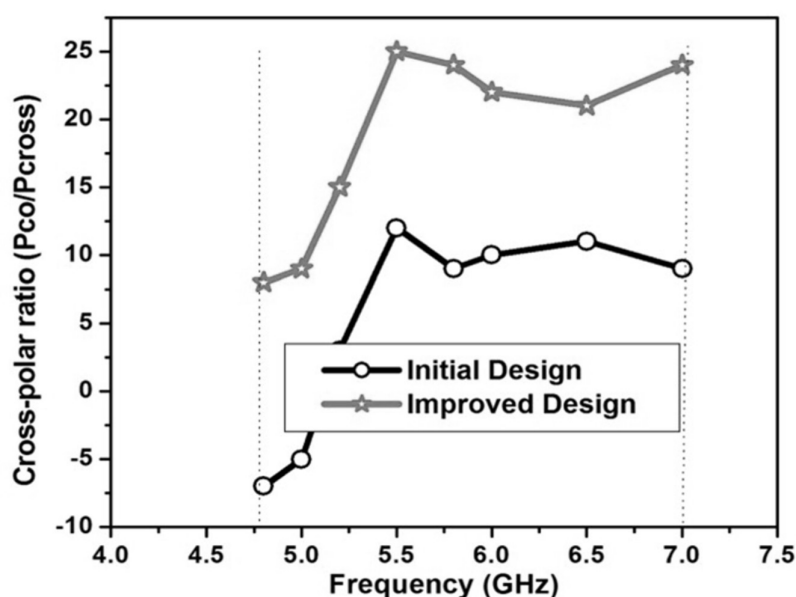


Figure 2.14 Cross-polar power ratio of the initial stacked antenna and final stacked antenna. Reproduced with permission from IEEE [5].

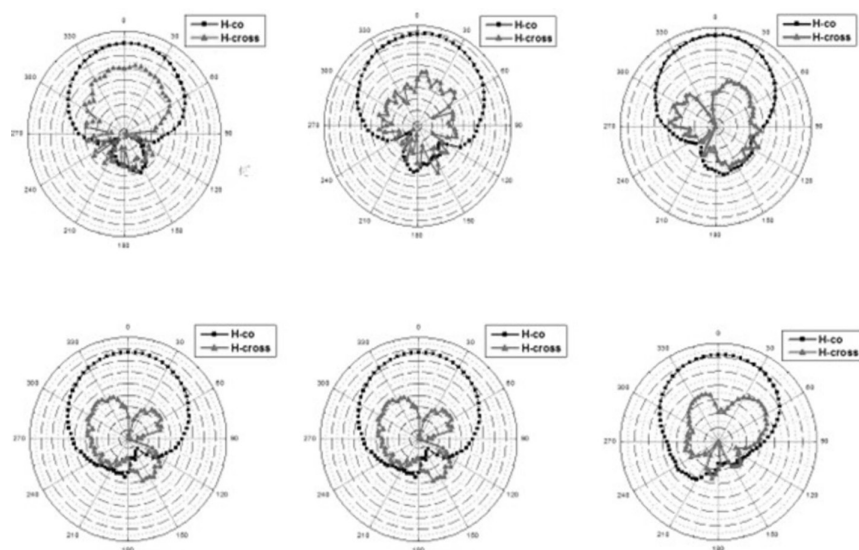


Figure 2.15 Measured H-plane co-polar and cross-polar radiation patterns of proposed antenna at different frequencies.

the antenna's response for varied ground plane sizes is studied and shown in Figure 2.16. The S_{11} response is almost stable for different ground plane sizes. Also, the S_{21} response shows less mutual coupling between consecutive elements if placed in an array structure, compared to other broadband antennas having slots at the ground (Figure 2.17). Further, the electric field distribution beneath the antenna also shows that any common ground integration with other circuits is more suitable in the case of antennas with planar ground planes, depicted in Figure 2.18 and Figure 2.19.

2.6.1.6 Modified design of stacked antenna

The bandwidth of stacked antenna is dependent on the number of stacked layers, the substrate parameters, and the relative patch parameters. The previous stacked antenna design resulted in 35% bandwidth with suppression of cross-polar power. The stacked antenna bandwidth can be further increased by increasing the upper substrate heights and some optimizations in terms of slot size and position, also offset between parasitic and driven patch along with feed offset. The new modified broadband stacked antenna design is shown in Figure 2.20. The three-layered stacked antenna has a slot at one of the radiating edges of the driven patch. The electrical length

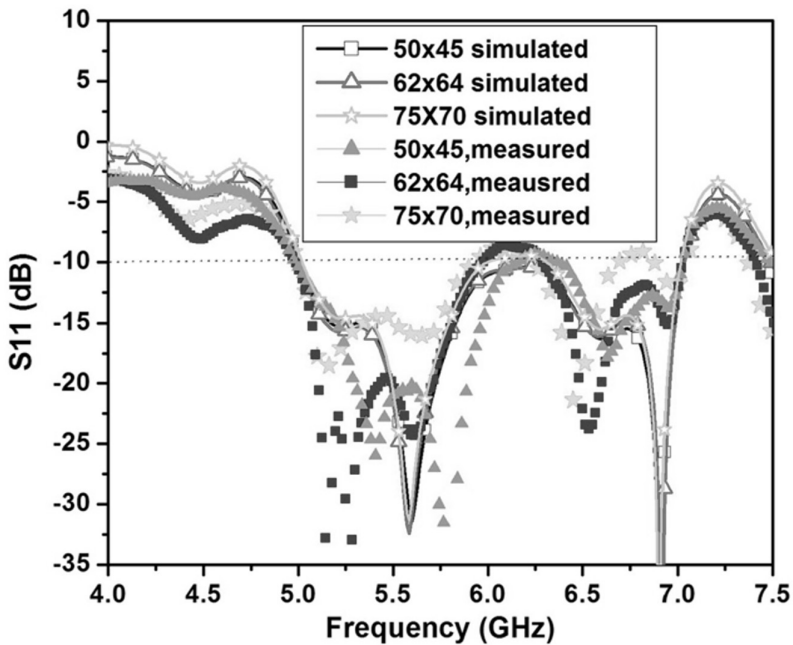


Figure 2.16 S_{11} response of proposed stacked antenna for different sizes of ground plane. Reproduced with permission from IEEE [5].

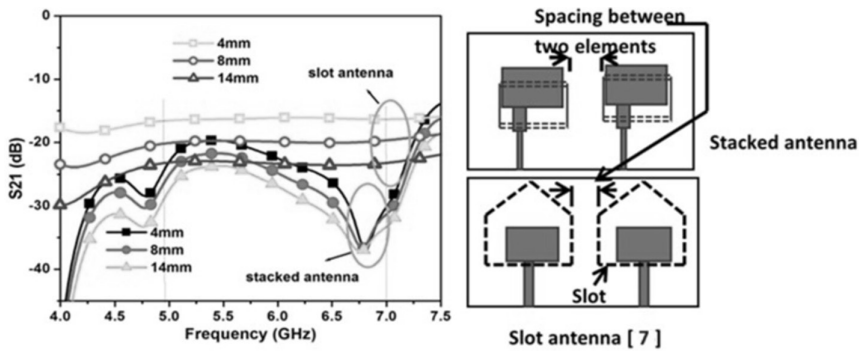


Figure 2.17 Simulated S_{21} of the proposed stacked antenna compared with a slot antenna [7] for different element spacing. Reproduced with permission from IEEE [5].

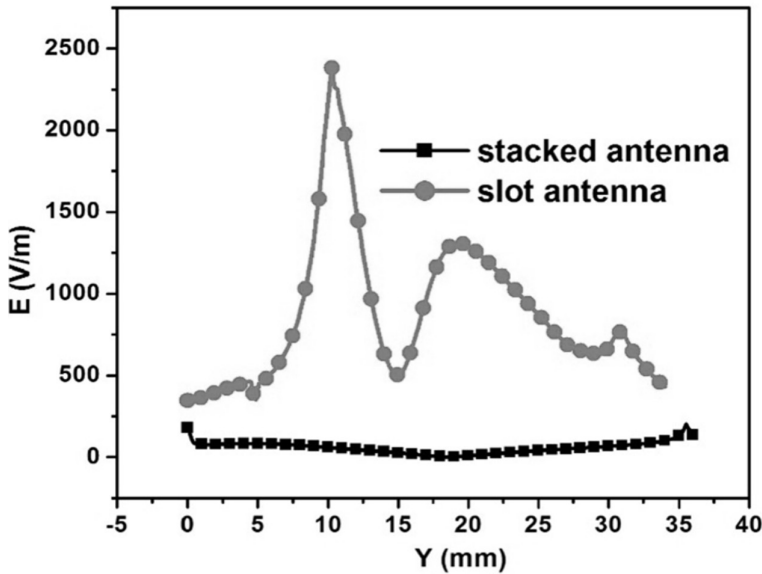


Figure 2.18 Electric field distribution beneath the ground plane and along the antenna length. Reproduced with permission from IEEE [5].

of the patch thus reduces longitudinally and the upper resonant frequency increases. Further, the slot at the radiating edge causes more fringing fields to get coupled to the parasitic patches. The antenna in this case also has the shifted feed line for achieving the broadband impedance matching, resulting in some amount of cross-polar power. The modified antenna has the bandwidth from 5.5–8.5 GHz (simulated), while 5.3–8.7 GHz (measured),

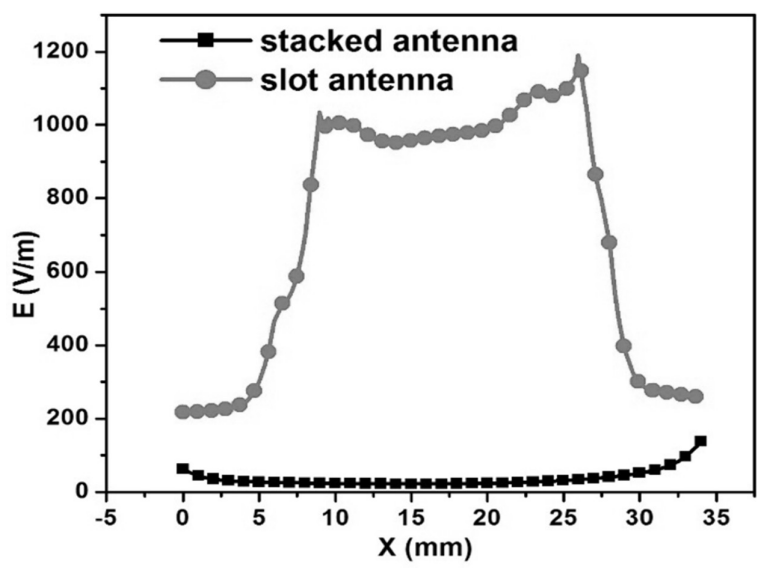


Figure 2.19 Electric field distribution beneath the ground plane, along the width of both antennas. Reproduced with permission from IEEE [5].

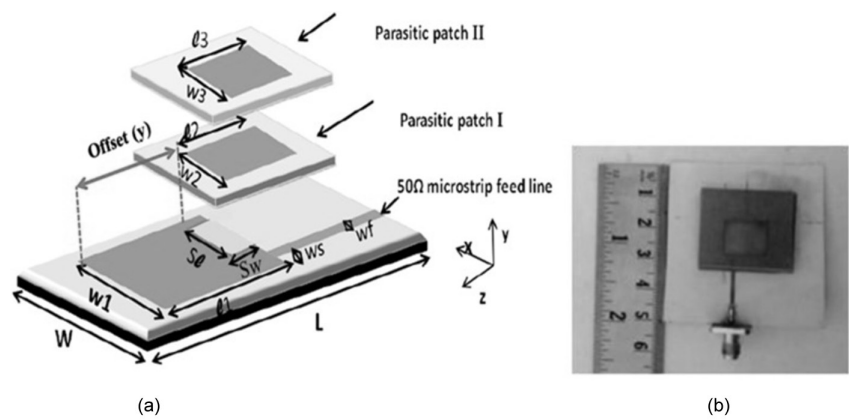


Figure 2.20 Proposed modified stacked antenna design, (a) layout, (b) fabricated antenna photograph. Reproduced with permission from IETE [8].

as shown in Figure 2.21. The antenna parameters are listed in Table 2.2 showing a compact design. The radiation patterns are showing co-polar and cross-polar power levels are depicted in Figure 2.22, and the antenna gain with respect to frequency is shown in Figure 2.23. For applications where cross-polarization power can be tolerated and need not be strictly

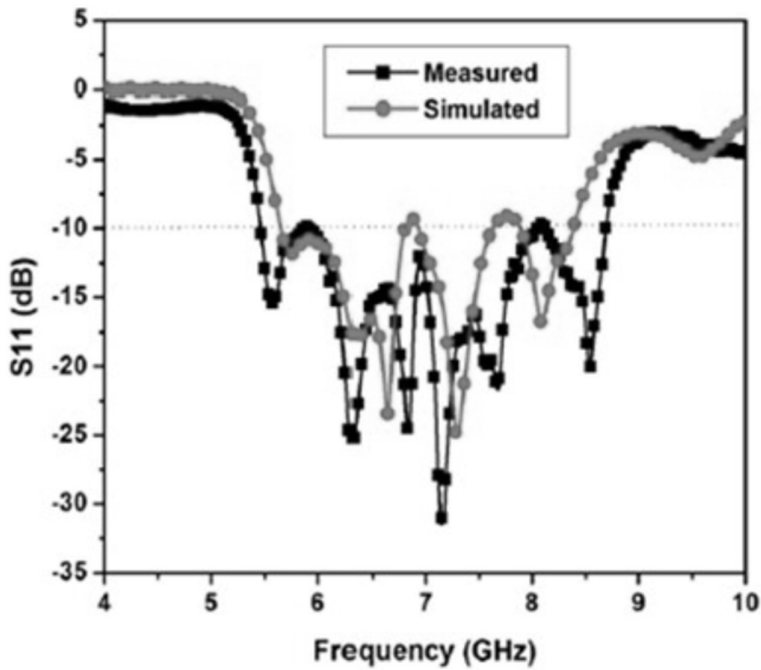


Figure 2.21 S11 response of the proposed modified stacked antenna showing improved bandwidth.

Table 2.2 Design parameters of proposed modified stacked antenna [8]

Parameter	Value (mm)	Parameter	Value (mm)
W	52	w_3	13.6
L	50	l_3	12
w_1	12	W_f	1.1
l_1	10.89	W_s	1.95
w_2	13	S_l	4.4
L_2	11	S_w	2.59
y	7.4	ϵ_{r1}	3.6
h_1	0.508	ϵ_{r2}	2.2
h_2	1.5	ϵ_{r3}	2.2
h_3	2.5		

suppressed, such an antenna ensures a much broader bandwidth with comparatively reduced dimensions. These antennas are useful in applications such as remote sensing, satellite communication, etc., where cross-polarized power is also useful for performance.

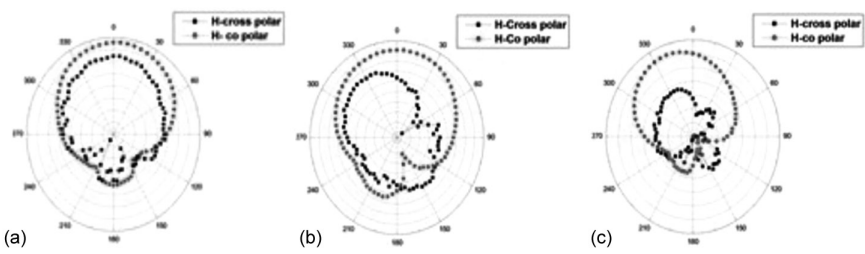


Figure 2.22 Radiation patterns of proposed modified stacked antenna at (a) 6 GHz, (b) 7 GHz, (c) 8 GHz, showing increased cross-polar levels. Reproduced with permission from IETE [8].

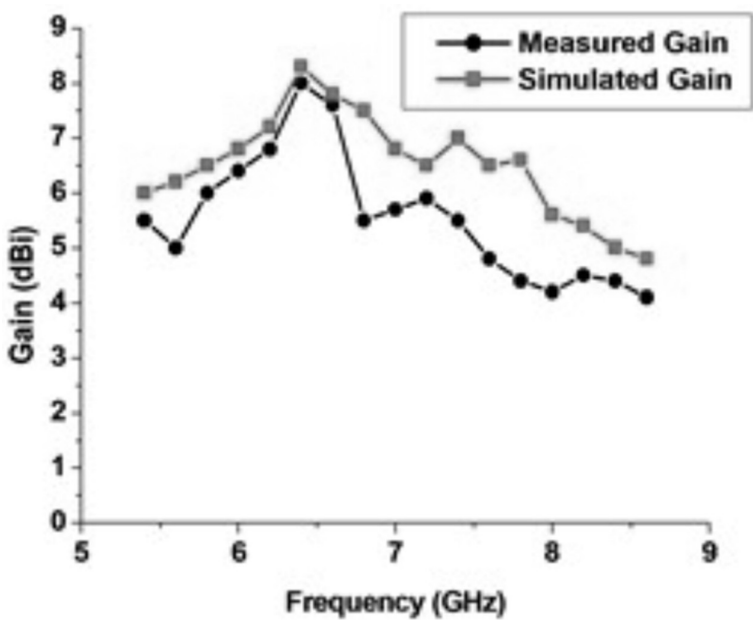


Figure 2.23 Simulated and measured gain of the proposed modified stacked antenna. Reproduced with permission from IETE [8].

2.6.2 H-shaped stacked patch antenna design

An H-shaped stacked antenna design, shown to have improved bandwidth along with a miniaturized design, is presented in [9], where two H-shaped patches are stacked one above the other. The proposed antenna geometry is shown in Figure 2.24. The initial antenna parameters for the rectangular patch are calculated using Equations (1.1)–(1.5), where $l \approx \lambda/2$, i.e. $\theta = \pi$.

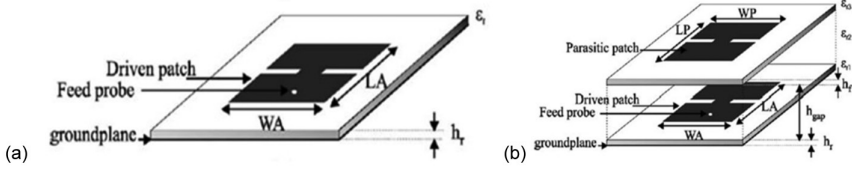


Figure 2.24 (a) Geometry of single-layer H-shaped patch antenna, (b) geometry of stacked H-shaped patch antenna. Dimensions in mm: $W_A = 40$, $L_A = 40$, $h_f = 1$, $W_P = 59$, $L_P = 59$, S_{LP} (upper patch slot length) = 26, S_{LA} (lower patch slot length) = 15 and 18, $h_{gap} = 16.5$, $\epsilon_{r1} = 3.38$, $\epsilon_{r2} = 1$, $\epsilon_{r3} = 4.15$. Reproduced with permission from IEEE [9].

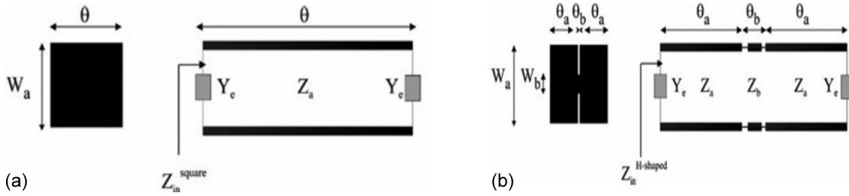


Figure 2.25 (a) Equivalent circuit of square patch, (b) equivalent circuit of H-shaped patch. Reproduced with permission from IEEE [9].

In the case of an H-shaped antenna, there is a discontinuity at the centre, compared to a rectangular patch design. A thin microstrip line connects the other two sides in an H-shaped patch. This junction gives additional freedom for performance control to the antenna design and can be tuned to improve the antenna's resonant response.

The antenna's resonant frequency can be decreased in this case by controlling the thin line parameters Z_b and θ_b . The transmission-line model of the H-shaped antenna is approximated as per Figure 2.25, which is further modified according to Figure 2.26 with the assumption that line width is significantly less and $\theta_b \ll \pi$. A simplified transmission-line equivalent is shown in Figure 2.27. The model further explains that the input impedance of an H-shaped patch antenna is equal to a square patch antenna of reduced electrical length, thus resulting in antenna miniaturization, as explained by Equations (2.22)–(2.24). This gives the expression of L as given by Equation (2.26). Further, the miniaturization factor can be chosen and controlled according to Equation (2.27).

$$Z_{in2(H-shaped)} = j2\pi fL / 2 - jZ_a \cot(\theta_a) \quad (2.22)$$

$$Z_{in2(square)} = -jZ_a \cot(\theta'_a / 2) \quad (2.23)$$

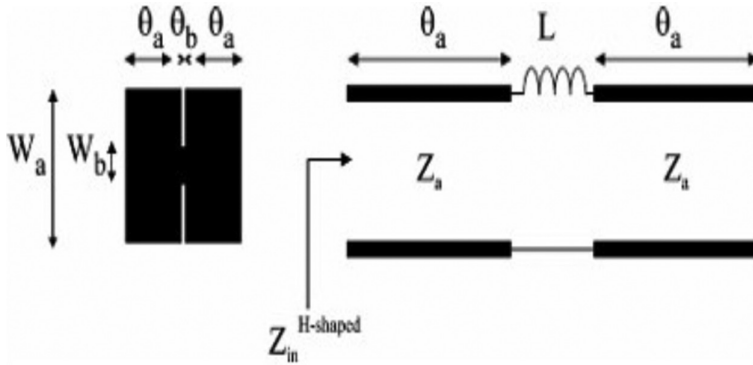


Figure 2.26 Modified equivalent circuit of H-shaped patch antenna. Reproduced with permission from IEEE [9].

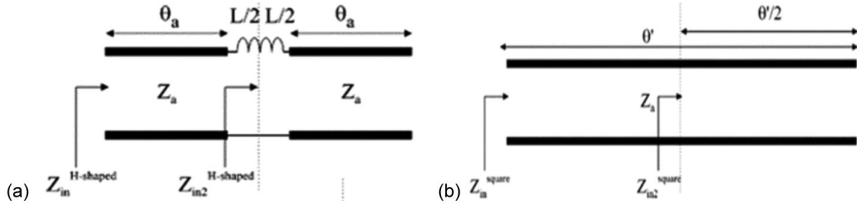


Figure 2.27 Simplified TLM equivalent of: (a) H-shaped patch antenna and (b) square-shaped patch antenna. Reproduced with permission from IEEE [9].

By equating (2.22) and (2.23), we get:

$$Z_{in2(H-shaped)} = Z_{in2(square)} \quad (2.24)$$

This gives:

$$L = \frac{2Z_a \left[\cot(\theta_a) - \cot\left(\frac{\theta'}{2}\right) \right]}{2\pi f} \quad (2.25)$$

For miniaturization, L needs to be calculated for the new frequency such that $f = n.f_o$. Thus, replacing this f in Equation (2.25) gives:

$$L = \frac{2Z_a \left[\cot(\theta_a) - \cot\left(\frac{\theta'}{2}\right) \right]}{2\pi f} \quad (2.26)$$

Further, since $2\theta_a \approx \pi$ at $f = f_o$

$$\text{Then } \theta_a \approx (n.\pi)/2 \text{ at } f = n.f_o \quad (2.27)$$

$$\text{As } \theta' = \pi \text{ at } f = n.f_o \text{ (i.e. } 1 = \lambda/2) \quad (2.28)$$

$$\text{Now } L = \frac{2Z_a [\cot(\theta_a)]}{2\pi n f_o} = \frac{2Z_a [\cot(n.\pi/2)]}{2\pi n f_o} \quad (2.29)$$

$$X_L = 2\pi n f_o L = 2Z_a \cot(n.\pi/2) \quad (2.30)$$

Thus, for the given miniaturization factor “ n ”, the new inductance of the thin line along with its reactance can be obtained by Equation (2.30).

Further, the physical length of the thin line of an H-shaped patch, now resonating at a new frequency, can be obtained from Equation (2.31) based on its relation with given physical parameters.

$$L = \frac{Z_b.l\sqrt{\epsilon_r}}{c} \quad (2.31)$$

Based on the above-mentioned design equations, the miniaturized H-shaped patch design can be obtained for the chosen miniaturization factor n , where $n = f/f_o$. The additional capacitive effect is also considered in the equivalent circuit as shown in Figure 2.28, where C_g is optimized to get the required antenna performance. The designed H-shaped antenna now resonates at its desired resonant frequency and achieves miniaturization.

Further, another H-shaped miniaturized patch is stacked above the driven H-shaped patch, as shown in Figure 2.24(b). This stacking of the parasitic patch widens the operating bandwidth of the antenna as it improves broad-band impedance matching. The results of the single-layer antenna having

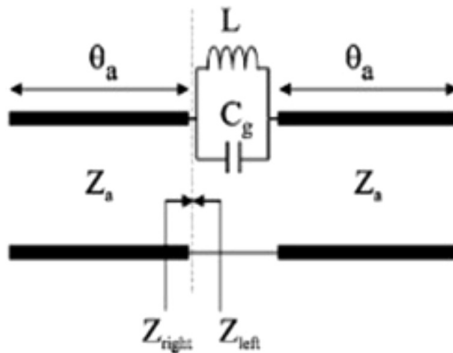


Figure 2.28 Modified TLM equivalent of H-shaped stacked antenna. Reproduced with permission from IEEE [9].

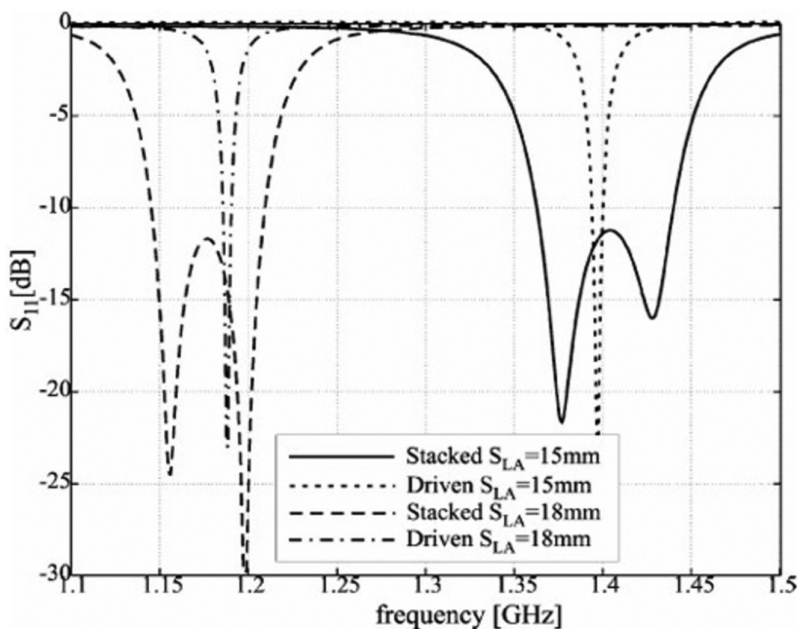


Figure 2.29 Measure return loss of H-shaped antenna for different slot lengths (S_{LA}) (H-slot) for the single layer and the stacked antenna. Reproduced with permission from IEEE [9].

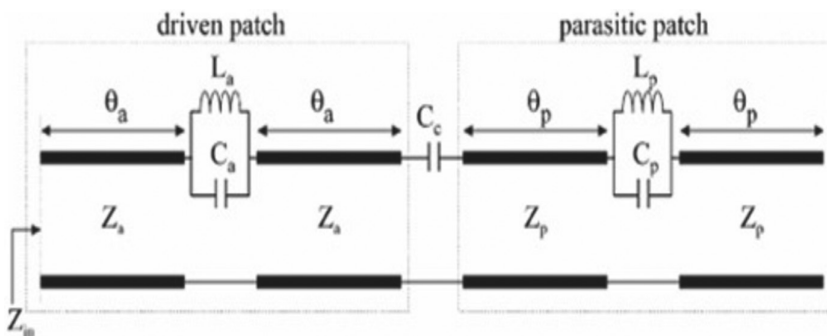


Figure 2.30 Approximate TLM equivalent of H-shaped stacked patch antenna with optimized coupling capacitance. Reproduced with permission from IEEE [9].

only a driven patch and the two-layered stacked patch antenna are shown in Figure 2.29 for different lengths of thin line in the H-shape structure (the slot/discontinuity of the H-shaped patch). The response indicates a significant bandwidth increase for the stacked antenna design. The approximate circuit model of the stacked H-shaped stacked antenna is shown in Figure 2.30.

2.6.3 E-shaped stacked patch antenna design

Microstrip antennas are typically narrowband, but their bandwidth can be expanded using various techniques. One effective method is to insert slots in the patch. The U-shaped slot, for example, has been shown to enhance antenna bandwidth due to its symmetrical structure, which increases the antenna's electrical length by causing the surface currents to follow the U-shaped boundary. In a particular study [10], a stacked antenna with a U-shaped slot in the driven patch and an E-shaped patch stacked over it as a parasitic patch was presented, as shown in Figure 2.31. The E-shaped patch, featuring two symmetrically placed slots, further contributes to broadening the antenna's bandwidth.

The initial dimensions of the patch can be determined using Equations (1.1)–(1.5). Furthermore, the final antenna dimensions can be obtained by incorporating a U-shaped slot and carrying out design optimization. The

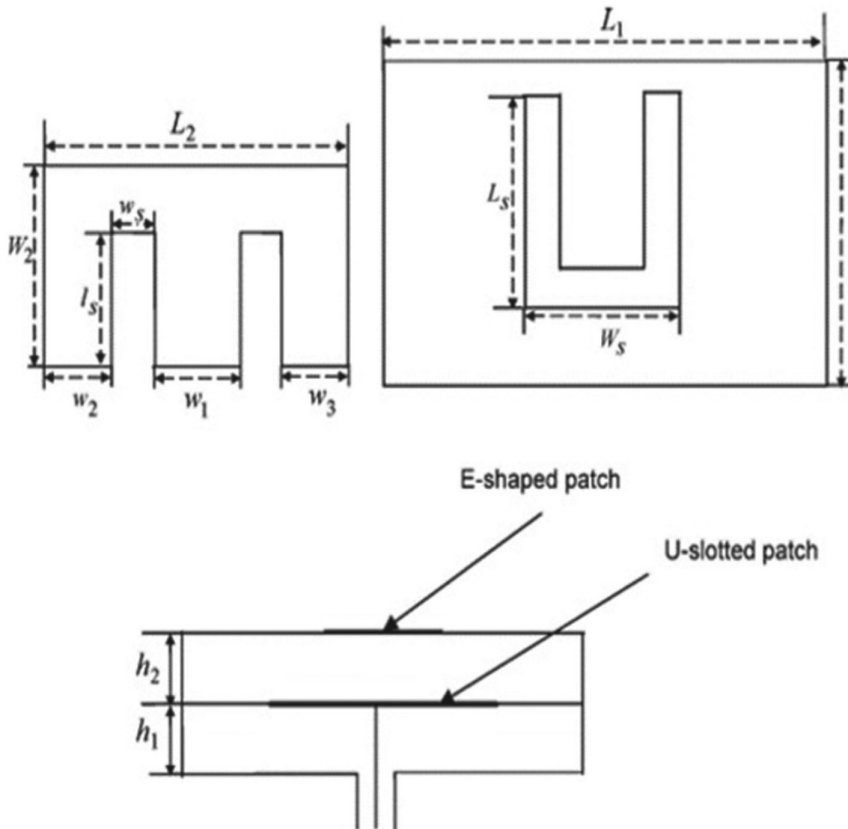


Figure 2.31 Probe-fed stacked antenna structure with U-slot in the driven patch and E-shaped parasitic patch. Reproduced with permission from IEEE [10].

antenna is designed using a 6-mm thick dielectric substrate with a relative permittivity (ϵ_r) value of 1.1.

The E-shaped patch cuts are strategically positioned above the low current distribution region of the lower patch with a slot. Placing the E-shape cuts above the U-shape cuts, with a length offset towards the low current region, plays a critical role in enhancing the antenna bandwidth. The optimized offset position is crucial in this regard. The current distribution of the proposed antenna at different frequencies (on both patches) is shown in Figure 2.32.

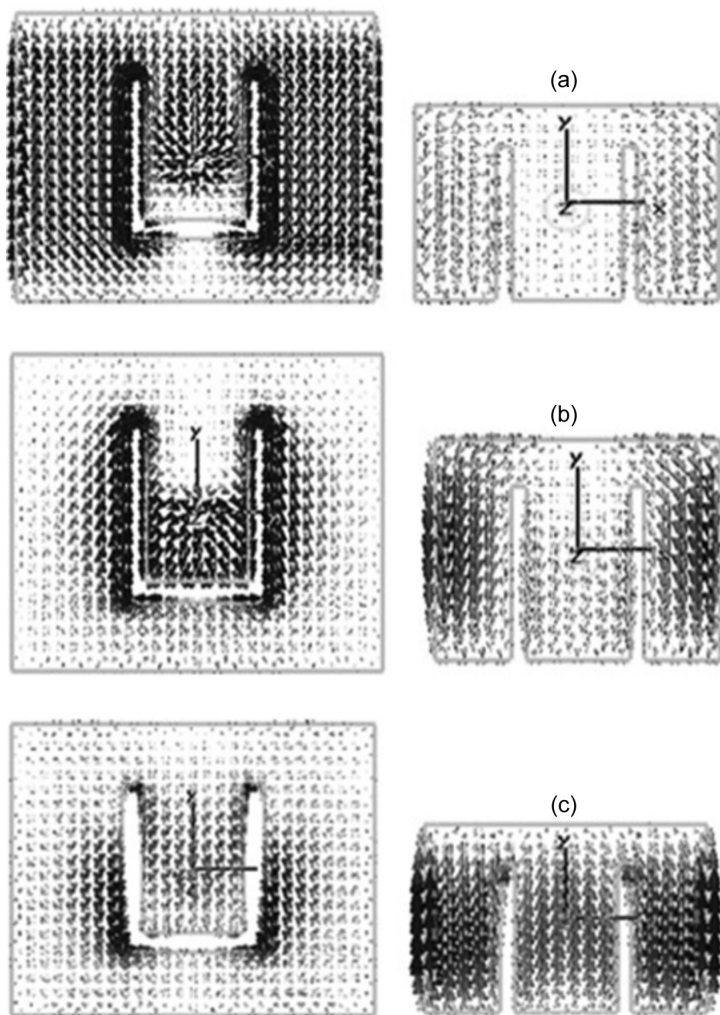


Figure 2.32 Current distributions at lower and upper patches respectively at (a) 3.48 GHz, (b) 4.48 GHz, (c) 5.60 GHz. Reproduced with permission from IEEE [10].

The dimensions of the E-shaped patch need to be calculated based on the equations for a rectangular patch antenna design with necessary modifications after inserting the two slots. The dimensions of the parasitic patch should differ from those of the lower patch (in this case, they are smaller) to create resonance through coupling at a different but nearby frequency. In this antenna design, various parameters can be adjusted to alter the antenna's performance. Factors such as the length and width of each slot, the separation of the two slots, the position and alignment of slots on different layers, and the position of the probe feed are some of the critical design parameters that contribute to the antenna's performance optimization. These parameters play a crucial role in enhancing coupling between the layers and consequently improving the antenna's input impedance matching. Variation in simulated antenna response for different distance values between the two patches is shown in Figure 2.33.

When excited at the centre, the E-shaped patch with three wings (one central and two side-wings) produces two resonances. Therefore, using it as a parasitic patch adds extra resonances to the driven patch resonance, thereby increasing the total antenna bandwidth. Further, improvement in impedance matching in this probe-fed stacked antenna can be obtained by cancelling the probe-feed reactance through the use of a washer [3]. This washer can add a capacitive effect and, when chosen properly, helps in cancelling the inductive effect of the probe, as discussed in Section 2.5. The

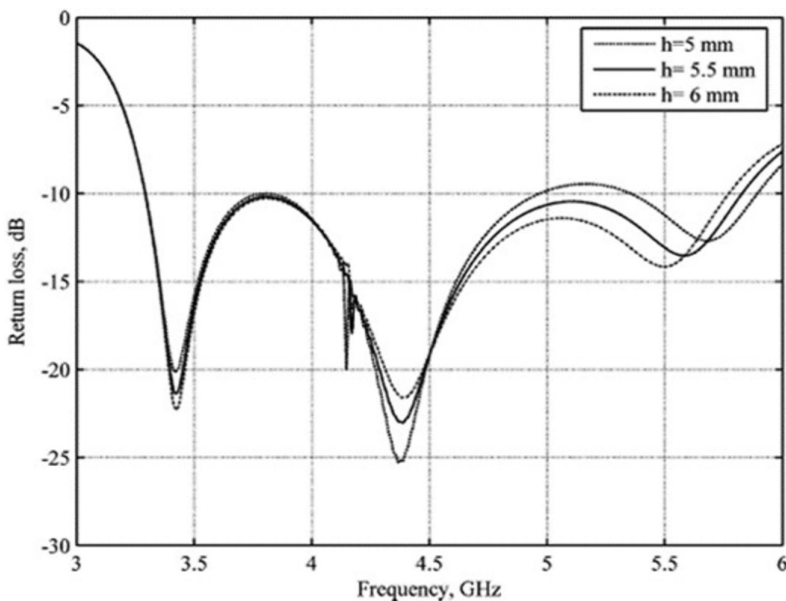


Figure 2.33 Simulated return loss response of proposed antenna for different heights between two patches. Reproduced with permission from IEEE [10].

Table 2.3 Design parameters of the proposed E-shaped stacked antenna [10]

Parameter	L_1	W_1	L_s	W_s	L_2	W_2	L_3	w_s	w_l	w_2	w_3	h_1	h_2	ϵ_r
Value (in mm)	39.4	29.4	17	15.4	26.5	18	14.2	1.4	9.6	7.05	7.05	6	5.5	1.1

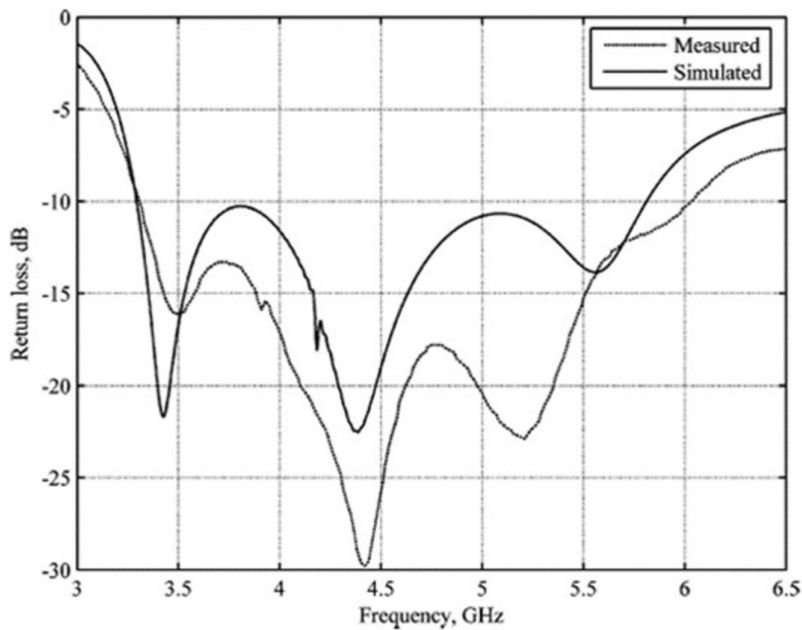


Figure 2.34 Measured and simulated return loss of proposed antenna for $h_2 = 5.6$ mm and other parameters listed in Table 2.3. Reproduced with permission from IEEE [10].

10 dB return loss bandwidth obtained for the present design is 3.275–6.07 GHz (measured). The average gain of the antenna is about 8 dBi \pm 1.4 dBi across the bandwidth. Detailed dimensions of all the antenna parameters are given in Table 2.3. The measured and simulated return loss of the proposed design is shown in Figure 2.34.

2.6.4 F-probe-fed stacked patch antenna design

In the previous sections, the design of stacked antennas fed via microstrip feed line and probe feed is discussed. A stacked antenna fed via four F-probes is presented in [11] for the base station application. The antenna has dual polarization with broad bandwidth. The four F-probes are fed through a 180° phase shift feeding network to provide good reduction in cross-polarization levels. A Wilkinson power divider is used as feeding network to provide proper 180° phase shift at the output ports with high

isolation. In this case isolation of 18 dB is achieved between the two output ports of the feeding network to obtain dual polarization.

Three 0.8-mm-thick stacked layers are used in the design made of FR 4 substrate. The upper two layers comprise of two stacked patches, while the lower layer consists of a feeding network. The upper and lower patch layers are supported by a copper cylinder in the centre of radius 1.5 mm. The antenna geometry is as shown in Figure 2.35. The upper patch has the shape of a rectangle and the lower patch is an isosceles trapezoid. A wide-band Wilkinson power divider is designed with noncoupled-line broadband 180° phase shifter [11] to feed the antenna. The upper parasitic patch adds another resonance and enhances the overall bandwidth.

Initially, L-shaped probes are used which act as an LC series circuit, where the inductance is contributed by the L-probe while capacitance is contributed by the gap between the probe and the patch. Then it is converted to

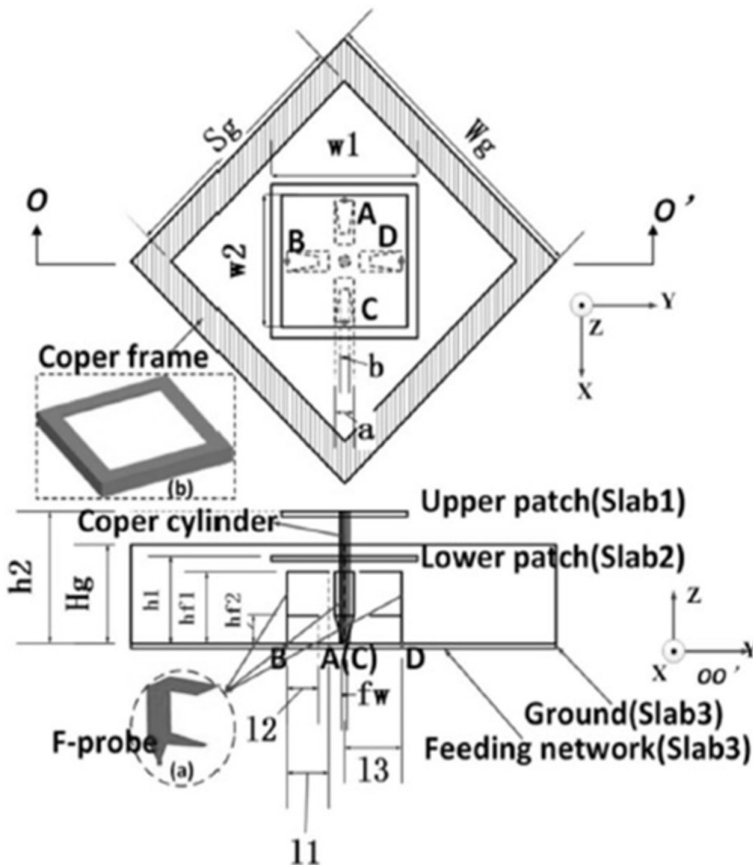


Figure 2.35 Geometry of proposed dual polarized F-probe-fed antenna. Reproduced with permission from IEEE [11].

an F-probe by adding another strip to it. The F-probe has more freedom to adjust the matching circuit and broaden the bandwidth. The width of L-probes controls the impedance matching and thus the impedance bandwidth in this case. In Ant. 1, two L-probes are used, which show high mutual coupling due to surface waves in the thicker substrate being used. In Ant. 2, a differential feeding is used through a balanced feed with 180° phase shift and an additional two L-probes in the design of Ant. 1. The four equally spaced L-probes make the radiation pattern of the antenna more stable. Further, impedance matching is improved by stacking another patch above the driven patch and changing the L-probe to the F-probe. This gives the design of Ant. 3, which has wide impedance bandwidth, compared to Ant. 2, which has a multiband response. Next Ant. 4 has a copper frame added to the design and this frame further improves antenna bandwidth along with reducing the back-side radiation of the antenna.

The geometry of the proposed dual-polarized antenna is shown in Figure 2.35 and the feeding network is shown in Figure 2.36. The antenna design parameters are listed in Table 2.4. In the given antenna design, four vias are used to connect F-probes with the output ports such that A and C vias are connected to port 1, while B and D vias are connected to port 2. F-probes have proven to give improved broadband impedance matching and the 180° -degree phase shift feeding network provided the required dual polarization. Thus, the antenna is suitable for base station application,

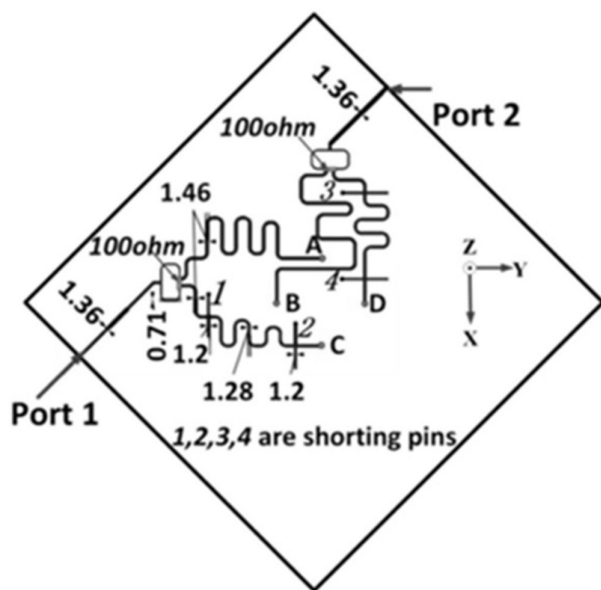


Figure 2.36 Detailed view of the feeding network with the line widths mentioned in mm. Reproduced with permission from IEEE [11].

Table 2.4 Proposed F-probe-fed stacked antenna design parameters [11]

Parameter	l_1	l_2	l_3	w_1	w_2	h_1	h_2	h_{fl}
Value (in mm)	13	12.5	18.5	52	44	23	32	17
Parameter	h_{f2}	f_w	a	b	D	W_g	S_g	H_g
Value (in mm)	5	1	9	2	3	280	210	30

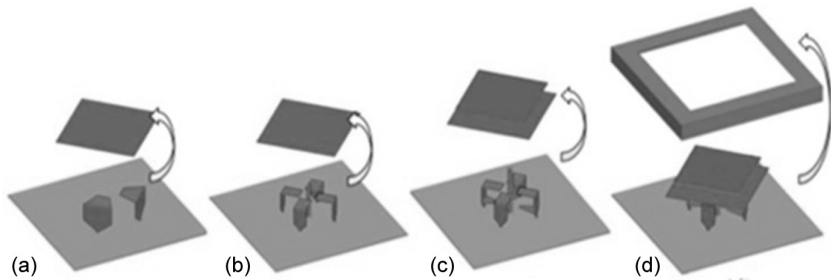


Figure 2.37 Different stages of proposed antenna design (a) Ant. 1 two L-probes fed patch, (b) Ant. 2 with four balanced L-probe-fed patch, (c) Ant. 3 with four balanced F-probe-fed stacked antenna, (d) Ant. 4, proposed F-probe stacked antenna with copper frame. Reproduced with permission from IEEE [11].

requiring both polarizations along broad bandwidth operation. The antenna's response is analysed at each stage by adding one F-probe at a time. The response shows clear improvement in impedance matching of the antenna. The design is further modified to improve back radiation, by adding a metallic frame to the antenna design as shown in Figure 2.37. The VSWR response of the antenna at different stages is shown in Figure 2.38.

The overall response of the F-probe-fed antenna is shown in Figure 2.39 and Figure 2.40. The antenna has 45% bandwidth at a centre frequency of 2.2 GHz, covering PCS/DCS/UMTS/LTE2300/LTE2500 bands. The obtained gain is 9–10 dBi with efficiency ranging from 55 to 85% throughout the band of operation. A balanced feed with 180-degree phase shift gives a dual-polarized response along with high isolation between the two ports. The isolation achieved is around 30 dB and XPD is around 23 dB. The radiation patterns are quite unidirectional with a front-to-back ratio of more than 22 dB. The antenna array of the proposed antenna has been developed and presented in [12] with an improved gain of 13–14 dBi.

2.6.5 Stacked patch antenna design for 5G using magneto-dielectric material

Magneto-dielectric materials have high permittivity and high permeability properties and are proven to be useful for the miniaturization of antenna design [13–15].

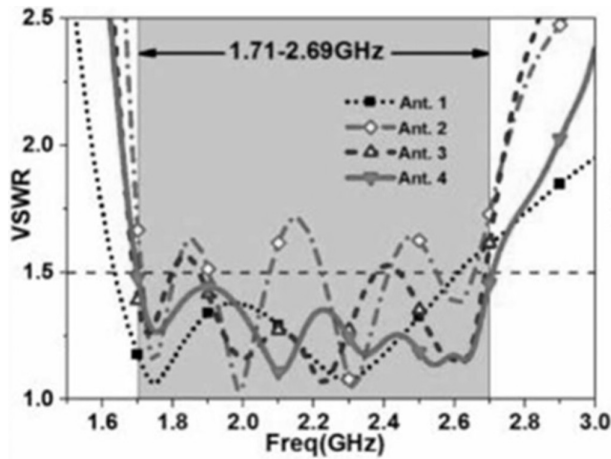


Figure 2.38 VSWR response of proposed antenna at different stages. Reproduced with permission from IEEE [11].

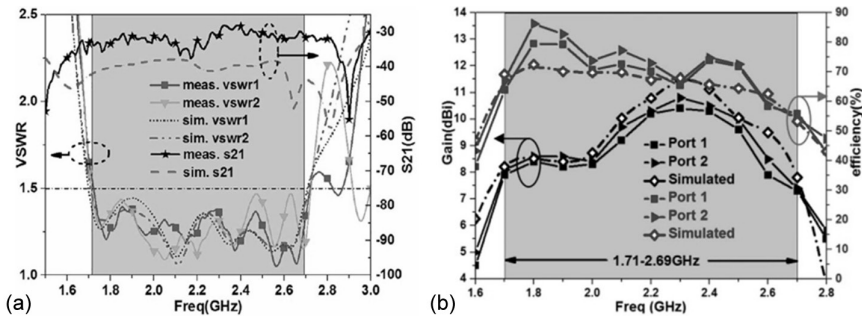


Figure 2.39 (a) Measured and simulated VSWR of proposed antenna at both the ports, (b) measured and simulated gain as well as efficiency of proposed stacked antenna at both ports. Reproduced with permission from IEEE [11].

An inset-fed microstrip antenna etched on a magneto-dielectric (MD) composite material to minimize the patch dimensions is proposed in [16]. The MD material here is made of a mixture of magnetite powder (Fe_3O_4), PDMS elastic polymer material (polydimethylsiloxane), and $\text{BaFe}_{12}\text{O}_{19}$.

Magnetic materials are commonly used in the antenna design, with one of the most commonly used being the ferrite materials [17–20]. Generally, losses in magnetic materials increase with higher frequencies, according to Snoek's law [21]. Therefore, a mixture of other materials is also needed along with magnetic material at higher frequencies. This makes MD composite material most suitable for high-frequency applications. But it still exhibits losses at higher frequencies and this needs to be compensated in the antenna design. In the presented work, MD composite material is used to

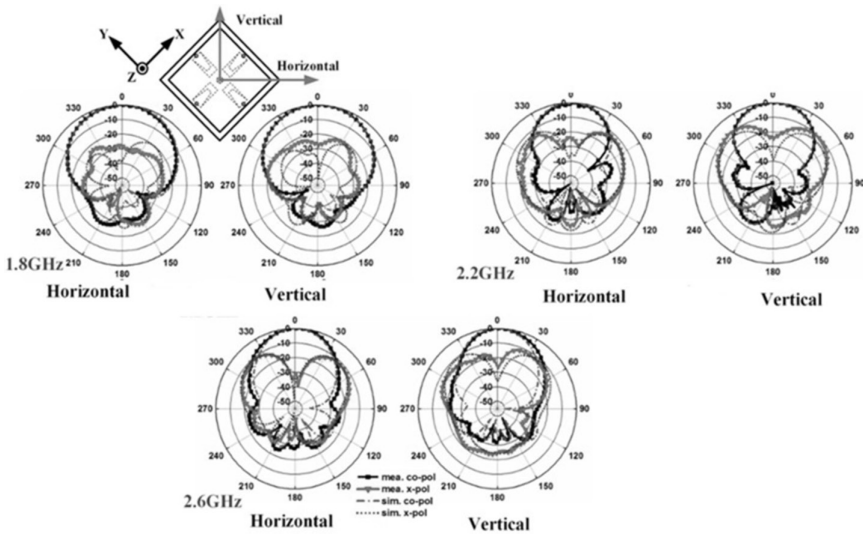


Figure 2.40 Measured and simulated radiation patterns of proposed F-probe-fed stacked antenna at different frequencies for port 1. Reproduced with permission from IEEE [11].

reduce the dimensions of the antenna, while the SRR array structure is used along with it to improve the bandwidth and gain of the antenna.

In the proposed stacked antenna design, the upper-most layer is the patch over the MD layer. Beneath the MD layer another substrate layer of RT Duroid 5880 is attached through double-sided tape. The last layer is the ground plane with a split-ring resonator (SRR) array etched over it. The SRR array provides sufficient electric and magnetic coupling among the layers and contributes towards the improvement of the antenna's performance. The antenna's structure is shown in Figure 2.41, while a photograph of the fabricated antenna is shown in Figure 2.42 and the final dimensions are listed in Table 2.5. The magnetic properties of the MD composite material have been extracted through experimentation in this work, along with the study of the designed SRR structure. It has been observed that the higher the value of the relative permeability of the material, the more the frequency shifts towards the lower side. Further, the use of the SRR array broadens the impedance bandwidth of the antenna. Thus, the optimum material selection for MD composite and carefully optimized design of the SRR structure at the ground plane layer are crucial to obtain the desired antenna performance in this proposed work.

The antenna has a peak gain of 4.33 dBi with 10% fractional bandwidth in the C-band region and a 19 dB front-to-back ratio. The antenna being miniaturized by 64% in size (30 mm × 30 mm) compared to conventional antennas does not compromise the performance parameters. The antenna's responses are shown in Figures 2.43 and 2.44.

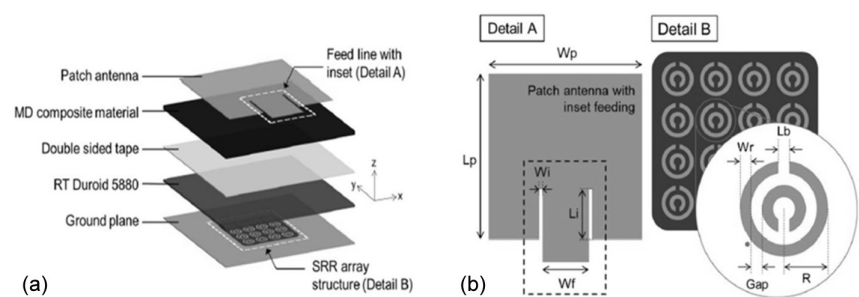


Figure 2.41 (a) Design of proposed MD material based stacked patch antenna, (b) detailed view of patch and SRR array structure. (Source: Yohanes Galih Adhiyoga, Siti Fauziyah, Catur Apriono, and Eko Tjipto, “Miniaturized 5G Antenna with Enhanced Gain by Using Stacked Structure of Split-Ring Resonator Array and Magneto-Dielectric Composite Material”, IEEE Access, Vol. 10, pp: 35876–35887, March 2022 [16].)

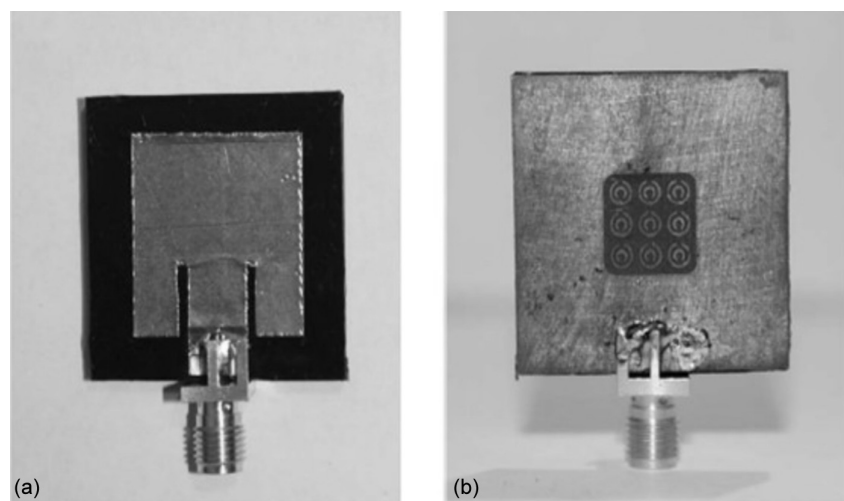


Figure 2.42 Fabricated prototype of proposed stacked antenna on MD material, front and back side, respectively. (Source: Yohanes Galih Adhiyoga, Siti Fauziyah, Catur Apriono, and Eko Tjipto, “Miniaturized 5G Antenna with Enhanced Gain by Using Stacked Structure of Split-Ring Resonator Array and Magneto-Dielectric Composite Material”, IEEE Access, Vol. 10, pp: 35876–35887, March 2022 [16].)

Table 2.5 Design parameters of proposed annular-ring-shaped stacked antenna [22]

Parameter	a_1	a_2	b_1	b_2	h_1	h_2	R_{stub1}	R_{stub2}	R_p	h_{sub}
Value (in mm)	21.6	39	12	22.5	11	7.2	60	90	33.5	2

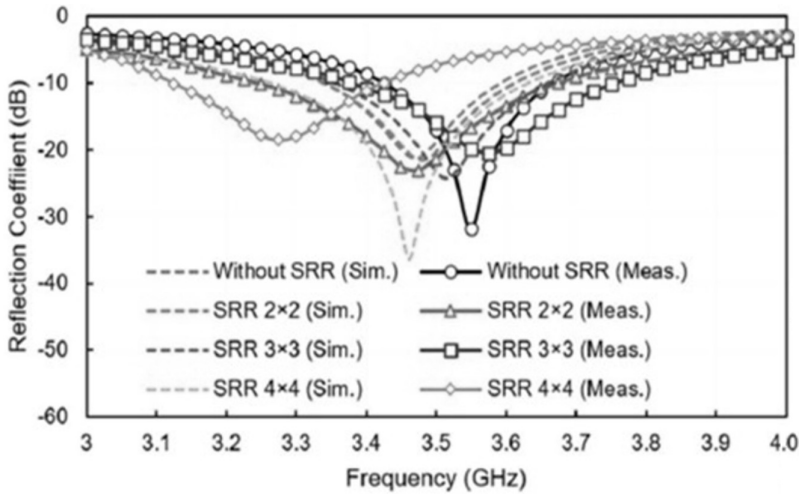


Figure 2.43 Measured and simulated return loss of proposed stacked antenna with and without SRR array structure. (Source: Yohanes Galih Adhiyoga, Siti Fauziyah, Catur Apriono, and Eko Tjipto, "Miniaturized 5G Antenna with Enhanced Gain by Using Stacked Structure of Split-Ring Resonator Array and Magneto-Dielectric Composite Material", IEEE Access, Vol. 10, pp: 35876–35887, March 2022 [16].)

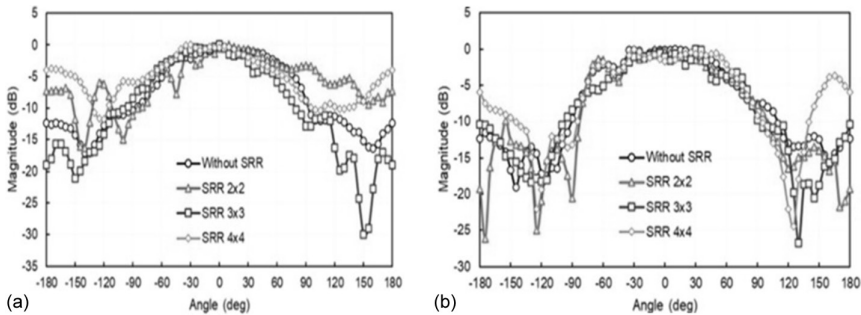


Figure 2.44 Radiation patterns of proposed stacked antenna with different SRR array structures, (a) E-plane, (b) H-plane. (Source: Yohanes Galih Adhiyoga, Siti Fauziyah, Catur Apriono, and Eko Tjipto, "Miniaturized 5G Antenna with Enhanced Gain by Using Stacked Structure of Split-Ring Resonator Array and Magneto-Dielectric Composite Material", IEEE Access, Vol. 10, pp: 35876–35887, March 2022 [16].)

2.6.6 Annular ring microstrip stacked antenna design

A three-layered annular-ring-shaped stacked microstrip antenna is presented in [22]. The three-layered stacked antenna comprises three metal layers with two dielectric substrates sandwiched between them. The top

layer features a circular parasitic metallic patch with a radius of R_p . The middle layer hosts an annular ring patch with a feeding network printed between the inner radius of the annular ring. This feeding network utilizes a power divider to evenly split the power into two output ports with a 90° phase difference. The output legs of the power divider for the middle patch are positioned 90° apart along the circumference of the inner ring, thereby exciting the fundamental TM_{11} mode with broadside radiation. The bottom layer also contains an annular-ring-shaped patch, which is larger than the ring of the middle layer. The antenna geometry with different layers is shown in Figure 2.45. The antenna design parameters are listed in Table 2.6. Selecting different dimensions for the middle and lower patches

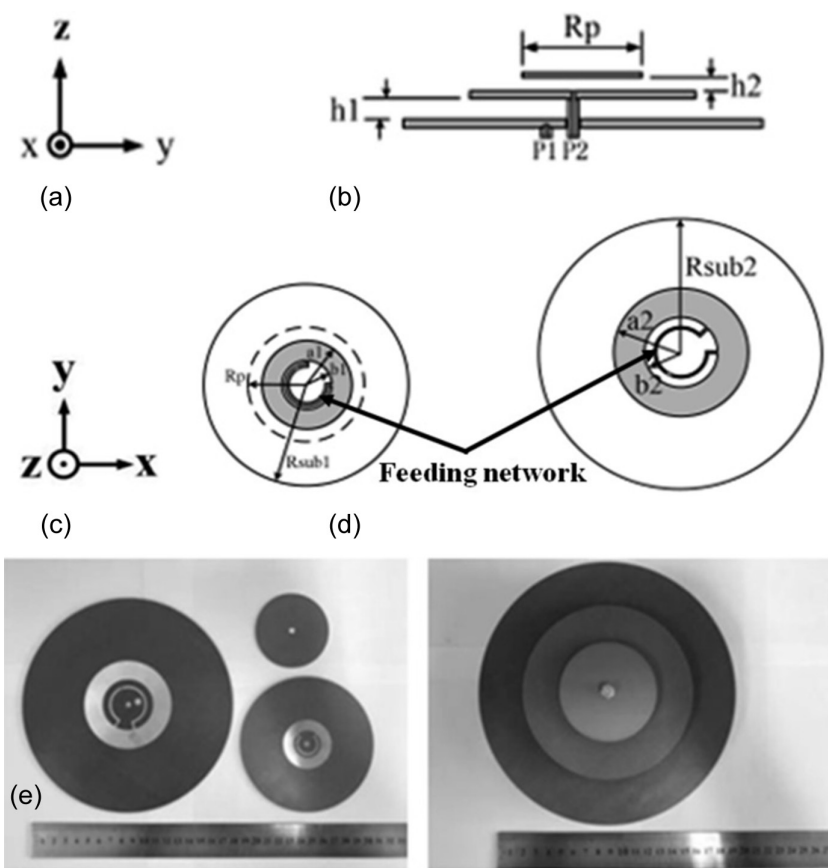


Figure 2.45 Proposed annular-ring-shaped stacked antenna design (a) side view, (b) top view of middle layer, (c) top view of bottom layer, (d) three layers of fabricated antenna, (e) fabricated stacked antenna. (Source: Yi Liu, Yanhua Cao, Ke Wang and Wei Hong, “A Broadband Multimode Circularly Polarized Stacked Antenna with Pattern Diversity”, IEEE Access, Vol. 12, pp: 53448–53453, Jan 2024 [22].)

Table 2.6 Design parameters of proposed MD-based stacked patch antenna [16]

Parameter	W_{sub}	L_{sub}	W_p	L_p	W_f	W_r	R	Gap	L_b	W_i	L_i	h_{MD}	$h_{dielectric}$
Value (in mm)	30	30	20	21.51	7	0.3	1.26	0.31	0.43	1	7.5	2	12.575

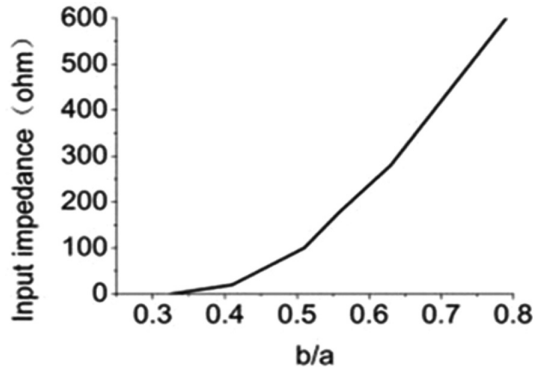


Figure 2.46 Input impedance variation of the antenna with the ratio a/b . (Source: Yi Liu, Yanhua Cao, Ke Wang and Wei Hong, “A Broadband Multimode Circularly Polarized Stacked Antenna with Pattern Diversity”, IEEE Access, Vol. 12, pp: 53448–53453, Jan 2024 [22].)

facilitates the generation of multiple resonances, as the resonant frequency of the annular ring patch relies on the ratio of the inner and outer radii. The variation of the input impedance value with the inner and outer radius ratio is illustrated in the Figure 2.46. The resonant frequencies for two modes can be determined based on the annular ring dimensions using the provided Equation (2.32). Additionally, the lower layer is fed through a feeding network consisting of a power network printed on the same layer inside the inner radius of the ring. This power divider produces equal amplitude signals at the output ports with a 90° phase shift. In this case, the output legs of the feeding network are spaced 45° apart along the ring circumference, resulting in the generation of the TM_{21} mode with a conical radiation pattern. The two 90° out-of-phase signals at both output ports lead to the circular polarization of the antenna with different radiation patterns when probe feed 1 is excited and when probe feed 2 is excited. Probe feed 1 feeds the lower patch, generating the TM_{21} mode, while probe feed 2 feeds the middle patch, generating the TM_{11} mode. The current distribution for TM_{11} at the middle layer and for TM_{21} at the bottom layer is shown in Figure 2.47. The radiation patterns due to two probe feeds are given in Figure 2.48. The axial ratio bandwidths for the two modes are shown in Figure 2.49 which is 0.29 GHz for TM_{11} mode and 0.25 GHz for TM_{21} mode. The S11 bandwidth of TM_{11} mode is 0.34 GHz while for TM_{21} mode

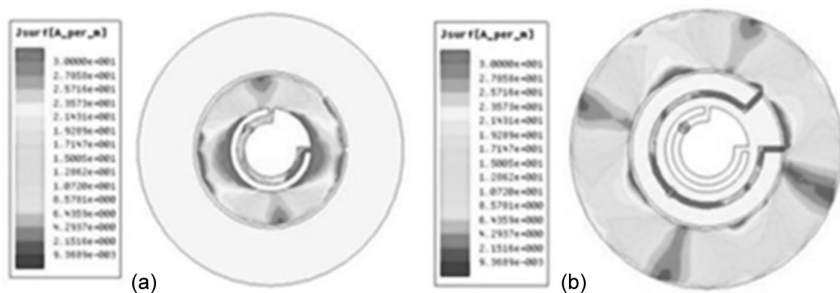


Figure 2.47 Current distribution at different layers of stacked antenna for different modes (a) TM_{11} mode (middle layer), (b) TM_{21} mode (bottom layer). (Source: Yi Liu, Yanhua Cao, Ke Wang and Wei Hong, “A Broadband Multimode Circularly Polarized Stacked Antenna with Pattern Diversity”, IEEE Access, Vol. 12, pp: 53448–53453, Jan 2024 [22].)

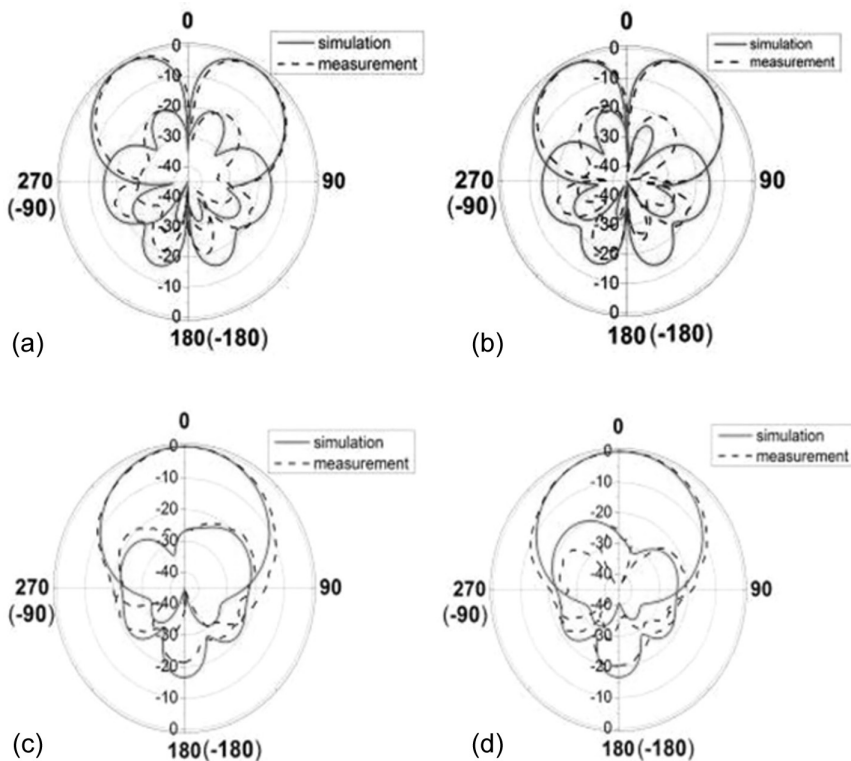


Figure 2.48 Measured and simulated radiation patterns of annular ring stacked antenna for $\Phi = 0^\circ$ and $\Phi = 90^\circ$ respectively in two orthogonal planes, (a) when port 1 is excited, (b) when port 2 is excited. (Source: Yi Liu, Yanhua Cao, Ke Wang and Wei Hong, “A Broadband Multimode Circularly Polarized Stacked Antenna with Pattern Diversity”, IEEE Access, Vol. 12, pp: 53448–53453, Jan 2024 [22].)

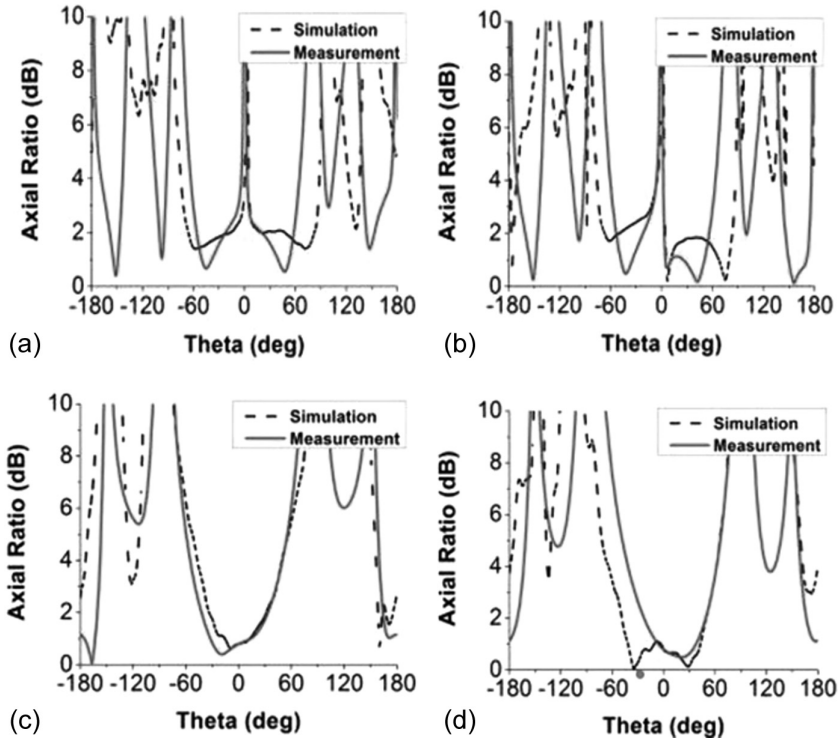


Figure 2.49 Axial ratio bandwidths of the proposed annular ring stacked antenna for two modes, i.e. $\Phi = 0^\circ$ and $\Phi = 90^\circ$ respectively, (a) when port 1 excited, (b) when port 2 is excited. (Source: Yi Liu, Yanhua Cao, Ke Wang and Wei Hong, “A Broadband Multimode Circularly Polarized Stacked Antenna with Pattern Diversity”, IEEE Access, Vol. 12, pp: 53448–53453, Jan 2024 [22].)

it is 0.28 GHz, shown in Figure 2.50. Further, measured gains are 8.5 dBic and 5.1 dBic respectively for TM_{11} and TM_{21} modes.

$$f_{11} = \frac{c}{\pi(a+b)\sqrt{\epsilon_e}} \quad , \quad f_{21} = \frac{2c}{\pi(a+b)\sqrt{\epsilon_e}} \quad (2.32)$$

2.7 SIMULATION AND MEASUREMENT OF STACKED MICROSTRIP ANTENNAS

In the preceding section, we thoroughly examined various examples of stacked antenna designs. These designs are initially simulated and optimized using EM simulators such as CST Studio Suite, Ansys HFSS, or IE3D. Some of the optimizations can also be performed using circuit simulators

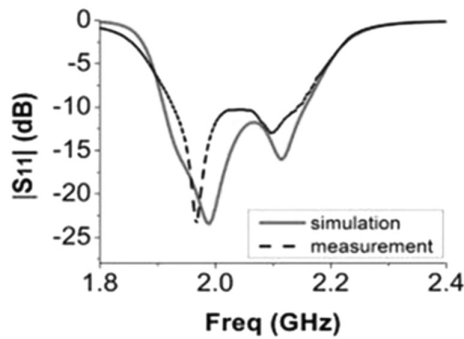


Figure 2.50 Measured and simulated S_{11} parameter of proposed annular ring stacked antenna. (Source: Yi Liu, Yanhua Cao, Ke Wang and Wei Hong, “A Broadband Multimode Circularly Polarized Stacked Antenna with Pattern Diversity”, IEEE Access, Vol. 12, pp: 53448–53453, Jan 2024 [22].)

like ADS software. Circuit simulators model antennas in terms of transmission-line segments and lumped elements. The TLM model details of stacked antennas are provided in the next chapter. The initially simulated antenna design model is then fabricated and tested for measured results. In the case of stacked antennas, the fabrication of the antenna involves different layers. These multiple printed layers are then stacked using adhesive material or metallic screws. The alignment and placement of parasitic patches in relation to the driven patch and feed are crucial and require careful positioning after fabrication. Typically, errors in the fabricated antenna design can be more pronounced in the case of stacked antennas due to potential variations in the manual placement of parasitic patches. Moreover, losses increase due to the use of adhesive to stack the layers together. Even metallic screws may cause interference, particularly in compact antenna designs. Therefore, achieving an optimal placement of stacked layers with minimal losses is essential. The measurements of the fabricated stacked antenna are conducted in a similar standard manner to single-layer antennas. VNA is used for S-parameter measurements, while radiation pattern measurements are carried out in an anechoic chamber using a standard broadband transmitter. However, in the case of stacked antennas, care should be taken to ensure proper alignment of stacked layers, especially when adhesive is used to hold them together, during placement in the anechoic chamber for pattern as well as gain measurements.

2.8 SUMMARY

In this chapter we have explored various design techniques for stacked microstrip antennas, which are essential in today’s communication and advanced applications such as satellite communication and remote sensing.

Detailed discussions on the relevant design parameters, equations, and methodologies are provided to help readers grasp the fundamental design concepts of these complex multi-layered structures. The chapter further delved into essential antenna design phenomena such as surface waves and surface currents, along with methods to manage them. It also elaborated on the different stages of designing multi-layered stacked antennas and the impact of key design parameters on their performance. A clear explanation is provided on how stacking the parasitic layers enhances antenna bandwidth and gain.

REFERENCES

1. C. A. Balanis, "*Antenna Theory: Analysis and Design*" Wiley Publications, 2001.
2. G. Kumar, and K. P. Ray, "*Broadband Microstrip Antennas*" Artech House Antenna and Propagation Library, 2003.
3. Zhang-Fa Liu, Pang-Shyan Kooi, Le-Wei Li, Mook-Seng Leong, and Tat-Soon Yeo, "A method for designing broad-band microstrip antennas in multilayered planar structures", *IEEE Trans. Antennas Propag.*, Vol. 47, No. 9, pp:1416–1420, September 1999.
4. H. Pues, and A. Van de Capelle, "Accurate transmission-line model for the rectangular microstrip antenna", *IEE Proceedings*, Vol. 131, No. 6, pp:334–340, December 1984.
5. Ankita Katyal, and Ananjan Basu, "Compact and broadband stacked microstrip patch antenna for target scanning applications", *IEEE Antennas and Wirel. Propag. Lett.*, Vol. 16, pp:381–384, 2017.
6. E. Nishiyama, M. Aikawa, and S. Egashira, "Stacked microstrip antenna for wideband and high gain", *IEE Proceedings on Microwave Antenna Propagation*, Vol. 151, No. 2, pp:143–148, April 2004.
7. R. Azim, M. T. Islam, and N. Misran, "Compact tapered-shape slot antenna for UWB applications," *IEEE Antenna Wireless Propag. Lett.*, vol. 10, pp. 1190–1193, 2011.
8. Ankita Malhotra, "Broadband miniaturized c-band stacked antenna design and analysis using TLM", *IETE J Res.*, pp:1–8, November 2023. <https://doi.org/10.1080/03772063.2023.2282079>
9. Jaume Anguera, Lluís Boada, Carles Puente, Carmen Borja, and Jordi Soler, "Stacked H-shaped microstrip patch antenna", *IEEE Trans. Antennas Propag.*, Vol. 52, No. 4, pp:983–993, April 2004.
10. M. A. Matin, B. S. Sharif, and C. C. Tsimenidis, "Probe fed stacked patch antenna for wideband applications", *IEEE Trans. Antennas Propag.*, Vol. 55, No. 8, pp:2385–2388, August 2007.
11. Yiyun Jin, and Zhengwei Du, "Broadband dual-polarized F-probe fed stacked patch antenna for base stations", *IEEE Antennas and Wirel. Propag. Lett.*, Vol. 14, pp:1121–1124, 2015.
12. Yiyun Jin, and Zhengwei Du, "Broadband Stacked F-Probe Patch Antenna and Its Array for Base Station", 2015 IEEE International Wireless Symposium (IWS 2015), March 2015.

13. Yohanes Galih Adhiyoga, Siti Fauziyah Rahman, Catur Apriono, and Eko Tjipto Rahardjo, "Magneto-dielectric properties of PDMS–magnetite composite as a candidate for compact microstrip antennas in the C-band 5G frequency", *Springer Journal of Materials Science: Materials in Electronics*, Vol. 32, pp:11312–11325, April 2021.
14. Zongliang Zheng, "Flexible High Magnetodielectric Materials for Antenna Applications", International Conference on Microwave and Millimeter Wave Technology (ICMMT), May 2018.
15. Abdullah Al-Sehemi, Ahmed Al-Ghamdi, Nikolay Dishovsky, Nikolay Atanasov, and Gabriela Atanasova, "Miniaturized wearable antennas with improved radiation efficiency using magneto-dielectric composites", *IETE J. Res.*, Vol. 68, pp:1157–1167, July 2019.
16. Yohanes Galih Adhiyoga, Siti Fauziyah, Catur Apriono, and Eko Tjipto, "Miniaturized 5G Antenna with enhanced gain by using stacked structure of split-ring resonator array and magneto-dielectric composite material", *IEEE Access*, Vol. 10, pp:35876–35887, March 2022.
17. R. Durbha, and M. N. Afsar, "Miniaturization techniques using magnetic materials for broadband antenna applications", *IEEE Trans. Magn.*, Vol. 55, No. 7, p:17, July 2019.
18. X. Wu, and Z. Zheng, "A Novel Compact Microstrip Antenna Embedded with Magneto-Dielectric Ferrite Materials for 433 MHz Band Applications", Preface of the 13th International Conference Antennas Propagation (EuCAP), March 2019.
19. Y. Yang, J. Li, H. Zhang, G. Wang, Y. Rao, and G. Gan, "TiO₂ tailored low loss NiCuZn ferrite ceramics having equivalent permeability and permittivity for miniaturized antenna", *J. Magn. Magn. Mater.*, Vol. 487, Art. 165318, October 2019.
20. A. Saini, A. Thakur, and P. Thakur, "Matching permeability and permittivity of Ni_{0.5}Zn_{0.3}Co_{0.2}In_{0.1}Fe_{1.9}O₄ ferrite for substrate of large bandwidth miniaturized antenna", *J. Mater. Sci., Mater. Electron.*, Vol. 27, No. 3, p:28162823, March 2016.
21. T. Nakamura, "Snoek's limit in high-frequency permeability of polycrystalline Ni Zn, MgZn, and Ni ZnCu spinel ferrites", *J. Appl. Phys.*, Vol. 88, No. 1, pp:348–353, 2000.
22. Yi Liu, Yanhua Cao, Ke Wang, and Wei Hong, "A broadband multimode circularly polarized stacked antenna with pattern diversity", *IEEE Access*, Vol. 12, pp:53448–53453, January 2024.

Methods for static analysis of stacked microstrip antennas

3.1 INTRODUCTION

Printed stacked microstrip antennas are multi-layered complex structures, with multiple resonators positioned on top of one another to achieve electromagnetic coupling among the layers. This coupling provides broadband impedance matching. Analyzing these structures is crucial to understand the impact of various design parameters on the antenna's overall performance. Full-wave analysis is an effective method for accurately analyzing these complex structures, although it can be quite intricate and time-consuming due to the antennas' complex design. In full-wave analysis, a complete set of integral equations is solved using exact Green's functions and boundary conditions along the metallic patch boundaries. These integral equations are employed for analysis in the spectral domain. The resulting integral equations are then transformed into linear equations using the method of moments to produce a matrix, which in turn depicts the current distribution on the patch. This current distribution further provides the near-field and far-field distribution of the antenna. In addition to the integral approach, the finite-difference time domain (FDTD) approach is utilized for full-wave analysis of antennas. This method is commonly applied to the complex antenna structures and can also be used in the presence of a finite antenna ground in the case of microstrip antennas. However, these numerical methods have the drawback of not readily providing direct information about the influence of structural or geometrical parameters on the antenna's performance [1].

The book will delve into a thorough discussion of static analysis of printed stacked antennas, emphasizing its comparative simplicity and time efficiency when dealing with complex structures. Despite employing simplified assumptions, static analysis models yield ample information about the system, aiding in understanding the physical phenomena and essential design parameters of the antenna. These analytical methods are instrumental in calculating the overall input impedance and radiation characteristics of the antenna. Additionally, they facilitate the interpretation of known physical phenomena and offer structural insights into the antenna. Crucial

design parameters impacting the antenna's performance and optimization can be identified and fine-tuned to achieve the desired antenna behaviour. The chapter will cover the details of fundamental analytical models for the analysis of simple microstrip antennas, such as the transmission-line model and cavity model, which respectively model the antenna structure as a transmission line or a cavity.

Furthermore, in the analysis of stacked microstrip antennas, it is essential to carefully consider the electromagnetic coupling among the layers in the analytical models. The book will also address static analysis models for analyzing various multi-layered structures, including multi-layered microstrip lines and stacked microstrip antennas. It will cover methods such as the conformal mapping technique that calculates the effective dielectric constant of complex structures, and the thorough details of the transmission-line model analysis of stacked antennas. Subsequent sections of the book will unveil further details of these methods along with implementation examples.

3.2 CONFORMAL MAPPING

Conformal mapping is an analytical analysis technique used for the analysis of multiple dielectric layer transmission-line, striplines, and coplanar waveguides. The concept of conformal mapping is based on orthogonal transformation applied on a complex variable plane. The quasi-TEM wave propagation assumption is considered and a relation between electrical and structural properties is established for static analysis. According to [2], the important electrical characteristic is wave resistance while the important physical characteristic is the shape ratio (metal patch/strip width versus separation with respect to ground or the substrate height). The conductors are assumed to be perfectly conducting and thin, while dielectric is assumed to be free of dispersion. A relation between shape ratio and wave resistance is established in [2], where the physical boundaries or potential boundaries (edges of the patch or the transmission line) along with flux boundaries of the fringing fields are mapped into contours as shown in Figure 3.1 and Figure 3.2. The flux-potential plane makes wave resistance calculation easier and dependent on the aspect ratio of the plane, i.e. g/π or g'/π after modification. The transmission-line parameters calculation based on this aspect ratio is given by Equations (3.1)–(3.3):

$$R = R_c \pi / g' \quad (3.1)$$

$$L = \mu l \pi / g' \quad (3.2)$$

$$C = \epsilon l g' / \pi \quad (3.3)$$

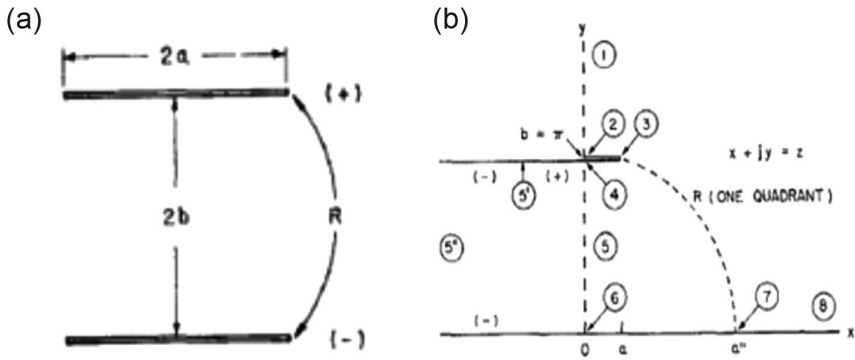


Figure 3.1 (a) Transmission line made of two parallel strips, (b) Space coordinates on z -plane. Reproduced with permission from IEEE [2].

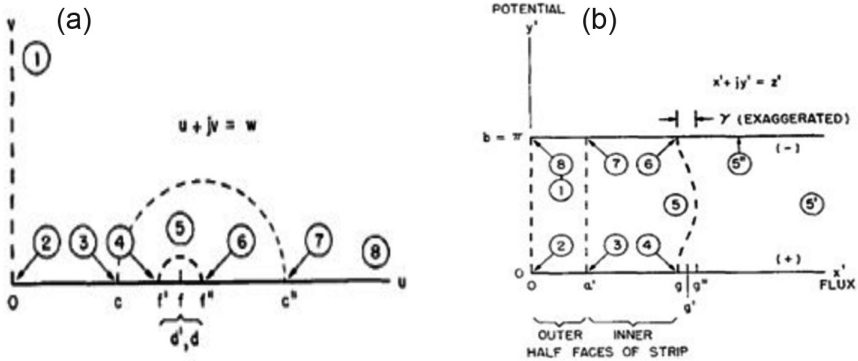


Figure 3.2 (a) Collinear coordinates on w -plane, (b) flux-potential coordinates on z' -plane. Reproduced with permission from IEEE [2].

where l is the length of the transmission line.

In the microstrip patch antennas, a quasi-TEM mode of propagation exists as fields propagate both through the air and dielectric substrate. The electromagnetic waves propagating through the patch fringe out at the edges; they propagate in the air and terminate to the ground through the dielectric. The curve 3–7 in the Figure 3.1(b) indicates fields fringing out and the rest of the points indicate physical boundaries of the transmission line. In the w -plane and the further modified z' -plane, both the electrical and physical boundaries are mapped to calculate incidental relations between wave resistance and shape ratio.

When multiple dielectric layers are placed in the transmission lines, the overall capacitive effect changes due to the change in the effective dielectric constant. According to [3], using Wheeler's transformation (discussed above) individual interfaces between multiple dielectric layers are transformed into

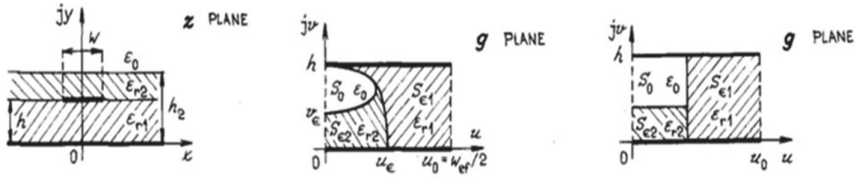


Figure 3.3 Three-layer microstrip line of first type and its transformations. Reproduced with permission from IEEE [3].

the z' -plane or g -plane, as shown in Figure 3.3. The transformed plane is a closed area divided into multiple cross-sections whose boundaries represent individual dielectric interfaces of multi-dielectric structure. The filling of the entire closed area by these individual cross-sections is dependent upon the filling factors determined based on ratios of area taken up by them in the closed cross section with respect to the total area. The filling factors are given by Equations (3.4)–(3.11). The study shows that the conformal mapping technique helps in the static analysis of stacked microstrip antennas with multiple substrate layers as shown by results given in Figure 3.3, depicting microstrip line of the first type. With the help of these filling factors the effective dielectric constant of the multi-layered microstrip line is calculated given by Equation (3.12).

This effective dielectric constant is then used to calculate the characteristic impedance of the multi-layered microstrip line using Equations (3.13) and (3.14) for the case of a thick line and thin line respectively. The obtained results are in line with the computed (based on full-wave analysis) and the measured results. The static analysis methods, however, provide quicker results and are easier to implement.

$$q_1 = \frac{S_{\epsilon 1}}{S_c} = \frac{S_c - S_o - S_{\epsilon 2}}{S_c} = 1 - \frac{S_o + S_{\epsilon 2}}{S_c} \quad (3.4)$$

$$q_2 = \frac{S_{\epsilon 2}}{S_c} = \frac{S_c - S_{\epsilon 1} - S_o}{S_c} = 1 - \frac{S_{\epsilon 1}}{S_c} - \frac{S_o}{S_c} = 1 - q_1 - \frac{S_o}{S_c} \quad (3.5)$$

$$q_1 = 1 - \frac{1}{2} \frac{\ln \left(\frac{\pi}{h} w_{ef} - 1 \right)}{\frac{w_{ef}}{h}} \quad (3.6)$$

$$q_2 = 1 - q_1 - \frac{1}{2} \cdot \frac{h - v_e}{w_{ef}} \cdot \ln \left[\pi \frac{w_{ef}}{h} \frac{\cos \frac{v_e}{2} \cdot \frac{\pi}{h}}{\pi \left(\frac{h_2}{h} - \frac{1}{2} \right) + \frac{v_e}{2} \cdot \frac{\pi}{h}} \right] \quad (3.7)$$

Here the effective line width is:

$$w_{ef} = w + \frac{2h}{\pi} \ln \left[17.08 \left(\frac{w}{2h} + 0.92 \right) \right] \quad (3.8)$$

And v_e is given by:

$$v_e = 2 \frac{h}{\pi} \arctg \left[\frac{\pi}{\frac{\pi}{2} \frac{w_{ef}}{h} - 2} \left(\frac{h_2}{h} - 1 \right) \right] \quad (3.9)$$

Then the filling factors are:

$$q_1 = \frac{1}{2} + \frac{0.9}{\pi \ln \frac{h}{w}} \quad (3.10)$$

$$q_2 = \frac{1}{2} - \frac{0.9 + \frac{\pi}{4} \ln \left(\frac{h_2/h + 1}{h_2/h + w/4h - 1} \right) \cdot \arccos \left\{ \left[1 - \frac{h}{h_2} \left(1 - \frac{w}{8h} \right) \right] \sqrt{\frac{h_2/h + 1}{h_2/h + w/4h - 1}} \right\}}{\pi \ln \frac{8h}{w}} \quad (3.11)$$

$$\varepsilon_{efr} = \varepsilon_{r1} q_1 + \varepsilon_{r2} \cdot \frac{(1 - q_1)^2}{\varepsilon_{r2} (1 - q_1 - q_2) + q_2} \quad (3.12)$$

Characteristic impedance is calculated for wide line $w/h \geq 1$ as:

$$Z_0 = \frac{120\pi}{\sqrt{\varepsilon_{efr}}} \cdot \frac{h}{w_{ef}} \quad (3.13)$$

While for the thin line

$$Z_0 = \frac{60}{\sqrt{\varepsilon_{efr}}} \cdot \ln \frac{8h}{w} \quad (3.14)$$

The computed result of characteristic impedance of the first type of microstrip line using the described method is shown and compared with other work [4], calculated through Green's function, as shown in Figure 3.4.

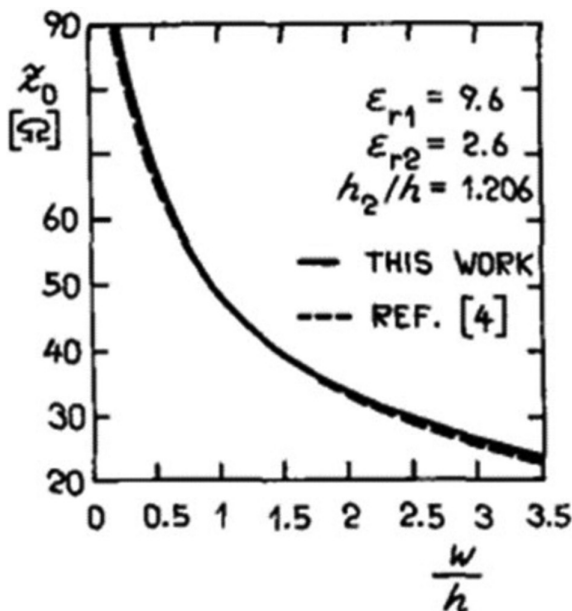


Figure 3.4 Characteristic impedance of three-layered microstrip of the first type discussed here. Reproduced with permission from IEEE [3].

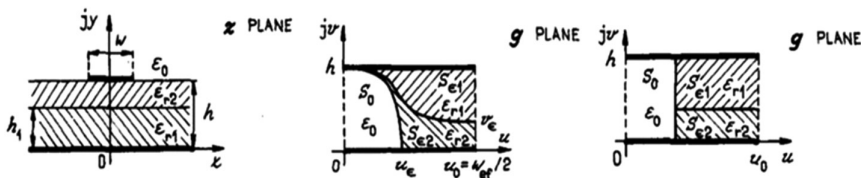


Figure 3.5 Three-layer microstrip line of second type and its transformations. Reproduced with permission from IEEE [3].

Similarly, the filling factors for the second type of multi-layered transmission lines, where two dielectric materials are placed between the metallic strips, are shown in Figure 3.5

The filling factors can be modified as given by Equations (3.15) and (3.16) and the computed effective dielectric constant is as given by Equation (3.17). The characteristic impedance of the second type of microstrip line discussed here can be then computed using Equation (3.13) or (3.14). The comparison of the computed characteristic equation using the proposed method is compared with that presented in [5], based on the variational capacitance of the line, and the results are depicted in Figure 3.6.

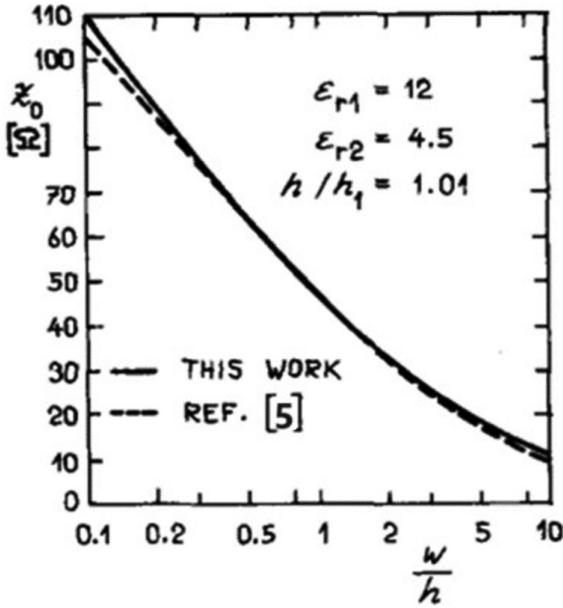


Figure 3.6 Characteristic impedance of microstrip line of the second type. Reproduced with permission from IEEE [3].

$$q_1 = \frac{S_{\epsilon 1}}{S_c} = \frac{1}{2} \cdot \frac{h_1}{h} \left[1 + \frac{\pi}{4} - \frac{h}{w_{ef}} \ln \left(\frac{\pi}{h} \cdot w_{ef} \frac{\sin \frac{\pi h_1}{2h}}{\frac{\pi h_1}{2h}} + \cos \left(\frac{\pi h_1}{2h} \right) \right) \right] \quad (3.15)$$

$$q_2 = \frac{S_{\epsilon 2}}{S_c} = 1 - q_1 - \frac{1}{2} \cdot \frac{\ln \left(\frac{\pi}{h} w_{ef} - 1 \right)}{\frac{w_{ef}}{h}} \quad (3.16)$$

$$\epsilon_{eff} = 1 - q_1 - q_2 + \epsilon_{r1} \epsilon_{r2} \cdot \frac{(q_1 + q_2)^2}{\epsilon_{r1} q_2 + \epsilon_{r2} q_1} \quad (3.17)$$

This concept is extended to obtain the effective permittivity of a multi-layered stacked antenna and a modified improved transmission-line model is proposed in [6], by considering attenuation in lossy TLM. The conformal mapping technique was thus extended to analyze a stacked microstrip antenna. According to [7, 8] the input admittance of an antenna is given as:

$$Y_m = Y_C \left[\frac{Y_s + Y_C \tanh \gamma L1}{Y_C + Y_s \tanh \gamma L1} + \frac{Y_s + Y_C \tanh \gamma (L - L1)}{Y_C + Y_s \tanh \gamma (L - L1)} \right] \quad (3.18)$$

Here Y_c is characteristic admittance of the patch, Y_s is the radiation admittance of the main radiating slots, and γ is the complex propagation constant of the patch. Further, it is to be noted that:

$$\gamma = \alpha + j\beta, \beta = k_o \sqrt{\epsilon_{eff}} \quad (3.19)$$

$$\forall \epsilon_{eff} = \epsilon_r - \frac{\epsilon_r - \epsilon_e}{1 + P(f)} \quad (3.20)$$

Here ϵ_r is the relative permittivity of a dielectric substrate with height h , ϵ_e is the quasi-static value of ϵ_{eff} , and $P(f)$ is the frequency-dependent term.

According to the CMA theory discussed above, the quasi-static value of ϵ_{eff} , i.e. ϵ_e , can be written according to Equation (3.21) for three-layered stacked dielectric substrate layers in a stacked antenna design.

$$\epsilon_e = \epsilon_{r1}\epsilon_{r2} \frac{(q_1 + q_2)^2}{\epsilon_{r1}q_2 + \epsilon_{r2}q_1} + \epsilon_{r3} \frac{(1 - q_1 - q_2)^2}{\epsilon_{r3}(1 - q_1 - q_2 - q_3) + q_3} \quad (3.21)$$

Further, to consider the effect of fringing ϵ_r' for a patch antenna, can be expressed as:

$$\epsilon_r' = \frac{2\epsilon_e - 1 + A}{1 + A}, \quad \forall \quad A = \left(1 + \frac{12h}{W}\right)^{-1/2} \quad (3.22)$$

Here h is the height of the dielectric substrate between the patch and the ground, while W is the width of the patch. Thus, using CMA, the effective dielectric constant of multiple stacked layers can be obtained and the total input impedance of the antenna can be obtained by using Equation (3.13). However, this method has become obsolete and other techniques like the cavity model and transmission-line model are more frequently used nowadays because of their simplicity and better relation with respect to the antenna's physical design parameters.

3.3 TRANSMISSION-LINE MODEL ANALYSIS APPROACH

The transmission-line model of a microstrip patch antenna treats the patch as a transmission line with a dielectric separating it from the ground beneath. The open ends of the patch antenna, which create fringing fields

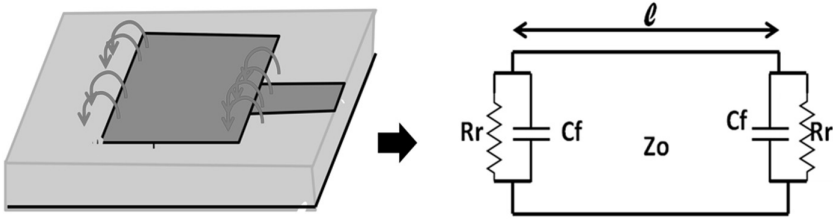


Figure 3.7 Transmission-line equivalent model of microstrip patch antenna.

and contribute to antenna radiation, are represented by fringing capacitance and radiation resistance in the shunt. The transmission-line model of a rectangular microstrip patch antenna is illustrated in Figure 3.7. According to [9], this model provides a physical understanding of the antenna's radiation parameters. The signal is considered to be propagating along the patch similar to a transmission line with characteristic impedance Z_o , of length l equal to the length of the patch ($l \approx \lambda_g/2$). The fields fringe out across the width of the patch when using longitudinal antenna feeding, and this is accounted for by the fringing capacitance C_f . The resulting radiation is accounted for by the radiation resistance R_r . The equations for the transmission-line model parameters can be expressed as given below.

The parasitics R_r and C_f shown in Figure 3.7 are radiation resistance and fringing capacitance respectively, as discussed above. Z_o is the characteristic impedance of the transmission-line segment of length ' l '. The values of these parameters can be obtained using the formulas given in Equations (3.23)–(3.30).

$$Z_o = \frac{377}{\sqrt{\epsilon_r}} \left\{ \frac{w}{h} + 0.833 + \left(\frac{\epsilon_r + 1}{\pi \epsilon_r} \right) * \left[\ln \left(\frac{w}{2h} + 0.94 \right) + 1.451 \right] + 0.165 \left(\frac{\epsilon_r - 1}{\epsilon_r^2} \right) \right\}^{-1} \quad (3.23)$$

$$C_f = \frac{1}{2} * l * \left(\frac{\sqrt{\epsilon_{re}}}{c Z_o} - \frac{\epsilon_o \epsilon_r w}{h} \right) \quad (3.24)$$

$$R_r = \frac{\lambda_o^2 * P}{w h \sqrt{\epsilon_r}} \quad (3.25)$$

$$\text{where } P = a_2 * a_3 \quad (3.26)$$

$$a_2 = 1.255 - 0.124 \epsilon_r + 0.01 \epsilon_r^2 \quad (3.27)$$

$$a_3 = \left(h * \frac{\sqrt{\epsilon_r}}{\lambda_o} \right)^{(0.1+b)} * \left(10 + \left(\epsilon_r^{-0.5} * 200^b \right) \right) \text{ where } b = \frac{w}{\lambda_o} \quad (3.28)$$

$$\lambda_o = 2(l + \Delta l) \sqrt{\epsilon_{re}} \text{ where } \Delta l = 0.412 * h * \frac{(\epsilon_{re} + 0.3) \left(\frac{w}{h} + 0.264 \right)}{(\epsilon_{re} - 0.258) \left(\frac{w}{h} + 0.8 \right)} \quad (3.29)$$

$$\epsilon_{re} = \frac{\epsilon_r + 1}{2} + \frac{\epsilon_r - 1}{2} \left(1 + \frac{12h}{w} \right)^{-0.5} \quad (3.30)$$

Z_o representing the characteristic impedance is calculated as given in Equation (3.23) [10], while the radiation resistance R_r given by Equation (3.25) is obtained from the CAD formula given in [11]. The fringing capacitance C_f is as given in Equation (3.24) [12], and μ_{re} gives the effective dielectric constant of the transmission-line. The above-mentioned parameters can be readily computed using well-established formulas. As a result, this transmission-line model can effectively serve as a fundamental component in analyzing circuitry for stacked microstrip antennas. This same foundational concept can be further applied to represent stacked microstrip antennas in relation to equivalent circuit parameters, which can then be utilized for the static analysis of the stacked antennas.

The transmission-line model described above is further modified in [13]. In addition to the individual slot (patch edge) admittance, the coupling admittance between the two slots is also considered. Moreover, the admittance of side slots (edges along the width) is analyzed along with the correction of admittance formulas for narrow patches, which are not considered in the basic transmission-line model of a rectangular microstrip patch. For the analysis of stacked antennas, the basic transmission-line model will be the main focus due to the increased complexity of the design itself and its dependence on several design parameters. Numerous research works have been conducted on the transmission-line equivalent model of these complex multi-layered stacked antennas. As mentioned earlier, static antenna analysis methods are approximate models, but they are relatively fast and simple and provide sufficient insights into the antenna's performance. This section will discuss the various ways in which transmission-line model theory can be applied to stacked antenna analysis.

3.3.1 Analysis of aperture-coupled microstrip antenna

A simple transmission-line model for the analysis of an aperture-coupled microstrip antenna is presented in [14]. The analysis of mutual coupling is

Figure 3.8 Aperture-coupled microstrip line with tilted slot, (a) geometry, (b) proposed circuit-level equivalent model. Reproduced with permission from IEEE [15].

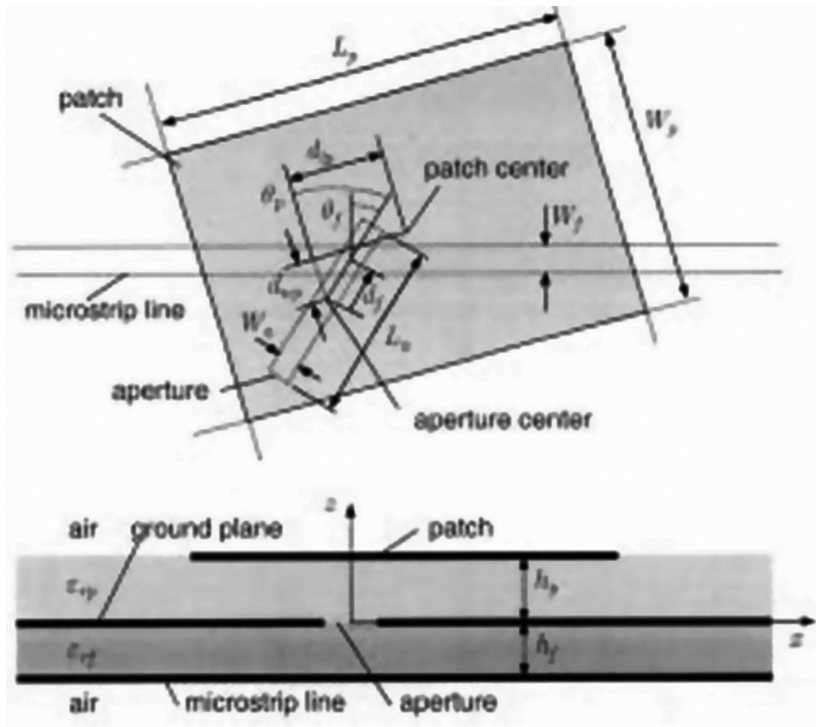
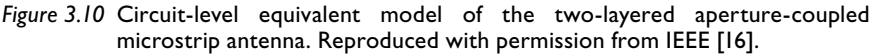


Figure 3.9 Aperture-coupled microstrip antenna with tilted slot geometry. Reproduced with permission from IEEE [16].

orthogonal field components, to represent the driven patch. The electromagnetic coupling of the driven patch with the slot is incorporated through the inductance of the transformer coil. The driven patch and the metallic layer containing the slot are considered as an equivalent transmission line with a characteristic impedance Z_o calculated based on their dimensions. The transmission-line edges are terminated with admittances representing radiation resistance and fringing capacitance. As the driven patch is treated as the intersection of two orthogonal transmission-line segments, the equivalent circuit model, depicted in Figure 3.10, illustrates this configuration through two parallel transmission lines. Each of the orthogonal transmission lines is subdivided into two sections based on the location of the slot beneath the driven patch. The electromagnetic fields extending from the slot are linked to the driven patch, and the electromagnetic energy is subsequently coupled to the driven patch. The electromagnetic coupling between the fields of the driven patch and the slot is addressed using a transformer coil, and the coupling between the slot and the ground is also considered using a transformer coil.


$$\mathbf{E}_s = V_s \bar{\mathbf{e}}_s \quad (3.31)$$
$$\bar{e}_s = -x, \frac{1}{\pi \sqrt{\left(\frac{W_s}{2}\right) 2 - x^2}} g(y), \quad (3.32)$$
$$n_f = \frac{\sqrt{Z_{of}}}{2} \left[(n_{fx1} - n_{fx2}) \sin \theta_{sf} + (n_{fy1} + n_{fy2}) \cos \theta_{sf} \right] \quad (3.33)$$
$$n_{fx1} = \iint_S e_s h_{fx} e^{-j\beta x} dS \quad (3.34)$$

$$n_{fy1} = \int_S e_s h_{fy} e^{-j\beta x} dS \quad (3.35)$$

$$g_f(y') = \begin{cases} \cos p_f(y' - d_f), & \text{for } -(Ls/2) < y' < d_f \\ \cos q_f(y' - d_f), & \text{for } d_f < y' < (Ls/2) \end{cases} \quad (3.36)$$

where

$$p_f = \frac{\pi}{2(Ls/2 + df)} \quad (3.37)$$

$$q_f = \frac{\pi}{2(Ls/2 - df)} \quad (3.38)$$

Exactly the same procedure is used to evaluate n_{p1} and n_{p2} . The model is further modified to consider the antenna's physical parameters and an optimized compensation length to account for slot proximity with respect to the patch. The transmission-line parameters, Z_0 , β , and Δl , are calculated using analytical methods given in [17]. The compensation length L_c expression is obtained based on comparison with the method of moments results as:

$$L_c = 7.0 \times 10^{-2} \frac{W_f}{h_f \sqrt{\epsilon_{rf}} / \lambda_0} n_f \sqrt{n_{p1}^2 + n_{p2}^2} \quad (3.39)$$

where λ_0 is the free-space wavelength. With the calculation of all the circuit parameters, the input impedance of the circuit model can be evaluated. The results of the proposed theory are close to the measured results as given in [16].

3.3.2 Transmission-line model of stacked microstrip antenna with inter-layer coupling modelled through mutual capacitance

In this work a compact stacked antenna operating at dual frequency is analyzed using the transmission-line equivalent model [18]. The proposed stacked antenna is made of two patches, placed over two substrates and backed by the ground plane. The two stacked patches are inter-connected through a via-hole. The via-hole connection between the two stacked patches increases coupling among the layer and improves its overall response. Proposed antenna geometry is shown in Figure 3.11. The position of the

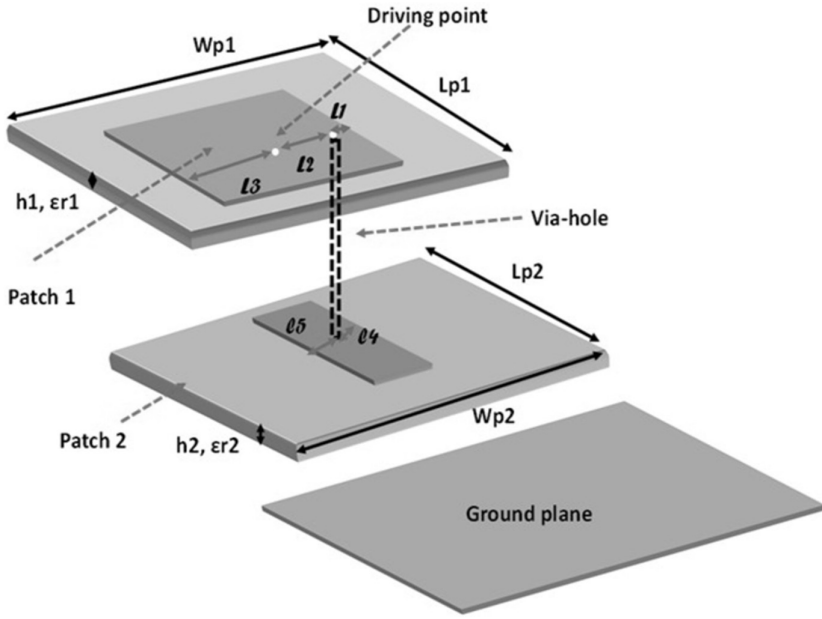


Figure 3.11 Geometry of proposed stacked antenna with parasitic patch at the middle. Redrawn from [18].

via-hole is also studied for better performance of the antenna. When the via-hole is placed close to the radiating edge of the patch, the current path length increases and for the same dimensions the resonant frequency decreases. This leads to miniaturization of the antenna design. Moreover, the location of the via-hole must be along the driving point/feed point axis, or else the current distribution across the patch will become asymmetric.

The antenna is designed to operate at 2.4 GHz and 5.2 GHz; thus, the patch dimensions are obtained as: $h_1 = 0.8$, $h_2 = 0.8$, $L_{p1} = 14.2$, $W_{p1} = 14.2$, $L_{p2} = 4.7$, and $W_{p2} = 15$ mm, respectively, with both substrates of dielectric constant 4.4. The stacked antenna with via-hole resonates at the dual frequency when properly optimized and the relation between resonant frequencies with respect to patch dimensions are given by Equations (3.40) and (3.41). Here p_1 , p_2 , p_3 , p_4 , q_1 , and q_2 are the weighing factors that can be calculated by linear fitting.

$$\lambda_1/2 = p_1 L_{p1} + p_2 W_{p1} + p_3 L_{p2} + p_4 W_{p2} + h_1 \quad (3.40)$$

$$\lambda_2/2 = q_1 L_{p1} + q_2 W_{p1} \quad (3.41)$$

These relations explain that the first resonant frequency is dependent on the dimensions of the patches as the current flows through the via-hole,

increasing the overall electrical length. While the second resonant frequency is dependent only on the upper patch dimensions.

The proposed antenna is then analyzed based on transmission-line theory, where each patch of the antenna is modelled as a transmission-line segment which is terminated at the edges by radiating resistance (conductance in shunt) and fringing capacitance (to represent radiating slots). The via-hole connecting the two patches is modelled through a capacitor, while the coaxial feed line is modelled as an inductor. The edge admittance parameters are given by Equation (3.42):

$$Y_s^i = G_s^i + jB_s^i \quad (3.42)$$

The radiation conductance (G_s^i) and radiation susceptance (B_s^i) can be calculated as follows [18]:

$$G_s^i = \begin{cases} \frac{1}{90} \left(\frac{W_i}{\lambda_o} \right)^2, & W_i < 0.35\lambda_o \\ \frac{W_i}{120\lambda_o} - \frac{1}{60\pi^2}, & 0.35\lambda_o \leq w_i < 2\lambda_o \\ \frac{w_i}{120\lambda_o}, & 2\lambda_o < w_i \end{cases} \quad (3.43)$$

$$B_s^i = Y_s^i \tan \beta_i \Delta l_i \quad (3.44)$$

where λ_o is the wavelength in free space, and β_i and Δl_i are the phase propagation constant and fringing lengths of the patch.

$$Y_o^i = \begin{cases} \frac{\sqrt{\epsilon_e^i}}{377} \left\{ \frac{w_i}{h_i} + 0.883 + 0.615 \frac{\epsilon_e^i - 1}{(\epsilon_e^i)^2} \right. \\ \quad \left. + \frac{\epsilon_e^i + 1}{\pi \epsilon_e^i} \left[\ln \left(\left(\frac{w_i}{h_i} + 1.88 \right) + 0.758 \right) \right] \right\}, & \frac{w_i}{h_i} > 1 \\ \frac{\sqrt{2(\epsilon_e^i + 1)}}{120} \left[\ln \frac{8h_i}{w_i} + 32 \left(\frac{w_i}{h_i} \right)^2 \right]^{-1}, & \frac{w_i}{h_i} \leq 1 \\ \quad \left[-\frac{\epsilon_e^i - 1}{\epsilon_e^i + 1} \left(0.2258 + \frac{0.1208}{\epsilon_e^i} \right) \right], & \frac{w_i}{h_i} \leq 1 \end{cases} \quad (3.45)$$

The inductance of the coaxial probe and via-hole is calculated according to [19] as given by Equation (3.46):

$$L_f = \frac{377h}{2\pi c_o} \ln \left(\frac{c_o}{\pi f_r d \sqrt{\epsilon_e}} \right) \quad (3.46)$$

In the above equations c_o is the speed of light, d and h are the diameter and thickness of the coaxial probe used, and f_r is the antenna's resonant frequency respectively. Now the capacitance of the coupling capacitor which indicates mutual coupling among the driven patch and the parasitic patch needs to be evaluated. In a conventional stacked antenna, where the lower patch is fed via coaxial feed and the upper parasitic patch is stacked above it, the coupling capacitance between the two is given by Equation (3.47) [20]. The antenna design in the present case has a parasitic patch lying beneath the driven patch and therefore the amount of coupling present among the layers has reduced. This results in a modified coupling capacitance expression as given by Equation (3.48). The parameters C_1 , C_2 , and k_c are obtained according to the cavity model discussed in [19]. The input impedance of the proposed stacked antenna is given by Equation (3.49) according to Figure 3.12. The computed input impedance of the antenna closely approximates the measured input impedance [18].

$$C_v = \frac{-(C_1 + C_2) + \left[(C_1 + C_2)^2 - 4(1 - k_c^{-2})C_1C_2 \right]^{1/2}}{2} \quad (3.47)$$

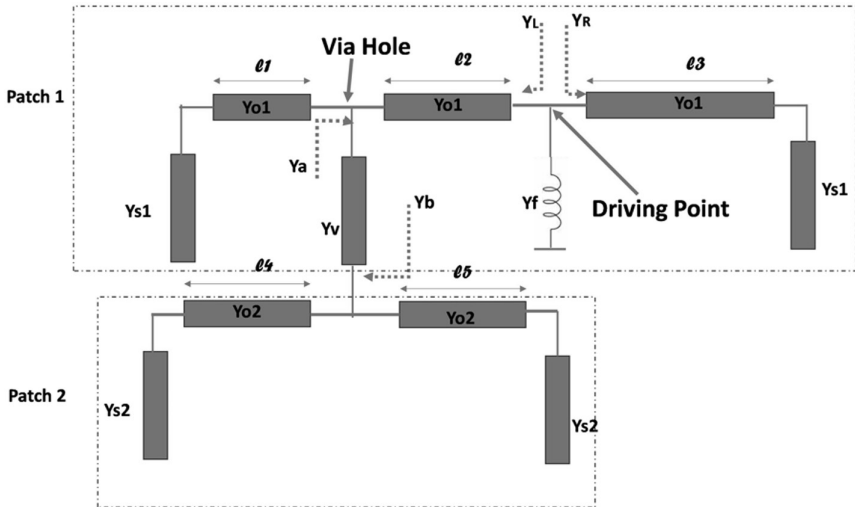


Figure 3.12 TLM based circuit-level equivalent of the proposed stacked antenna. Redrawn from [18].

$$C_v = \frac{-(C_1 + C_2) + \left[(C_1 + C_2)^2 - k_c^2 (1 - k_c^{-2}) C_1 C_2 \right]^{1/2}}{2} \quad (3.48)$$

$$Z_{in} = j\omega L_f + (Y_R + Y_L)^{-1} \quad (3.49)$$

where Y_R and Y_L are the driving point admittances as shown in Figure 3.12:

$$Y_R = Y_0^1 \left[\frac{Y_s^1 + Y_0^1 \tanh(\gamma_1 l_3)}{Y_0^1 + Y_s^1 \tanh(\gamma_1 l_3)} \right] \quad (3.50)$$

$$Y_L = Y_0^1 \left[\frac{Y_a^1 + Y_0^1 \tanh(\gamma_1 l_2)}{Y_0^1 + Y_a^1 \tanh(\gamma_1 l_2)} \right] \quad (3.51)$$

$$Y_a = Y_0^1 \left[\frac{Y_s^1 + Y_0^1 \tanh(\gamma_1 l_1)}{Y_0^1 + Y_s^1 \tanh(\gamma_1 l_1)} \right] + \left(\frac{1}{Y_v} + \frac{1}{Y_b} \right)^{-1} \quad (3.52)$$

and

$$Y_b = Y_0^2 \left[\frac{Y_s^2 + Y_0^2 \tanh(\gamma_2 l_4)}{Y_0^2 + Y_s^2 \tanh(\gamma_2 l_4)} \right] + Y_0^2 \left[\frac{Y_s^2 + Y_0^2 \tanh(\gamma_2 l_5)}{Y_0^2 + Y_s^2 \tanh(\gamma_2 l_5)} \right] \quad (3.53)$$

3.3.3 TLM analysis model with EM coupling modelled using fringing admittance

The given analysis model of the stacked microstrip antenna is based on the basic transmission-line model of the microstrip antenna. The method involves extending the concept of fringing fields that exist between the patch and the ground (for the case of a basic microstrip patch antenna), to the fields coupled between the stacked patches. This analysis model considers the interaction of fringing fields among the stacked layers as the electromagnetic coupling among the layers, when the antenna is excited with the feed line. Similar to the basic microstrip antenna's transmission-line model, which considers antenna radiation through fringing capacitance and radiation resistance, the multiple stacked patches are coupled through these fringing fields of the driven patch and the parasitic patches are stimulated through electromagnetic coupling. The details of the proposed analysis method based on the transmission-line model and the detailed methodology of its implementation are covered extensively. The stacked antennas considered here are fed with a microstrip feed line and feature a planar unbroken ground plane. The proposed transmission-line model is applicable for generalized multi-layered stacked antenna analysis with a planar

ground plane, and the propagating modes are also considered to make it applicable to all antennas. The implementation of the model is discussed in detail, initially considering antennas without slots and then extending it to stacked antennas with slots.

3.3.3.1 Concept of implementing proposed TLM model

Consider the case of two-layered stacked antenna as shown in Figure 3.13 [21]. The antenna can be seen as two transmission-line segments, one between the ground and driven patch and one between the driven patch and parasitic patch. The fringing effect is modelled by a fringing capacitance and radiation resistance in shunt at the open terminals of the transmission line. These effects are taken into account at each layer. The fringing admittance is considered between the driven patch and ground plane, the parasitic patch and ground plane, and the parasitic patch and driven patch as shown in Figure 3.13. These contemplations encompass overall electromagnetic coupling among the two resonant layers and the ground plane.

Similarly, let's assess the two-layered stacked antenna with parasitic patch at an offset with respect to the driven patch as shown in Figure 3.14. In this scenario, the patches should be represented by multiple transmission-line segments to account for the offset of the parasitic patch. One segment consists of a transmission-line pair between the driven patch and ground only (without overlapping the parasitic patch), with a characteristic impedance of Z_{o1} . The length of this segment extends from the edge to the overlap margin of the parasitic patch. The remaining length of the driven patch forms a transmission-line segment with the ground and terminates in fringing admittance with respect to the ground. This division of the driven patch length incorporates information about the parasitic patch offset in the antenna

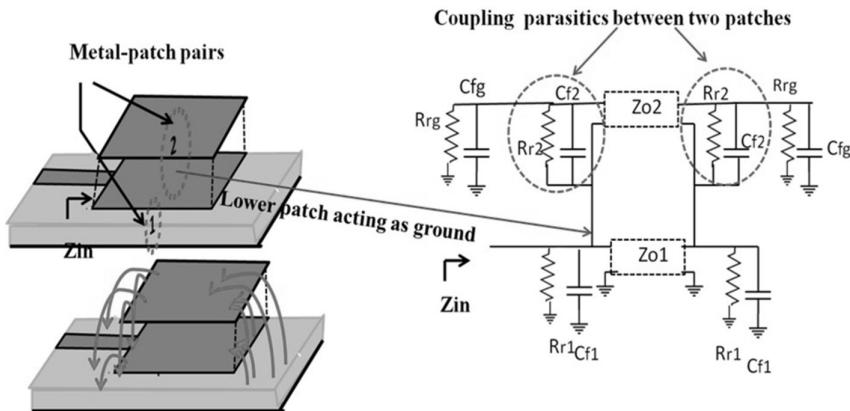


Figure 3.13 Two-layered stacked microstrip antenna and its equivalent TLM model based on proposed method. Reproduced with permission from IET [21].

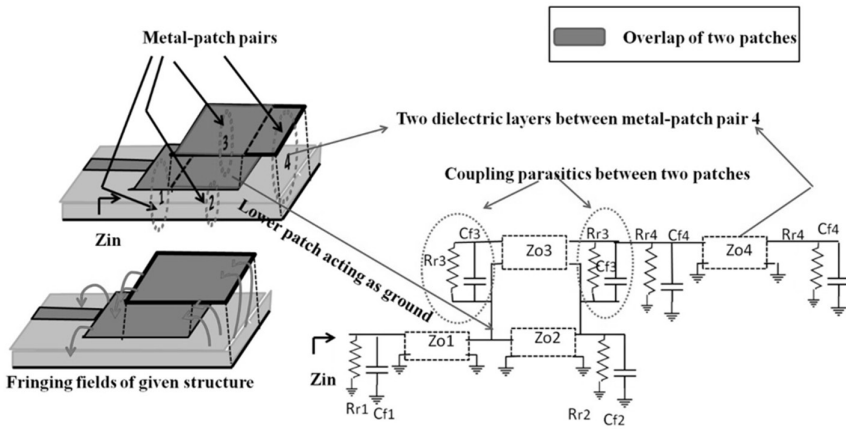


Figure 3.14 Two-layered stacked microstrip antenna geometry with parasitic patch at offset, and its equivalent TLM model based on proposed method. Reproduced with permission from IET [21].

design. Similarly, the parasitic patch is represented by two transmission-line segments of different lengths: one with a length equal to the overlap with the driven patch, and the second with a length that is offset with respect to the driven patch. The fringing admittance of the parasitic patch is taken into account with respect to the driven patch and with respect to the ground. Notably, the section of the parasitic patch directly above the ground experiences strong electromagnetic coupling with respect to the ground. All the transmission-line parameters and fringing parameters are calculated using closed-form expressions given in Equations (3.23)–(3.30).

Further, the three-layered stacked antenna design shown in Figure 3.15 is an extension of a previous design, featuring an additional parasitic patch offset from the lower parasitic patch. The inclusion of an upper parasitic patch at an offset leads to the segmentation of the lower parasitic patch. By modeling the upper parasitic patch in a manner similar to the lower parasitic patch, the patch can be divided into two sections, allowing for a better assessment of circuit-level parameters and an improved representation at the circuit level. In this design, electromagnetic coupling exists not only between the ground and driven patch, and the driven patch and the lower parasitic patch, but also between the upper and lower parasitic patches. As a result, the fringing admittance needs to be evaluated for each section of the transmission-line representation of the patch segments with respect to the layer beneath it.

3.3.2 Implementation of proposed TLM on stacked antenna

A three-layered stacked microstrip antenna operating in X-band, is shown in Figure 3.16. In this section, the analysis of this antenna is discussed

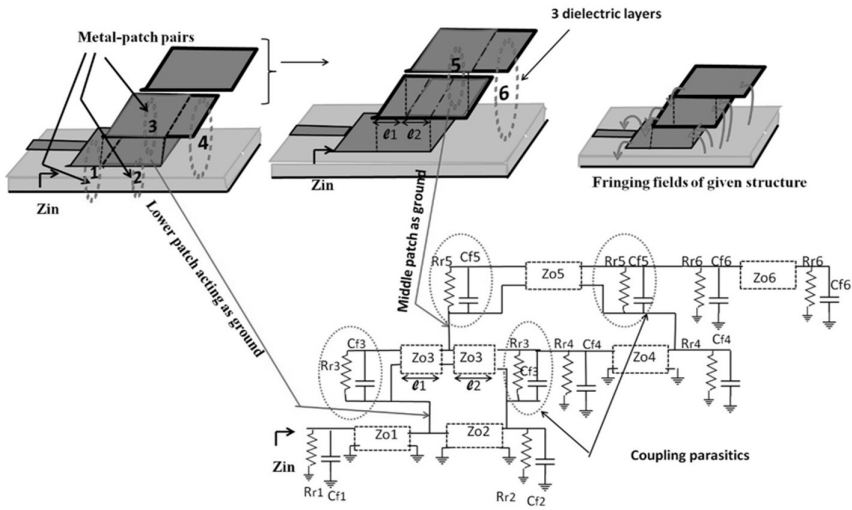


Figure 3.15 Three-layered stacked microstrip antenna with the patch offset and its equivalent TLM model based of proposed method. Reproduced with permission from IET [21].

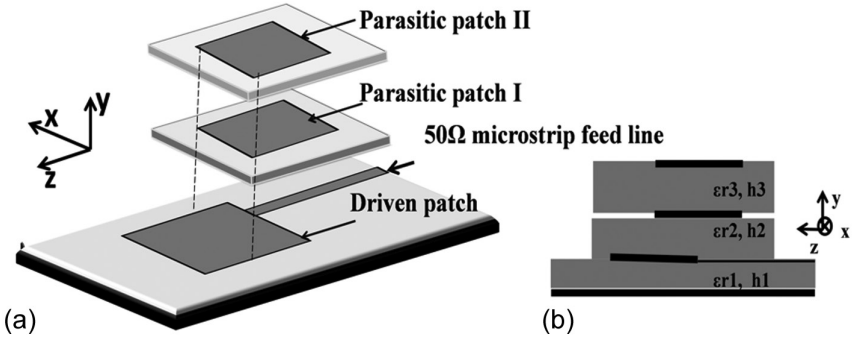


Figure 3.16 Proposed three-layered stacked antenna (a) design, (b) side view. Reproduced with permission from IET [21].

based on the transmission-line model with EM coupling modelled using fringing admittance. The implementation of the proposed transmission-line model on the stacked antenna design is done in different stages. The stacked antenna is analyzed layer-by-layer to evaluate the response of the antenna at each stage and then review the response with the addition of each layer. To begin with, the model is implemented on the lower-most layer, i.e. the driven patch and ground pair, with its patch segments and the current distribution shown in Figure 3.17

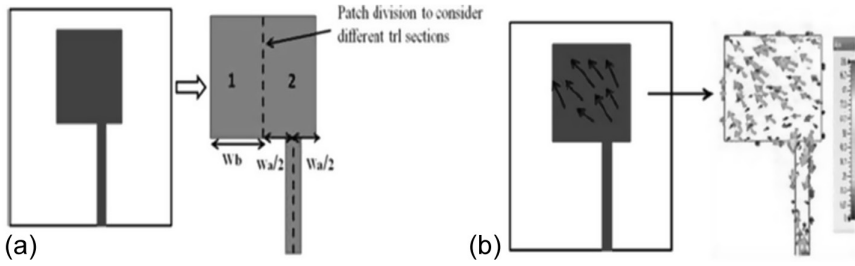


Figure 3.17 Geometry of shifted-fed patch, (a) patch segments accounting for shift in the feed, (b) current distribution across the patch.

The driven patch is fed with the shifted feed and the current flow is therefore diagonal through it. Representing the patch and ground pair as a transmission line terminated at open ends is not possible in this scenario. The transmission-line model only considers the longitudinal current flow through it. However, in this particular design, the current flows diagonally through the driven patch. To incorporate this into the model, the patch will be divided into multiple transmission-line segments. In this instance, the patch is divided into four transmission-line segments – two vertical and two horizontal. The width of two horizontal transmission-line segments (along the patch width) is chosen so that the feed line lies at the centre of the first segment with width W_a , while the width of the second transmission-line segment W_b is the remaining width of the patch. Vertical segmentation occurs at half the patch length. The feed and driven patch connection is modelled through a step transition between different width transmission lines, as shown in Figure 3.18. The following Equations (3.54)–(3.57) give the expressions to calculate the parameters at the step transition which are used in the model. The overall circuit-level model of the driven patch is shown in Figure 3.19.

$$C = 0.00137 * h * \frac{\sqrt{\epsilon_{re1}}}{Z_{c1}} \left(1 - \frac{w_2}{w_1} \right) \left(\frac{\epsilon_{re1} + 0.3}{\epsilon_{re1} - 0.258} \right) \left(\frac{\frac{w_1}{h_1} + 0.264}{\frac{w_1}{h_1} + 0.8} \right) \quad (3.54)$$

$$L_1 = \frac{L_{o1}}{L_{o1} + L_{o2}} * L, \quad L_2 = \frac{L_{o2}}{L_{o1} + L_{o2}} * L \quad (3.55)$$

$$L_{oi} = Z_{oi} * \frac{\sqrt{\epsilon_{rei}}}{c} \quad (3.56)$$

$$L = 0.000987 * h * \left(1 - \frac{Z_{o1} \sqrt{\epsilon_{re1}}}{Z_{o2} \sqrt{\epsilon_{re2}}} \right)^2 \quad (3.57)$$

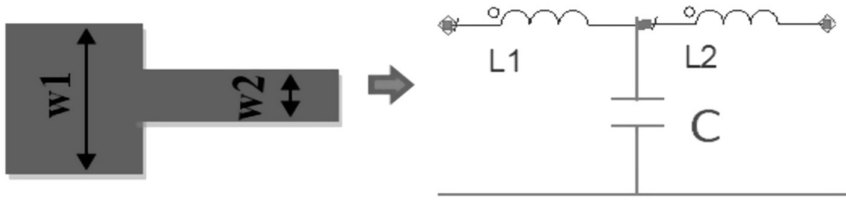


Figure 3.18 Step-transition and the equivalent circuit parameters. Reproduced with permission from IET [21].

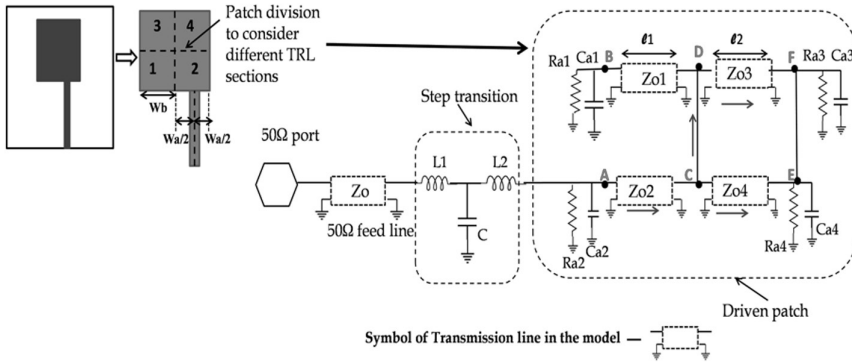


Figure 3.19 Shifted-fed driven patch of the proposed stacked antenna and its equivalent TLM model based on proposed method, including the effect of orthogonal current flow across the patch. Reproduced with permission from IET [21].

In the above equations, L_{oi} for $i = 1, 2$ represent inductance per unit length of the respective microstrip segments with widths w_1 and w_2 respectively, while Z_{oi} and ϵ_{rei} are respective characteristic impedances and effective dielectric constants.

The circuit model describes the parameters of the driven patch, fed via shifted microstrip feed line. The transmission-line segments are represented by their respective characteristic impedances and are terminated with fringing capacitance and radiation resistance calculated corresponding to the respective segment dimensions and substrate parameters. The diagram shows that transmission-line segments 1 and 2 are kept open (as shown by open nodes A and B) at one end, while segments 3 and 4 are connected to each other (as shown by nodes C, D, E, and F) at both ends. This connection ensures current flows diagonally through these segments as per the directions shown in Figure 3.19. This diagonal flow of current confirms the presence of orthogonal modes propagating in the antenna which are considered through this driven patch model of the stacked antenna.

The complete circuit-level model of the driven patch fed by a shifted microstrip feed line is developed based on the transmission-line equivalent

of a microstrip antenna with required modifications to consider changes in the physical and electrical parameters. As discussed earlier, the fringing admittance, comprising of fringing capacitance and radiation resistance in shunt, is calculated according to Equations (3.23)–(3.30). The response of the developed model for the given driven patch is in line with its simulated response as shown in Figure 3.20.

The next step in the analysis based on the proposed transmission-line model involves considering the design with the addition of a parasitic patch to the lower part of the stacked antenna. In this case, the lower parasitic patch is offset with respect to the driven patch. This offset enhances the antenna impedance matching and needs to be evaluated in the analysis model. The two-layered stacked antenna can be modelled at the circuit level by treating this structure as a combination of multiple transmission-line segments. The circuit model of the driven patch is adjusted at this stage to incorporate the overlap of the parasitic patch above it. The length division of the driven patch is modified, with l_1 representing the length of the overlap of the parasitic patch on the driven patch and l_2 representing the remaining length of the driven patch.

The model representation of the parasitic patch also involves multiple patch segments, with the length division represented by l_1 and l_3 due to its offset relative to the driven patch. It is important to consider the overlap of the parasitic patch with the feed line due to strong electromagnetic coupling between the feed and the parasitic patch. The model includes the positioning of shifted feed geometry again at this step. The width of the parasitic patch section directly above the feed and the ground is divided into three

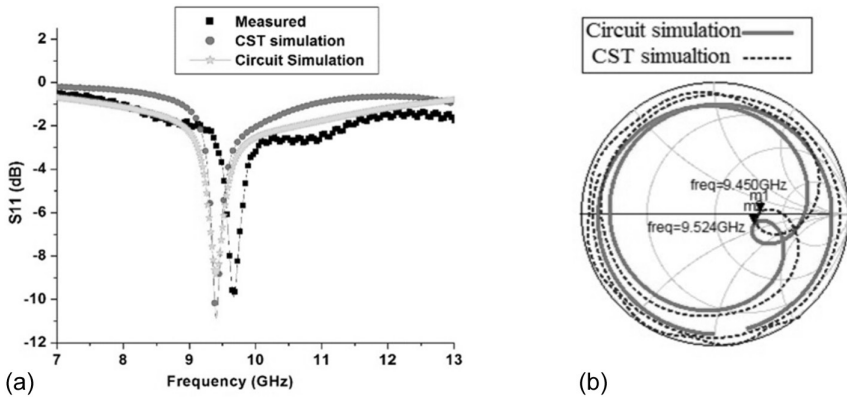


Figure 3.20 Response of the shifted-fed driven patch of the proposed antenna (a) S_{11} response with comparison of measured, CST simulation, and proposed model's circuit simulation results, (b) Smith chart response with comparison of CST and proposed model's circuit simulation results. Reproduced with permission from IET [21].

segments: one segment lying directly above the feed and equal to the width of the feed (segment 7), and the other two segments lying on either side of the remaining width (segments 5 and 6). The corresponding fringing admittance for each transmission-line segment is calculated based on their dimensions.

The fringing admittance of the section of the parasitic patch lying above the feed line (segment 7) is calculated with respect to the feed line, i.e. the feed line acts as a ground plane for it. The fringing admittance (fringing capacitance and radiation resistance) of segments 5 and 6 is calculated with respect to the ground plane of the antenna with two substrates lying between them: substrates 1 and 2. In this case, the effective dielectric constant is calculated according to Equation (3.58). Further the analysis must consist of information on the diagonal flow of current through the parasitic patch too due to the shifted feed used to drive the driven patch. To understand this, two orthogonal transmission-line sections are connected in parallel to represent two orthogonal modes getting excited. One section represents the TM_{001} mode while the second section represents the TM_{100} mode. The representation of the second section is also similar to the first one and the patch segments are considered here too, but along the width. As shown in Figure 3.21(c), transmission-line segments 3' and 4' are considered along the width, with segment 3' being a transmission-line made between the parasitic patch and the driven patch (as its ground) while segment 4' is a transmission-line between the parasitic patch and the ground plane. Again, two dielectrics need to be taken into consideration to calculate fringing admittance at the outer edge of segment 3' (towards the feed), which will be calculated with respect to the ground. As the fields fringe out towards the ground plane from the edge of segment 3', they will get coupled through both substrates and an effective dielectric constant ϵ_r is calculated for the same.

Considering all these physical parameters, i.e., the lengths and widths of different segments and the dielectric constant values, the circuit parameters like characteristic impedance, fringing capacitance, and radiation resistance are calculated to evaluate the overall input impedance of the antenna at this stage.

$$\epsilon_{ref} = \frac{\sum_{i=1}^n h_i}{\sum_{i=1}^n \frac{h_i}{\epsilon_{ri}}} \quad (3.58)$$

The complete transmission-line model, developed with the inclusion of a parallel section to take into account the orthogonal mode too, is shown in Figure 3.22(a), and the model's response compared with EM simulated and

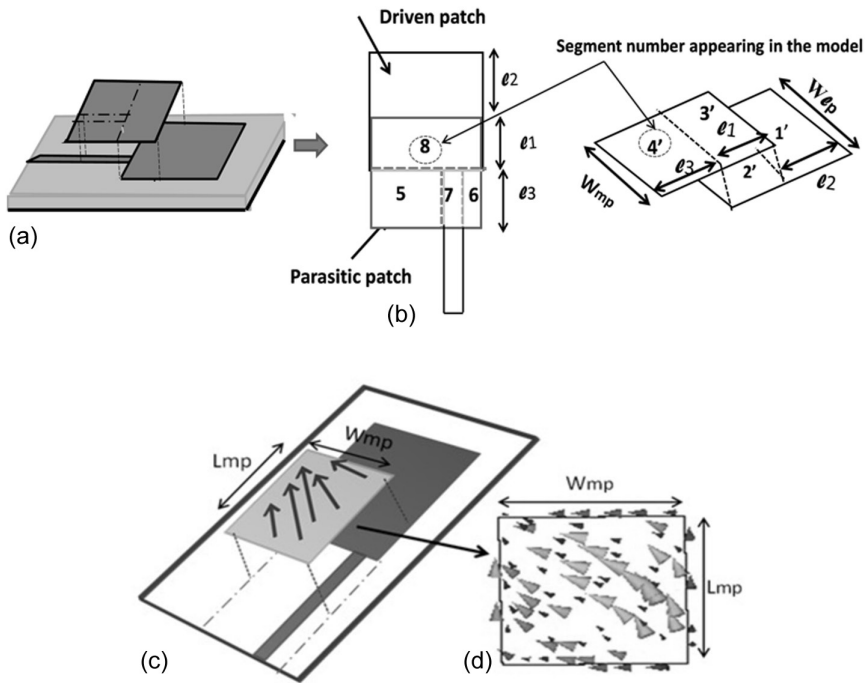
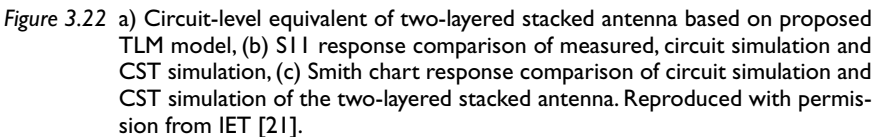


Figure 3.21 Two-layered stacked antenna, (a) layout, (b) patch segmentation along the patch length, and (c) patch segmentation along the width considered for proposed TLM implementation, (d) surface current distribution across the parasitic patch showing orthogonal current flow. Reproduced with permission from IET [21].

measured response of the antenna at this stage is shown in Figure 3.22(b) and Figure 3.22(c).

The final stage of the circuit-level analysis model of the proposed stacked antenna is the addition of the last stacked layer, i.e. the upper parasitic patch in the model. At this stage, the model just needs to be extended with consideration of the upper-most layer, while following the same method of the model analysis developed in the previous stage. As depicted in Figure 3.23, the current distribution across the upper-most patch is also orthogonal. So to incorporate this, again two parallel sections of the TLM model will be considered. This ensures consideration of both orthogonal modes being generated.

As the upper parasitic patch is smaller in dimension compared to the lower parasitic patch and lies just above the lower parasitic patch, just one transmission-line segment is enough to represent the upper parasitic patch in both sections (one representing the TM_{001} mode and the other representing the TM_{100} mode propagation). In the present model, segment



The model implementation can be extended for antennas with slots in their design using the concept of the mesh network equivalent of the patch

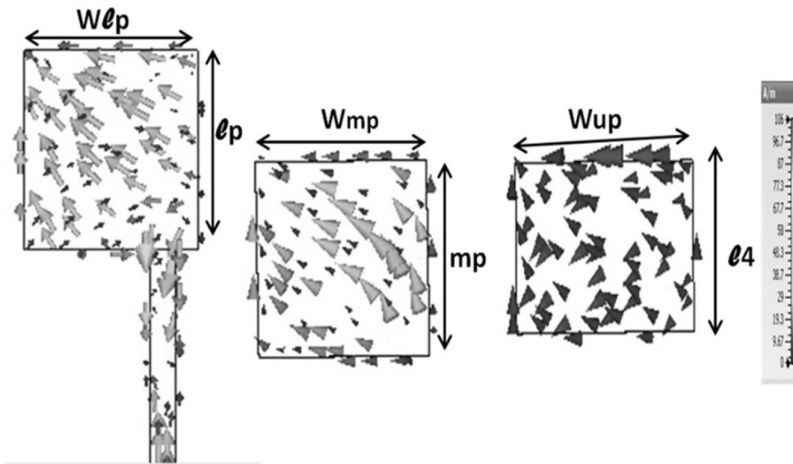


Figure 3.23 Current distribution at different layers of three-layered proposed stacked antenna. Reproduced with permission from IET [21].

as given in detail in [22]. Similar to the method discussed above, where patch segmentation is used to introduce the structural information of the antenna in the model, the mesh equivalent of the patch also divides the antenna patch into multiple small transmission-line segments. These transmission lines are repeated if the patch structure is uniform. However, if there is any discontinuity in the patch structure, the corresponding transmission-line segments exhibit the change to include the structural change in the model. The discontinuity in the patch can exist due to slots or due to different feeding positions. Further higher-order modes can be considered in parallel with the basic mode, as proposed in the above-discussed TLM-based circuit model.

3.4 CAVITY MODEL ANALYSIS OF STACKED RING PATCH ANTENNA

The cavity model of a microstrip patch antenna considers the patch to be a cavity resonator that can exhibit higher order resonances too, where cavity walls are modelled as perfect magnetic conductors. Considering the walls of the cavity as lossless, the cavity would not radiate and its input impedance in this case would be purely reactive. To make this antenna radiate according to the cavity model, it has to be made lossy by introducing loss tangent δ_{eff} [9], which lowers the Q value of the antenna ($Q = 1/\delta_{eff}$). This concept can be extended to a probe-fed antenna (shown in Figure 3.26) and also to probe-fed stacked ring antenna (shown in Figure 3.27) as presented in [23]. Initially, Green's function for TM modes can be determined as given in [23]

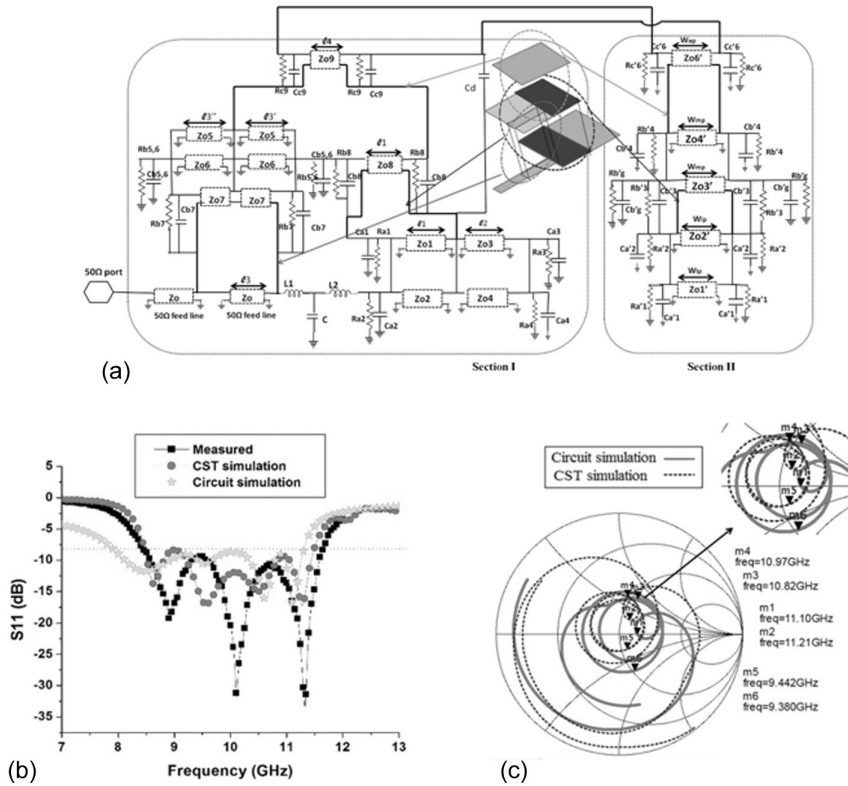


Figure 3.24 (a) Circuit-level equivalent of the proposed three-layered stacked antenna based on proposed TLM model, (b) S_{11} response comparison of measured, circuit simulation and CST simulation, (c) Smith chart response comparison of circuit simulation and CST simulation of the proposed three-layered stacked antenna. Reproduced with permission from IET [21].

assuming the substrate height is smaller than the wavelength ($h \ll \lambda$) such that the EF and electric current have no z variations. With coaxial feed, it can be assumed that the current has only a z -component.

According to the cavity model, assuming perfect magnetic walls (lossless), the tangential MF must vanish at the edge of the patch (ring in this case) and the complex wave number can be obtained by applying these boundary conditions.

Considering the fringing field effect, and the dispersion effect in the dielectric substrate, making the dielectric constant a function of frequency and introducing loss tangent with considerations of all the losses in the substrate gives rise to effective ring patch dimensions. The effective ring dimensions are given by Equations (3.59)–(3.62) [24, 25], for the probe-fed antenna shown in Figure 3.26.

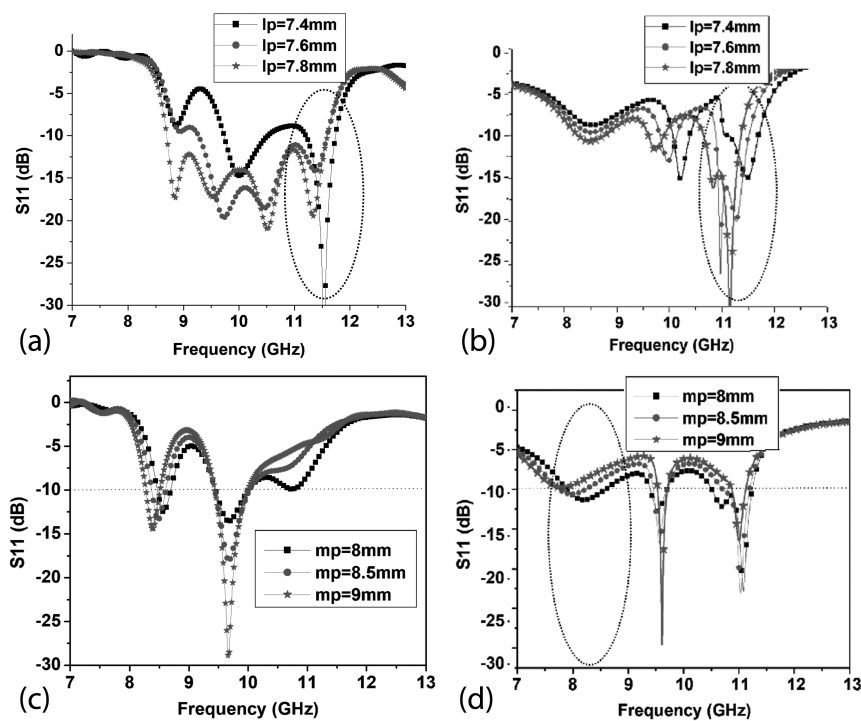


Figure 3.25 Comparison of CST simulation and circuit simulation results for changes in S11 response of the proposed three-layered stacked antenna with the changes in its physical dimensions, (a) CST simulation results and (b) circuit simulation results of antenna for different lower patch lengths (l_p), (c) CST simulation results and (d) circuit simulation results of antenna for different middle patch lengths (m_p). Reproduced with permission from IET [21].

Table 3.1 Design parameters of proposed three-layered stacked antenna

Parameter	Value (mm)	Parameter	Value (mm)
$W_{\ell p}$	7.5	W_{mp}	7.4
ℓ_p	8	m_p	7.5
W_b	4.5	W_c	0.65
W_a	1.5	W_d	5.65
Feed width [W_f]	1.1	W_{up}	7.56
ℓ_1	3.6	ℓ_4	5
ℓ_2	4.4	h_1	0.508
ℓ_3	3.9	h_2, h_3	0.762
$\ell_{3'}$	1.4	ϵ_{r1}	3.6
$\ell_{3''}$	2.5	$\epsilon_{r2}, \epsilon_{r3}$	2.2

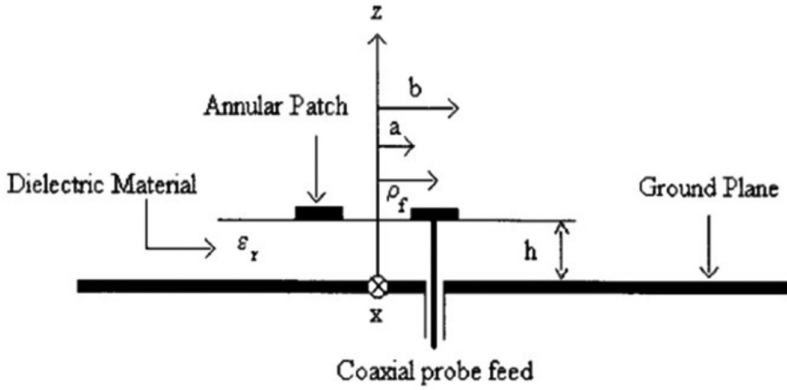


Figure 3.26 Geometry of probe-fed annular-ring patch antenna. Reproduced with permission from IEEE [23].

$$\Delta C_a = \ln\left(\frac{a}{2h}\right) + 1.41 \cdot \epsilon_r + 1.7726 + \frac{h}{a} (0.286\epsilon_r + 1.65) \quad (3.59)$$

$$a_{eff} = a \sqrt{1 - \frac{2h}{\pi a \epsilon_r}} \cdot \Delta C_a \quad (3.60)$$

And, for the effective outer radius, the expressions are given as:

$$\Delta C_b = \ln\left(\frac{b}{2h}\right) + 1.41 \cdot \epsilon_r + 1.7726 + \frac{h}{b} (0.286\epsilon_r + 1.65) \quad (3.61)$$

$$b_{eff} = a \sqrt{1 - \frac{2h}{\pi b \epsilon_r}} \cdot \Delta C_b \quad (3.62)$$

To consider the dispersion effect, the frequency-dependent effective dielectric constant of the material, according to [23], can be calculated as:

$$\epsilon_{eff}(f) = \epsilon_r - \frac{\epsilon_r - \epsilon_{eff}(0)}{1 + g(f)} \quad (3.63)$$

where $g(f)$ is a lengthy frequency function with the expression mentioned in [25] and $\epsilon_{eff}(0)$ is the effective permittivity expressed as:

$$\epsilon_{eff}(0) = \frac{\epsilon_r + 1}{2} + \frac{\epsilon_r - 1}{2} \cdot \frac{1}{\sqrt{1 + 12 \cdot \frac{h}{b - a}}} \quad (3.64)$$

The input impedance of the probe-fed ring patch antenna can be calculated according to the formula given in [23]

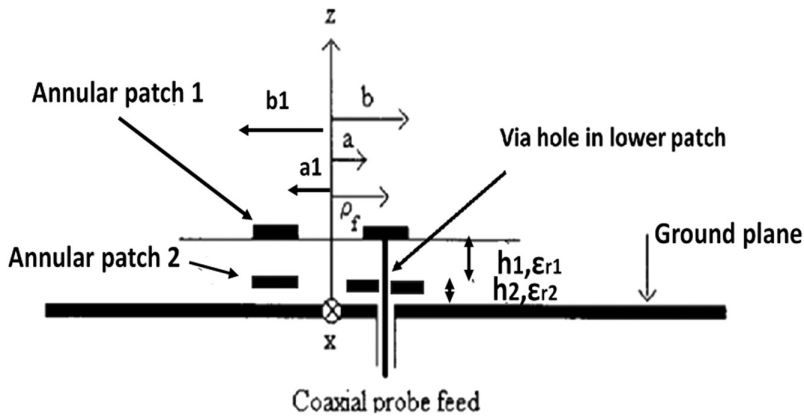


Figure 3.27 Geometry of probe-fed stacked annular-ring patch antenna. Redrawn from [23].

Similarly, parameters for the probe-fed stacked patch, shown in Figure 3.27, can be calculated by assuming the effective dielectric constant of the two substrates beneath the parasitic stacked patch and the ground. This effective dielectric constant can be obtained according to [26, 27] and should not be confused with ϵ_r , which considers the fringing effect, and $\epsilon_{eff}(f)$, which considers the dispersion effect. The resonant frequency of the lower patch with the dielectric layer above it can be calculated as Equation (3.65).

$$f_r = \frac{k_d}{2\pi\sqrt{\mu_o \cdot \epsilon_o \cdot \epsilon_{ef}}} \quad (3.65)$$

Also, for the upper parasitic patch, the resonant frequency can be calculated similarly, considering it to be covered with air as a dielectric. The theoretical and experimental input impedances of the stacked microstrip ring antenna for TM_{11} and TM_{21} modes are shown in Figure 3.28. The results of the proposed theoretical model are in agreement with the measured results.

3.5 SUMMARY

In this chapter, we explored various static analysis models for stacked microstrip antennas. We extensively covered several different cases of microstrip antenna designs and their static analysis. The development of the analysis models was explained at each design stage. We compared the results of the different analysis models with the measured results of the respective antennas. In most cases, the response of the static analysis models closely matched the measured results.

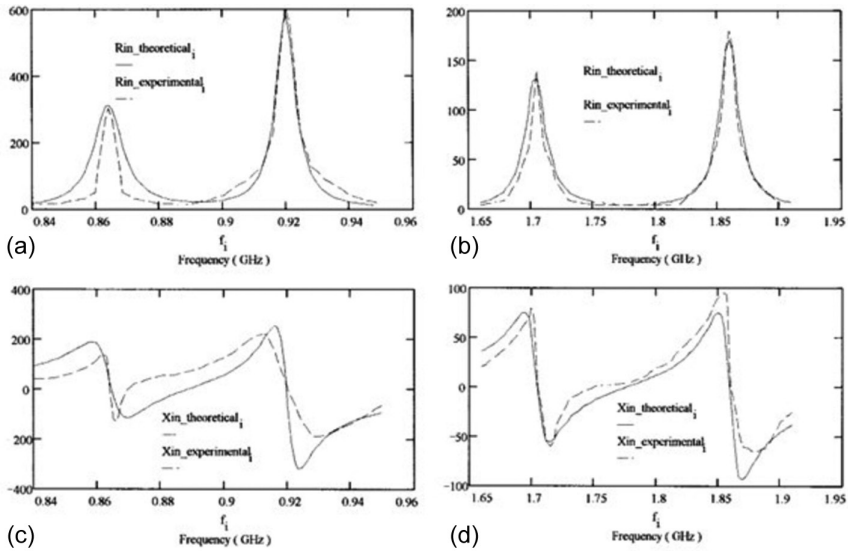


Figure 3.28 (a) Comparison of theoretical and experimental input impedance of a stacked microstrip ring antenna working in the TM₁₁ mode with $a_1 = a_2 = 2.5$ cm, $b_1 = b_2 = 5$ cm, $\epsilon_{r1} = \epsilon_{r2} = 2.32$, $h_1 = h_2 = 1.59$ cm with coaxial feed at 2.7 cm from the centre, (b) comparison of theoretical and experimental input impedance of a stacked microstrip ring antenna working in the TM₁₁ mode with $a_1 = a_2 = 2.5$ cm, $b_1 = b_2 = 5$ cm, $\epsilon_{r1} = \epsilon_{r2} = 2.32$, $h_1 = h_2 = 1.59$ cm with coaxial feed at 2.7 cm from the centre. Reproduced with permission from IEEE [23].

REFERENCES

1. Ramesh Garg, Prakash Bhatia, Inder Bahl, and Apisak Ittipiboon, "Microstrip Antenna Design Handbook" Artech House, 2000.
2. A. H. Wheeler, "Transmission line properties of parallel wide strips by a conformal mapping approximation", *IEEE Trans. Micro. Theory Tech.*, Vol. 12, No. 3, pp:280-289, 1964.
3. J. Svacina, "Analysis of multilayer microstrip lines by a conformal mapping method", *IEEE Trans. Microw. Theory Tech.*, Vol. 40, No. 4, pp:769-772, April 1992.
4. A. Farrar, and A. T. Adams, "Multilayer microstrip transmission lines," *IEEE Trans. Microw. Theory Tech.*, vol. MTT-22, no. 10, pp:889-891, 1974.
5. E. Yamashita, "Variational method for the analysis of microstrip-like transmission lines," *IEEE Trans. Microw. Theory Tech.*, Vol. MTT-16, No. 8, pp:529-535, 1968.
6. Shunshi Zhong, Gang Lin, and V. Stashevich, "Improved Transmission-line Model for Input Impedance of Rectangular Microstrip Antennas with Multi-Dielectric Layers", IEEE Antennas and Propagation Society International Symposium and URSI National Radio Science Meeting, June 1994.
7. E. Lier, "Improved formulas for input impedance of coax-fed microstrip patch antennas," *IEE Proc.*, Vol. 129, pp:161-164, August 1982.

8. H. Pues, and A. R. Van de Capelle, "Accurate transmission-line model for the rectangular microstrip antenna," *IEE Proc.*, Vol. 131, pp:334–340, December 1984.
9. C. A. Balanis, "*Antenna Theory: Analysis and Design*" Wiley Publications, 2001.
10. K. C. Gupta, R. Garg, and I. J. Bahl, "*Microstrip Lines and Slotlines*" Artech House, 1979.
11. K. Guney, "Closed-form expression for radiation resistance of a resonant rectangular microstrip patch antenna", *Int. J. Microw. Computer-Aided Eng.*, Vol. 5, No.1, pp:31–39, January 1995.
12. I. J. Bahl, "*Lumped Elements of RF and Microwave Circuits*", Artech House, 2003.
13. H. Pues, and A. Van de Capelle, "Accurate transmission-line model for the rectangular microstrip antenna", *IEE Proc.*, Vol. 131, No. 6, pp:334–340, December 1984.
14. M. Himdi, J. P. Daniel, and C. Terret, "Transmission line analysis of antenna aperture-coupled microstrip", *Electron. Lett.*, Vol. 25 No.18, pp:1229–1230, 23 June 1989.
15. Jeong Phill Kim, and Wee Sang Park, "An improved network modeling of slot-coupled microstrip lines", *IEEE Trans. Microw. Theory Tech.*, Vol. 46, No. 10, pp:1484–1491, October 1998.
16. Jeong Phill Kim, and Wee Sang Park, "Analysis and network modeling of an aperture-coupled microstrip patch antenna", *IEEE Trans. on Antennas and Propag.*, Vol. 49, No. 6, pp:849–854, June 2001.
17. K. C. Gupta, R. Garg, I. Bahl, and P. Bhartia, "*Microstrip Lines and Slotlines*", 2nd ed. Artech House, 1996.
18. L. Han, G. Wu, L. Li, Y. Geng, Y. Zhang, and W. Zhang, "Design and transmission line model analysis of a compact dual-frequency antenna", *IET Microw. Antennas Propag.*, Vol. 6, No. 4, pp:404–410, 2012.
19. J. J. Wang, Y. P. Zhang, K. M. Chua, et al., "Circuit model of microstrip patch antenna on ceramic land grid array package for antenna-chip codesign of highly integrated RF transceivers", *IEEE Trans. Antennas Propag.*, Vol. 53, No. 12, pp:3877–3883, 2005.
20. J. A. Ansari, P. Singh, S. K. Dubey, et al., "H-shaped stacked patch antenna for dual band operation", *Prog. Electromagn. Res. B*, Vol. 5, pp:291–302, 2008.
21. Ankita Katyal, and Ananjan-Basu, "Analysis and optimization of broadband stacked microstrip antenna using transmission-line model", *IET, Microw. Antennas Propag.*, Vol. 11, pp:81–91, 2017.
22. Srinaga Nikhil Nallandhigal, Yunlong Lu, and Ke Wu, "Mesh-network equivalent model for unified rectangular microstrip antenna analysis", *IEEE Trans. Microw. Theory Tech.*, Vol. 68, No. 12, pp:5244–5258, December 2020.
23. Javier Gomez-Tagle and Christos G. Christodoulou, "Extended cavity model analysis of stacked microstrip ring antennas", *IEEE Trans. Antennas and Propag.*, Vol. 45, No. 11, pp:1626–1635, November 1997.
24. L. C. Shen, "Analysis of circular-disk printed circuit antenna", *Proc. Inst. Elect. Eng.*, Vol. 126, pp:1220–1222, December 1979.

25. S. Yano, and A. Ishimaru, "A theoretical study of the input impedance of a circular microstrip disk antenna", *IEEE Trans. Antennas Propagat.*, Vol. AP-29, pp:77–83, January 1981.
26. M. Kirschning, and R. H. Jansen, "Accurate model for effective dielectric constant of microstrip with validity up to millimeter wave frequencies," *Electron. Lett.*, Vol. 18, No. 6, pp:272–273, 1982.
27. I. J. Bahl, and S. S. Stuchly, "Analysis of a microstrip covered with a lossy dielectric," *IEEE Trans. Microwave Theory Tech.*, Vol. MTT-29, pp:104–109, February 1980.
28. I. J. Bahl, S. S. Stuchly, and M. A. Stuchly, "A new microstrip radiator for medical applications," *IEEE Trans. Microwave Theory Tech.*, Vol. MTT-28, pp:1464–1468, December 1980.

Reconfigurable stacked microstrip antennas

4.1 INTRODUCTION

Reconfigurable antennas are antennas that are capable of dynamically changing/modifying any one of the operating parameters like frequency, radiation pattern, and polarization. Accordingly, they are referred to as frequency reconfigurable, pattern reconfigurable, or polarization reconfigurable antennas. Reconfigurable stacked antennas also exhibit similar reconfigurability properties if antenna currents are properly controlled to achieve the desired performance. The only difference is that, due to multiple stacked layers, the number of design parameters that can be controlled/tuned increases and thus it becomes easier to incorporate reconfigurability.

There are many reconfigurable stacked antenna designs proposed in the literature for various applications, and some will be discussed in this chapter. The stacked antennas already have the advantage of being compact and high gain; the reconfigurability adds an additional useful property to the antenna's performance. There are many techniques to introduce reconfigurability in the antennas like using PIN diodes, varactor diodes, RF-MEMS switches, and metamaterials. The types of reconfigurability introduced in antennas are mostly frequency reconfigurability, polarization reconfigurability, and pattern reconfigurability. Sometimes these can be combined to obtain compounded reconfigurable antenna; however, this increases the design complexity.

4.2 RECONFIGURATION TECHNIQUES

There are various methods to incorporate reconfigurability into antenna design, depending on the system requirements. The reconfigurability in the antenna design can be categorized into electronic reconfigurability, mechanical/physical reconfigurability, optical reconfigurability, and reconfigurability using smart materials.

4.2.1 Electronic reconfigurability

In this type of reconfiguration technique, the antenna's characteristics are adjusted using electronic components such as PIN diodes, varactors, and MEMS. By incorporating these switches into the antenna structure, the antenna can be made reconfigurable, allowing for changes in the surface current distribution. When controlled properly, this redistribution of surface current can alter the antenna's properties, including frequency, polarization, or radiation pattern.

- a) **PIN diodes:** PIN diodes demonstrate ON and OFF states when subjected to forward and reverse biases, respectively. This characteristic allows for modulation of the current flow through the diode, leading to variations in antenna properties. To achieve this, the DC bias circuit must be positioned near the patch, with the separate fabrication of DC blocks. Careful design and placement of these circuits are essential to minimize interference with the antenna's performance. Additionally, the insertion loss and isolation of these switches must be thoroughly evaluated across the operating band to minimize overall losses in reconfigurable antennas. Before integration with the antenna, the performance of PIN diodes should be analyzed independently. The implementation of PIN diodes allows for various forms of reconfigurability to be achieved [1–4] with comparatively easy design modifications. The equivalent circuit of PIN diode is shown in Figure 4.1. The drawback with the use of PIN diodes in the circuit is that they need high DC bias current for switching them ON and also high-power handling capacity.
- b) **Varactor diodes:** Varactor diodes have the ability to change their capacitance with the change in applied bias. The equivalent circuit of a varactor diode is shown in Figure 4.2, where C_j is junction capacitance, R_R is reverse diode resistance while L_F and R_G are series inductance and resistance respectively. This property alters the antenna's input

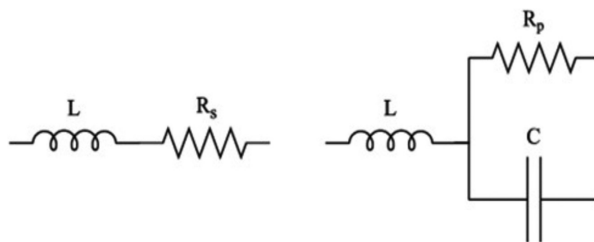


Figure 4.1 Equivalent circuit of PIN diode, (a) ON state, (b) OFF state.

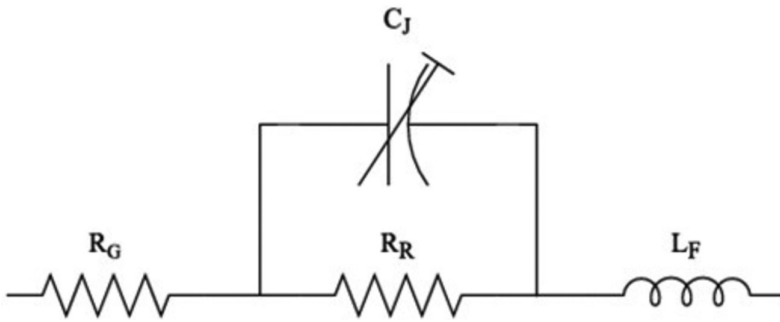


Figure 4.2 Equivalent circuit of varactor diode.

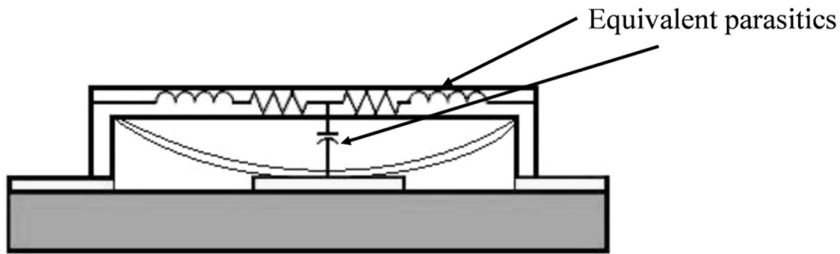


Figure 4.3 MEMS switch with equivalent parasitics [9].

impedance with the applied DC bias and provides reconfigurability in the antenna's response. Typically, varactor diodes provide continuous tuning of the antenna's input impedance and therefore a continuous change in the antenna's response can be obtained [5].

- c) **MEMS-based switches:** MEMS-based switches, similar to PIN diodes, provide discrete switching operation. Typically, a MEMS switch has three terminals: source, gate, and drain. The voltage applied at the gate generates electrostatic force and helps in controlling the switch operation. A flexible membrane is used in the design to make contact between the source and drain with applied bias voltage and operate in the ON state; otherwise it stays in the OFF state. An example of a shunt capacitive RF MEMS switch is shown in Figure 4.3. A characterization of an RF shunt capacitive MEMS switch is also presented in detail in [6]. Reconfigurable stacked antennas using MEMS switches have been proposed in [7, 8].

4.2.2 Optical reconfigurability

Optically reconfigurable antennas make use of photoconductive elements comprised of semiconductor materials such as silicon or gallium arsenide to

switch and modify antenna properties. When integrating electronic switching, metallic bias lines and DC blocks must be included near the antenna structure, which can lead to interference in the antenna's radiation pattern. Conversely, optical switches rely on optical fibres for their biasing, causing no interference and being electromagnetically transparent. As a result, these switches are preferred in scenarios where the avoidance of complex circuitry and electromagnetic interference is necessary [10–12].

4.2.3 Mechanical reconfiguration

In the mechanical reconfiguration technique, the main radiator of the antenna is physically altered/modified to obtain a change in the operating characteristics of the antenna. Since this method does not require any biasing circuit, this method of reconfiguration is free from electromagnetic interference and complex additional circuitry. In [13] an H-sectoral horn antenna is mechanically reconfigured using two movable plates to change the aperture of the horn antenna. In [14], a structurally embedded vascular antenna that enables physical reconfiguration of the meandering dipole is presented. A rotating patch polarization reconfigurable antenna is proposed in [15], where implementation of the physical reconfiguration technique is demonstrated.

4.2.4 Reconfiguration through smart materials

Smart materials like ferrites, liquid crystals, etc., can be used to achieve reconfigurability in the antenna design when incorporated in the antenna structure appropriately. A composite substrate made of magnetic meta-material is used in [16] to obtain a frequency reconfigurable antenna design. An SIW resonant cavity antenna is designed to achieve frequency and polarization reconfigurability through the use of ferrite-loaded slabs in the antenna structure [17].

4.3 TYPES OF RECONFIGURABLE ANTENNAS

4.3.1 Frequency reconfigurable antennas

Frequency reconfigurable antennas can electronically and dynamically change their frequency of operation. These antennas are useful for multi-band applications where the operating frequency needs to be adjusted based on the scenario. Typically, frequency reconfigurability in antenna design is achieved using PIN diodes and varactor diodes to keep the design simple. In cases where miniaturized design, low insertion loss, and low power operation are required, RF-MEMS switches are utilized to dynamically change the frequency of operation in frequency reconfigurable antennas.

4.3.2 Pattern reconfigurable antennas

Pattern reconfigurable antennas can dynamically provide spatial diversity of the radiation pattern through various methods. These antennas are particularly useful in applications where the radiation beam needs to be directed in different directions, such as target scanning, point-to-point communication, and multi-beam applications. Pattern reconfigurability can generally be categorized into two types: beam steering and beam shaping. Beam steering antennas dynamically change the direction of the beam, while beam shaping antennas have dynamically changing beam shapes and are referred to as multi-beam antennas. Phased array antennas are utilized for beam steering and achieving pattern diversity, as shown in Figure 4.4. Additionally, meta-materials and frequency selective surfaces (FSS) are valuable in achieving pattern diversity of the antennas. In the context of user communication, adaptive beamforming may be necessary, requiring the system to intelligently adjust the antenna's beam towards the dedicated user. This plays a crucial role in today's 5G communication technology. A comprehensive study of different types of pattern reconfigurable antennas is presented in [18].

4.3.3 Polarization reconfigurable antennas

The antenna polarization depends on the antenna's surface current distribution which affects the radiated fields and their orientation. Thus, polarization reconfigurability can be achieved by altering surface current distribution along the radiating patch. Typically, current distribution can be altered through patch meandering or by inserting slots at appropriate locations. Antenna feeding position is also an important parameter for the orientation of surface currents across the patch. In [19] aperture-coupled antenna design is modified to obtain polarization reconfigurability by

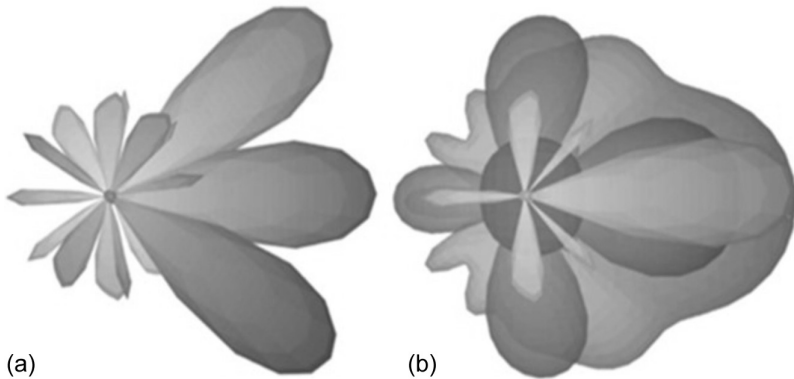


Figure 4.4 Depiction of two different types of pattern reconfiguration, (a) beam steering, (b) beam shaping [18].

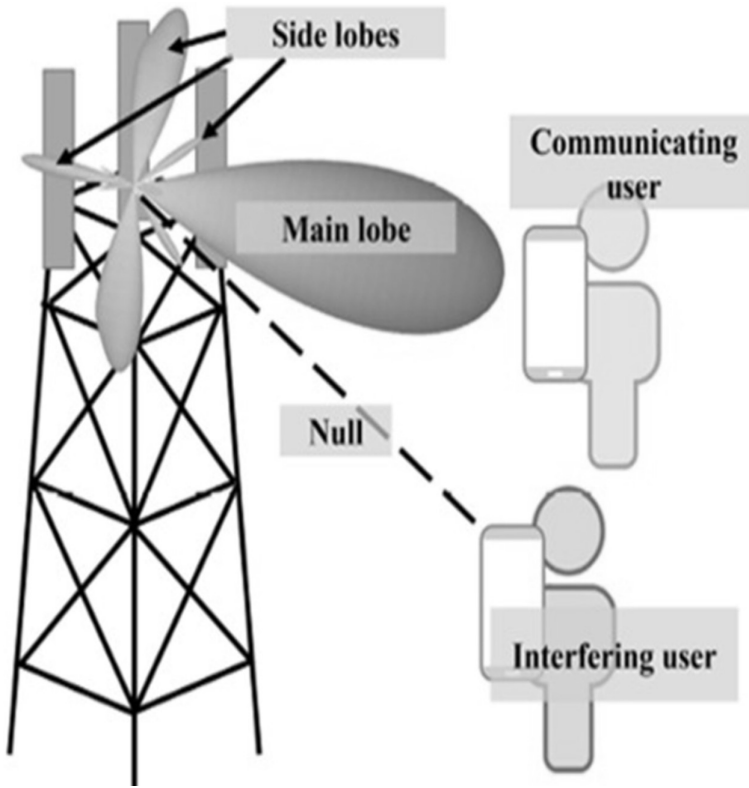


Figure 4.5 Adaptive beamforming for communication systems [18].

altering the electromagnetic coupling through the slot via the insertion of diodes within the slots. Further in [20], a proximity-coupled patch antenna design is demonstrated. The patch has two cross-shaped slots with PIN diodes placed in the vicinity. These diodes are given regulated DC bias voltage to obtain three different polarization states: horizontal, vertical, and RHCP. Moreover, a meta-surface-based polarization reconfigurable antenna is proposed in [21], where two linearly polarized feeding elements are used to generate multiple polarizations by controlling the amplitude and relative phase of two feeds.

4.4 RECONFIGURABLE STACKED MICROSTRIP ANTENNAS

Reconfigurable stacked microstrip antennas refer to a class of printed stacked microstrip antennas that are capable of electronically or dynamically adjusting their operating parameters. These compact broadband

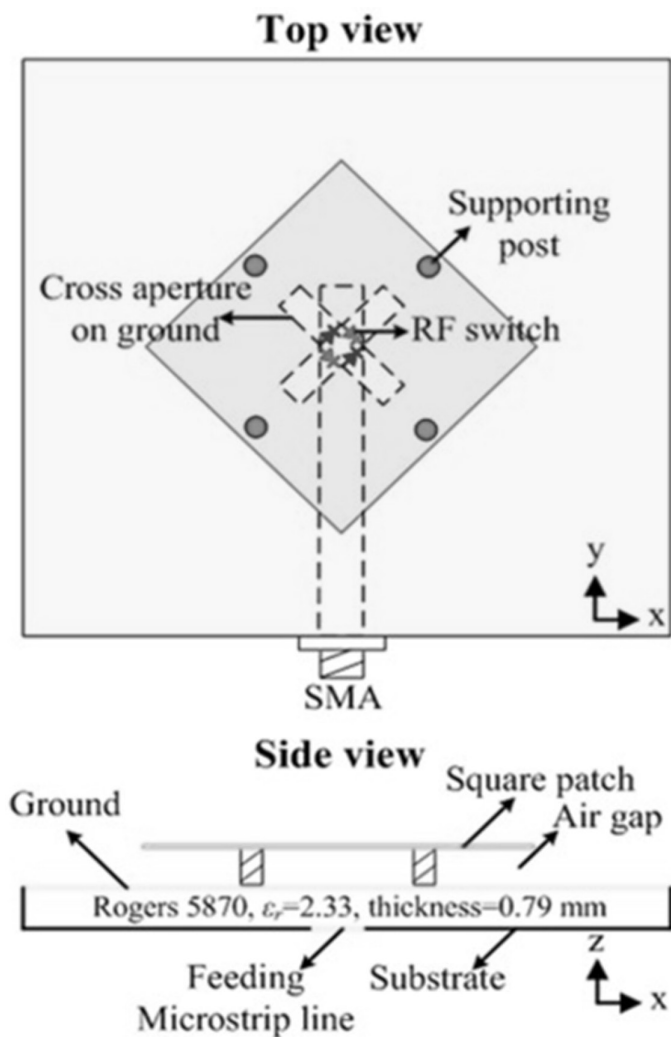


Figure 4.6 A polarization reconfigurable antenna design. (Source: Wei Lin, & Hang Wong, “Polarization Reconfigurable Aperture-Fed Patch Antenna and Array”, IEEE Access, Vol. 4, pp: 1510–1517, 2016 [19].)

printed antennas possess the additional capability to reconfigure their frequency, pattern, polarization, or a combination of these properties. The design of these antennas involves optimizing various parameters to ensure that the antenna’s output meets the system requirements. The integration of reconfigurability with stacked antennas enhances their utility in practical applications due to their compact nature and ability to integrate with other circuitry. The literature discusses numerous designs

of reconfigurable stacked antennas, indicating ongoing research on their design methodology.

In the stacked antennas, multiple layers of resonant structures provide increased scope for antenna parameter tuning and control. Reconfigurability can be easily introduced by modifying the parasitic patch layers, without affecting the driven patch design. Further, a combination of parameter tuning at driven patch and parasitic patches can be made to achieve reconfigurability. The use of meta-materials is a promising technology in antenna design nowadays; it is also prominently used in reconfigurable stacked antennas at parasitic layers.

4.5 DESIGN METHODOLOGY OF RECONFIGURABLE STACKED MICROSTRIP ANTENNAS

The initial design of reconfigurable stacked microstrip antennas follows the basic design strategies used for the design of printed stacked microstrip antennas to achieve an initial broadband, high-gain, and compact antenna design. Reconfigurability is then introduced through either a reconfigurable feeding network or reconfigurable elements. The reconfigurable feeding network comprises switching feeding networks implemented through PIN diodes or varactor diodes. Reconfigurable elements may be composed of metamaterials or frequency selective surfaces (FSS) and can also include PIN diode/varactor diode/RF-MEMS switching among multiple resonant elements. Numerous reconfigurable stacked microstrip antennas have been reported in published works, and the design techniques and performance of select designs are discussed in detail in the following section.

4.5.1 Frequency reconfigurable stacked microstrip antenna design with continuous narrowband frequency shift

A probe-fed frequency reconfigurable stacked patch antenna is proposed in [22] with two stacked layers having dielectric material of $\epsilon_r = 2.33$ at upper layer and air at lower layer. There are two square patches in the antenna structure of different sizes, with the upper one smaller than the lower patch. The upper patch is directly fed by the probe, while the lower patch is electromagnetically coupled by the fringing fields of the upper patch. The lower patch has a via-hole to pass the inner conductor of the SMA connector, without touching the patch. The SMA connector used as the probe feed in the design has a diameter of 1.3 mm. The clearance hole of a diameter of 3 mm is selected for the impedance matching of the lower patch. The lower patch is located above the centre of the ground plane, while the upper patch is placed at an offset with respect to the feed and the lower patch along the y -axis. This helps improve the overall input impedance matching.

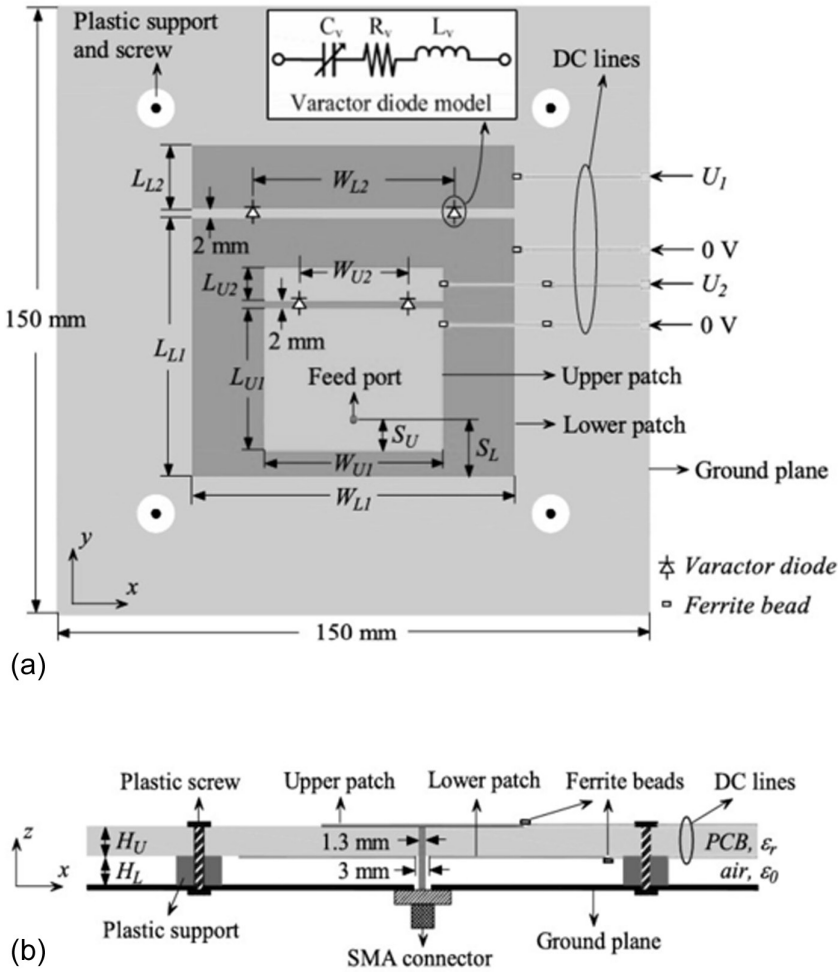


Figure 4.7 Proposed frequency reconfigurable stacked patch antenna, (a) top view, (b) side view. Reproduced with permission from IEEE [22].

To incorporate reconfigurability in the proposed stacked antenna, both patches are added with an additional patch separated by an optimized gap. The two sections of metallic patches at each layer are connected via varactor diodes, placed in the gaps. The varactor diodes used in the design of the proposed antenna are SMV2019 from Skyworks. The capacitance of such diodes changes from 2.22 to 0.30 pF with an increase in the reverse bias voltage from 0 to 20 V [23]. This particular varactor diode is selected to meet the required capacitance tuning range. This capacitor also has a low series resistance and is thus favourable for use without much loss being introduced in the design. Further, the isolation of the DC lines from the input

RF signals is achieved through the use of the ferrite beads (Model Murata BLM18G) [24] in this proposed work. Specifically, this ferrite bead is chosen in the design as it has a very low resistance for DC signals (approximately 1Ω), but it has a very high resistance for RF signals.

Each of the patches contains two varactor diodes and two ferrite beads to achieve frequency reconfigurability in the design. Two different control voltages U_1 and U_2 are used to change the capacitance of varactor diodes at both layers. With the change in applied voltage bias, the operating frequency of the antenna changes as it changes the input impedance of the antenna. In this case, both voltages can control the operating frequency independently. Thus, V_1 controls only the lower band frequency change, while V_2 controls only the upper band frequency change.

The proposed frequency reconfigurable stacked antenna achieves a lower band frequency change of 1.68–1.93 GHz, and an upper band frequency change of 2.11–2.51 GHz, with an increase in the applied reverse bias voltage from 0 to 20 V. The variation in frequency of operation of the proposed antenna with changes in U_1 and U_2 is shown in Figure 4.8 and Figure 4.9 respectively.

4.5.2 Frequency reconfigurable stacked microstrip antenna design with broadband frequency shift

An innovative design of a broadband frequency reconfigurable stacked microstrip antenna is introduced in [25]. This three-layered antenna is

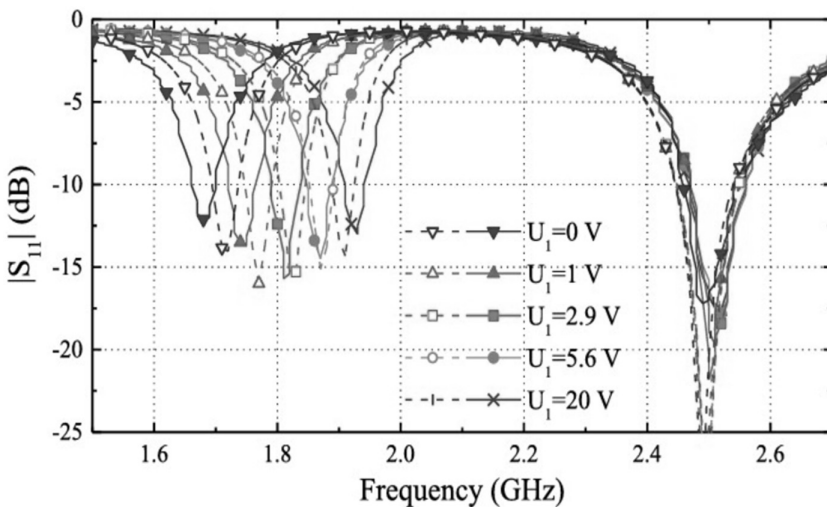


Figure 4.8 Simulated and measured S_{11} of proposed frequency reconfigurable antenna for variations in U_1 and $U_2 = 20$ V. Reproduced with permission from IEEE [22].

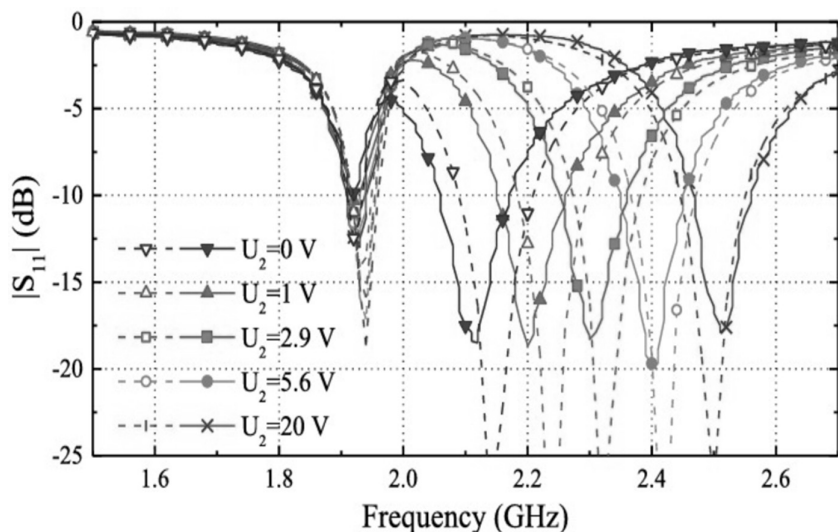


Figure 4.9 Simulated and measured S_{11} of proposed frequency reconfigurable antenna for variations in U_2 and $U_1 = 20$ V. Reproduced with permission from IEEE [22].

Table 4.1 Design parameters of proposed frequency reconfigurable stacked patch antenna [22]

Parameter	L_{L1}	L_{L2}	W_{L1}	W_{L2}	S_L	H_L
Value (in mm)	64	16	82	51	14	3
Parameter	L_{U1}	L_{U2}	W_{U1}	W_{U2}	S_U	H_U
Value (in mm)	35	8	45	27.5	7.5	3.17

capable of dynamically adjusting the entire operating bandwidth using just one PIN diode. The antenna consists of a rectangular driven patch fed through a shifted microstrip feed line, with two stacked parasitic patches above it. The topmost parasitic layer includes two patches connected through a PIN diode. When the PIN diode is activated, both patches in the upper-most layer are connected, leading to a shift in the antenna's complete frequency response. With the diode activated, current flows through the additional upper patch, which becomes coupled to the driven patch and to the ground. This results in increased electromagnetic coupling of radiated fields in this section of the upper patch compared to the larger section. Thus, the resonance due to the upper patch is now predominantly due to the smaller section, causing the resonance to shift towards the higher frequency side.

The design of a reconfigurable stacked antenna is depicted in Figure 4.10 and the detailed parameters are shown in Figure 4.11 while the dimensions

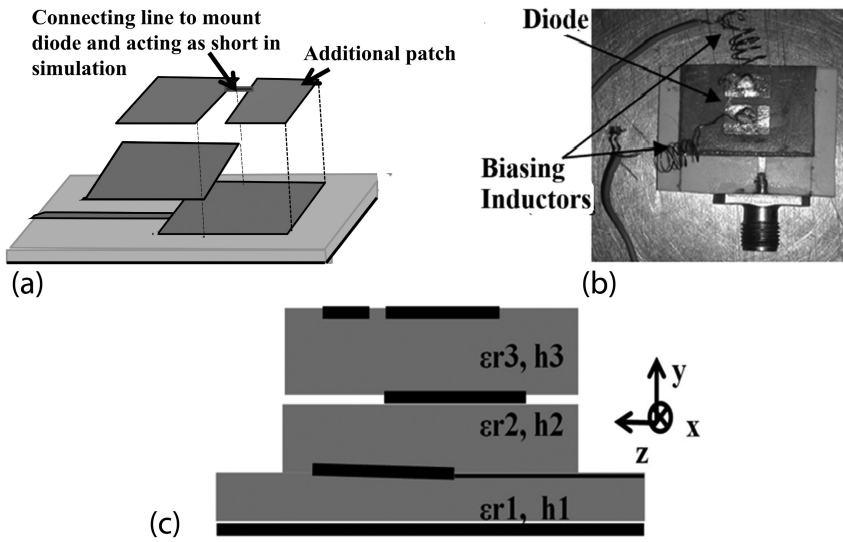


Figure 4.10 (a) X-band reconfigurable antenna design and (b) fabricated antenna, (c) 3D view [25].

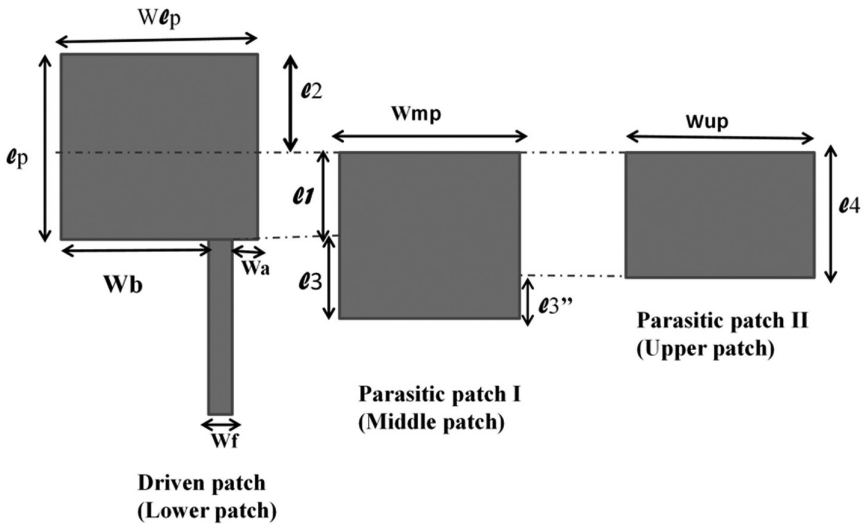


Figure 4.11 Detailed parameters of reconfigurable stacked antenna [25].

are listed in Table 4.2. The S_{11} response of the antenna for different diode states is presented in Figure 4.12, which shows the shift in the whole operating bandwidth towards the higher frequency side with the diode in the ON state, compared to the diode in the OFF state.

Table 4.2 Design parameters of reconfigurable stacked antenna [25]

Parameter	Value	Parameter	Value
W_p	7.5mm	W_{mp}	7.4 mm
L_p	8 mm	L_3	7.5 mm
W_b	5.45 mm	W_{up}	7.56 mm
W_a	0.95 mm	l_4	5 mm
Feed Width [W_f]	1.1 mm	h_1	0.508 mm
l_1	3.6 mm	h_2, h_3	0.762mm
l_2	4.4 mm	ϵ_{rl}	3.6

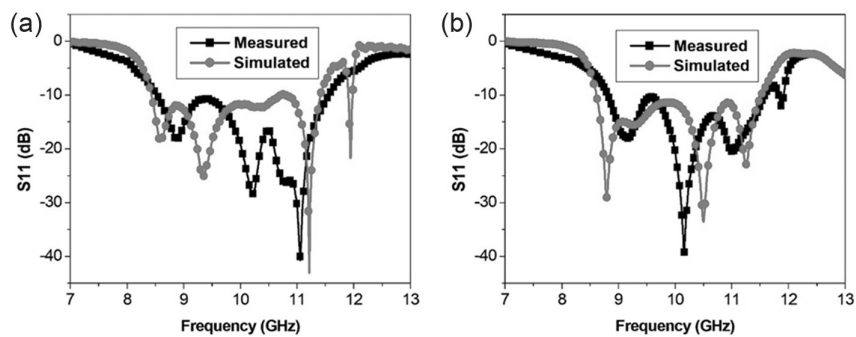


Figure 4.12 S11 response of reconfigurable stacked antenna (a) when diode is OFF, (b) when diode is ON.

4.5.3 Pattern reconfigurable stacked microstrip antenna design

A stacked pattern reconfigurable microstrip antenna is proposed in [26]. The antenna has three stacked layers: a feeding network layer, a driven patch layer, and a parasitic patch layer. Two substrate layers, one of 0.508 mm TLY-5 ($\epsilon_r = 2.2$) and the other of 0.508 mm Rogers RO4350 ($\epsilon_r = 3.66$) substrate, are used between the feeding network and the driven patch. The ground plane is placed between the feeding network and driven patch layers as shown in Figure 4.13. These two substrates are bonded together through a bonding layer of RO4450 substrate of 0.1 mm thickness ($\epsilon_r = 3.48$). The upper substrate layer bearing the parasitic patch is separated by the driven patch layer through an air gap of 2 mm. The upper substrate is the same as the lower substrate of driven patch, i.e. 0.508 mm RO4350. The design parameters are listed in Table 4.3.

The initial dimensions of the driven and parasitic patches (their widths) are obtained using the standard formulae given by Equation 4.1 [27], where λ_0 is the free-space wavelength and ϵ_r is the relative dielectric constant of the material used. In this case the value of ϵ_r should be calculated as ϵ_{reff} for the case of the parasitic patch due to the existence of three dielectrics

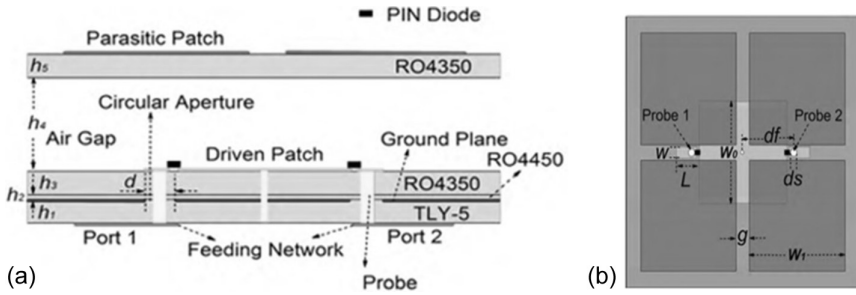


Figure 4.13 Pattern reconfigurable stacked patch antenna (a) side view, (b) top view. (Source: Jun Hu, Zhang-Cheng Hao, and Yi Wang, “A Wideband Array Antenna with 1-Bit Digital-Controllable Radiation Beams”, IEEE Access, Vol. 6, 2018 [26].)

Table 4.3 Design parameters of proposed pattern reconfigurable stacked antenna [26]

Parameter	W	L	w_l	w_0	g	d_f	d_s	d	h_l, h_3, h_5	h_2	h_4
Value (in mm)	1.5	3.5	14.6	13.4	2.2	7.8	1	1.4	0.508	0.1	2

between it and the ground plane: two substrate layers of RO4350 and the air gap.

$$w_0 = w_1 = \frac{\lambda_0}{2\sqrt{\epsilon_r}} \quad (4.1)$$

The proposed stacked antenna has one square patch in the driven patch layer, while four patches separated by gaps are etched at the parasitic layer. The driven patch square lies at the centre of the set of four parasitic patches. The driven patch is connected to the feeding network through two probes, with PIN diodes connecting the probes and patch. This gives the control to connect the driven patch to the selected probe at a time. The complete feeding network is placed at the third layer, beneath the ground plane. The designed feeding network is shown in Figure 4.14, which is symmetrical with respect to both the ports. If the phase of the antenna when excited with port 1 is 0° , then its phase when excited with port 2 will be 180° (due to the opposite placement of both ports with respect to the driven patch). In this proposed work, this condition is utilized to make a pattern reconfigurable antenna array, based on a high-gain broadband stacked antenna. The single antenna element's gain and S11 response (for both ports) are shown in Figure 4.15, with peak gain of 11 dBi and bandwidth of 21.9% from 5.05 to 6.3 GHz.

The pattern reconfigurable stacked antenna array in the proposed work is comprised of a 4×4 array of 16 elements, shown in Figure 4.16. Considering different input combinations at the antenna element feeding ports can result in radiation patterns directed in different directions. Let's

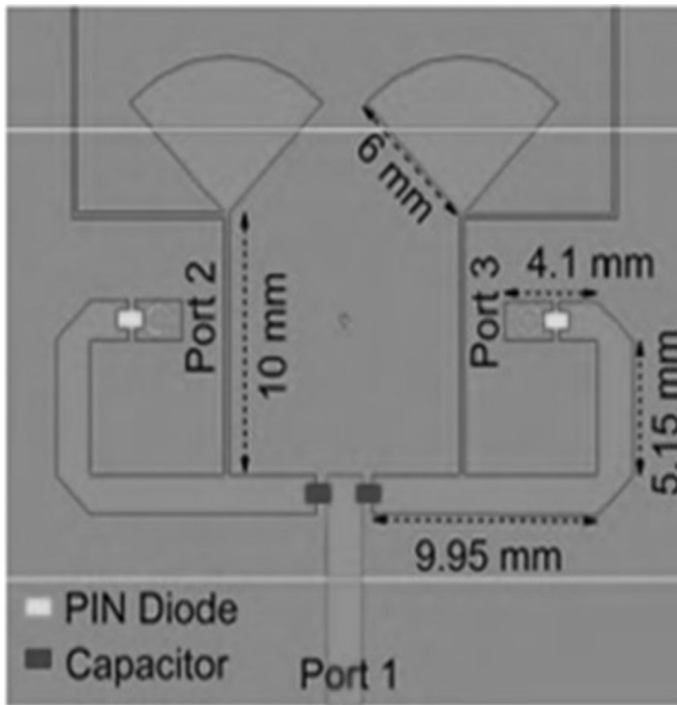


Figure 4.14 Layout of the feeding network implemented in proposed pattern reconfigurable stacked antenna. (Source: Jun Hu, Zhang-Cheng Hao, and Yi Wang, “A Wideband Array Antenna with 1-Bit Digital-Controllable Radiation Beams”, IEEE Access, Vol. 6, 2018 [26].)

take the condition of feeding an antenna element through probe 1 as state “0” and feeding the antenna element through probe 2 as state “1”. Then, making different combinations of these states (i.e. different feeding ports for different antenna elements in the array) can change the radiation pattern of the entire antenna array.

To change the antenna states dynamically, DC bias lines are connected to the feeding network through PIN diodes. With the change in DC bias at different lines, respective PIN diodes can be switched “ON” and “OFF”, resulting in different states in each antenna element. The Figure 4.17 shows resultant radiation patterns for various combinations of bias conditions (or each antenna element state).

4.5.4 Polarization reconfigurable stacked antenna design

A circularly polarized reconfigurable and pattern switchable stacked antenna array, with dynamically switching LHCP and RHCP (for polarization reconfigurability), is proposed in [28]. The proposed antenna consists

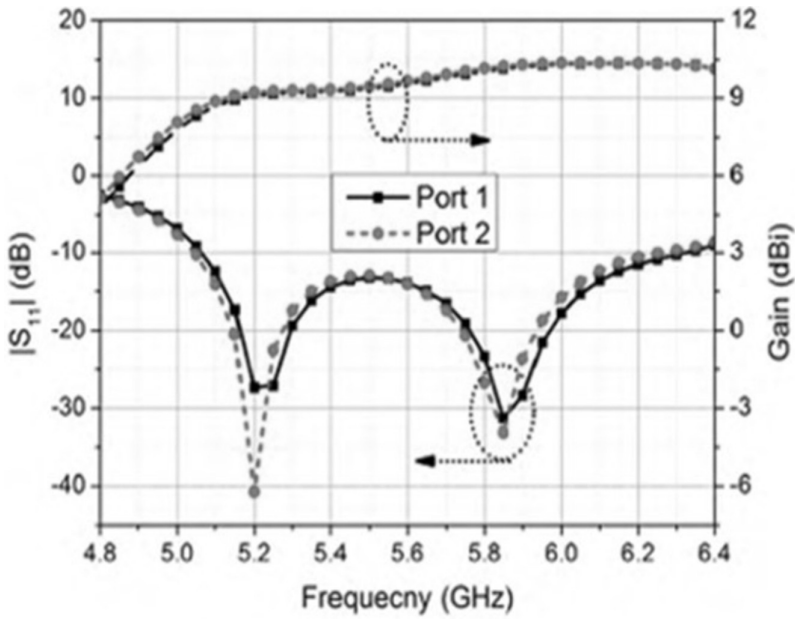


Figure 4.15 S_{11} response and gain response of one antenna element of the proposed pattern reconfigurable stacked antenna. (Source: Jun Hu, Zhang-Cheng Hao, and Yi Wang, "A Wideband Array Antenna with 1-Bit Digital-Controllable Radiation Beams", IEEE Access, Vol. 6, 2018 [26].)

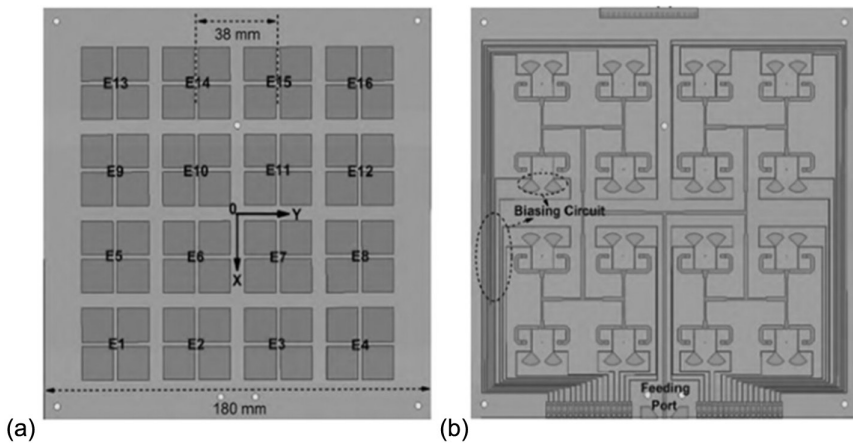


Figure 4.16 Array structure of proposed pattern reconfigurable stacked antenna (a) top view, (b) back view of the feeding network. (Source: Jun Hu, Zhang-Cheng Hao, and Yi Wang, "A Wideband Array Antenna with 1-Bit Digital-Controllable Radiation Beams", IEEE Access, Vol. 6, 2018 [26].)

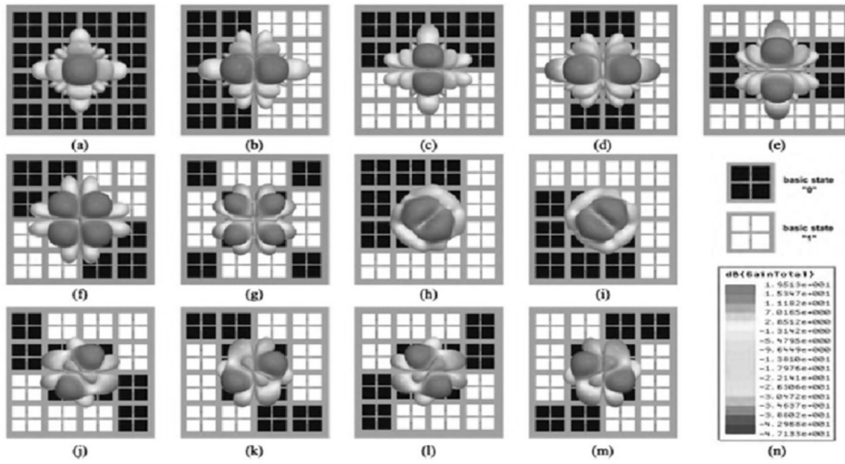


Figure 4.17 Simulated 3D radiation patterns of proposed pattern reconfigurable array antenna capable of 1-bit digital control of the beam at 5.7 GHz for different modes due to different input sequences, (a) Mode 0 (0000000000000000), (b) Mode 1 (0011001100110011), (c) Mode 3 (0000000011111111), (d) Mode 4 (1001100110011001), (e) Mode 5 (1111000000001111), (f) Mode 6 (1100110000110011), (g) Mode 7 (0110100110010110), (h) Mode 8 (11100110001001), (i) Mode 9 (0001000100111111), (j) Mode 10 (1110100000010111), (k) Mode 11 (1100100110010011), (l) Mode 12 (0111000110001110), (m) Mode 13 (0011100110011100). (Source: Jun Hu, Zhang-Cheng Hao, and Yi Wang, “A Wideband Array Antenna with 1-Bit Digital-Controllable Radiation Beams”, IEEE Access, Vol. 6, 2018 [26].)

of three different layers. The lowest layer has a feeding network for the reconfigurable antenna. The middle layer is the substrate integrated waveguide (SIW) structure which is separated by the feeding network through 0.762 mm RO4350B ($\epsilon_r = 3.66$) substrate. Also, the SIW is made using 0.762 mm RO4350B ($\epsilon_r = 3.66$) substrate. The final upper-most layer is the parasitic patch layer, etched over 0.508 mm RO4350B substrate and with an air gap of 1.9 mm between it and the middle layer. This layer has four square patches printed over it in a symmetrically arranged manner as shown in Figure 4.18. The design parameters are listed in Table 4.4.

The SIW cavity layer has an annular slot and two feeding ports with a microstrip feedline and microstrip to SIW transition, placed at orthogonal sides. The microstrip to SIW transition is designed to have a 50-ohm impedance to match it with the 50-ohm microstrip feedline. The annular slot when fed from one side, i.e. either of the two ports (port 1 or port 2), excites two orthogonal modes. But these are in phase; thus it has linear polarization. To have a 90-degree phase difference between these two excited orthogonal modes in this case, two additional rectangular slots are placed symmetrically about the annular slot for proper signal perturbation along

Table 4.4 Design parameters of proposed polarization reconfigurable stacked antenna [28]

Parameter	h_1	h_2	h_3	h_4	W_1	Gap 1	Gap 2	$r1$	$r2$	l_f	L_1	L_2	L_3
Value (in mm)	0.762	0.762	1.9	0.508	14.1	0.6	0.9	4.1	5.7	7.5	9	6.8	2.9
Parameter	L_4	L_5	L_6	L_7	L_8	d	p	w_{50}	w_2	w_3	W_{54}	w_5	
Value (in mm)	5	1.8	12.3	3.8	2.3	1	1.7	1.6	5	5	0.5	30.96	

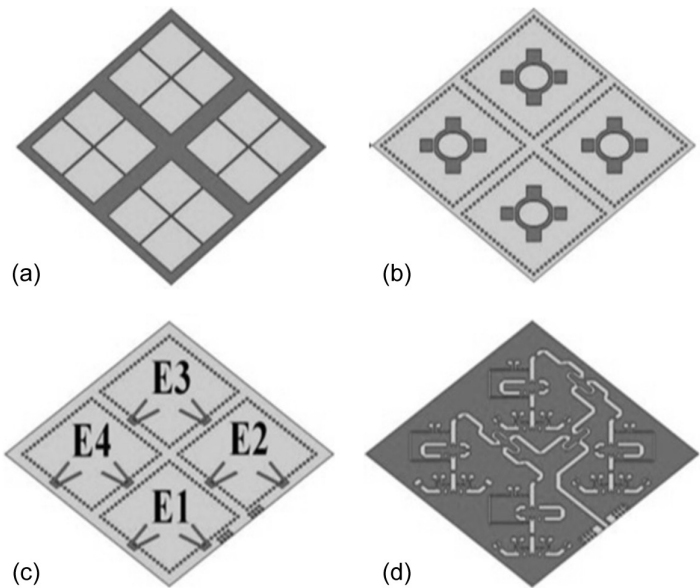


Figure 4.19 Array structure of proposed antenna element, (a) top view, (b) SIW cavity layer, (c) feed port view, (d) feeding network. (Source: Chao Liu, Yongfeng Li Jiafu Wang, Tonghao Liu, Yajuan Han, and Shaobo Qu, “Polarization Reconfigurable and Beam-Switchable Array Antenna Using Switchable Feed Network”, IEEE Access, Vol. 10, pp: 29032–29039, Feb. 2022 [28].)

the surface. This SIW cavity, bearing an annular slot along with orthogonally arranged rectangular slots, now yields circular polarization. The orientation of circular polarization can be changed by changing the port of excitation (i.e. switching between port 1 and port 2), which is achieved by proper feeding methodology.

The feeding layer is comprised of a polarization switching and phase switching network (which changes the direction of radiation pattern). There are two states selection for polarization, i.e. LHCP and RHCP, and two phases, i.e. 0° and -130° . As shown in Fig.4ure 18(d), multiple switches are used to switch the signal path before it is fed to the SIW cavity and is then coupled to the parasitic patch. According to the proposed feeding

Table 4.5 Different states of operation of the antenna array [28]

Polarization states	E_1, E_2, E_3, E_4	Coding	Beam	Direction (ϕ, θ)
0/1	$-130^\circ,$ -130°	0/1 1111	B1	$0^\circ, 0^\circ$
	$-130^\circ,$ -130°			
	$0^\circ, 0^\circ$	0/1	B2	$0^\circ, 22^\circ$
	$-130^\circ,$ -130°	0011		
	$-130^\circ,$ -130°	0/1	B3	$90^\circ, -22^\circ$
	$0^\circ, -130^\circ$	1001		
	$-130^\circ,$ -130°	0/1	B4	$0^\circ, -22^\circ$
	$0^\circ, 0^\circ$	1100		
	$0^\circ, -130^\circ$	0/1	B5	$90^\circ, 22^\circ$
	$-130^\circ, 0^\circ$	0110		

structure path 1, which corresponds to D1 and D4 “ON” and D2 and D3 “OFF”, yields LHCP with -130° phase. Next the case D1 and D4 “OFF” while D2 and D3 “ON” yields RHCP with 0° phase. Similarly other states can be achieved by changing the biasing of diodes arranged in the feeding network.

To make the proposed polarization reconfigurable antenna pattern reconfigurable too, an array of 2×2 antenna elements is used to modify the overall radiation pattern of the array antenna by utilizing the different phases achieved for different states of the feeding network, as shown in Figure 4.19. The summary of the antenna array’s beam angles for different phase state combinations of four antenna elements of the array is given in Table 4.5. The obtained return loss and gain of the proposed antenna are shown in Figure 4.20. The simulated 3D radiation patterns of the 2×2 antenna array made using proposed antenna element for different input coding sequences are given in Figure 4.21.

4.6 SUMMARY

In this chapter, we discussed the fundamental concepts of reconfigurable antennas and reconfigurable stacked microstrip antennas, including reconfiguration techniques and various types of reconfigurability introduced in the antenna design. The primary focus was on the design methodologies of a variety of reconfigurable stacked microstrip antennas with different types of reconfigurability, covering the details of the design process and the results obtained.

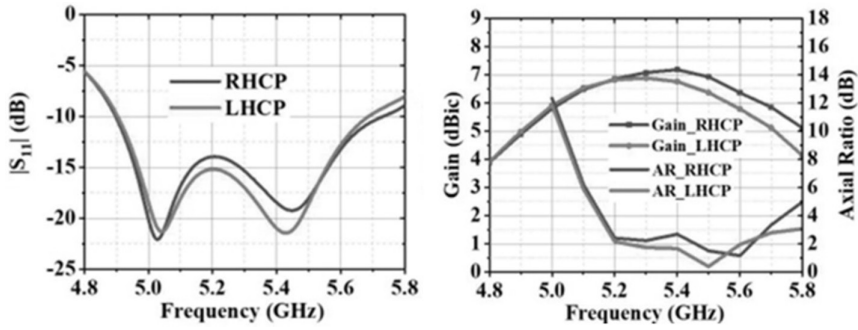


Figure 4.20 Response of single element of proposed polarization reconfigurable antenna, (a) S_{11} response, (b) antenna gain, for different polarization states. (Source: Chao Liu, Yongfeng Li Jiafu Wang, Tonghao Liu, Yajuan Han, and Shaobo Qu, “Polarization Reconfigurable and Beam-Switchable Array Antenna Using Switchable Feed Network”, IEEE Access, Vol. 10, pp: 29032–29039, Feb. 2022 [28].)

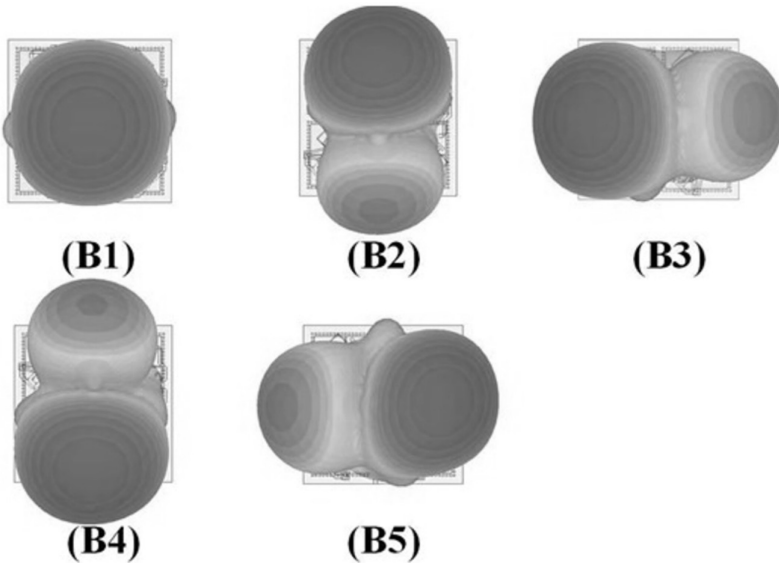


Figure 4.21 Simulated 3D radiation patterns of the antenna array made of proposed polarization reconfigurable stacked antenna for different input coding sequences for LHCP mode. (Source: Chao Liu, Yongfeng Li Jiafu Wang, Tonghao Liu, Yajuan Han, and Shaobo Qu, “Polarization Reconfigurable and Beam-Switchable Array Antenna Using Switchable Feed Network”, IEEE Access, Vol. 10, pp: 29032–29039, Feb. 2022 [28].)

REFERENCES

1. B. D. Nguyen, and C. Pichot, "Unit-cell loaded with PIN diodes for 1-bit linearly polarized reconfigurable transmitarrays", *IEEE Antennas Wirel. Propag. Lett.*, Vol. 18, pp:98–102, 2019.
2. S. Ojaroudi, Y. Ojaroudi, and N. Ojaroudi, "Novel design of reconfigurable microstrip slot antenna with switchable band-Notched Characteristic", *Microw. Opt. Technol. Lett.*, Vol. 57, pp:849–853, 2015.
3. Y.-H. Cho, and G. M. Rebeiz, "Two- and four-pole tunable 0.7–1.1-GHz bandpass-to-bandstop filters with bandwidth control", *IEEE Trans. Microw. Theory Tech.*, Vol. 62, pp:457–463, 2014.
4. Yubin Cai, Daisong Zhang, and Yahya Rahmat-Samii, "Mars Exploration: Wideband Frequency Reconfigurable Electrically Small Multi-Turn Loop Antenna Using MEMS Switch", Proceedings of the IEEE International Symposium on Antennas and Propagation and USNC-URSI Radio Science Meeting, Atlanta, GA, USA, 7–12 July 2019.
5. Y. Tawk, and J. Costantine, and C. G. Christodoulou, "A varactor-based reconfigurable filtenna", *IEEE Antennas Wirel. Propag. Lett.* Vol. 11, pp:716–719, 2012.
6. K. Srinivasa Rao, Lakshmi Narayana Thalluri, Koushik Guha, and K. Girja Sravani, "Fabrication and characterization of capacitive RF MEMS perforated switch", *IEEE Access*, Vol. 6, pp:77519–77528, 2018.
7. John P. Gianvittorio, Member, IEEE, and Yahya Rahmat-Samii, "Reconfigurable patch antennas for steerable reflectarray applications", *IEEE Trans. Antennas Propag.*, Vol. 54, No. 5, pp:1388–1392, May 2006.
8. Carla Medeiros, Jorge R. Costa, and Carlos A. Fernandes, "MEMS Reconfigurable Stacked Antenna for WLAN Applications", 2008 IEEE Antennas and Propagation Society International Symposium, July 2008.
9. Zhongliang Deng, Yucheng Wang, Kun Deng, Chengqi Lai, and Jiali Zhou, "Novel high isolation and high capacitance ratio RF MEMS switch: Design, analysis and performance verification", *MDPI Micromachines*, Vol. 13, No. 5, April 2022.
10. Y. Tawk, A. R. Albrecht, S. Hemmady, G. Balakrishnan, and C. G. Christodoulou, "Optically pumped frequency reconfigurable antenna design", *IEEE Antennas Wirel. Propag. Lett.*, Vol. 9, pp:280–283, 2010.
11. V. A. Manasson, L. S. Sadovnik, V. A. Yepishin, and D. Marker, "An optically controlled millimeter wave beam-steering antenna based on a novel architecture" *IEEE Trans. Microw. Theory Tech.*, Vol. 45, pp:1497–1500, 1997.
12. D. Patron, A. S. Daryoush, and K. R. Dandekar, "Optical control of reconfigurable antennas and application to a novel pattern reconfigurable planar design", *J. Lightwave Technol.*, Vol. 32, pp: 3394–3402, 2014.
13. A. Jouade, M. Himdi, A. Chauloux, and F. Colombel, "Mechanically pattern-reconfigurable bended horn antenna for high-power applications", *IEEE Antennas Wirel. Propag. Lett.*, Vol. 16, pp:457–460, 2017.
14. G. H. Huff, H. Pan, D. J. Hartl, G. J. Frank, R. L. Bradford, and J. W. Baur, "A physically reconfigurable structurally embedded vascular antenna", *IEEE Trans. Antennas Propag.*, Vol. 65, pp:2282–2288, 2017.

15. I. T. McMichael, "A mechanically reconfigurable patch antenna with polarization diversity", *IEEE Antennas Wirel. Propag. Lett.*, Vol. 17, pp:1186–1189, 2018.
16. Mousa Al-Omari, Hussein Attia, Khurram K. Qureshi, and Sharif Sheikh, "Design of frequency-reconfigurable antenna on dielectric and magnetic metamaterial composite substrate", *IEEE Antennas Wirel. Propag. Lett.*, Vol. 22, No. 4, pp:943–947, April 2023.
17. Li-Rong Tan, Rui-Xin Wu, and Yin Poo, "Magnetically reconfigurable SIW antenna with tunable frequencies and polarizations", *IEEE Trans. Antennas Propag.*, Vol. 63, No. 6, pp:2772–2776, June 2015.
18. H. Pablo Zapata Cano, Zaharias D. Zaharis, Traianos V. Yioultsis, Nikolaos V. Kantartzis, Pavlos I. Lazaridis, "Pattern reconfigurable antennas at millimeter-wave frequencies: A comprehensive survey", *IEEE Access*, Vol. 10, pp:83029–83042, August 2022.
19. Wei Lin, and Hang Wong, "Polarization reconfigurable aperture-fed patch antenna and array", *IEEE Access*, Vol. 4, pp:1510–1517, 2016.
20. M. S. Nishamol, V. P. Sarin, D. Tony, C. K. Aanandan, P. Mohanan, and K. Vasudevan, "An electronically reconfigurable microstrip antenna with switchable slots for polarization diversity", *IEEE Trans. Antennas Propag.*, Vol. 59, No. 9, pp:3424–3427, September 2011.
21. Wentao Li, Yi Ming Wang, Yongqiang Hei, Bo Li, Xiaowei Shi, "A compact low-profile reconfigurable metasurface antenna with polarization and pattern diversities", *IEEE Antennas Wirel. Propag. Lett.*, Vol. 20, No. 7, pp:1170–1174, July 2021.
22. Lei Ge, Mingjian Li, Jianpeng Wang, and Hui Gu, "Unidirectional dual-band stacked patch antenna with independent frequency reconfiguration", *IEEE Antennas Wirel. Propag. Lett.*, Vol. 16, pp:113–116, 2017.
23. SMV2019 Varactors Datasheet. [Online]. Available: www.skyworksinc.com
24. BLM18G Series Murata Ferrite Bead Datasheet. [Online]. Available: www.murata.com
25. Ankita Katyal, and Ananjan Basu, "Broadband Reconfigurable Stacked Microstrip Patch Antenna at X-band", IEEE International Symposium on Antenna and Propagation, pp:85–86, 2014.
26. Jun Hu, Zhang-Cheng Hao, and Yi Wang, "A wideband array antenna with 1-bit digital-controllable radiation beams", *IEEE Access*, Vol. 6, pp:10858–10866, 2018.
27. J. Hu, Z.-C. Hao, and W. Hong, "Design of a wideband quad-polarization reconfigurable patch antenna array using a stacked structure", *IEEE Trans. Antennas Propag.*, Vol. 65, No. 6, pp:3014–3023, June 2017.
28. Chao Liu, Yongfeng Li Jiafu Wang, Tonghao Liu, Yajuan Han, and Shaobo Qu, "Polarization reconfigurable and beam-switchable array antenna using switchable feed network", *IEEE Access*, Vol. 10, pp:29032–29039, February 2022.

Stacked microstrip antenna arrays

5.1 INTRODUCTION

Antenna arrays are widely used in several applications owing to their high gain and directivity as the multiple antenna elements are fed simultaneously to work as a single antenna. The power is fed to these multiple antennas according to a specific phase relationship between them to control the overall radiation pattern. The relative phase of the adjacent antenna elements is controlled to obtain directional radiation patterns for point-to-point communication, beam steering for target scanning, rejecting interference from a particular angle, to give path diversity in the case of MIMO applications, and more. Printed stacked antennas themselves have multiple vertically arranged printed resonators to enhance the gain and bandwidth of the single layer patch antenna. Antenna arrays made using such printed stacked antennas, along with the features of directive radiation pattern and ability to control it, have an added advantage of being broadband with high gain.

Antenna arrays are fed by a properly designed feeding network to maintain the desired phase relation among the antenna elements. The relative phase difference and excitation amplitude of the consecutive antenna elements are the controlling factors of the radiation pattern of the whole array. The direction of radiation and the beamwidth can be controlled by adjusting these two factors in the array. The phase difference is dependent on the lengths of the transmission lines feeding different array elements and the excitation current is dependent on the source. The element-to-element spacing is also a crucial parameter in the design of the antenna array and its feeding network, as it affects the overall radiation efficiency and gain of the array antenna. These feeding networks are designed to operate in the antenna's operating frequency range. In the case of broadband stacked antenna elements, used to construct an antenna array, these feeding networks must be designed at the centre frequency of the operating bandwidth. Further, the feeding network must operate over the desired wide bandwidth in case of any broadband antenna array and specifically for these inherently broadband stacked antenna arrays. Various stacked antenna array design techniques have been discussed in this chapter. Furthermore, some design

examples along with their measurement results are discussed thoroughly in the upcoming sections.

5.2 ANTENNA ARRAY FEEDING NETWORK

5.2.1 Traditional feeding network

As discussed in the previous section, feeding network design is crucial for the operation of antenna arrays. The design of the feeding network is decided by the output parameters, such as direction of maximum radiation, beamwidth, etc. The feeding network controls the phase relationship among the multiple elements of the antenna array and therefore affects the individual element radiation pattern, which in turn affects the overall radiation pattern of the array. In [1] mathematical relations have been developed to calculate excitation at each antenna element of the array to obtain the desired phase relation between them and thus the desired overall radiation pattern of the antenna array. A complete procedure of designing a feed network based on transmission lines is discussed in this work, which can achieve the desired excitations of each antenna element of the array. Moreover, in [2], a surface-current model approach is used to analyze the total radiated power of the antenna array. Here each radiating patch and feeding transmission-line is replaced with an equivalent current source element. Currents for radiating patches are obtained using transmission-line or cavity model concepts, while for the feeding transmission-lines, they are calculated as travelling waves. Through these currents, the power radiated and power in surface waves are calculated based on the proper Green function. Also, conductor and dielectric losses can be calculated through standard formulae. This approach thus helps in the overall calculation of total power radiated and dissipated for the given input power in every antenna element. Also, the phase relationship among the elements is calculated and controlled. This method helps in designing the antenna array based on the desired output radiation, through an analytical approach. Moreover, it is shown that dissipative losses are increased with the increase in transmission-line lengths of the feeding network. Thus, if antenna elements are spaced far from each other, the surface wave losses increase. This shows that losses are minimal for the separation of $\lambda_o/2$, while they are maximum for the separation of λ_o . Further, it is observed that dielectric and ohmic losses increase with a greater number of antenna elements in the array.

5.2.2 Sequential feeding network

Apart from a traditional feeding network with equal power and phase distribution in the elements, different variations in the geometry of the feeding network can be carried out to change the phase relation between the consecutive antenna elements. In [3], a sequential-phase feeding network is

proposed to achieve circular polarization of the antenna array. In this work, a series-parallel curved transmission-line-based feed line is designed which sequentially feeds four equally spaced radiating elements arranged in a circular fashion about the feed. This geometry allows each element to be fed with a different phase and this phase can be controlled through the length of transmission-line segments between the two elements. In this case, to achieve circular polarization, the phases among the four antenna elements are maintained at 0° , 90° , 180° , and 270° respectively. Moreover, antenna elements are truncated at the corners to enhance the axial ratio bandwidth.

5.2.3 Slot-coupled feeding network

The feeding networks described in the previous sections are made of printed microstrip transmission-lines. A different approach for designing the feeding network is also reported in the literature, where the slot-coupling type of feed is proposed. In slot/aperture-coupled antennas, power to the antenna is fed through a slot placed above the feed line. Similarly, for the antenna array, a complete feeding network can be coupled to the radiating patches through the slot, where input power is divided through the feed network and is coupled as electromagnetic energy to the antenna elements. A feeding network is proposed in [4] where there is a microstrip-slot line transition for energy transfer from the feed to the patch. A printed feed line couples and distributes energy to radiating elements through a slot-line. The slot-line is placed orthogonally with respect to the feed line (which provides 180° phase shift at the output port) and couples energy to two series-fed elements on each side of the slot-line. To keep the power distribution among the elements equal, the feed line is placed centrally with respect to the antenna elements and also the slot-line is placed symmetrically and centrally with respect to the elements.

Further, a slot-coupled feed network for an 8×8 antenna array is also proposed in [5]. However, here, series-fed antenna elements are fed centrally through a slot at the centre of each column, i.e. at the centre of the eight elements (four on each side) in each column. A 1:8 power divider is designed and printed at the lowest layer. The slot is etched at the middle layer, placed centrally above each output port of the feeding network and also placed centrally with respect to antenna elements arranged in series in a line. This arrangement yields a series-parallel feeding of 64 antenna elements through reduced transmission-lines in the feeding network and also reduced overall losses.

5.3 PRINTED STACKED ANTENNA ARRAY DESIGN TECHNIQUES

There are many proposed printed stacked antenna arrays in the literature for applications targeting broad bandwidth and high gain. Different design

techniques are used to achieve the desired antenna array response. A few design cases are discussed in the section below.

5.3.1 Planar stacked microstrip antenna array

In [6] a broadband circularly polarized stacked antenna array is presented which operates in the S-band frequency region. The antenna element comprises a microstrip-fed driven patch and a parasitic patch, both printed on RT Duroid 5870 substrate separated by an air gap of 5 mm. The lower substrate is 3.15 mm thick while the upper substrate has a thickness of 1.575 mm. To achieve circular polarization, the square patch is truncated at the two orthogonal edges. The stacking of two patches, with different dimensions, yields a broadband response due to the two different resonant frequencies of the driven and parasitic patches. This designed stacked antenna element is then used to make an array of 2×2 elements arranged in a square fashion. A corporate feed network is used for feeding the array, where the probe feed is connected at the centre of the network as shown in Figure 5.1. The spacing between antenna array elements kept in the present design is 0.75λ (λ is calculated at the centre frequency of the band, i.e. 2.2 GHz), which is obtained after optimization. The proposed antenna array has 17 dBi peak gain and sufficiently wide bandwidth of 16% (2.02–2.38 GHz) and an axial ratio below 3 dB in the range 2.15–2.4 GHz. Thus, a stacked antenna array is a solution to high gain and broad bandwidth requirements. The design parameters of the proposed circularly polarized antenna are listed in Table 5.1.

5.3.2 Planar stacked antenna array design using meta-surface

An aperture-coupled stacked antenna array is proposed in [7], where a quadruple cluster of leaf-shaped meta-surface-based antenna elements are designed. The antenna is circularly polarized and has a wide operating bandwidth in the sub-6 GHz band. The antenna geometry is depicted in Figure 5.2, where 4 clusters of 4×4 leaf-shaped (modified truncated patches) antenna elements at the upper patch layer are shown. The middle layer of the stacking consists of a slot in the ground plane to couple the radiated electromagnetic energy to the upper patch (driven patch). The lower-most layer consists of the feed network, where a single feed element looks as depicted in Figure 5.2(c). The feed consists of a microstrip feed line along with the fan-shaped structure truncating the feed line. This fan-shaped structure helps in improved impedance matching of the antenna.

The stacked substrates have a dielectric constant of 4.3 and dimensions of 60 mm \times 60 mm. The heights of the upper, middle, and lower substrates are 1.6 mm, 1.6 mm, and 0.8 mm respectively. The upper substrate has 4

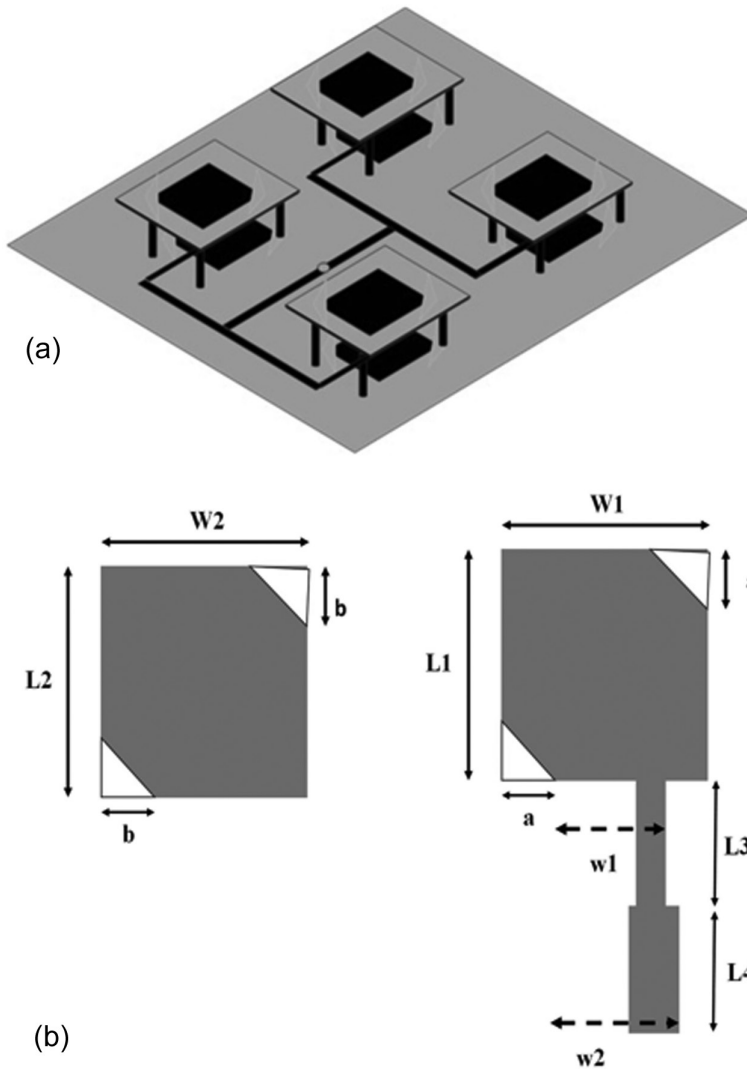


Figure 5.1 Circularly polarized stacked antenna array, (a) 3D view, (b) two layers of the antenna. Redrawn from [6].

$\times 4$ leaf-shaped structures, made of truncated squares of size 12.6 mm and a truncation radius of 6 mm. The gap between subsequent leaf structures is maintained at 0.8 mm in this present design. The middle layer has a slot of dimensions 2 mm \times 32 mm and the lower layer contains the feed line of width 1.5 mm and length 30 mm, terminated with a fan-shaped stub of radius $\theta = 120^\circ$. The final design of the antenna is obtained in three phases as shown in Figure 5.3.

Table 5.1 Design parameters of the proposed circularly polarized antenna [6]

Parameter	L_1	W_1	L_2	W_2	w_1	w_2	a	b	L_3	L_4
Value (in mm)	33.8	33.8	37.7	37.7	4.3	6.5	10.2	7.72	28	25

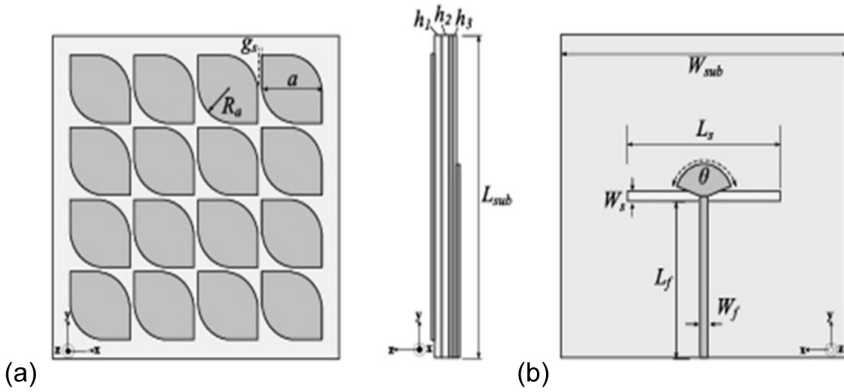


Figure 5.2 Geometry of proposed antenna with quadruple leaf-shaped patches (a) top view, (b) side view, (c) bottom view showing aperture and the fan shaped truncated feed line. (Source: Nathapat Supreeyattikul, Pisit Janpangnorn, Titipong Lertwiriayarpa, Monai Krairiksh, and Chuwong Phongcharoenpanich, “CMA-Based Quadruple-Cluster Leaf-Shaped Metasurface-Based Wideband Circularly-Polarized Stacked-Patch Antenna Array for Sub-6 GHz 5G Applications”, IEEE Access, Vol. 11, pp: 14511–14523, 2023 [7].)

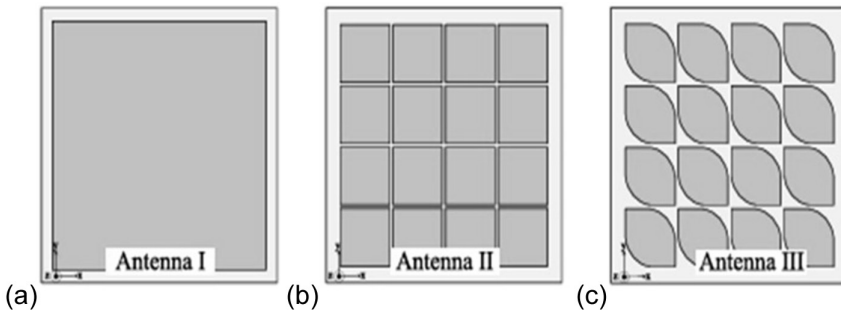


Figure 5.3 Stages of evolution of the proposed antenna (a) Antenna I (1 square patch), (b) Antenna II (16 small square patches), (c) Antenna III (16 small leaf-shaped patches). (Source: Nathapat Supreeyattikul, Pisit Janpangnorn, Titipong Lertwiriayarpa, Monai Krairiksh, and Chuwong Phongcharoenpanich, “CMA-Based Quadruple-Cluster Leaf-Shaped Metasurface-Based Wideband Circularly-Polarized Stacked-Patch Antenna Array for Sub-6 GHz 5G Applications”, IEEE Access, Vol. 11, pp: 14511–14523, 2023 [7].)

Initially, a square-shaped patch (Antenna I) of dimensions $54.4 \text{ mm} \times 54.4 \text{ mm}$ was designed to operate in the C-band region around 3 GHz. Then the design modification resulted in Antenna II, where one patch is replaced by 4×4 small square patches of dimensions $12.6 \text{ mm} \times 12.6 \text{ mm}$ with a gap of 0.8 mm. This modification resulted in improved impedance bandwidth of the antenna. In the third phase, the antenna design is further modified, where the edges of square patches have been curved out to transform the shape to a leaf-like structure, which resulted in Antenna III. The final design Antenna III has 53.45% bandwidth from 3.6 to 5.7 GHz. The S_{11} response of all three antenna designs is shown in Figure 5.4(a). Moreover, Figure 5.4(b) shows the axial ratio of all three antenna designs with respect to frequency. The axial ratio response of antenna designs I and II shows that they are linearly polarized, while the truncation of square patches in Antenna III results in circular polarization as evident by the 15.25% axial ratio bandwidth (3.8–4.5 GHz) of this final design. The design parameters of the proposed antenna are listed in Table 5.2.

The proposed aperture-coupled broadband stacked antenna is further used to make an array of 4 elements, with each element comprising 4×4

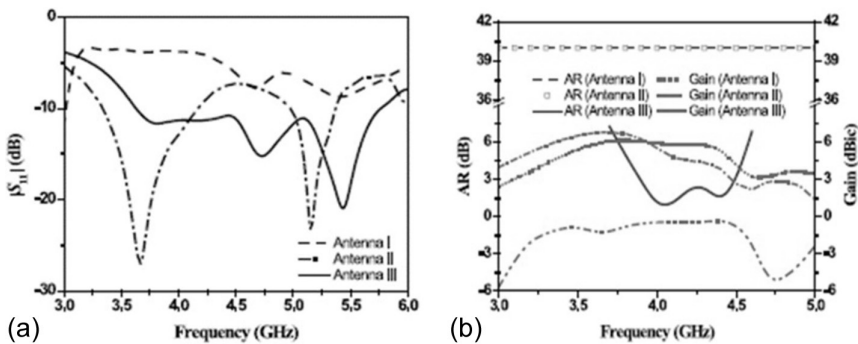


Figure 5.4 Response of proposed antenna at different design stages, (a) S_{11} response, (b) axial ratio bandwidth and gain. (Source: Nathapat Supreeyattikul, Pisit Janpangnarn, Titipong Lertwiriayarpa, Monai Krairiksh, and Chuwong Phongcharoenpanich, “CMA-Based Quadruple-Cluster Leaf-Shaped Metasurface-Based Wideband Circularly-Polarized Stacked-Patch Antenna Array for Sub-6 GHz 5G Applications”, IEEE Access, Vol. 11, pp: 14511–14523, 2023 [7].)

Table 5.2 Design parameters of proposed quadruple leaf-shaped antenna array [7]

Parameter	W_{sub}	L_{sub}	h_1	h_2	h_3	a	R_g
Value (mm)	60	60	1.6	1.6	0.8	12.6	6
Parameter	g_s	W_s	L_s	W_f	L_f	θ	
Value (mm)	0.8	2	32	1.5	30	120°	

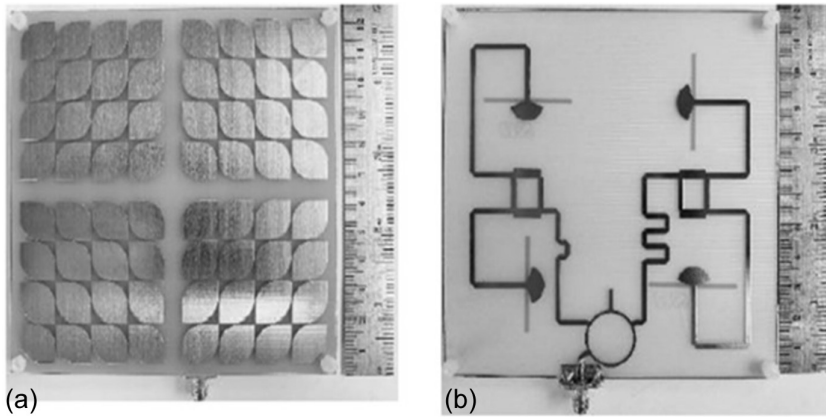


Figure 5.5 Fabricated four element array structure of proposed antenna (a) top view, (b) feeding network. (Source: Nathapat Supreeyattikul, Pisit Janpangnarn, Titipong Lertwiriayapa, Monai Krairiksh, and Chuwong Phongcharoenpanich, “CMA-Based Quadruple-Cluster Leaf-Shaped Metasurface-Based Wideband Circularly-Polarized Stacked-Patch Antenna Array for Sub-6 GHz 5G Applications”, IEEE Access, Vol. 11, pp: 14511–14523, 2023 [7].)

(16) leaf-shaped patches, depicted in Figure 5.5. The array is fed through three hybrid couplers, where one is a hybrid ring coupler and two are quadrature hybrid couplers. The ring hybrid coupler design and dimensions are obtained at a centre frequency of 4 GHz and this is used to divide power in the two output ports with a 180° phase shift. The quadrature hybrid coupler is also designed at a centre frequency of 4 GHz, and to give a 90° phase shift between the two output ports. The input port is connected to a hybrid ring coupler, which in turn is connected to two hybrid quadrature couplers with two output ports each at the quadrature phase. Thus, there are a total of four output ports with a quadrature phase shift among each other, with equal magnitude for circularly polarized radiation. The measured impedance bandwidth of the proposed antenna array is 69% while the axial ratio bandwidth is 21%, shown in Figure 5.6.

5.3.3 Shared aperture stacked antenna array

A shared aperture dual-band patch antenna array is proposed [8], which uniquely combines two different operating band antennas arranged in a single shared aperture. The concept is to utilize the difference between antenna dimensions at different operating frequency bands. Here the two frequency bands used are Ka-band and E-band, where antenna dimensions at these operating frequencies differ a lot. The smaller E-band patches are made to adjust within the larger aperture/dimension of the Ka-band patch, such that the E-band patches are adjusted within the square perforations made

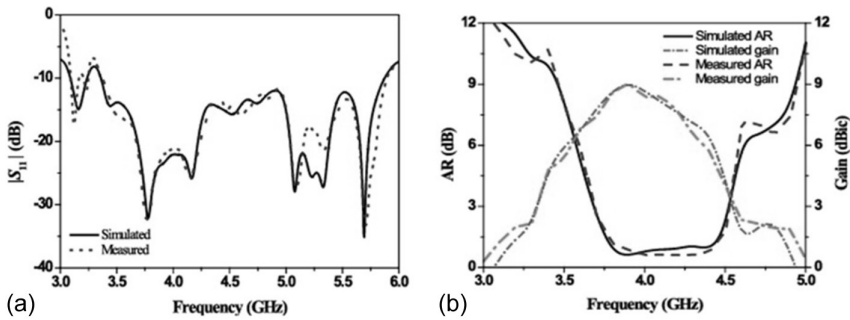


Figure 5.6 Response of four element antenna array of the proposed antenna (a) S_{11} response, (b) axial ratio bandwidth and gain. (Source: Nathapat Supreeyattikul, Pisit Janpangern, Titipong Lertwiriwarapa, Monai Krairiksh, and Chuwong Phongcharoenpanich, “CMA-Based Quadruple-Cluster Leaf-Shaped Metasurface-Based Wideband Circularly-Polarized Stacked-Patch Antenna Array for Sub-6 GHz 5G Applications”, IEEE Access, Vol. 11, pp: 14511–14523, 2023 [7].)

inside the Ka-band patch as shown in Figure 5.7. Further, another layer of E-band patches is arranged in a stacked configuration beneath the first driven layer of the Ka-band patch. This stacked configuration of the E-band patch array is fed through a slot-coupling mechanism to avoid losses at higher frequency. To feed the E-band antenna array through slot-coupling, a corporate feed network is printed beneath the lower-most substrate layer, above which is placed the ground plane with a slot, which then feeds the two-layered E-band stacked antenna array (placed above the ground plane) through the slots etched below each antenna element. The 3D geometry of the proposed stacked shared aperture antenna array is shown in Figure 5.8 and the feeding network for the E-band antenna is shown in Figure 5.9. The proposed antenna’s design parameters are listed in Table 5.3.

The E-band antenna array is designed keeping two design constraints in mind: one is to reduce the E-band patch size as much as possible to fit them inside Ka-band perforations, and the second is to keep the element spacing between E-band array elements in the range $0.5\lambda_o$ to $0.8\lambda_o$ to avoid side lobes (λ_o is the free-space wavelength at the centre frequency of the operating band).

The feeding of this shared aperture dual-band antenna needs to be done carefully as the feed line of the K-band antenna is at the upper-most layer, while the feed network of the E-band stacked antenna array is at the lower-most layer. The Ka-band patch is fed by a 50-ohm microstrip feed line, connected to the patch through a quarter-wave transformer. The E-band stacked antenna array is fed via an antipodal fin-line waveguide to a microstrip transition line feeding the corporate feed network which couples the energy to the E-band stacked array through a slot-coupling mechanism.

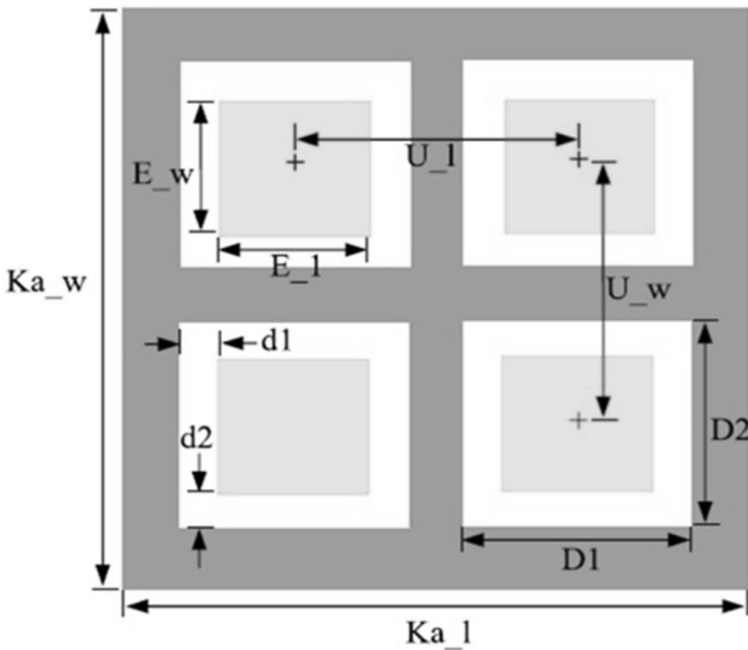


Figure 5.7 Proposed antenna top view showing aperture sharing among Ka-band and E-band patches. (Source: Zongxin Wang and Zeqin Huang, “A Microwave/Millimeter Wave Dual-Band Shared Aperture Patch Antenna Array”, IEEE Access, Vol. 8, pp: 218585–218591, Nov 2020 [8].)

This minimizes losses at the SMA connector and microstrip feed line connection at higher frequencies. The response of this dual-band antenna is shown in Figure 5.10 and Figure 5.11, depicting the response of the E-band and Ka-band antennas respectively. The antenna is finally placed in the metal cavity as shown in Figure 5.12. The fabricated prototype is shown in Figure 5.13.

The above-mentioned shared aperture antenna is further used to design an antenna array of 2×4 Ka-band antenna elements and 8×16 E-band antenna elements as shown in Figure 5.14(a). Here the corporate feed network is designed for both E-band and Ka-band antenna elements, with Ka-band elements being directly fed via microstrip feed line through matching transmission-line sections; the E-band stacked antenna array is fed via waveguide-to-microstrip line transition through the slot-coupling mechanism, shown in Figure 5.14(b). The matching transmission-line sections are also inserted in the E-band feeding network to improve the impedance matching. This dual-band stacked antenna array has high gain in both operating bands. In the E-band the obtained peak co-polarization gain is 24.7 dB while in the Ka-band region it is 15.5 dB.

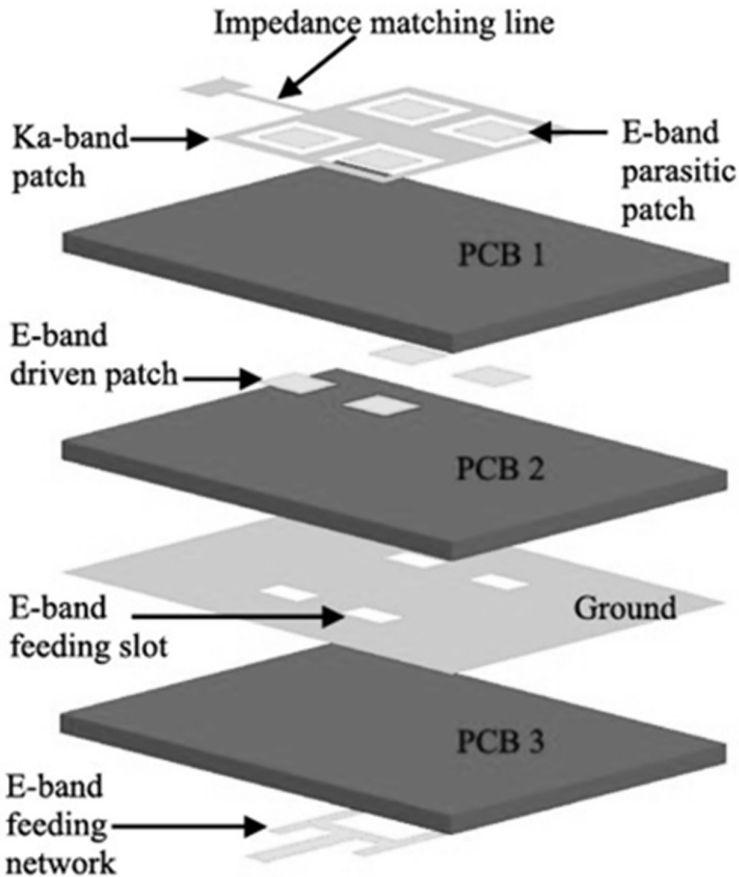


Figure 5.8 3D view of proposed shared aperture stacked antenna comprising of E-band and Ka-band elements. (Source: Zongxin Wang and Zeqin Huang, “A Microwave/Millimeter Wave Dual-Band Shared Aperture Patch Antenna Array”, IEEE Access, Vol. 8, pp: 218585–218591, Nov 2020 [8].)

5.3.4 Stacked antenna array fed vertically

A vertically arranged antenna array is presented in [9], wherein stacked antenna elements are treated as directors when only the lower patch is excited as well as array elements when all the patches are independently excited. These two cases are called directivity mode and diversity mode respectively. In the directive mode the antenna acts as a printed stacked yagi-uda antenna with only the lower patch being fed and the upper layer patches act as directors to increase the directivity and gain of the antenna, shown in Figure 5.15. While in diversity mode, all the stacked patch elements are being fed through multiple ports, which causes diverse radiation

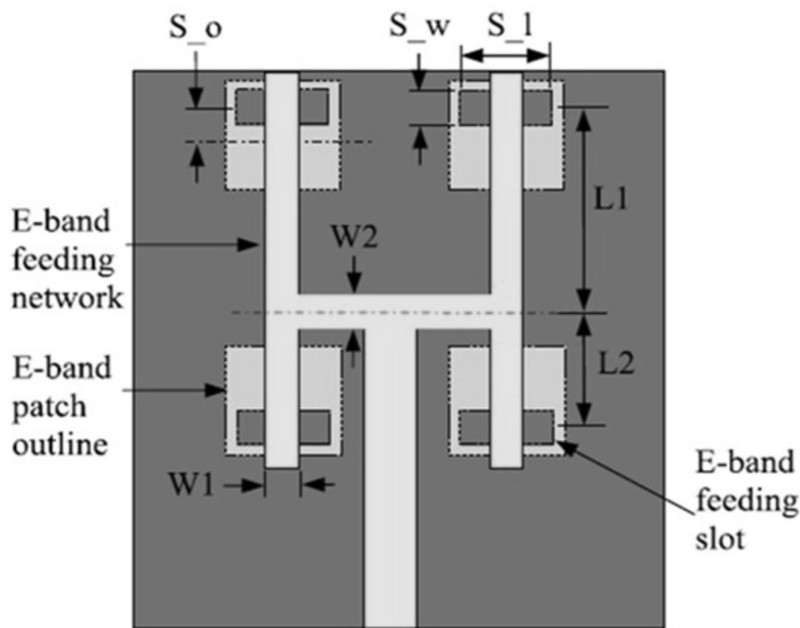


Figure 5.9 Feeding network of E-band array elements through aperture-coupling. (Source: Zongxin Wang and Zeqin Huang, “A Microwave/Millimeter Wave Dual-Band Shared Aperture Patch Antenna Array”, IEEE Access, Vol. 8, pp: 218585–218591, Nov 2020 [8].)

Table 5.3 Design parameters of aperture-shared stacked antenna [8]

Parameter	K_{a_j}	K_{a_w}	E_j	E_w	U_j	U_w	S_j	S_w	S_o
Value (mm)	3.1	3.6	0.8	0.7	1.5	1.5	0.8	0.144	0.262
Parameter	W_1	W_2	W_s	D_1	D_2	h_{PCB1}	h_{PCB2}	h_{PCB3}	
Value (mm)	0.25	0.3	0.4	1.3	1.04	0.254	0.254	0.127	

patterns when the other three ports, i.e. at layers 2, 3, and 4, are excited. To operate in diversity mode, all the patch layers need to be fed through the source. To achieve this without increasing impedance mismatch at port 1 for directivity mode, a hybrid microstrip-CPW feed line is used. The patch at layer 1 is microstrip-fed with a matching transmission-line section, while the patches at the above layers are fed with CPW feed, a long curved feeding transmission-line, as an additional stub for improved impedance matching in both directivity and diversity modes of operation, as shown in Figure 5.16. The simulated S_{11} response at different ports is shown in Figure 5.17. The gain of the stacked antenna array in directivity mode is shown in

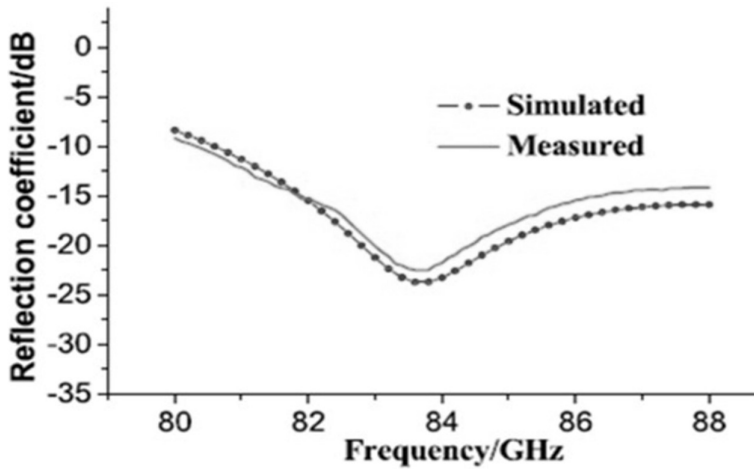


Figure 5.10 S_{11} response of the proposed shared aperture stacked antenna at E-band. (Source: Zongxin Wang and Zeqin Huang, "A Microwave/Millimeter Wave Dual-Band Shared Aperture Patch Antenna Array", IEEE Access, Vol. 8, pp: 218585–218591, Nov 2020 [8].)

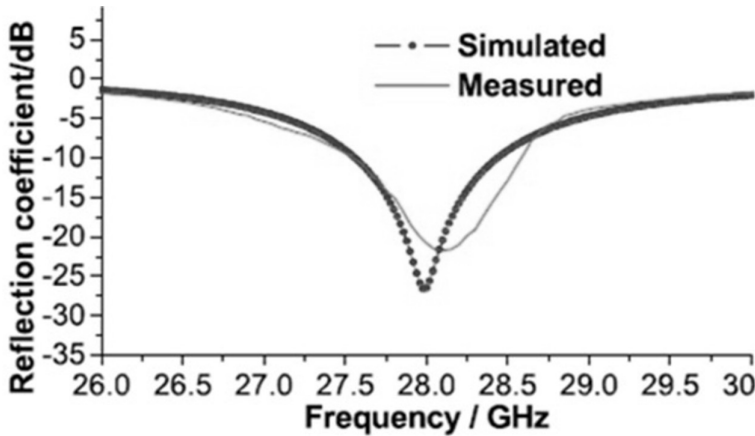
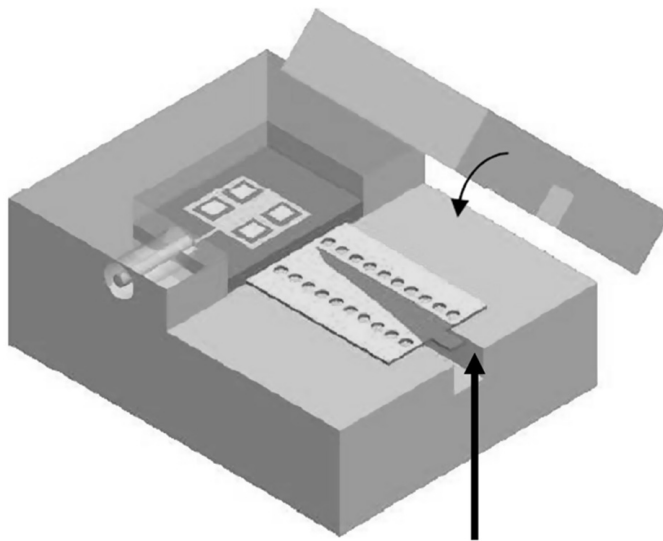


Figure 5.11 S_{11} response of proposed shared aperture stacked antenna at Ka-band. (Source: Zongxin Wang and Zeqin Huang, "A Microwave/Millimeter Wave Dual-Band Shared Aperture Patch Antenna Array", IEEE Access, Vol. 8, pp: 218585–218591, Nov 2020 [8].)

Figure 5.18, which is around 7 dBi, while the radiation patterns in diversity mode are shown in Figure 5.19. In diversity mode isolation is higher than 17.5 dB at the operating frequency of 2.45 GHz. The design parameters of the proposed antenna array are listed in Table 5.4.



Waveguide port to microstrip line transition

Figure 5.12 View of shared aperture stacked antenna inside metal cavity. (Source: Zongxin Wang and Zeqin Huang, “A Microwave/Millimeter Wave Dual-Band Shared Aperture Patch Antenna Array”, IEEE Access, Vol. 8, pp: 218585–218591, Nov 2020 [8].)

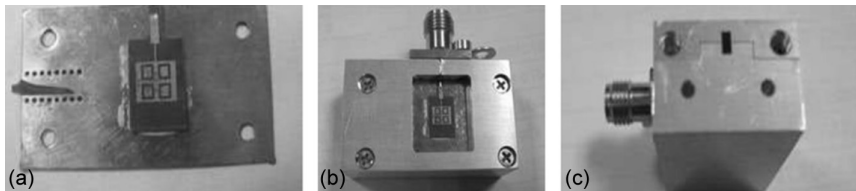


Figure 5.13 Fabricated prototype of shared aperture stacked antenna, (a) antenna without metal cavity, (b) top view with metal cavity, (c) side view showing with metal cavity waveguide port. (Source: Zongxin Wang and Zeqin Huang, “A Microwave/Millimeter Wave Dual-Band Shared Aperture Patch Antenna Array”, IEEE Access, Vol. 8, pp: 218585–218591, Nov 2020 [8].)

5.4 APPLICATIONS OF STACKED ANTENNA ARRAYS

As discussed earlier in this chapter, stacked antenna arrays have the added advantage of being broadband along with conventional array benefits of high gain and high directivity. As microstrip stacked antennas are printed

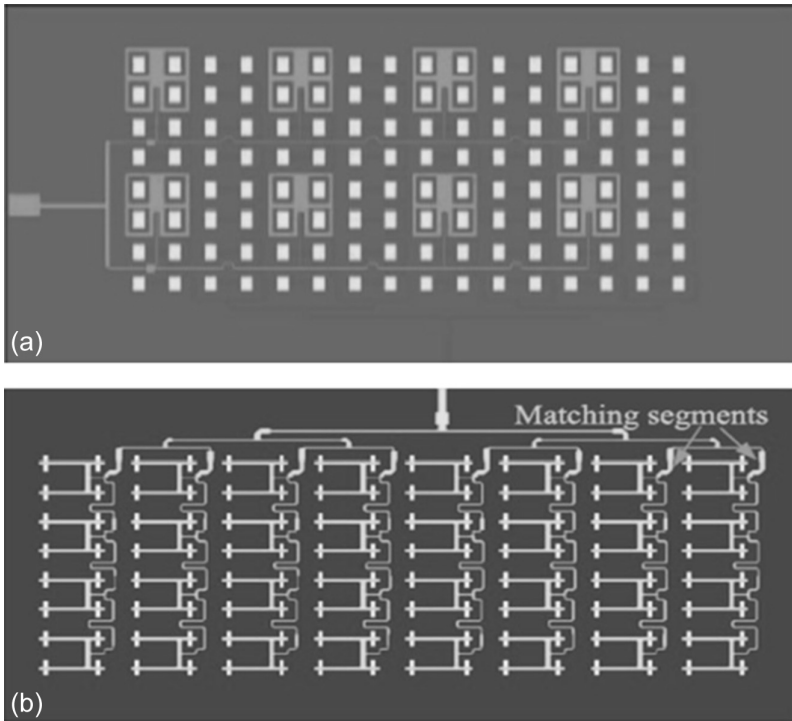


Figure 5.14 Antenna array made of aperture shared stacked antenna, (a) top view showing E-band and Ka-band patches and Ka-band feeding network, (b) bottom view showing the E-band feeding network. (Source: Zongxin Wang and Zeqin Huang, “A Microwave/Millimeter Wave Dual-Band Shared Aperture Patch Antenna Array”, *IEEE Access*, Vol. 8, pp: 218585–218591, Nov 2020 [8].)

structures and are compact too, they are quite useful in wireless communication applications where other circuits are mostly PCBs. These printed stacked antennas can be easily integrated with other circuit components and additionally provide wide bandwidth for communication purposes. Antenna arrays made of stacked antenna elements are quite useful for the high bandwidth and high data rate requirements of today’s wireless communication industry. These stacked antenna arrays are high-gain wide-bandwidth antennas and can be used for applications like sub-6 GHz 5G band [10, 11], and are also commonly used in base-station applications [12]. Circularly polarized antenna arrays are also very useful in the wireless industry, as orthogonal polarizations can be both transmitted and more importantly received without any significant losses. These stacked antenna arrays also find applications in back-haul services [13] and recent millimetre-wave applications

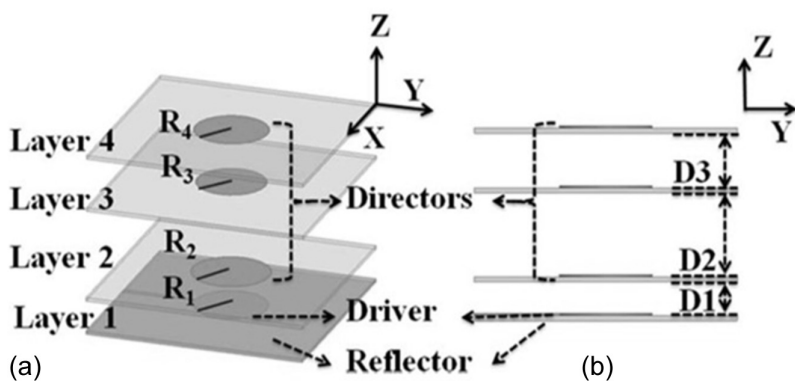


Figure 5.15 Geometry of stacked antenna array in directivity mode with only driven patch being fed, (a) 3D view, (b) side view. Reproduced with permission from IEEE [9].

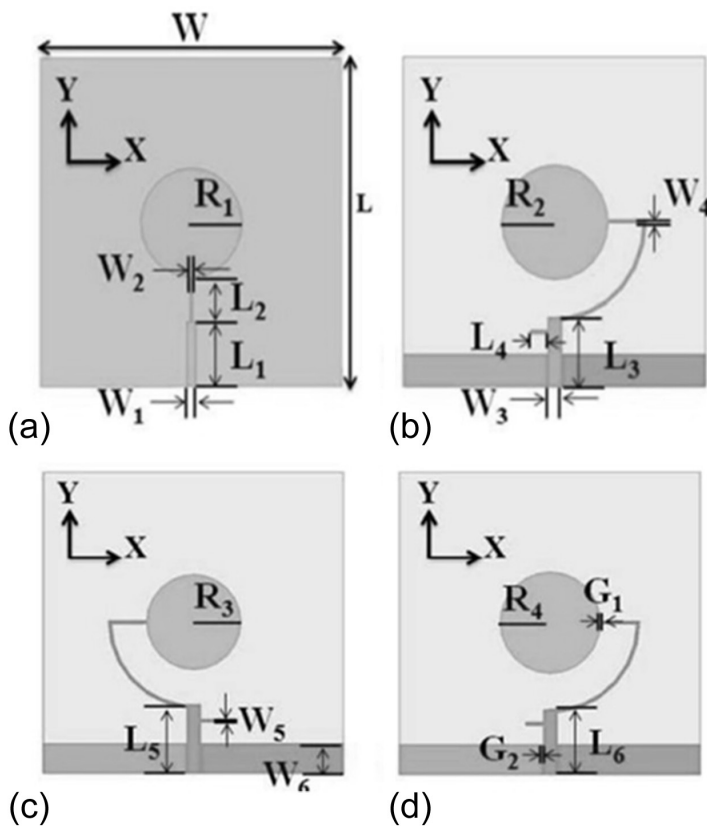


Figure 5.16 Geometry of stacked antenna array in diversity mode, (a) Layer 1, (b) Layer 2, (c) Layer 3, (d) Layer 4. Reproduced with permission from IEEE [9].

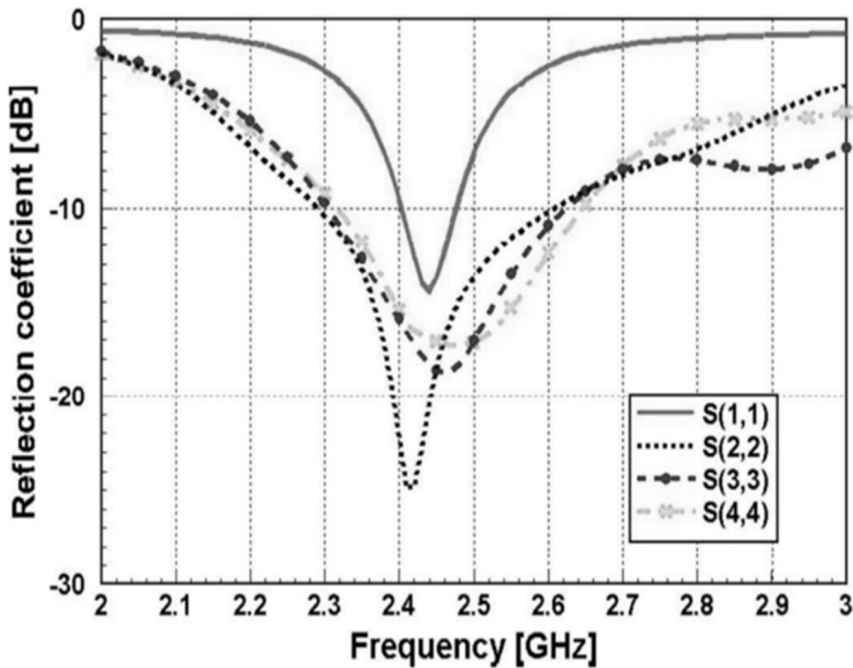


Figure 5.17 Simulated S-parameters of stacked antenna array in diversity mode. Reproduced with permission from IEEE [9].

[14]. Such high-gain and broad bandwidth antenna arrays are an important component of satellite communication applications [15] and for point-to-point as well as point-to-multipoint communications [16].

Overall, these printed stacked antenna arrays are a very useful component of today's wireless communication industry where the property of high gain is of prime importance for long-distance communications, while the property of wide bandwidth is essential for high data rates.

5.5 SUMMARY

This chapter demonstrated the design and the concepts related to different types of printed stacked antenna arrays. The basics of antenna arrays were detailed initially, along with different types of antenna array feeding networks. The chapter then delved into various types of printed stacked antenna array design techniques along with their measured results. The chapter then concluded with the wide range of applications of stacked antenna arrays.

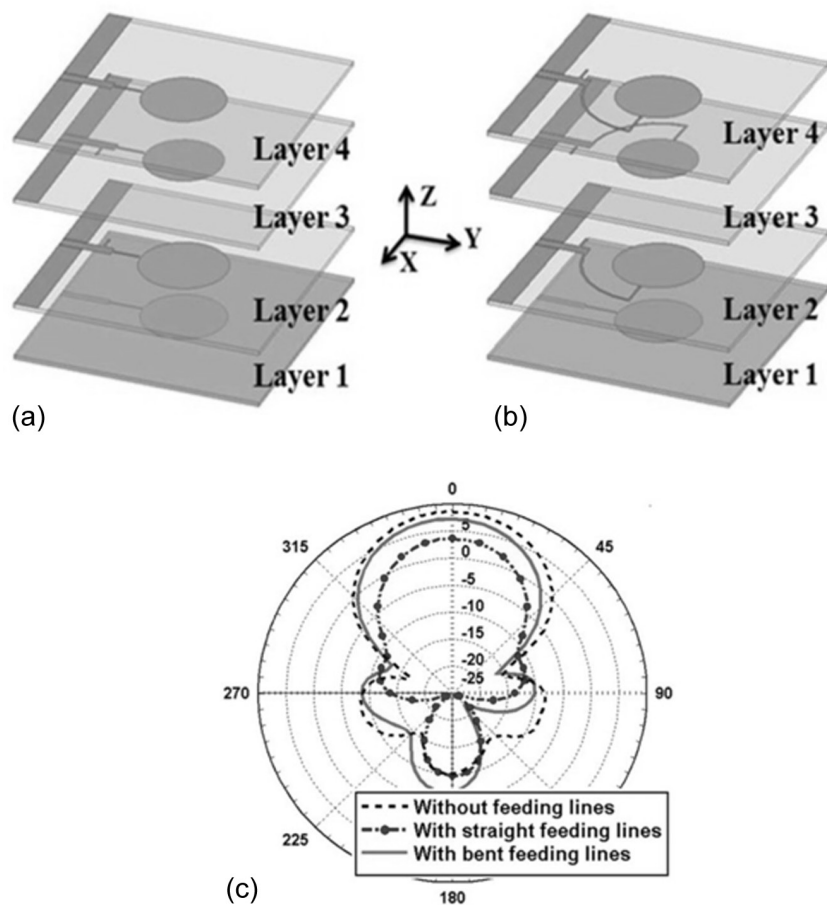


Figure 5.18 Stacked antenna array (a) with straight feeding lines, (b) with curved feeding lines, (c) gain for different types of feeding lines at 2.45 GHz. Reproduced with permission from IEEE [9].

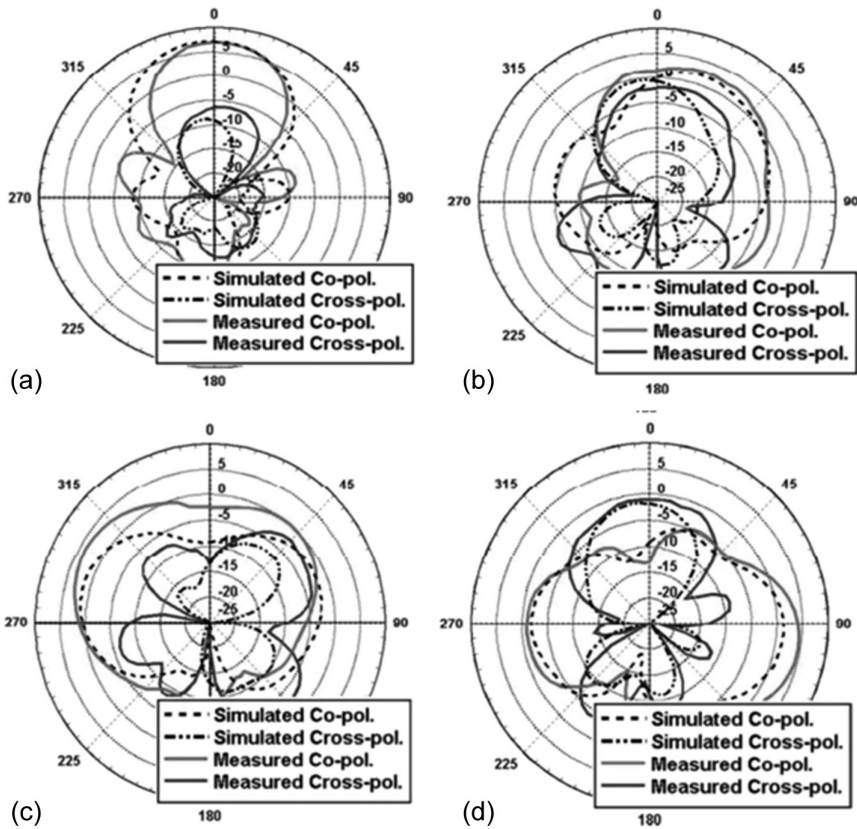


Figure 5.19 Simulated and measured radiation patterns of stacked antenna array (a) when port 1 is excited (directivity mode), and in diversity mode when (b) port2, (c) port3, and (d) port4 are excited. Reproduced with permission from IEEE [9].

Table 5.4 Design parameters of proposed stacked antenna array [9]

Parameter	W	L	R_1	R_2	R_3	R_4	W_1	W_2	W_3	G_1
Value (in mm)	102.2	102.2	17.2	18	16	17	3	0.7	4.6	0.5
Parameter	W_4	W_5	W_6	L_1	L_2	L_3	L_4	L_5	L_6	G_2
Value (in mm)	1	1	10	20	13.9	21.38	6	23.19	21.89	0.4

REFERENCES

1. Harvey Schuman, and Jules Cummins, "Practical feed network design for antenna arrays", 862 *IEEE Trans. Antennae Propag.*, Vol. 21, No. 6, pp:862–864, November 1973.
2. E. Levine, G. Malamud, S. Shtrikman, and D. Treves, "A study of microstrip array antennas with the feed network", *IEEE Trans. Antennas Propag.*, Vol. 31, No. 4, pp:426–434, April 1989.

3. Chen Ming, "Compact wideband microstrip antenna array using sequential-phase feed network and metasurfaces", *Wireless Personal Comm*, Springer, Vol. 110, pp:563–572, September 2019.
4. Dai-liang Zhai, Chen-xin Zhang, Zi-mu Yang, and Shuai-jiang Hu, "Design of The Antenna Array with A Novel Feeding Network", 2012 International Conference on Microwave and Millimeter Wave Technology (ICMMT), May 2012.
5. Krzysztof Wincza, and Slawomir Gruszczynsk, "Microstrip antenna arrays fed by a series-parallel slot-coupled feeding network", *IEEE Antennas Wirel. Propag. Lett.*, Vol. 10, pp:991–994, 2011.
6. M. Saad Khan, and Farooq A. Tahir, "A Circularly Polarized Stacked Patch Antenna Array for Tracking Applications in S-Band," 9th European Conference on Antennas and Propagation (EuCAP), April 2015.
7. Nathapat Supreeyattitukul, Pisit Janpangnarn, Titipong Lertwiriayapa, Monai Krairiksh, and Chuwong Phongcharoenpanich, "CMA-based quadruple-cluster leaf-shaped metasurface-based wideband circularly-polarized stacked-patch antenna array for sub-6 GHz 5G applications", *IEEE Access*, Vol. 11, pp:14511–14523, 2023.
8. Zongxin Wang, and Zeqin Huang, "A microwave/millimeter wave dual-band shared aperture patch antenna array", *IEEE Access*, Vol. 8, pp:218585–218591, November 2020.
9. Hyeonhyeong Choe, and Sungjoon Lim, "Directivity and diversity dual-mode stacked antenna array using directors of yagiuda antenna as monopole antennas", *IEEE Antennas Wirel. Propag. Lett.*, Vol. 13, pp:575–578, 2014.
10. Tuan Dao, Andrew Kearns, David Reyes Paredes, and Gernot Huebe, "Antenna array on standard PCB for D-band 6G communications", *IEEE Antennas Wirel. Propag. Lett.*, Vol. 23, No. 2, pp:478–482, February 2024.
11. Amir Reza Dastkhosh, Mehdi Naseh, and Fujiang Lin, "K/Ka Slotted Stacked Patch Antenna and Active Array Antenna Design for a 5G/6G Satellite Mobile Communication System," 13th Global Symposium on Millimeter-Waves & Terahertz (GSMM), May 2021.
12. Tian-Yu Yan, Xin-Hao Ding, and Jun-Yao Yang, "A low-cost compact dual-polarized patch antenna array for 5G massive MIMO base station," *IEEE Antennas Wirel. Propag. Lett.*, Vol. 23, No. 4, pp:1381–1384, April 2024.
13. Archiman Lahiry, Khoa N. Le, Vo Nguyen Quoc Bao, and Vivian W. Y. Tam, "Energy-efficient ground base station antenna array system for wireless backhauling and two state charging of drone base stations", *IEEE Internet Things J.*, Vol. 10, No. 15, pp:13798–13813, August 2023.
14. Yuqi He, Sihan Lv Luyu Zhao, Guan-Long Huang, Xiaoming Chen, and Wei Lin, "A compact dual-band and dual-polarized millimeter-wave beam scanning antenna array for 5G mobile terminals", *IEEE Access*, Vol. 9, pp:109042–109052, 2021.
15. Jin Fan Zhang, and Yu Jian Cheng, "K-/Ka-band planar shared-aperture beam-scanning array antenna for simultaneous transmitting and receiving low earth orbit satellite communication terminal", *IEEE Trans. Antennas Propag.*, Vol. 71, No. 8, pp:6617–6627, August 2023.
16. Shengying Liu, Kaibo Jiang, Guobing Xu, Xumin Ding, Kuang Zhang, Jiahui Fu, and Qun Wu "A dual-band shared aperture antenna array in ku/ka-bands for beam scanning applications", *IEEE Access*, Vol. 7, pp:78794–78802, June 2019.

Advantages, limitations, and applications of stacked microstrip antennas

6.1 INTRODUCTION

Printed stacked microstrip antennas are used in many applications nowadays due to their low profile, improved gain, and wide bandwidth properties. Further, these printed stacked antennas find ease of integration with other printed circuits in many applications. The stacked microstrip antennas, specifically having planar/unbroken ground planes, are useful for integration with circuits having a common large ground plane without altering their performance. However, along with their advantages, these antennas also exhibit some limitations in implementation in some cases. Further, these antennas also suffer from some design constraints and also design complexity. The details related to several advantages and also the limitations exhibited by these stacked microstrip antennas will be discussed in the upcoming sections of this chapter. The chapter will further unfold various possible applications of stacked antennas in many diverse fields.

6.2 ADVANTAGES OF STACKED MICROSTRIP ANTENNAS

Stacked microstrip antennas have been discussed in detail in the previous chapters in terms of their design techniques, mathematical relations involved, design simulations, and the measured results. These printed stacked antennas have many advantages and are therefore useful in a lot of applications. The advantages of printed stacked microstrip antennas are listed as follows:

- a) Low profile/compact
- b) Ease of integration with printed circuits
- c) Multiple resonances for multiband operation
- d) Wideband response for broadband applications
- e) High gain
- f) Stable unidirectional radiation patterns

Stacked microstrip antennas have the advantages of a low profile and easy integration with other printed circuitry, as the basic microstrip antennas have. They are designed similarly to other printed microstrip antennas, with the only difference of additional vertically arranged parasitic patch layers. They are fed through either a microstrip feed line or probe feed and in some cases aperture-coupled feed or proximity-coupled feeds are also used. These feeding techniques can all be easily implemented in printed circuitry and thus can be integrated easily with other printed components. If limited stacked layers are used (two to three), the overall antenna volume is also low and can fit in small areas, for example in handsets. Furthermore, as discussed in Chapter 1, multiple parasitic resonator layers stacked above the driven patch, when excited through electromagnetic coupling, create multiple resonances. These multiple resonances are useful for many communication applications where different operating bands are targeted simultaneously. Moreover, these multiple resonances may result in a broadband response when the resonances lie close to each other in the frequency band. This property of the wide operating bandwidth of stacked microstrip antennas is very useful in wireless communication with high data rate requirements.

The stacked parasitic layers in these stacked antennas act as directors of the energy radiated by the driven patch. Therefore, the stacked microstrip antennas have an advantage of having higher gain compared to single-layer printed antennas. The multiple stacked substrate layers also increase the effective substrate thickness of the antenna and therefore increase the total radiated energy. Moreover, the stacked microstrip antennas, specifically microstrip-fed stacked antennas, have mostly stable and unidirectional radiation patterns in the operating band due to their unbroken uniform ground plane. These unidirectional radiation patterns are very useful in applications like target scanning, remote sensing, satellite communication, and also dedicated user communication. Further, these stacked microstrip antennas are suitable for use in circuits employing integration of all the components on a common large ground plane, as their performance remains unaltered with the size of the ground plane (owing to their uniform ground plane geometry).

6.3 A FEW LIMITATIONS OF STACKED ANTENNAS

The advantages of stacked antennas are discussed in the previous section, which proves their potential for use in plenty of applications. However, there are some limitations of stacked antennas that need to be considered according to the specific application requirements. The limitations of stacked antennas are listed as follows:

- a) Complex design
- b) Complex analysis

- c) Limitation of the number of parasitic layers possible practically
- d) Overall increase in volume

The multi-layered stacked microstrip antennas have a complex design, where many design parameters play crucial roles and contribute to the antenna's response. Considering all the crucial design parameters is important to obtain the desired response and it sometimes becomes tedious to optimize all of them in the process of stacked antenna design and optimization. Many parameters need to be considered simultaneously: the substrate properties of multiple layers, the shape and relative placement/alignment of multiple patches, patch dimensions, and the type of excitation. This increases design complexity and total time consumed in the design of these multi-layered stacked antennas compared to single-layer antennas.

Along with the complex design, the analysis of these stacked antennas is quite complex. The computational time increases a lot in the case of full-wave analysis and also increases comparatively in the case of static analysis of these antennas. As discussed in Chapter 3, several circuit-level parameters need careful study for the complete static analysis of multi-layered stacked antennas. Any variation in any of the stacked layers directly affects and changes the overall input impedance of the antenna. Therefore, in static analysis, consideration of every effect is essential for the results to be in agreement with simulated results.

As discussed earlier, the stacked parasitic layers arranged vertically above the driven patch act as directors of radiated energy and can help in the improvement of overall antenna gain. However, there is a limitation to the number of stacked layers that can be added in the stacked configuration, as the energy coupled to these parasitic patches reduces with the addition of every other layer. The significant amount of electromagnetic energy being coupled to the parasitic patches reduces drastically with every new layer, and thus mostly beyond two or three stacked layers this becomes insignificant. Thus, one cannot go on increasing the effective dielectric height and the number of stacked layers for further improvement in antenna gain and bandwidth.

The vertical arrangement of stacked layers increases the overall antenna volume compared to single-layer antennas and may be avoided in case of volume constraints. In such cases, bandwidth can be increased by using defective ground surface (DGS) if a unidirectional radiation pattern is not a specific requirement of the application. The antenna structures with DGS will have bi-directional radiation patterns compared to broadband printed stacked microstrip antennas, which have unidirectional radiation patterns.

6.4 POTENTIAL APPLICATIONS OF STACKED MICROSTRIP ANTENNAS

Stacked microstrip antennas are widely used in plenty of applications these days. Owing to their compact nature, many applications requiring

integrated or on-chip antennas can benefit from the use of these stacked antennas, which inherently have broader bandwidth compared to single-layer printed antennas. Some of the potential applications are listed below and are then discussed briefly.

- a) 4G mobile communication
- b) 4G/5G/6G communication
- c) IoT applications
- d) Satellite communication
- e) Remote sensing
- f) Microwave imaging
- g) RF energy harvesting
- h) Wearable electronics

6.4.1 Application of stacked microstrip antennas in 4G/5G/6G communication

The stacked microstrip antennas play a crucial role in the wireless communication industry due to their wide bandwidth and improved gain. They are commonly used in mobile communication for 4G/5G/6G bands [1, 2]. Further, for advanced 5G/6G operation, where high data rates are essential, these broadband antennas with stable (and mostly unidirectional) radiation patterns are widely used. In 5G/6G communication, high-gain stacked antenna arrays are used to achieve beamforming for point-to-point communication for multiple users. The specific advantage of stacked antenna arrays in these applications is due to the system requirements of overall high gain for long-distance communication and wide bandwidth operation to accommodate high data rates. Due to these requirements, stacked antennas fit these applications well and are suitable for use in MIMO antenna arrays [3–7].

A stacked mm-wave antenna array design is demonstrated in [3], which provides the capability of beam scanning to multiple angles and is thus suitable for 5G communication at the upper 5G band. The layouts of the stacked antenna element and the designed array are shown in Figure 6.1. The antenna operates in two broad bands, i.e. from 24 to 28 GHz and 36 to 42 GHz. The beam scanning at 26 GHz is shown in Figure 6.2 and at 38 GHz in Figure 6.3 with different scanning angles. The beam scanning angle of $\pm 63^\circ$ is achieved at the lower band, while that of $\pm 45^\circ$ is achieved at the upper band with this given antenna array configuration.

Further, in Figure 6.4 a dual-port stacked MIMO antenna design is depicted, which has a quasi-omnidirectional radiation pattern with circular polarization, operating in the 9–14 GHz frequency range [4]. The stacking layers are comprised of reactive impedance surface (RIS) and frequency selective surface (FSS) layers. This proposed antenna has a high gain, with a quasi-omnidirectional radiation pattern owing to the semi-broken

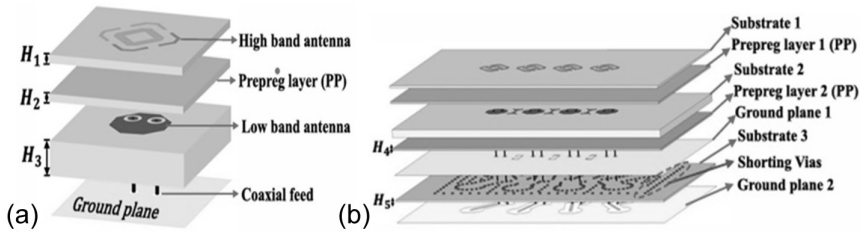


Figure 6.1 (a) Layout of mm-wave stacked antenna, (b) 3D layout of mm-wave stacked antenna array. (Source: Yuqi He, Sihan Lv, Luyuzhao, Guan-Long Huang, Xiaoming Chen, and Wei Lin, "A Compact Dual-Band and Dual-Polarized Millimeter-Wave Beam Scanning Antenna Array for 5G Mobile Terminals," IEEE Access, Vol. 9, pp: 109042–109052, Aug 2021 [3].)

ground plane. The measured SAR and power density values are within the acceptable limits, as shown in Figure 6.5. This type of antenna can be quite useful for mobile communication and also for satellite communication applications.

6.4.2 Application of stacked microstrip antennas in IoT

The Internet-of-Things (IoT) is a network of smart systems/machines capable of interacting with each other through the Internet. These systems include sensors to collect the data, the ability to process and interpret the data, and techniques to exchange the data with other systems. These are mostly indoor applications and require point-to-point communication. The important requirement in these systems is to have a low latency rate when the information is exchanged between the two systems. This needs wide bandwidth transceivers to be used at the front ends (at both the transmitter and receiver). Stacked patch antennas are again useful in this case, due to their wide bandwidth and miniaturized dimensions, and therefore many researchers have proposed their usage for future IoT applications [8–10].

6.4.3 Application of stacked microstrip antennas in satellite communication

Stacked antennas are used for satellite communication applications as they exhibit better gain and directivity, which is needed in satellite communication. In [11], a reconfigurable stacked antenna is used in the lower satellite communication band which can be useful in vehicle-bound satellite communication. A compact and broadband printed stacked antenna is proposed in [12], operating at Ka-band which is suitable for CubeSat applications. The antenna has a bandwidth of 5.53 GHz at a centre frequency of

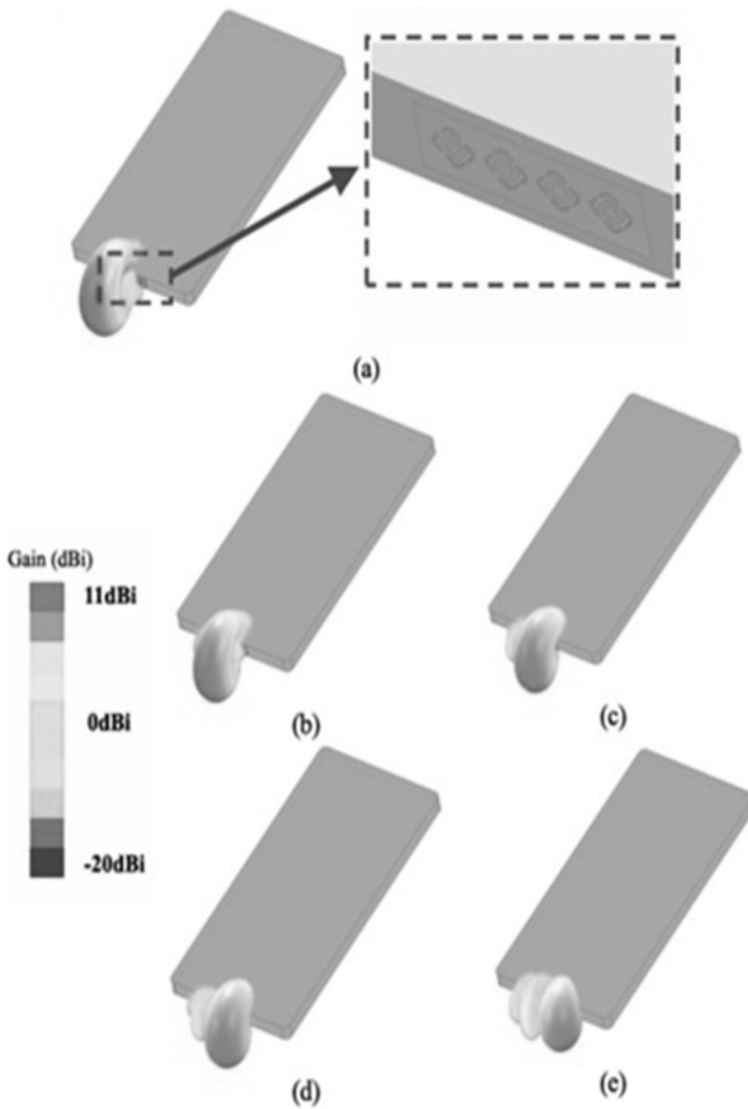


Figure 6.2 3D radiation patterns of $+45^\circ$ polarization at 26 GHz with different ϕ angles in the plane of $\theta = 90^\circ$ (a) 0° , (b) 15° , (c) 30° , (d) 45° , and (e) 60° . (Source: Yuqi He, Sihan Lv, Luyuzhao, Guan-Long Huang, Xiaoming Chen, and Wei Lin, "A Compact Dual-Band and Dual-Polarized Millimeter-Wave Beam Scanning Antenna Array for 5G Mobile Terminals," IEEE Access, Vol. 9, pp: 109042–109052, Aug 2021 [3].)

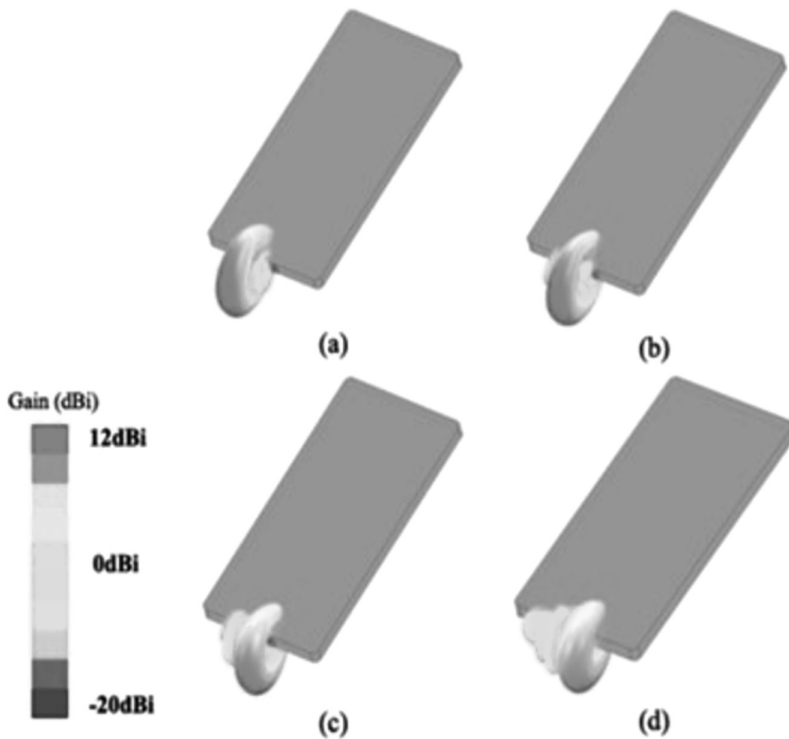


Figure 6.3 3D radiation patterns of $+45^\circ$ polarization at 38 GHz with different phi angles in the plane of theta 90° (a) 0° , (b) 15° , (c) 30° , and (d) 45° . (Source: Yuqi He, Sihan Lv, Luyuzhao, Guan-Long Huang, Xiaoming Chen, and Wei Lin, "A Compact Dual-Band and Dual-Polarized Millimeter-Wave Beam Scanning Antenna Array for 5G Mobile Terminals," IEEE Access, Vol. 9, pp: 109042–109052, Aug 2021 [3].)

33.185 GHz, with a gain of approximately 8 dBi. Furthermore, a stacked dielectric resonator antenna is proposed for Ka-band satellite communication for unmanned aerial vehicles (UAV) in [13]. In this work, a dual-band dielectric resonator antenna (DRA), with a single feed and two orthogonal circular polarizations (CPs) in K- and Ka-bands, is demonstrated for satellite communications used in UAV control. The antenna exhibits RHCP in the lower band of operation, and LHCP in the upper band of operation, with high isolation, making it suitable for UAV satellite systems.

6.4.4 Application of stacked microstrip antennas in remote sensing

Remote sensing is an emerging application these days, where hidden objects can be detected through non-destructive methods. For remote sensing

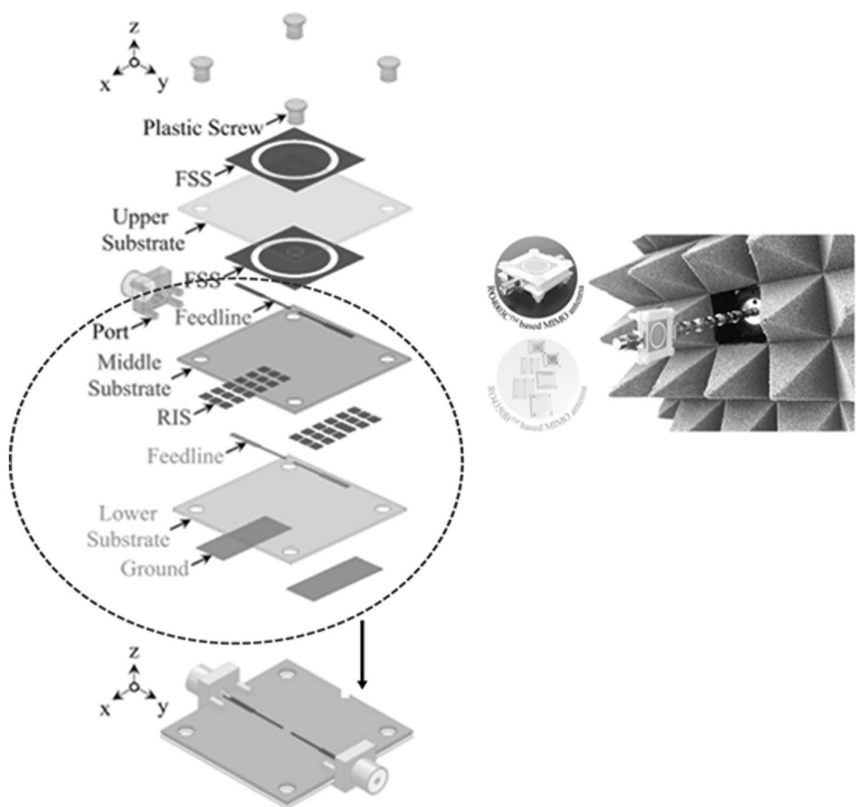


Figure 6.4 3D layout of the dual port stacked MIMO antenna and its fabricated prototype. (Source: Shahanawaz Amal, and Padmanavasan, “Microstrip-Ministered Proximity-Coupled Stacked Dual-Port Antenna for 6G Applications,” IEEE Access, pp: 2817–2829, Vol. 12, Jan 2024 [4].)

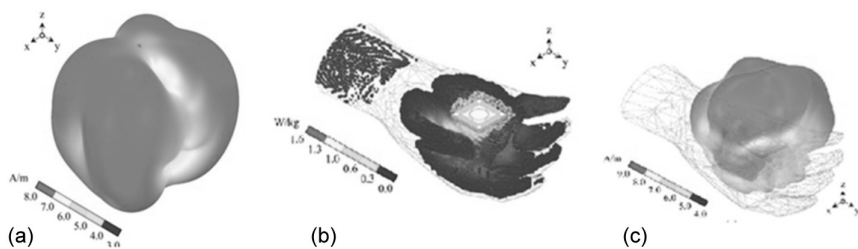


Figure 6.5 (a) 3D radiation pattern of proposed stacked MIMO antenna (quasi-omnidirectional), analysis of (b) SAR and (c) radiation pattern with human hand at 12 GHz. (Source: Shahanawaz Amal and Padmanavasan, “Microstrip-Ministered Proximity-Coupled Stacked Dual-Port Antenna for 6G Applications,” IEEE Access, pp: 2817–2829, Vol. 12, Jan 2024 [4].)

applications, wide bandwidth is an essential requirement for the improved processing of echo signals in the time-domain, along with high gain and directivity for improved wave penetration in different mediums. The stacked antennas can be used in such applications, where volume is not a constraint. A probe-fed dual-band antenna design is demonstrated in [14], operating in Ka- and Ku-bands. The two antennas are integrated vertically in the same design, with one being an aperture-coupled stacked antenna and the other being a printed dipole antenna. An array using this dual-band antenna is used to scan the antenna beam in different directions with a range from -45° to $+45^\circ$ with a step of 15° . To achieve this, an array element of four aperture-coupled stacked antennas with the dipole antenna arranged at their centre is used to make an array of 208 elements. The array and single antenna elements along with the radiation patterns of the proposed antenna are shown in Figure 6.6. This antenna array can find applications in remote sensing, radar detection, and other communication applications too.

Along with applications in radar detection, these stacked antennas can be used as transceivers in the microwave imaging set-up. Microwave imaging of unknown targets can be carried out by processing the echo signal received from the target placed in the area under scanning. Stacked antennas, especially printed stacked antennas, are a good candidate for such usage. The stacked antenna application in microwave imaging will be discussed in detail in Chapter 7. Biomedical imaging is also an emerging field where such antennas are quite useful owing to their printed and compact geometry. A cavity-backed aperture-coupled stacked antenna is deployed in a microwave imaging set-up for breast-cancer detection [15].

6.4.5 Application of stacked microstrip antennas in RF energy harvesting

RF energy harvesting is a new research area these days due to the huge usage of RF energy every day. This presence of RF energy is further going to increase with more and more IoT systems coming into place. Therefore, utilizing the available RF energy by extracting it in between the nodes and storing it for further applications can be quite useful. Stacked antennas can be used in the transmitter and receiver nodes of IoT systems to improve the transmitted signal strength and data rates owing to their better bandwidth and gain properties [16–18].

6.4.6 Application of stacked microstrip antennas in wearable electronics

With the advent of advancements in RF technology, research on smart wearable electronics has seen an exponential rise. These wearable sensors are comprised of transceiver unit and data extraction and data processing units too to sense the actual input and respond accordingly. The wearable sensors

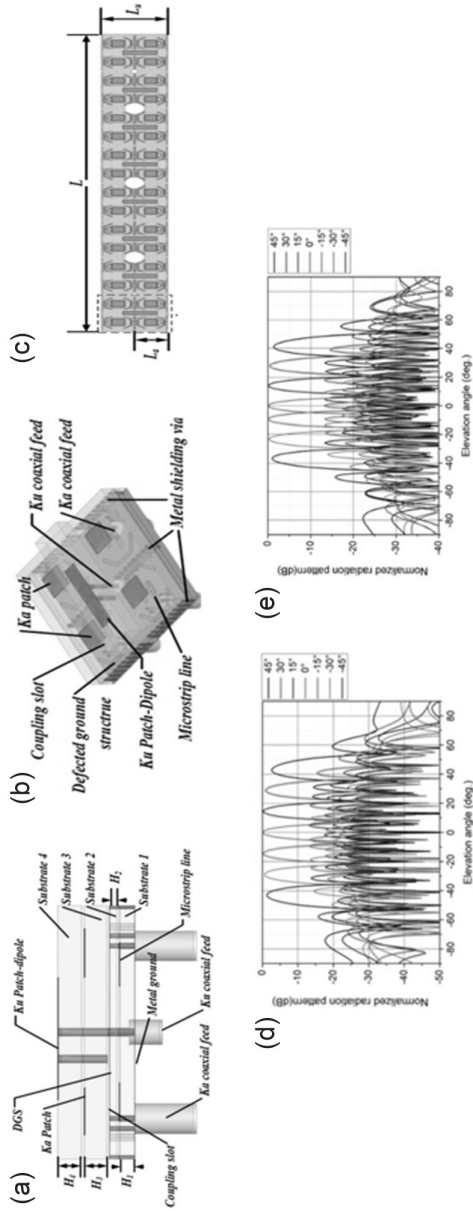


Figure 6.6 (a) Dual-band antenna side view, (b) top view of array element, (c) antenna array layout, (d) normalized radiation patterns in E-plane in Ku-band, (e) normalized radiation patterns in E-plane in Ka-band. (Source: Shengying Liu, Kaibo Jiang, Guobing Xu, Xumin Ding, Kuang Zhang, Jiahui Fu, and Qunwu, "A Dual-Band Shared Aperture Antenna Array in Ku/Ka-Bands for Beam Scanning Applications", IEEE Access, Vol. 7, pp: 78794–78802, June 2019 [14].)

should be made as compact and light-weight as possible and planar too to be easily printed on the flexible substrate/textile. The printed stacked antennas are again a good fit for this particular application owing to their compact printed geometry, and also good bandwidth and gain response. In [19–22] some of the stacked antennas used in wearable electronics are described. In [21] a triple-mode circular stacked patch antenna design is proposed which can provide pattern diversity when excited by three different ports. A simple via-loaded circular patch is printed on the lower substrate and the air-separated upper substrate contains a modified E-shaped upper patch, on both sides of the upper substrate. The E-shaped patch is also circular in design. The upper substrate in this case has different modified E-shaped patches printed on both of its sides, such that both E-slots are orthogonal to each other. The lower circular patch is fed at the centre via a coaxial probe feed, while the upper patches are fed via two orthogonal probes along the x - and y -axes to obtain orthogonal dual-polarization of the antenna. Thus, the antenna exhibits vertical polarization due to the lower patch, and dual horizontal polarization due to the upper patch. This stacked antenna is then tested for on- and off-body communications and is proven to be useful for both these applications. The antenna performance remains almost stable when tested in the presence of the human body. In [22] a printed modified stacked yagi antenna design is proposed which achieves a high gain of about 11 dBi with a bandwidth of 18% in mm-wave frequency band and unidirectional radiation patterns across the operating band. The antenna performs well for off-body communication of wearable devices.

6.5 DIRECTION FINDING AND LOCALIZATION WITH STACKED MICROSTRIP ANTENNAS

Stacked antenna advantages and potential applications are discussed in previous sections in this chapter. Their utility for several advanced applications has been highlighted. One of the important applications of stacked antennas is remote sensing where higher antenna gain is an essential requirement to combat through-the-wall or through-the-medium losses in the case of a hidden target. Target localization is achieved through the scanning of areas under observation from different angles. Received signals from different angles contain information about the target's presence. The processing of the received signal provides the target's location. To achieve this, the transmitter antenna should have a higher gain to penetrate the dielectric medium in the case of a hidden target, while increasing the detection range in the case of both open and hidden targets. Further, wide bandwidth is an essential parameter as the time-domain pulse becomes narrower and the extraction of the echo signal is improved. This increases the accuracy of target detection and localization.

The above discussion makes the requirement of transmitter and receiver antennas clear for target detection and localization: they should have

higher gain and wider bandwidth as an essential requirement. The stacked antennas with both these features are a suitable candidate for this particular application as proposed in [23–25]. Along with these properties, a unidirectional radiation pattern is an added advantage in the case of target detection, as the entire energy can be focused in the direction of the target only and the system can reject the backside noise too. The printed stacked antennas have unidirectional radiation patterns owing to the planar ground plane and they also find ease of integration with other circuits of the system, making them quite suitable for target detection and localization.

For target finding/tracking, the region under test needs to be scanned. This can be done either by moving the transmitter and receiver unit or by using the beamforming technique. Through the beamforming technique, the region under test can be scanned by changing the direction of the radiated beam of the transmitter antenna and coherently aligning the radiation pattern of the receiver. This beamforming can be achieved in the case of advanced antenna arrays [26], with the capability of altering the phase relationship between consequent antenna array elements and thus changing the direction of antenna array radiation.

6.6 FUTURE OUTLOOK FOR STACKED MICROSTRIP ANTENNAS IN 5G/6G COMMUNICATION

As discussed in Section 6.4, there are numerous potential applications of stacked microstrip antennas as they are compact antennas with improved bandwidth and gain, compared to single-layer antennas. Printed stacked antennas combine the benefits of stacking configuration with those of printed antennas which are compact and planar in geometry. The future applications are many for these antennas due to several advantages, apart from the increase in volume due to stacking, compared to one-layer printed antennas. Future wireless communication operation in 5G/6G bands requires compact and wide bandwidth antennas to be used in mobile handsets or other compact devices, where high data rates are an essential requirement. The stacked antennas for future 5G/6G communication are reported in [27–31].

In [29], a different type of stacked antenna design is proposed, where two different driven patches are designed, operating at different frequencies, i.e. X- and Ku-band. The antenna structure consists of one Ku-band patch at the centre and two X-band patches on either side of it at the driven layer. The superstrate consists of parasitic patches shared by all three driven patches. This dual-band stacked antenna, when excited with different ports, provides different polarizations. This stacked antenna is then used to make an array, useful for MIMO applications. In [32], a stack-up antenna-in-package design is proposed, with multiple metallic and dielectric layers and a patch loaded on the upper-most layer. The patch is capacitively fed through two orthogonal T-shaped feed lines to achieve circular polarization. Defected

ground structures are introduced beneath the patch, across the two sides of the patch placed symmetrically about it, to improve port-to-port isolation between two ports. The antenna has a wide bandwidth of 26.5–29.5 GHz in the mm-wave frequency band. An array of 4×4 elements is made using the designed antenna element to be used in MIMO applications, with high gain of 17.37 dBi in array configuration. The antenna array is capable of beam steering as well. The proposed antenna-in-package layout of a single element is shown in Figure 6.7, while its array layout is depicted in Figure 6.8. The S-parameter response for both ports is shown in Figure 6.9.

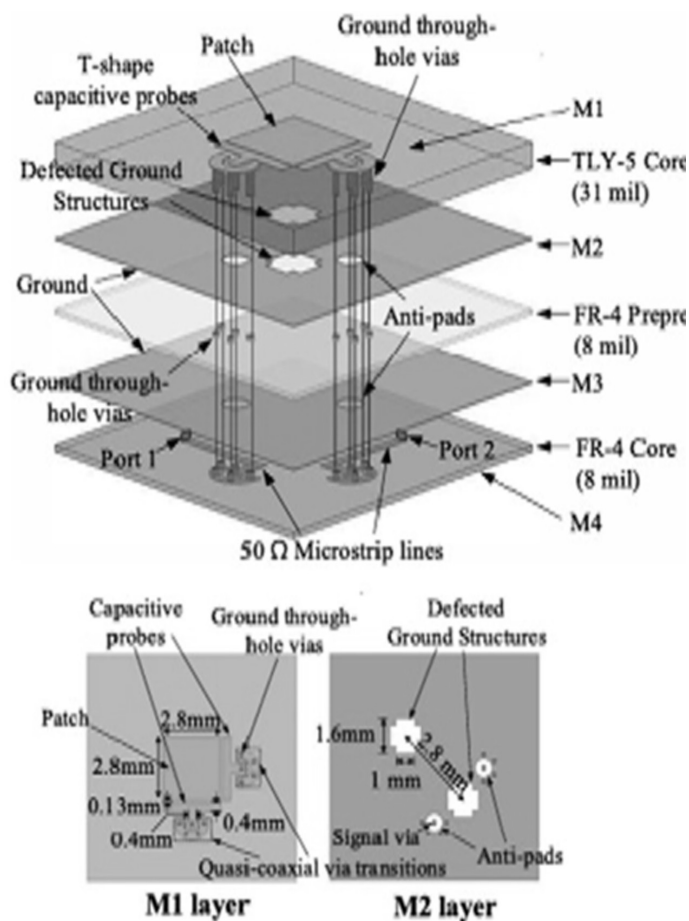


Figure 6.7 3D layout of the dual polarized mm-wave antenna-in-package and its top view with dimensions. (Source: Woojin Kim, Jihoon Bang, and Jaehoon Choi, “A Cost-Effective Antenna-in-Package Design With a 4 Dual-Polarized High Isolation Patch Array for 5G mm-Wave Applications”, IEEE Access, Vol. 9, pp: 163882–163892, 2021 [32].)

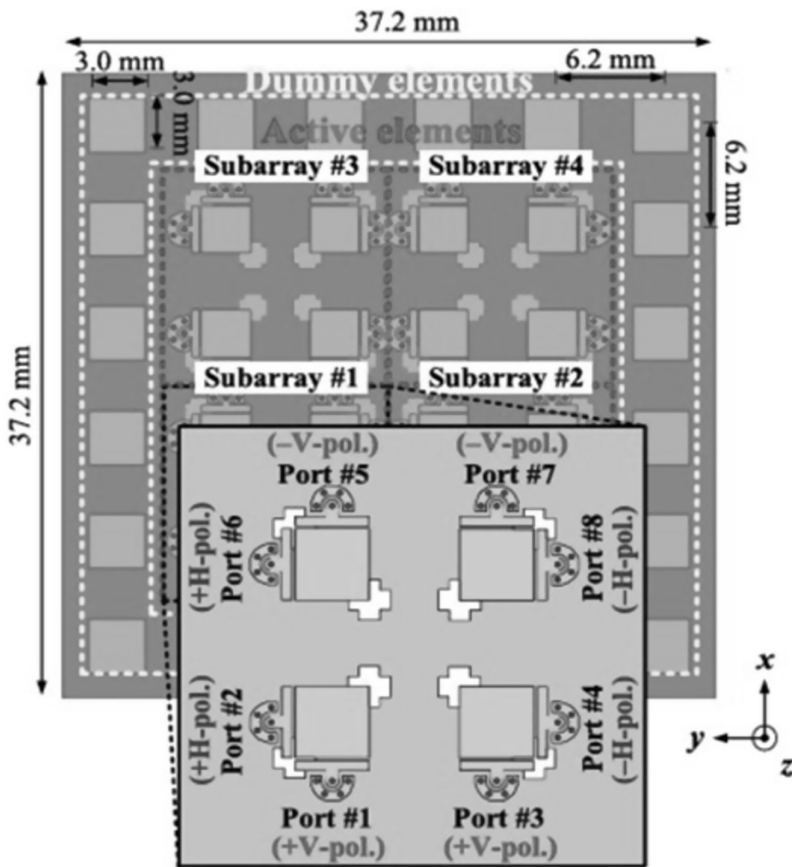


Figure 6.8 Layout of 4×4 array of the proposed dual polarized mm-wave antenna-in-package. (Source: Woojin Kim, Jihoon Bang, and Jaehoon Choi, "A Cost-Effective Antenna-in-Package Design with a 4 Dual-Polarized High Isolation Patch Array for 5G mm-Wave Applications", IEEE Access, Vol. 9, pp: 163882–163892, 2021 [32].)

6.7 APPLICATION OF STACKED ANTENNAS IN MICROWAVE/MM-WAVE IMAGING

Microwave/mm-wave imaging is a tool for non-destructive sensing of the area under interrogation and is helpful for hidden target detection as well as imaging. An image of the unknown target is obtained by processing the signal received from the target in the form of scattered/reflected/diffracted waves. When the transmitted electromagnetic waves hit the target, they are either reflected or scattered or sometimes diffracted by the target edges. These edges are the target boundaries and when the signal scattered from these angles is processed from different angles, information about its geometry can be

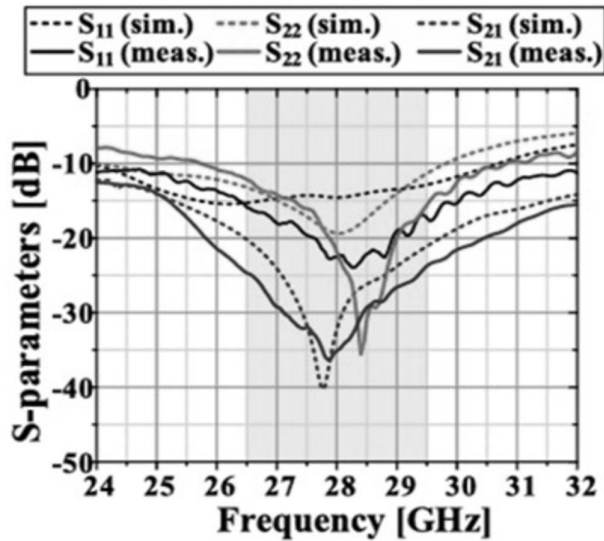


Figure 6.9 S-parameters of proposed dual-polarized mm-wave antenna-in-package. (Source: Woojin Kim, Jihoon Bang, and Jaehoon Choi, "A Cost-Effective Antenna-in-Package Design with a 4 Dual-Polarized High Isolation Patch Array for 5G mm-Wave Applications", IEEE Access, Vol. 9, pp: 163882–163892, 2021 [32].)

extracted. When the transmitted signal has a frequency in microwave/mm-wave bands, the imaging technique is called microwave/mm-wave imaging. The advantage of these frequency bands is that the signal's penetration depth in the dielectric medium is better due to the larger wavelength compared to high-frequency signals. Also, these microwave/mm-wave signals are more robust towards the weather conditions. Further, another major advantage is these waves are non-ionizing and thus safe for human body sensing.

The major requirement of the imaging system is a transceiver unit that will illuminate the target and then process the received signal. An important component of a transceiver unit is the transmitter/receiver antenna. The important antenna properties needed for imaging are similar to target detection, i.e. wide bandwidth and high gain. In the case of imaging, the wider the bandwidth of the illuminating signal, the finer the pixel of the reconstructed target image. To meet these requirements, stacked antennas are a good choice. A stacked microstrip antenna used as a transceiver unit in the imaging system is proposed in [25]. This reported work presents how the printed microstrip stacked antennas can fulfil the requirements of microwave imaging systems, along with an added advantage of being miniaturized. These transceivers are quite compact and have planar geometry too. By integrating these antennas with the other circuit elements of the microwave imaging system, the whole set-up can be employed as an

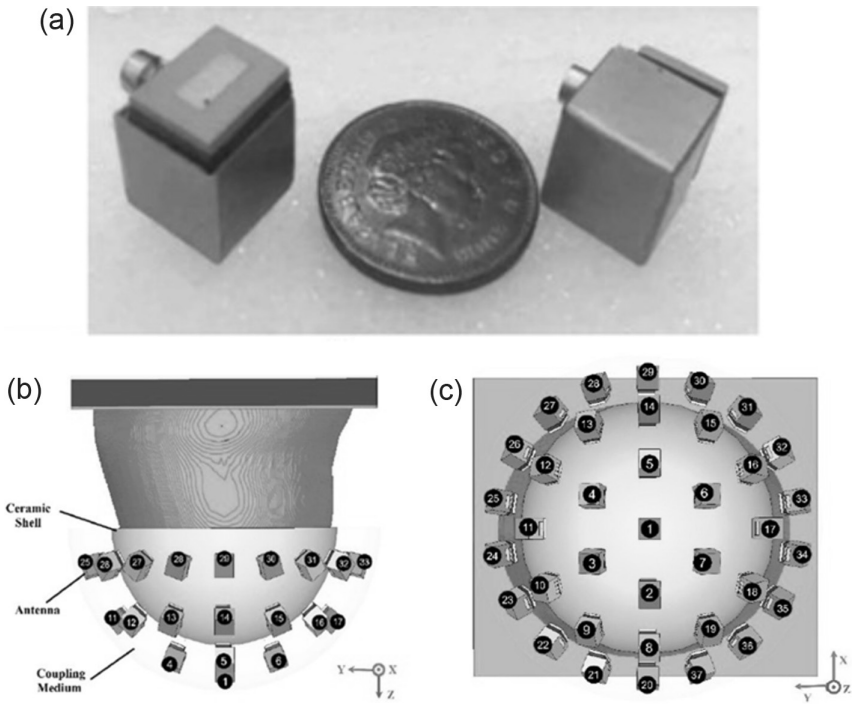


Figure 6.10 (a) Cavity-backed aperture-coupled stacked antenna fabricated prototype, and its deployment for breast-cancer scanning (b) side view, (c) top view. (Source: Mehdi Mehranpour, Saughar Jarchi, Asghar Keshtkari, Ayaz Ghorbani, Ali Araghi, Okan Yurduseven, and Mohsen Khalily, "Robust Breast Cancer Imaging Based on a Hybrid Artifact Suppression Method for Early-Stage Tumor Detection", IEEE Access, Vol. 8, pp: 206790–206805, 2020 [33].)

inconspicuous system for target identification in the case of suspicious hidden targets. Similarly, these antennas can find application in high resolution millimetre-wave imaging. Further, they are used in biomedical imaging owing to the non-ionizing nature of the waves in microwave and mm-wave bands [33, 34]. The details of stacked antennas' application in microwave imaging systems are discussed in Chapter 7. The cavity-backed aperture-coupled stacked antennas and their deployment in microwave imaging set-up for breast-cancer detection is shown in Figure 6.10. The obtained images are shown in Figure 6.11.

6.8 SUMMARY

This chapter provides a thorough discussion of the advantages and limitations of stacked microstrip antennas. Owing to their structural and

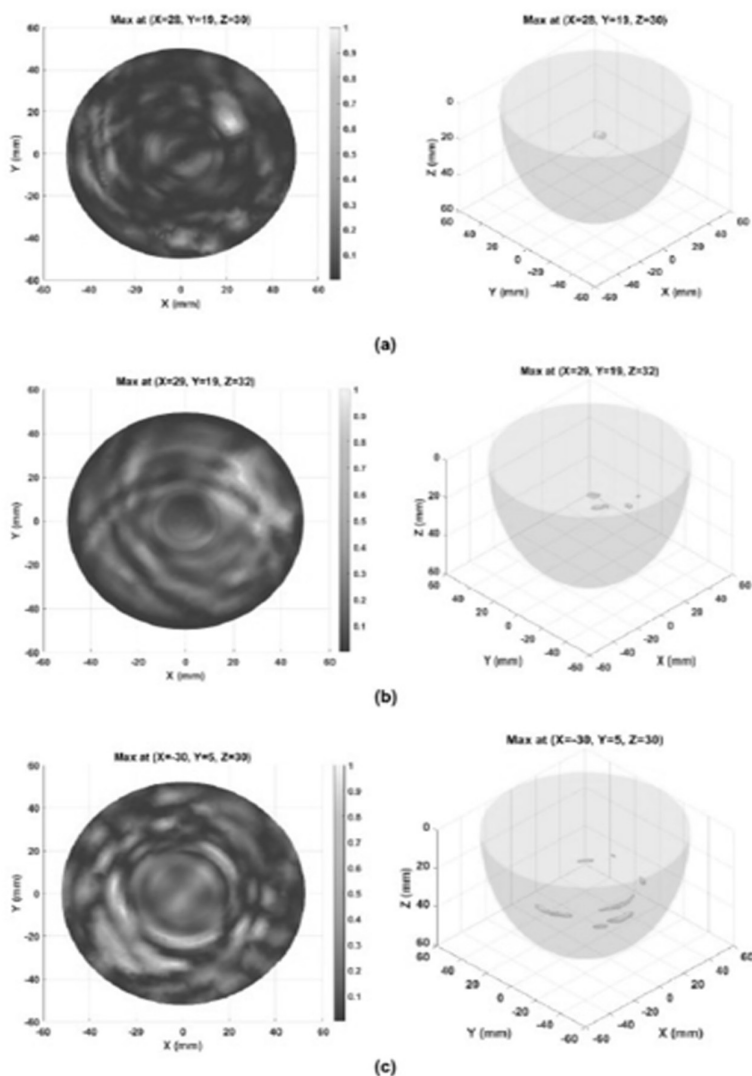


Figure 6.11 Microwave imaging results of the proposed imaging set-up deploying cavity backed aperture-coupled stacked antenna. (Source: Mehdi Mehranpour, Saughar Jarchi, Asghar Keshtkari, Ayaz Ghorbani, Ali Araghi, Okan Yurduseven, and Mohsen Khalily, "Robust Breast Cancer Imaging Based on a Hybrid Artifact Suppression Method for Early-Stage Tumor Detection", IEEE Access, Vol. 8, pp: 206790–206805, 2020 [33].)

operational advantages, these compact antennas are used in a variety of applications. In this chapter, most of the recent and advanced applications of such planar, low-profile, and broadband antennas are covered in detail. The chapter further delved into the potential application of these miniaturized broadband stacked microstrip antennas in microwave imaging systems, direction finding and localization, and future 5G/6G applications.

REFERENCES

1. Philip Ayiku Dzagbletey, and Young-Bae Jung, "An omnidirectional multilayer metasurface antenna for 2G, 3G, 4G and 5G applications", *IEEE Antennas Wirle. Propag. Lett.*, Vol. 17, No. 5, pp:780–783, May 2018.
2. Jaebaek Jung, Woojun Lee, Gyuha Lee, Songcheol Hong, and Jungsuek Oh, "Ultra-thinned metasurface-embedded smartphone antenna-in-package for millimeter-wave 5G/6G coverage enhancement", *IEEE Trans. Antennas Propag.*, Vol. 71, No. 10, pp:7766–7781, October 2023.
3. Yuqi He, Sihan Lv, Luyu Zhao, Guan-Long Huang, Xiaoming Chen, and Wei Lin, "A compact dual-band and dual-polarized millimeter-wave beam scanning antenna array for 5G mobile terminals," *IEEE Access*, Vol. 9, pp:109042–109052, August 2021.
4. Shahanawaz Amal, and Padmanava Sen, "Microstrip-ministered proximity-coupled stacked dual-port antenna for 6G applications," *IEEE Access*, Vol. 12, pp:2817–2829, January 2024.
5. Tuan Dao, Andrew Kearns, David Reyes Paredes, and Gernot Huebe, "Wideband high-gain stacked patch antenna array on standard PCB for D-band 6G communications," *IEEE Antennas Wirel. Propag. Lett.*, Vol. 23, No. 2, pp:478–48, February 2024.
6. Amir Reza Dastkhosh, Mehdi Naseh, and Fujiang Lin, "*K/Ka Slotted Stacked Patch Antenna and Active Array Antenna Design for a 5G/6G Satellite Mobile Communication System*", IEEE 2021 13th Global Symposium on Millimeter-Waves & Terahertz (GSMW), May 2021.
7. Md Hedayatullah Maktoomi, Zisong Wang, Huan Wang, Soheil Saadat, et al., "Sub-terahertz wideband stacked-patch antenna on a flexible printed circuit for 6G applications" *IEEE Trans. Antennas Propag.*, Vol. 70, No. 11, pp:10047–10061, November 2022.
8. Md Amanath Ullah, Rasool Keshavarz, Mehran Abolhasan, Justin Lipman, and Negin Shariati, "Multiservice compact pixelated stacked antenna with different pixel shapes for IoT applications", *IEEE Internet Things J.*, Vol. 10, No. 22, pp:19883–19897, 15 November 2023.
9. Sema Dumanli, "A Wrist Wearable Dual Port Dual Band Stacked Patch Antenna for Wireless Information and Power Transmission", 2016 10th European Conference on Antennas and Propagation (EuCAP), April 2016.
10. Sundeep Kumar, Manoj Kumar, and Ashwani Sharma, "A compact stacked multisector near-isotropic coverage rectenna array system for IoT applications", *IEEE Micro. Wirel. Tech. Lett.*, Vol. 34, No. 1, pp:123–126, January 2024.

11. Mohammad Ali, T. M. Sayem, and Vijay K. Kunda, "A reconfigurable stacked microstrip patch antenna for satellite and terrestrial links", *IEEE Trans. Vehicular Tech.*, Vol. 56, No. 2, pp:426–435, 2007.
12. Marco Simone, Matteo Bruno Lodi, Santi Concetto Pavone, Nicola Curreli, Giuseppe Mazzarella, and Alessandro Fanti, "Optimized design and multiphysics analysis of a Ka-band stacked antenna for CubeSat applications", *IEEE J. Multiscale Multiphysics Comput. Tech.*, Vol. 6, pp:143–157, 2021.
13. Hao Xu, Zhijiao Chen, Haiwen Liu, Le Chang, Taotao Huang, Sheng Ye, Lina Zhang, and Chao Du, "Single-fed dual-circularly polarized stacked dielectric resonator antenna for K/Ka-band UAV satellite communications", *IEEE Trans. Vehicular Tech.*, Vol. 71, No. 4, pp:4449–4453, April 2022.
14. Shengying Liu, Kaibo Jiang, Guobing Xu, Xumin Ding, Kuang Zhang, Jiahui Fu, and Qun Wu, "A dual-band shared aperture antenna array in Ku/Ka-bands for beam scanning applications", *IEEE Access*, Vol. 7, pp:78794–78802, June 2019.
15. Mehdi Mehranpour, Ayaz Ghorbani, Saughar Jarchi, Asghar Keshtkar, Ali Araghi, Okan Yurduseven, and Mohsen Khalily, "Robust breast cancer imaging based on a hybrid artifact suppression method for early-stage tumor detection", *IEEE Access*, Vol. 8, pp:206790–206805, 2020.
16. Hichem Mahfoudi, Hakim Takhedmit, and Mohamed Tellache, "Dual-Band Dual-Polarized Stacked Rectenna for RF Energy Harvesting at 1.85 and 2.45 GHz", 12th European Conference on Antennas and Propagation (EuCAP 2018), April 2018.
17. Shanpu Shen, Chi-Yuk Chiu, and Ross D. Murch, "A dual-port triple-band L-probe microstrip patch rectenna for ambient RF energy harvesting", *IEEE Antennas Wirel. Propag. Lett.*, Vol. 16, pp:3071–3074, 2017.
18. Hina Yadav, Sheetal Yadav, K. P. Ray, and Mridula Gupta, "Stacked Microstrip Antennas on Thin Dielectric Substrate for Power Harvesting Applications", 2019 IEEE Asia-Pacific Microwave Conference (APMC), pp:282–284, December 2019.
19. Simone Genovesi, Filippo Costa, Filippo Fanciulli, and Agostino Monorchio, "Wearable inkjet-printed wideband antenna by using miniaturized AMC for sub-GHz applications", *IEEE Antennas Wirel. Propag. Lett.*, Vol. 15, pp:1927–1930, 2016.
20. Rui Xu, and Zhongxiang Shen, "Wearable ungrounded tag antenna for UHF RFID applications", *Commun. IEEE Trans. Antennas Propag.*, Vol. 71, No. 4, pp:3665–3670, April 2023.
21. Ke Zhang Wei Hong, Zhi Hao Jiang, and Douglas H. Werne, "A low-profile and wideband triple-mode antenna for wireless body area network concurrent on/off-body communications", *IEEE Trans. Antennas Propag.*, Vol. 68, No. 3, pp:1982–1994, March 2020.
22. Qixin Ren, Xiaoqing Zhu, Xiongying Liu, and Hongcai Yang, "Millimeter Wave Wearable Modified Yagi Antenna", 2020 IEEE MTT-S International Wireless Symposium (IWS), 2020.
23. Amran Hossain, Mohammad Tariqul Islam, Gan Kok Beng, Saad Bin Abul Kashem, Mohamed S. Soliman, Norbahiah Misran, and Muhammad E. H. Chowdhury, "Microwave brain imaging system to detect brain tumor using metamaterial loaded stacked antenna array", *Sci. Rep. Nat.*, Vol. 12, p:16478, 2022.

24. Ankita Malhotra, and Ananjan Basu, "Broadband frequency reconfigurable printed transceivers for microwave imaging systems", *Int. J. Microw. Wire. Technol.*, Vol. 15, No. 7, pp:1130–1138, September 2023.
25. Ankita A Malhotra, and Ananjan Basu, "Miniaturised Distributed Transceivers for Far-Field Microwave Imaging", 2018 IEEE MTT-S International Microwave and RF Conference (IMaRC), pp:1–4, 2018.
26. F. William, Waleed Khalil, and John L. Volakis, "60-GHz two-dimensionally scanning array employing wideband planar switched beam network", *IEEE Antennas Wirel. Propag. Lett.*, Vol. 9, pp:818–821, 2010.
27. Yue Gao, Runbo Ma, Yapeng Wang, Qianyun Zhang, and Clive Parini, "Stacked Patch Antenna With Dual-Polarization and Low Mutual Coupling for Massive MIMO", *IEEE Trans. Antennas Propag.*, Vol. 64, No. 10, pp:4544–4549, Oct. 2016.
28. Han Zhou, Ronghong Jin, Junping Geng, Xianling Liang, Weiren Zhu, and Chong He, "Design of S/Ka Dual-Band Shared-Aperture Massive MIMO Antenna Array for 5G Communication", 13th European Conference on Antennas and Propagation (EuCAP 2019), 2019.
29. Lingyu Kong, and Xiaojian Xu, "A compact dual-band dual-polarized microstrip antenna array for MIMO-SAR applications", *IEEE Trans. Antennas Propag.*, Vol. 66, No. 5, pp:2374–2381, May 2018.
30. Tian-Yu Yan, Xin-Hao Ding, Jun-Yao Yang, and Jian-Xin Chen, "A low-cost compact dual-polarized patch antenna array for 5G massive MIMO base station", *IEEE Antennas Wirel. Propag. Lett.*, Vol. 23, No. 4, pp:1381–1385, April 2024.
31. Abel Zandamela, Nicola Marchetti, and Adam Narbudowicz, "Stacked-Patch MIMO Antenna for Dual-Plane Beamsteering", 2021 IEEE International Symposium on Antennas and Propagation and USNC-URSI Radio Science Meeting (APS/URSI), December 2021.
32. Woojin Kim, Jihoon Bang, and Jaehoon Choi, "A cost-effective antenna-in-package design with a 4 4Dual-polarized high isolation patch array for 5G mm-wave applications", *IEEE Access*, Vol. 9, pp:163882–163892, 2021.
33. Mehdi Mehranpour, Saughar Jarchi, Asghar Keshtkari, Ayaz Ghorbani, Ali Araghi, Okan Yurduseven, and Mohsen Khalily, "Robust breast cancer imaging based on a hybrid artifact suppression method for early-stage tumor detection", *IEEE Access*, Vol. 8, pp:206790–206805, 2020.
34. Md. Rokunuzzaman, Md. Samsuzzaman, and Mohammad Tariqul Islam, "Unidirectional wideband 3-D antenna for human head-imaging application," *IEEE Antennas Wirel. Propag. Lett.*, Vol. 16, pp:169–172, 2017.

Stacked microstrip antennas for microwave imaging

7.1 INTRODUCTION TO MICROWAVE IMAGING

Microwave imaging is an advanced sensing technique that involves using microwave signals to analyze a given scene and detect targets or objects within it. This non-destructive method utilizes electromagnetic signals in the microwave band to interact with the objects in the scene. When electromagnetic waves, particularly microwaves, encounter changes in the medium through which they propagate, they scatter. The nature of this scattering depends on the properties of the objects being examined. Due to variations in geometry and material composition, different targets interact uniquely with microwaves, resulting in complex scattered signals that contain valuable target-related information. This information can be extracted using specialized algorithms. Unlike optical or infrared methods, microwave imaging offers the unique capability to penetrate materials like paper, cloth, and wood, while effectively capturing images of metallic and other objects that strongly scatter microwave signals. As a result, microwave imaging has significant applications in security and surveillance, particularly for the detection of concealed weapons.

The basic block diagram of the microwave imaging system is shown in Figure 7.1 [1]. The signal generator generates a microwave signal which is then given to the transmitter. The transmitter antenna illuminates the target with the incident wave, which is present in the investigation domain. The incident wave, illuminating the target, interacts with it and is scattered due to the medium change which it encounters in the path of its propagation. The basis of microwave imaging is surface and volume scattering by dielectric and conducting materials [2]. In case of metallic targets, surface currents are introduced on the target due to illumination from incident fields. These currents in turn generate electric fields normal to their surface which creates scattered fields. These scattered fields from any metallic target are much stronger than fields scattered by the dielectrics. Microwave imaging techniques can be classified as qualitative or quantitative. Qualitative imaging considers only scattering/reflection from the target to reconstruct its shape. In the case of the qualitative approach for microwave imaging, the

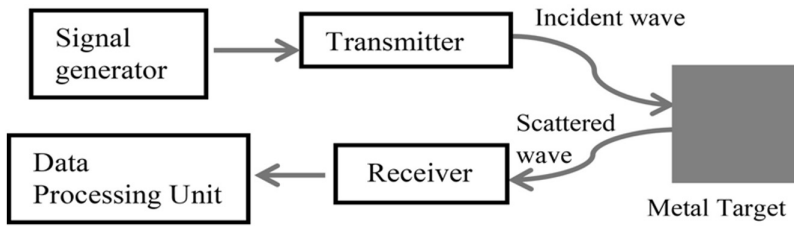


Figure 7.1 Block diagram of microwave imaging system. Reproduced with permission from IEEE [1].

problem is linear and therefore simpler in approach. Quantitative imaging on the other hand considers diffraction and scattering/reflection from the target and further maps it to the electrical and magnetic property distribution of the unknown target, along with obtaining its geometrical information. In the case of the quantitative approach, the problem is more ill-posed due to its non-linear nature, and therefore complex inversion algorithms are used to process the image from raw data.

Microwave imaging can map the dielectric contrast of the targets in the investigation domain; therefore it has been used in many biomedical applications [3–5]. Because of the penetration capability of microwaves, microwave imaging is used in hidden target detection and through-wall imaging, thus finding applications for security purposes. Hidden target detection even beneath the three-layer body model is possible and verified using triple sensors used in the microwave imaging set-up [6] and also the application of microwave imaging in the detection of concealed objects is being studied [7]. Near-field imaging is presented in [8], where a metallic strip loaded sub-wavelength aperture with dual-polarization is used to detect targets in free-space and in lossy media. The scattering phenomenon of microwaves allows the extraction of target geometry information, as the scattering property of a target depends on its structure. Image reconstruction of large metallic targets in an anechoic chamber is presented in [9] using a standard broadband horn antenna by applying the factorization method. Polarization diversity is exploited in [10] to enhance the efficiency of target classification according to the received back-scattered signals. A compressive-sensing technique can be applied to the case of non-weak targets to reconstruct the target shape [11]; also a holographic imaging approach using a phase-less radiation pattern of antenna can be applied to improve the image quality [12]. Furthermore, the imaging of a microwave absorber sample is possible using microwaves and is carried out in [13], where complex permittivity of the sample is utilized to obtain the image. This utilizes the fact that microwaves can map the dielectric losses too. Moreover, using a broadband horn antenna, microwave imaging of both the dielectric and conducting materials can be obtained [14].

7.2 CLASSIFICATION OF MICROWAVE IMAGING SYSTEMS

Microwave imaging systems can be classified into two categories: near-field imaging systems and far-field imaging systems, depending on the distance of the target from the measurement system. If a target is placed in the near-field of the transceiver unit, then the system is called a near-field imaging system, while if a target is kept in the far-field of the transceiver unit, the system is termed a far-field imaging system. In this chapter the focus will be on far-field microwave imaging only.

7.3 MICROWAVE IMAGING SYSTEM REQUIREMENTS

In imaging, the transmitter/receiver system plays an important role. It is responsible for acquiring information about the target through scattered microwaves. The transmitter sends microwave signals to illuminate the target, which are then scattered and received by the receiver. The received signal is then processed to obtain the target's image or signature. The transmitter and receiver's properties determine the quality of the image that can be achieved. The important properties of the transmitters and receivers, required for satisfactory imaging, are listed as follows:

- 1- *Radiation pattern*: For better target illumination the transmitter and receiver should have a directive radiation pattern with a high front-to-back ratio. This avoids illumination of any unwanted target at the back side of the transmitter/receiver system. A directive radiation pattern also avoids illumination of unwanted targets in the cross-range of the investigation domain.
- 2- *Bandwidth*: Wide bandwidth provides more spectral information on the target and ensures better spatial resolution.

Considering these properties, transmitter/receiver antenna selection has to be done. For these reasons, stacked microstrip antennas can be considered and implemented as transmitter and receiver in the imaging system, as they fulfil both above-mentioned criteria.

7.4 ADVANTAGES OF STACKED ANTENNAS AS TRANSCIVER UNITS IN MICROWAVE IMAGING SYSTEMS

As previously mentioned, the transmitter and receiver antennas are critical components of the imaging system, as they determine the appropriate target illumination and the reception of scattered waves. Additionally, they influence the system's overall complexity, as the rest of the circuitry is typically common in most microwave imaging systems. As detailed in earlier sections,

stacked microstrip antennas offer a broad frequency response and, due to their uninterrupted ground plane, exhibit a unidirectional radiation pattern. This characteristic significantly reduces backside clutter in the received signal or simply removes it altogether. These qualities make stacked antennas well-suited for use as the transceiver unit in a microwave imaging system. Furthermore, employing stacked microstrip patch antennas as the transceiver unit enables the imaging system to be compact, cost-effective, and easily integrated with the system circuitry. In practical applications, these antennas can be conveniently mounted on a common planar ground plane, facilitating the implementation of the scanning system. This is a better choice as compared to the scanning systems used in [15–18], where the scanning system is arranged around the target to achieve three-dimensional imaging. Such systems are more complex, bulkier, and of a fixed type, thus lacking the flexibility and ease of implementation provided by the stacked antennas.

Besides stacked microstrip patch antennas, UWB patch antennas can also be used as transceivers in the imaging system [19, 20], as they provide wide bandwidth along with reducing the system's volume and cost. However, UWB antennas are generally designed by altering the antenna's ground plane to achieve broadband response. This defect in the ground plane causes the radiation pattern to be bi-directional. The bi-directional radiation pattern of an antenna can introduce noise in the received signal due to back-side clutter. Therefore, such systems must be placed in an anechoic chamber, thus reducing the practical applicability of the imaging system.

7.5 MICROWAVE IMAGING MEASUREMENT SET-UP

The upcoming discussion will focus on qualitative microwave imaging. The synthetic aperture focusing technique has been employed to scan the area of interest containing the target. Subsequently, the processing is carried out using the SAR algorithm with an emphasis on target detection and shape reconstruction. In the measurement set-up, transceiver units are positioned in front of the target domain for interrogation. A dedicated source and data acquisition unit is essential for data collection and processing in the imaging set-up. If necessary, a vector network analyzer can serve as both the source and the data collection unit. If utilizing a vector network analyzer, it must be calibrated for the operating range of the transceiver antennas to eliminate cable loss and system errors. The measurement set-up for microwave imaging systems can be mainly of two types:

- i) 3D scanning measurement set-up
- ii) 2D scanning measurement set-up

A 3D scanning set-up is presented in [15, 16], where transceiver units are arranged three-dimensionally, around the target under observation. The

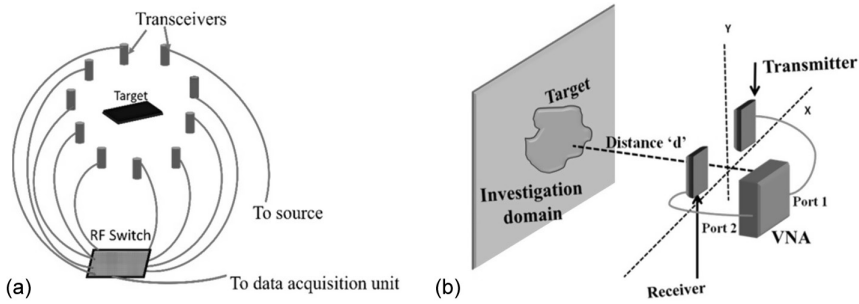


Figure 7.2 Scanning set-ups for microwave imaging, a) 3-D scanning measurement set-up, b) 2-D scanning measurement set-up.

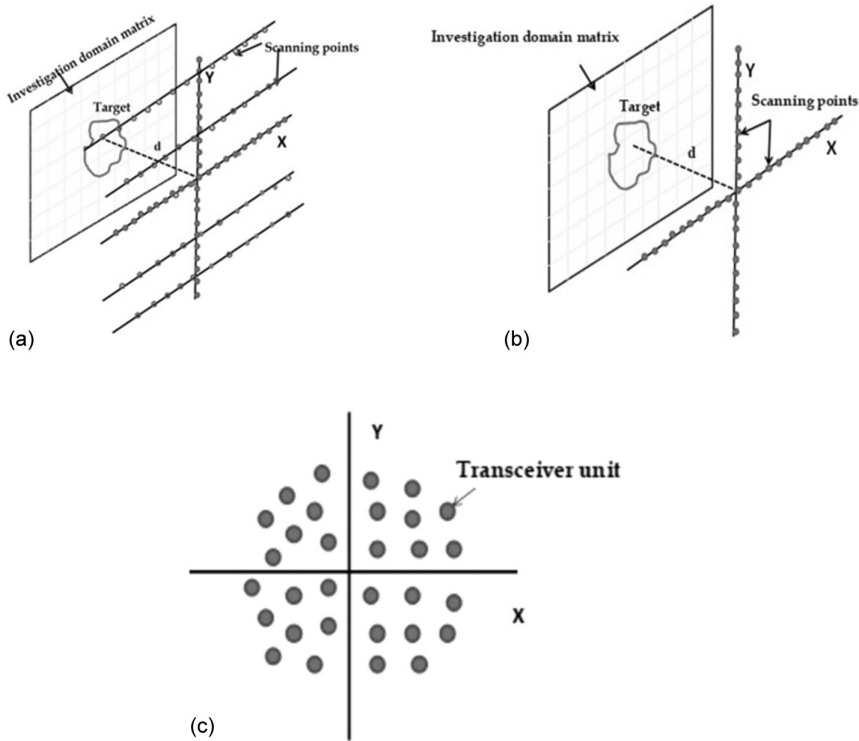


Figure 7.3 Different possible 2D scanning set-up scenarios, a) 2-D rectilinear scanning, b) 2-D scanning along 2 axes, c) Randomly distributed sensors for 2-D scanning.

block diagram of the set-up is depicted in Figure 7.2(a). A 2D scanning set-up has transceivers arranged only at one side of the target, arranged two-dimensionally in the plane parallel to the plane of the target shown in Figure 7.2(b). Further, different types of 2D scanning set-ups are shown in Figure 7.3.

Scanning is done two-dimensionally to ensure proper illumination of the target from all the view angles in a plane. A bistatic system is employed with one transmitter and one receiver acting as a trans-receiver unit. There are interesting possibilities for developing improved systems using a multi-static approach as presented in [21], where antenna arrays are used as transceivers, but these have not been considered here as the aim is to develop a compact and inconspicuous imaging system. Further, a multi-static system will also require phase locking of physically separated sensors, which is difficult to implement. Microwave imaging with distributed transmitters is presented in [22].

7.6 SAR ALGORITHM FOR 2D SCANNING

The target is scanned two-dimensionally using a synthetic focusing technique to capture its 2D image. This technique is commonly used in radar systems for illuminating ground targets by moving aircraft. In this method, the transceiver unit in the aircraft illuminates the target from different positions and captures signals from the targets while passing them.

The electric field produced by the source illuminates the cross-section of the target. This incident electric field induces electric current on the surface of the target, which in turn creates a scattered electric field. The interaction of this field with the target's cross-section is responsible for the scattered field, which contains the information about the target. The evaluation of scattered fields yields information about the target's properties, like its geometry, material property, location, etc. Let $E_{\text{inc}}(r)$ be the incident electric field. The total electric field is given by

$$E(r) = E_{\text{inc}}(r) + E_{\text{scat}}(r) \quad (7.1)$$

There are numerous techniques available for evaluating $E_{\text{scat}}(r)$, in a given scenario as discussed in [2]. The scattered field is received by the receiver placed at the other end of the target. If a dedicated source and data acquisition system are not available, the vector network analyzer (VNA) can be connected to the transmitter and receiver at both ports. The S-parameters of the received signal can be extracted from the VNA. In this case, the signal sent out from port 1 is proportional to E_{inc} , while the signal received at port 2 is proportional to E_{scat} , partially corrupted by signal leaking directly from port 1 to port 2. S21 parameters for different locations of the transceiver unit are captured and collected, which will be then processed through MATLAB®. The received frequency-domain S21 signal is first converted to its time-domain form using IFFT given by Equation (7.2).

$$S(t) = \frac{1}{2\pi} \int_{-\infty}^{\infty} S(f) * e^{j\omega t} d\omega \quad (7.2)$$

$$S_0(t) = S(t) - S'(t) \quad (7.3)$$

To mitigate the influence of stationary objects in the vicinity, such as fixed surroundings or support systems for heavy targets, it is essential to obtain and subtract the time-domain signal in the absence of the target from the signal received when the target is present in the scene. Thus according to Equation (7.3), $S_0(t)$ is the signal without the effect of a support system and other stationary objects in the nearby environment, where $S'(t)$ is the received signal in the absence of the target (time-domain signal), from the nearby objects that are not of interest, and also from the target's support system.

The signal-to-noise ratio of signal $S_0(t)$ can be further improved by applying an averaging filter to it. This results in signal smoothening, which leads to a further reduction of noise in the signal. The filter used here is Savitzky–Golay filter, which works on least-squares polynomial fitting on a small number of data points at a time. It considers a set of data points, called filter length, where an analytical solution to the least-squares equation can be found, in the form of a single set of convolution coefficients at the centre point of each set [23]. For filter length $2k + 1$, where the filter length varies from $-k$ to k with origin at centre, the smoothed data point is given by Equation (7.4):

$$(s_q)_s = \frac{\sum_{i=-k}^k A_i * s_{q+i}}{\sum_{i=-k}^k A_i} \quad (7.4)$$

A_i represents the coefficients of the polynomial. The value of the polynomial is evaluated at centre as discussed before. Here S_q represents the dataset of the original signal while $(S_q)_s$ represents the dataset of the smoothened (averaged) signal. According to the chosen filter length, the signal undergoes a corresponding level of smoothening/averaging. For the targets, which require high resolution in their geometry, a smaller filter length is better so as not to lose any information embedded in the signal. For large targets or targets with a geometry requiring minimum resolution, a larger filter length is a better choice to remove the noise from the signal, thus improving its signal-to-noise ratio. The filter order represents the polynomial order which has to be chosen properly. Here a third-order filter is chosen, as according to [24] the third order is the most suitable for small filter lengths. The filtered signal then undergoes time-windowing to remove any undesired data from the signal, given by Equation (7.5). This is also called the time-gating phenomenon, where the signal is captured for a dedicated

time duration only and the rest of the signal is rejected. This process rejects the direct signal coming directly from the transmitter and also the signal due to neighbouring objects (if the experiments are carried out in a real-life environment).

$$S_o'(t) = \int_{\tau_1}^{\tau_2} S_o(t) d\tau \quad (7.5)$$

The signal $S_o'(t)$ now represents only the signal due to the target, rejecting all the other data in the signal. The absolute value of the time-domain signal is considered. The range of τ_1 – τ_2 represents the duration of the echo signal from the target; thus the values of τ_1 and τ_2 always lie in the range of the rise and fall time of the echo signal only. These values may need to be slightly varied/optimized to capture only the desired signal. The data processing done on the received scattered waves is shown in Figure 7.4. The Figure 7.4(a) shows the received signal in the frequency domain, i.e. S21 in this case of a bistatic system. However, the received signal in the time-domain is depicted in Figure 7.4(b). The absolute value of the time domain signal is given in Figure 7.4 c), while Figure 7.4(d) shows the smoothened/averaged signal obtained after applying the Savitzky–Golay filter along with time-gating.

7.6.1 Image reconstruction

The process of forming the target image involves using a simplified synthetic aperture radar (SAR) approach. The region under investigation is depicted by a two-dimensional matrix $M(q \times q)$ that contains the target, with “ q ” representing the length of the matrix. The fundamental principle behind image reconstruction lies in assigning higher values of received signal intensity to the matrix cells that encompass the target compared to those that do not. The signal scattered and received by the receiver carrying the target echo is processed using the algorithm detailed in the previous section. Subsequently, the processed data is utilized to populate the matrix cells in accordance with Equations (7.6)–(7.9). Let the signal described by Equation (7.5) in its discrete form be written as:

$$S(n)' = [x(n1), x(n2), x(n3), \dots, x(ni)] \quad (7.6)$$

The amplitude vector and time vector of the signal are given by:

$$A(n)' = [a(n1), a(n2), a(n3), \dots, a(ni)] \quad T(n)' = [t(n1), t(n2), t(n3), \dots, t(ni)] \quad (7.7)$$

where $T(n)$ lies in the range $\tau_2 - \tau_1$.

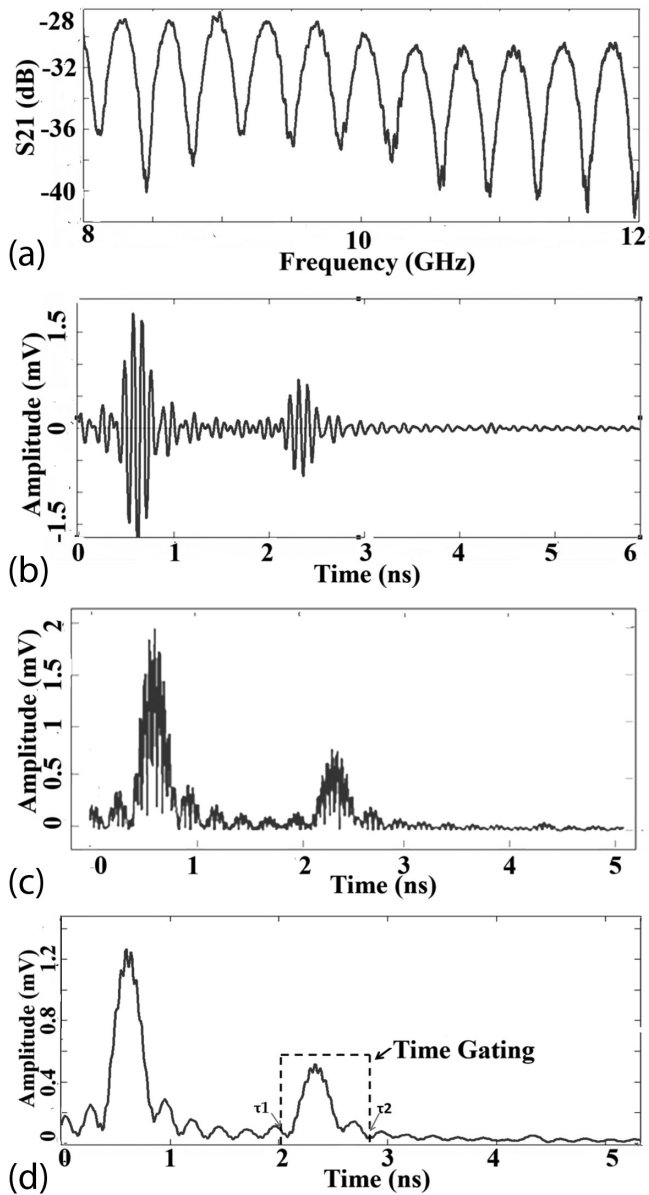


Figure 7.4 Data processing, (a) scattered signal in frequency-domain received by X-band waveguide antenna, (b) time-domain scattered signal obtained after IFFT, (c) absolute value of time-domain signal, (d) smoothed signal after applying Savitzky-Golay filter and applying time-gating to it. Reproduced with permission from IEEE [1].

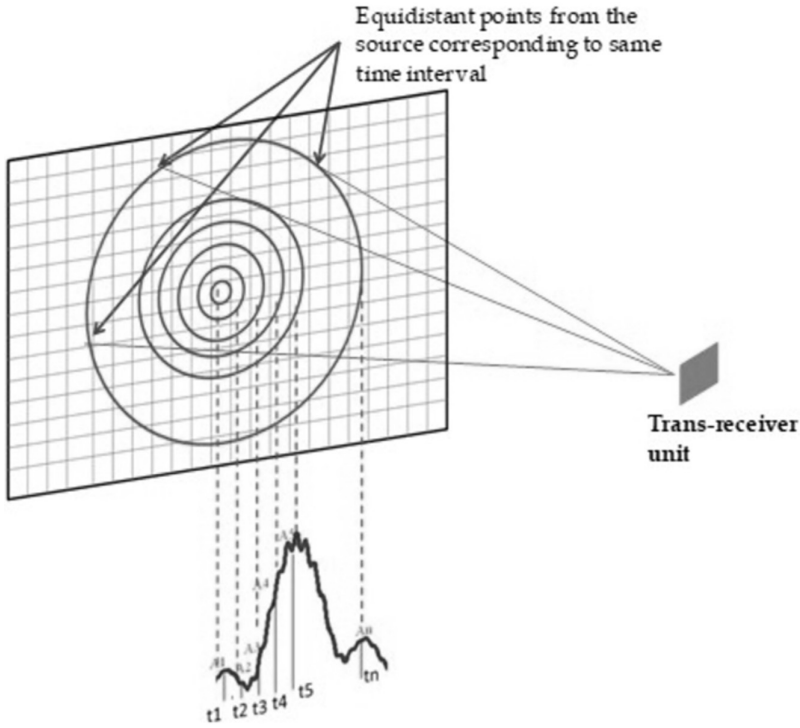


Figure 7.5 Matrix formation using processed data for image formation.

Then the matrix $M(q \times q)$ is filled such that for any cell $M(l, m)$ of the matrix (where l is the position of the cell in the x -axis, while m is the position of the cell in the y -axis from the centre of the matrix); for any j^{th} position of the sensor is:

$$M_j(l, m) = S(t_{l, m}) \quad (7.8)$$

Here $S(t_{l, m})$ is the value/amplitude of signal at time $t(l, m)$.

$$t(l, m) = 2 * D / c \quad (7.9)$$

where D = distance between the j^{th} sensor with location $(x_j, y_j, z = 0)$ and the cell $(l * \Delta x, m * \Delta y, z = d)$; Δx and Δy are the dimensions of each unit cell.

Here, $t(l, m)$ is not unique to a particular cell $M(l, m)$; rather it will be the same for all the cells that lie on a circle passing through $M(l, m)$. This is so because all these cells will be equidistant from the transceiver unit

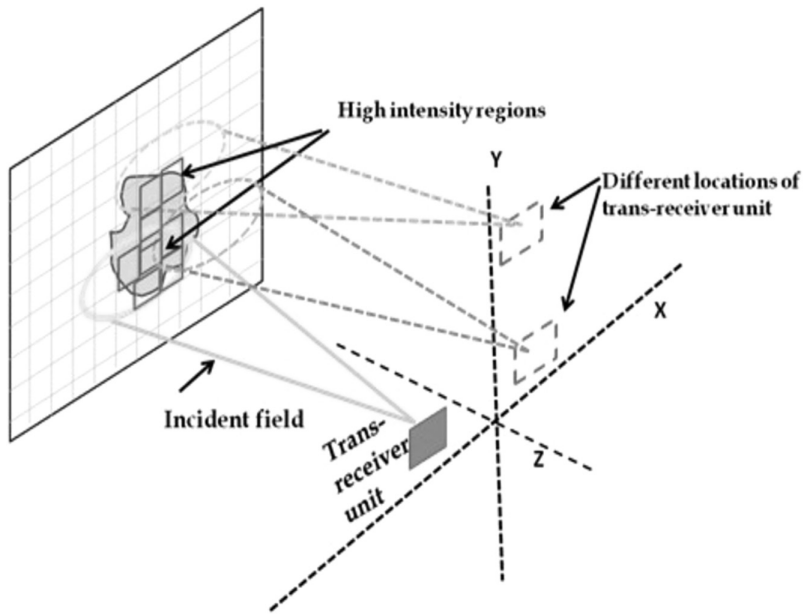


Figure 7.6 Illumination of target from different scanning locations.

(for a given location) and the time of flight for all of them will be equal. Further, it should be noted that the least/initial time of the echo signal $t(n1)$ corresponds to the matrix cell exactly perpendicular (aligned) to the transceiver unit, as it is at the shortest distance from the transmitter, while the maximum time $t(ni)$ corresponds to the scattering from the farthest point or the corner of the target. The matrix formation is shown in Figure 7.5. Let the centre of the investigation domain/matrix be aligned with the trans-receiver unit for the first scanning position (i.e. at the origin of the transceiver unit); then $t(n1)$ and $a(n1)/S(t_1)$ will correspond to the centre of the matrix. Similarly, for other scanning positions, the centre of the intensity circles shifts equivalent to the shift in the trans-receiver (along the “x”- and “y”-axes). Thus, a square matrix $M_j(q \times q)$ is obtained for each j^{th} scanning location, where q is the number of cells (often called pixels) along the “x”- and “y”-axes of the investigation domain.

Figure 7.6 shows that the high intensity regions seem to be distributed in each matrix (for different sensor location) along the circle. These matrices for different scanning locations are then added as given by Equation (7.10), which gives a localized high intensity region corresponding to the presence of the target, as the intensity at cells containing the target is added constructively, thus highlighting the target region.

$$M_T(q \times q) = \sum_{j=1}^p M_j(q \times q), p = \text{total number of scanning positions} \quad (7.10)$$

Several regularly and irregularly shaped objects are being used as targets to validate the imaging process and the reconstructed images are shown in the upcoming sections.

7.6.2 Resolution in range and cross-range in 2D scanning

The resolution achieved in the range and cross-range of the investigation domain mostly depends on antenna bandwidth and centre frequency along with other factors. The resolution factors considered are as defined in [25], and are given by Equations (7.11) and (7.12) as R (range resolution) and CR (cross-range resolution). Here k is the wave number at the respective frequency, D is the range of the target from the T/R module, L is the half-length of scanning axes, and θ_1 is the angle of illumination. Here it is considered as 0° .

$$R = \frac{2\pi}{2(k_2 - k_1)} \quad (7.11)$$

$$= \frac{c}{2(f_2 - f_1)}$$

$$CR = \frac{2\pi D}{4k_c L \cos(\theta_1)} \quad (7.12)$$

$$= \frac{cD}{4f_c L \cos(\theta_1)}$$

The above-mentioned equations show that range resolution is bandwidth dependent, while cross-range resolution is dependent on centre frequency keeping other parameters constant. Thus, different cross-range resolutions will be achieved for different operating bands, as will be seen in upcoming sections.

7.7 MULTIBAND STACKED MICROSTRIP ANTENNAS AS TRANSCEIVERS IN MICROWAVE IMAGING SYSTEM

As discussed earlier, stacked microstrip antennas, being planar, compact, and broadband compared to a basic patch antenna, can be easily used in microwave imaging applications to keep the overall system compact. To achieve better image resolution compared to UWB antennas, stacked

microstrip antennas operating at different frequency bands can be used, to obtain more spectral information of the target in different bands. As a case study proposed here, stacked antennas designed at two microwave frequency bands, i.e. X-band and C-band, are used. The targets chosen for imaging are different types of real-life metallic objects, placed in an open real environment. This will help validate the image reconstruction algorithm for real-life scenarios. Additionally, imaging also extends to objects concealed behind dielectric mediums, carried out across different frequency regions. Due to the substantial difference in wavelengths between the two frequency bands chosen in the present case, the resolution and penetration capabilities vary. In essence, higher frequencies provide better resolution, while lower frequencies offer superior penetration. The proposed work examines this phenomenon through a series of experiments conducted across different frequency bands. The insights gained from these experiments can be integrated to enhance target detection and geometry estimation.

7.7.1 Microwave imaging set-up comprised of X-band stacked antenna

Two X-band stacked antennas are employed in the proposed bistatic microwave imaging set-up, acting as a transmitter and a receiver (one transceiver unit). The 2D target scanning is achieved by moving the transceiver unit as a whole to various randomly distributed locations around the target. This random distribution of sensors allows for target illumination from multiple angles, unlike scanning at co-linear points. The aim is to capture images of multiple irregular and complex-shaped real-life objects. The objects are positioned in the far-field region of the antennas but at a short range (110 cm away from the set-up). The proposed stacked antenna used as a transceiver in the imaging system is depicted in Figure 7.7 [26]. The performance

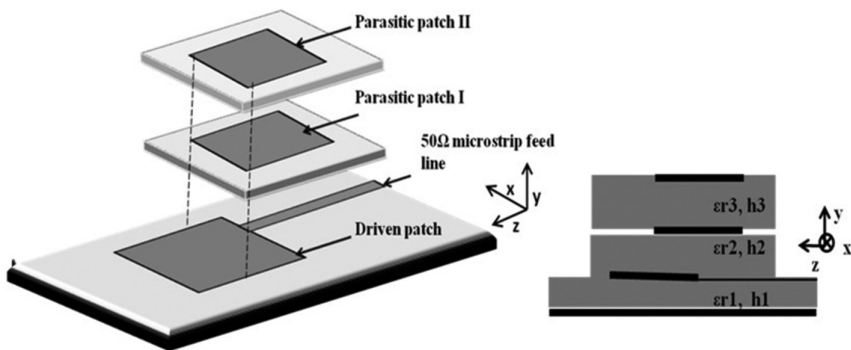


Figure 7.7 Proposed X-band stacked antenna. Reproduced with permission from IET [26].

comparison of the proposed stacked microstrip antenna is also done with the X-band waveguide adaptor to evaluate its relative performance. The waveguide adaptor antenna is chosen here, because it is similar to the proposed printed antenna in terms of wide beamwidth radiation pattern. The S_{11} response, radiation pattern, and gain graph of this X-band antenna are shown in Figure 7.8, Figure 7.9, and Figure 7.10, respectively. Its performance comparison with an X-band waveguide adaptor antenna is presented in Figure 7.11 when a large metallic sheet (ideal reflector) is placed in front of the transceiver unit comprising these antennas [27]. The microwave imaging set-up incorporating the X-band stacked antenna is illustrated in Figure 7.12.

7.7.2 Microwave imaging set-up comprised of C-band stacked antenna

The next case is evaluating the performance of C-band stacked microstrip antennas when used in a microwave imaging set-up as a transceiver unit. The proposed C-band stacked antenna geometry is shown in Figure 7.13 [28]. Similar to the previous case, scanning is carried out using randomly distributed sensors/transceivers in 2D. The antenna has a wideband

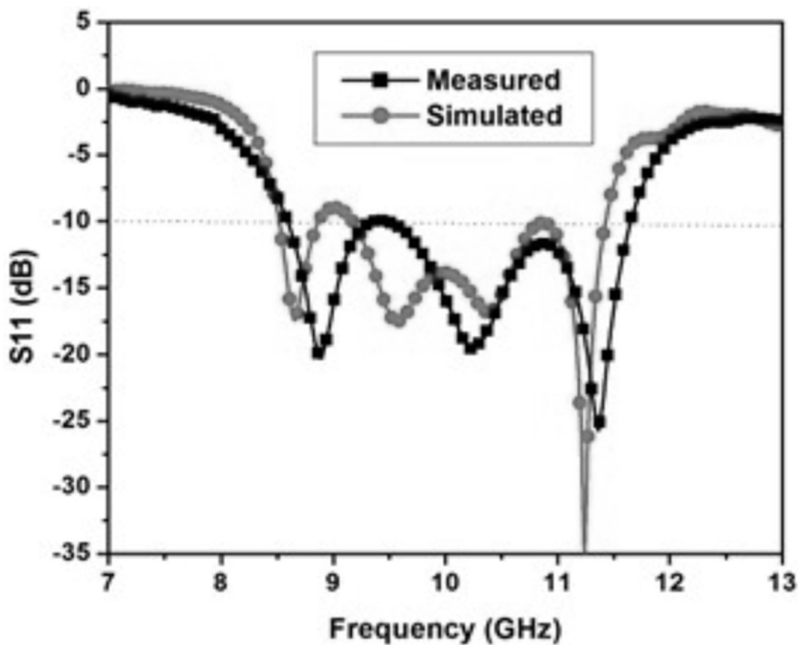


Figure 7.8 S_{11} response of the proposed X-band stacked antenna. Reproduced with permission from IET [26].

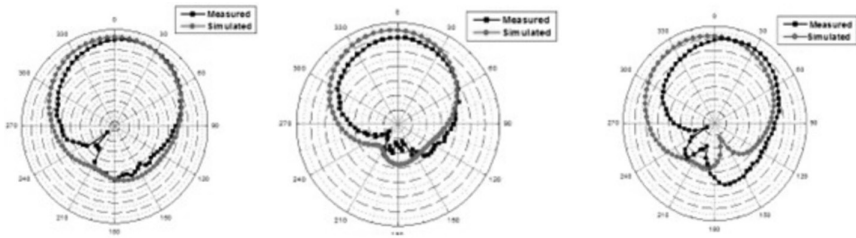


Figure 7.9 Radiation pattern of the proposed X-band antenna at different frequencies. Reproduced with permission from IET [26].

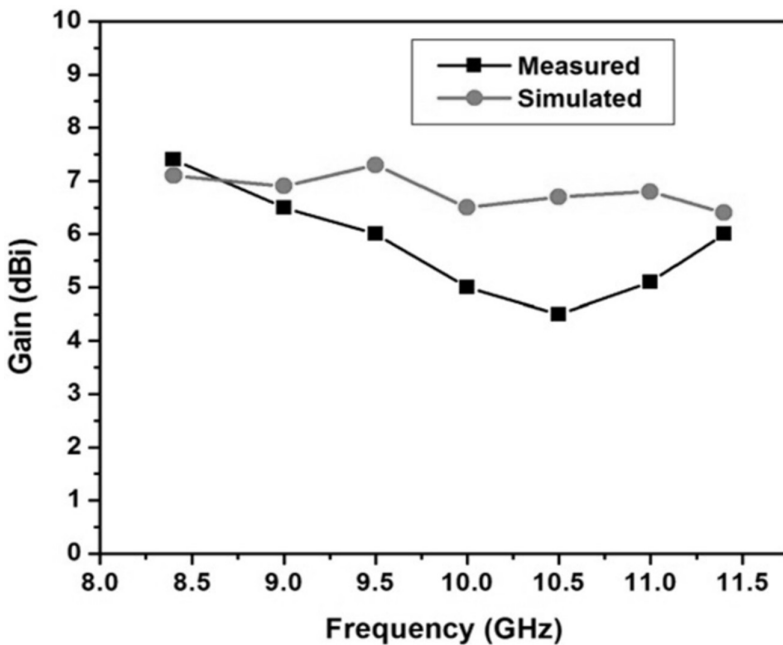


Figure 7.10 Gain graph of the X-band stacked antenna used as a transceiver in the imaging system. Reproduced with permission from IET [26].

response (3 GHz bandwidth) and unidirectional radiation patterns, which are depicted in Figure 7.14 and Figure 7.15, respectively, while the design parameters are listed in Table 7.1 The gain of the C-band stacked antenna is given in Figure 7.16, which shows the achieved peak gain of 8dBi, making it suitable to be deployed in the imaging system.

The response of the C-band is also compared with the C-band waveguide adaptor antenna (open-waveguide antenna) for the case of a large metal sheet (ideal reflector) as a target. S21 response for both antennas is given in Figure 7.17.

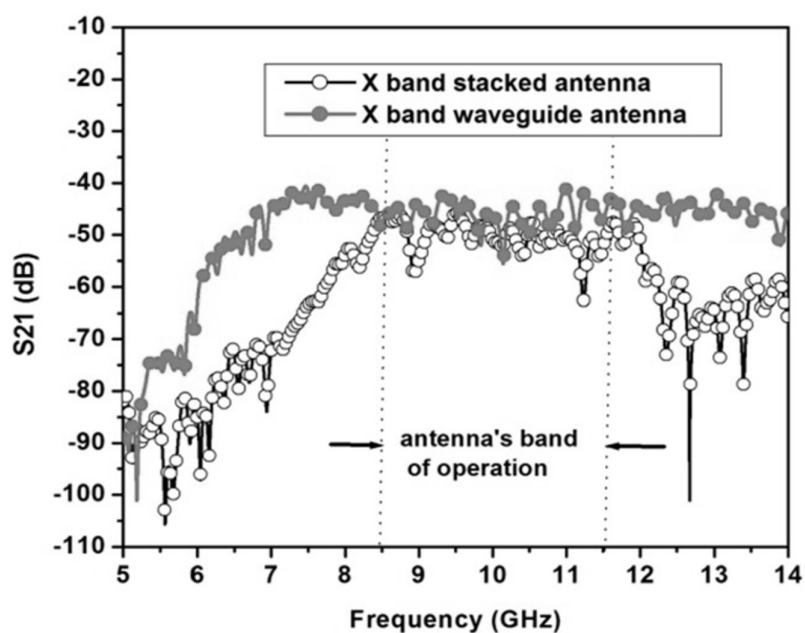


Figure 7.11 S_{21} response of X-band antenna and waveguide antenna (in E-plane) in the presence of a large metal sheet at 110 cm. Reproduced with permission from IEEE [27].

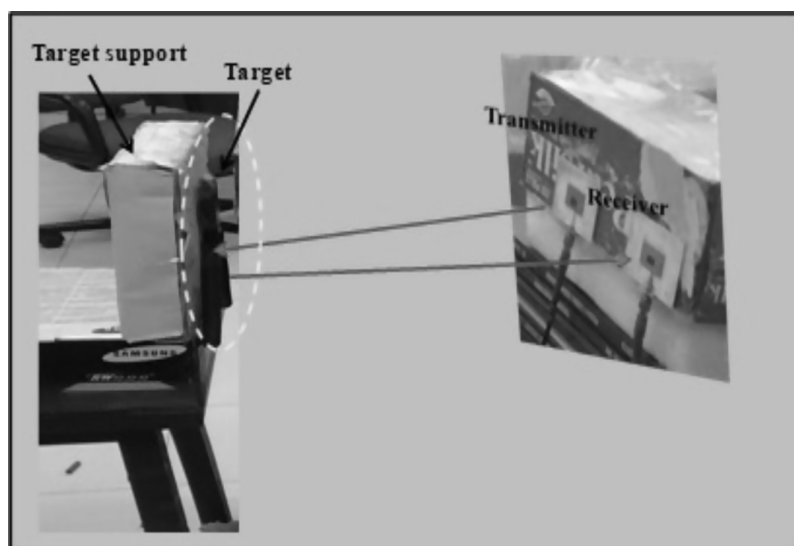


Figure 7.12 Microwave imaging set-up employing stacked microstrip antennas as transceiver.

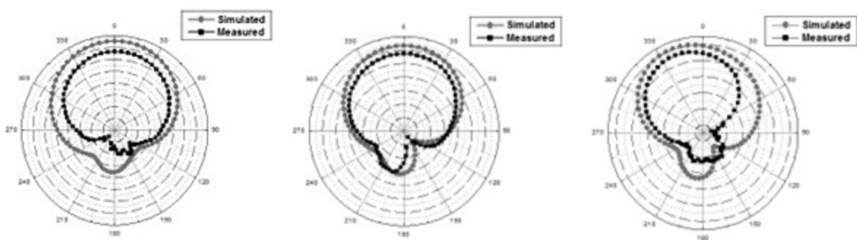


Figure 7.15 H-plane radiation patterns of the proposed stacked antenna at different resonant frequencies. Reproduced with permission from IETE [28].

Table 7.1 Design parameters of proposed C-band stacked antenna

Parameter	Value (in mm)	Parameter	Value (in mm)
W	52	w3	13.6
L	50	L3	12
w1	12	Wf	1.1
L1	10.89	Ws	1.95
w2	13	Sl	4.4
L2	11	Sw	2.59
y	7.4	er1	3.6(no unit)
h1	0.508	er2	2.2(no unit)
h2	1.5	er3	2.2(no unit)
h3	2.5		

The scattering of the incident waves from the target is a function of its shape and reflectivity; thus these scattered waves contain the target’s information. This information is then processed using the previously described algorithm. The different irregularly shaped objects used as targets and their reconstructed images are shown in Figure 7.18, while real-life objects used and their respective images are shown in Figure 7.19. The targets are kept at a distance of 110 cm from the plane containing the transceiver unit.

The obtained images for different geometries are quite distinguishable and resemble the targets very closely. In Figure 7.19, real-life objects such as pair of pliers and nose-pliers are considered targets to carry out micro-wave imaging process. The images of these objects show quite a similarity with the original structure, except for the fact that the legs of the pliers in both cases could not be detected. This is due to the strong plastic cover on the pliers’ legs, and also due to the very wide scattering angles of the legs which may require multiple receivers placed at wide angles or 3D scanning. These results show that a resolution of up to 2.5 cm is achievable, which is the width/separation of the mouth of pliers, in the present case of X-band stacked antennas as transceivers.

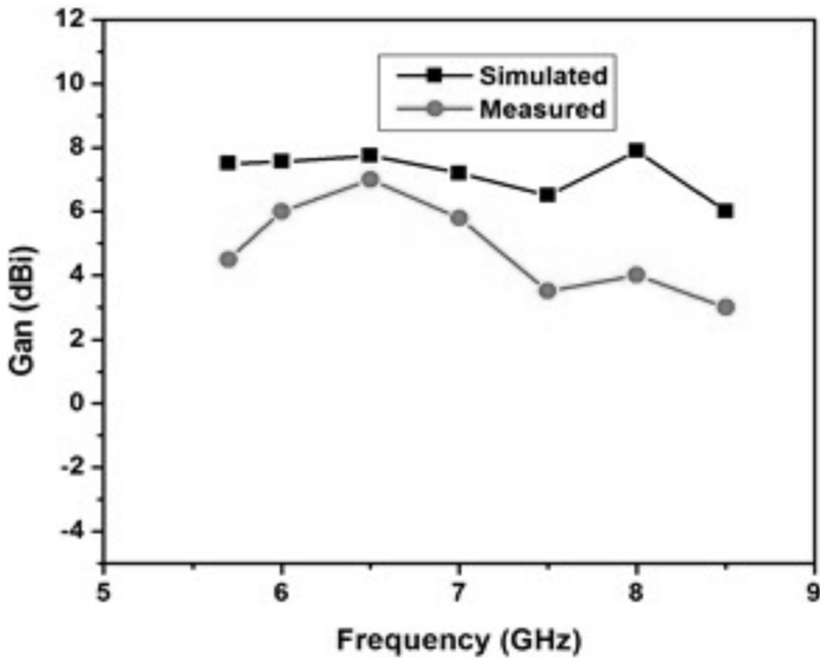


Figure 7.16 Simulated and measured gain of C-band stacked antenna. Reproduced with permission from IETE [28].

Additionally, we examine two targets that are separated in cross-range for image reconstruction. We consider two different cases: the first involves two pliers separated in cross-range, and the second involves pliers and a vertical rod separated in both range and cross-range. The corresponding image of two pliers separated from each other in the cross-range plane is shown in Figure 7.20. An image of the other case of pliers and one cylindrical rod separated in both range and cross-range is shown in Figure 7.21. The normalized cross-range separation in both cases is given by $x/d = 0.23$, ($x = 25.4$ cm, $d = 110$ cm); here d_1 is the range of the pliers ($d_1 = d = 85$ cm) and d_2 (110 cm) is the range of the rod from the T/R module.

The detection and shape reconstruction of multiple targets is possible because the responses from different targets are separated in the time domain as shown in Figure 7.22 and Figure 7.23, and therefore can be easily separated using time-gating described in earlier sections. The range resolution is inherently limited by the system's bandwidth, as it dictates the distribution of the echo signal in the time domain and, consequently, the overlap of two echoes. The first echo signal, or scattered wave, corresponds to the target nearest to the imaging system, while the subsequent echo pertains to a more distant target.

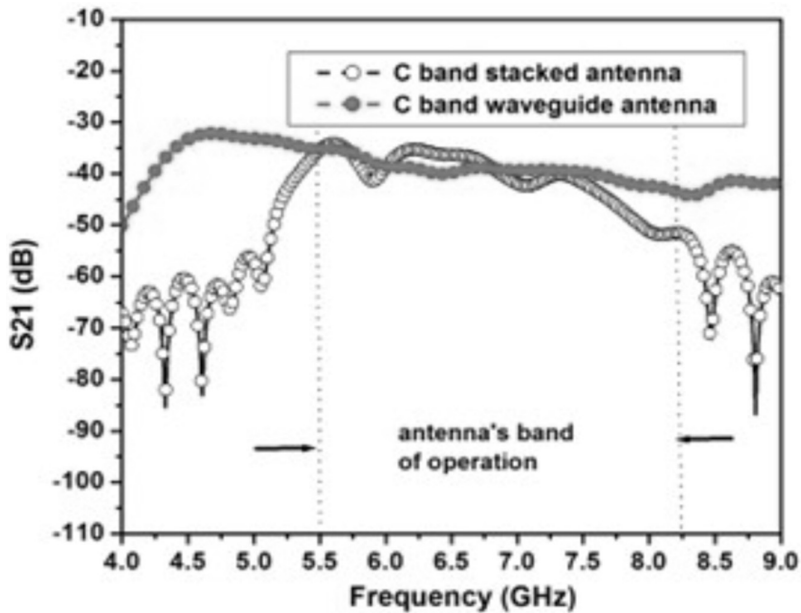


Figure 7.17 S_{21} response of C-band stacked antenna and waveguide adaptor in the presence of a very large metal sheet (acting as reflector) at 110 cm. Reproduced with permission from IEEE [27].

7.8.2 Reconstructed images of targets hidden behind dielectric medium in X-band

In scenarios where targets are concealed behind a dielectric medium, incident waves on the target undergo diffraction by the medium. While some waves are diffracted, others penetrate the material. Due to the long wavelength of microwaves, most of the signal strength goes through the dielectric, although losses occur at the dielectric-air boundary, resulting in noisy scattered signals from the target. Background subtraction proves effective in mitigating the signal noise caused by diffraction, and employing improved time-gating and signal processing techniques can enhance the image quality. In this study, we utilized the algorithm described previously (in Section 7.6) for image reconstruction, accompanied by refined time-gating and optimized signal averaging with a smaller filter length selection.

Now the targets used in experiments are a pair of pliers and an inverted cylindrical rod, as shown in Figure 7.24. The dielectric mediums used for the present study are foam, cardboard box, and plywood depicted in Figure 7.25. A 3.8 cm thick piece of foam is used to hide the targets in one case. In the second case, the targets are completely covered with a cardboard box, while in the third case, the targets are hidden behind 1.5 cm thick plywood.

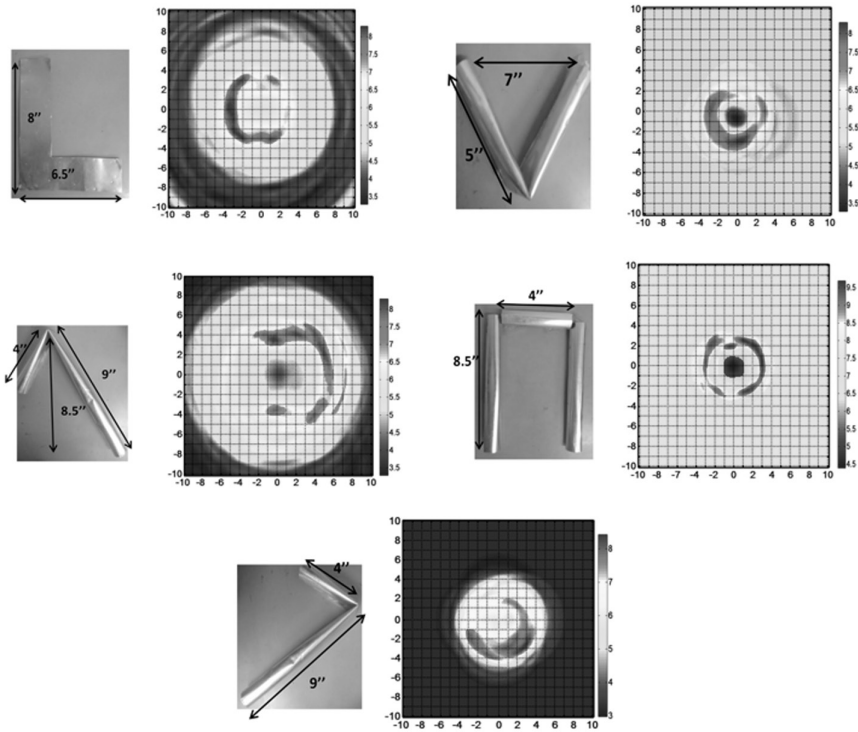


Figure 7.18 Irregular shaped targets at 110 cm and their respective images (1 unit = 2.54 cm = 1 inch).

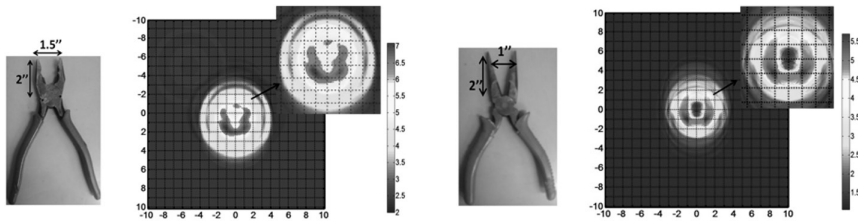


Figure 7.19 Real-life objects used as targets at 110 cm and their respective images (1 unit = 2.54 cm = 1 inch). Reproduced with permission from IEEE [27].

The respective images for the different dielectric mediums are shown in Figure 7.26, which show increased noise in the reconstructed image.

In all of these images, amplitude levels are scaled by a factor of 10^{-3} . The images indicate that when the targets are hidden, some distortion is observed in the reconstructed images. This distortion is primarily caused by wave diffraction at the air-dielectric interface when electromagnetic waves pass through the dielectric material. As the material density increases, so

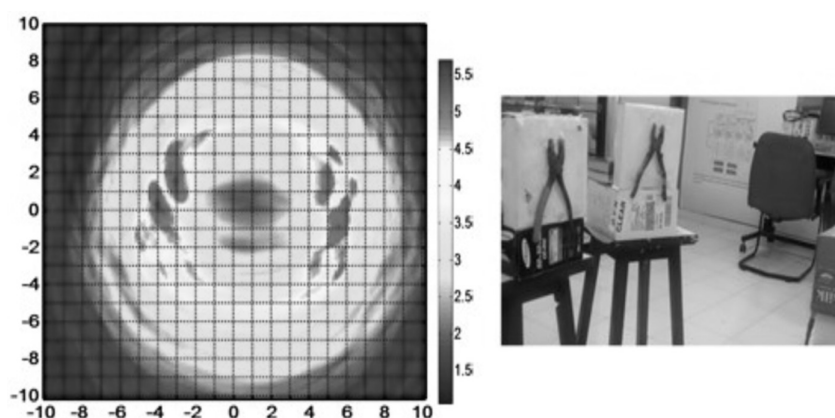


Figure 7.20 Two pliers in the investigation domain separated in cross-range and their image. Reproduced with permission from IEEE [27].

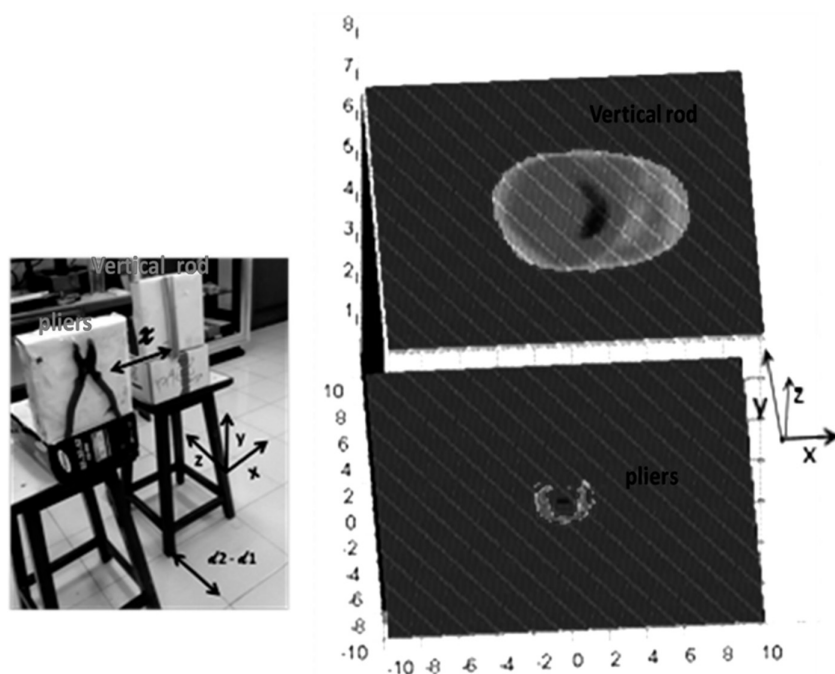


Figure 7.21 Image of pliers and rod separated both in range and cross-range. Reproduced with permission from IEEE [27].

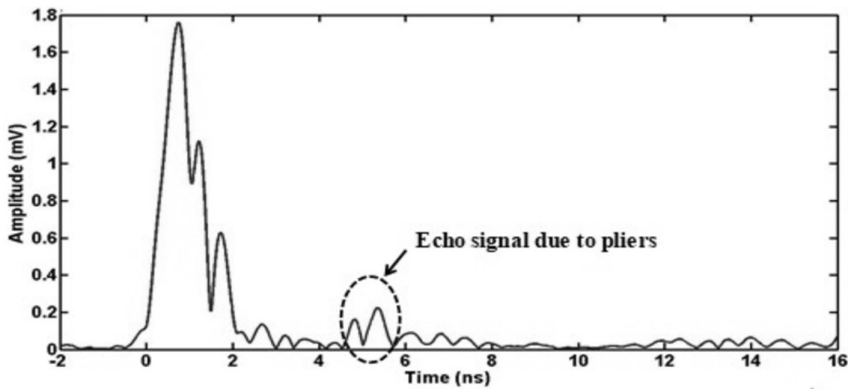


Figure 7.22 Time domain response of X-band antenna for the pair of pliers as target.

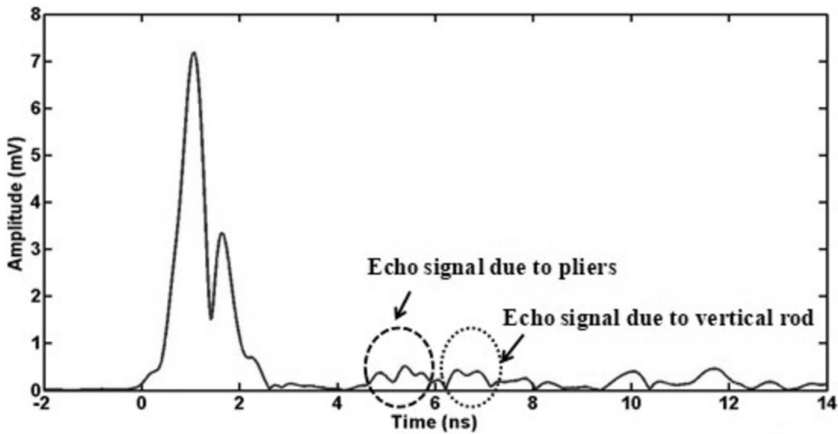


Figure 7.23 Time domain response of X-band antenna for the case of pliers and vertical rod in the investigation, separated both in range and cross-range.

does the diffraction. Consequently, when plywood is used as the dielectric medium in front of the targets, maximum distortion in the image occurs. In all the cases discussed above, the thickness of the dielectric medium is less than the operating wavelength, allowing wave penetration. However, since the wavelength and the thickness are still comparable, distortions persist. To achieve better imaging results for the case of hidden targets, it is advisable to use transceivers operating at lower frequencies (larger wavelengths). Next, we will discuss microwave imaging carried out in the C-band frequency region using a C-band stacked antenna.

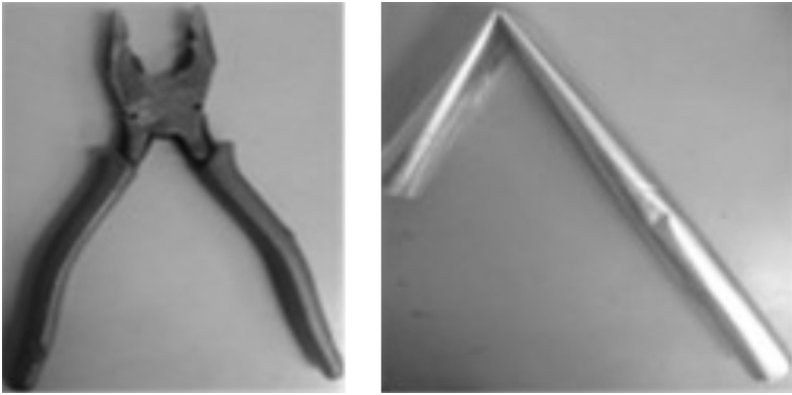


Figure 7.24 Targets under test for the case of dielectric medium placed in front of targets, (a) pair of pliers, (b) bent aluminium rod.

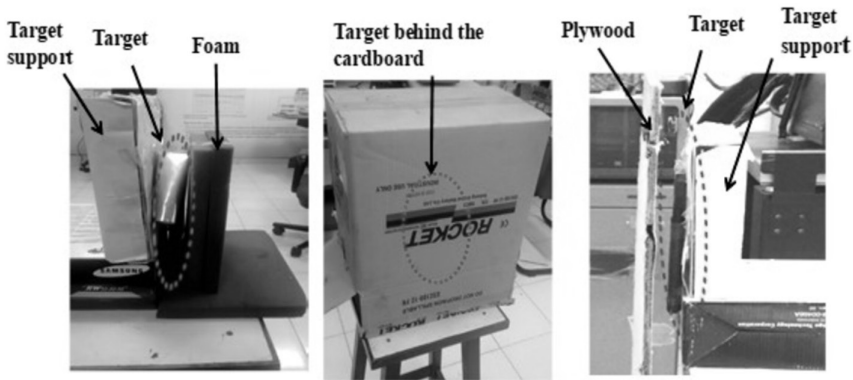


Figure 7.25 Set-up for various dielectric mediums in front of the targets. Reproduced with permission from IEEE [27].

7.8.3 Reconstructed images of targets (in free-space) using C-band antenna

Like the previous case, multiple objects, akin to those utilized in the previous section, are employed as targets and positioned in open space. Their image reconstruction is now carried out in the C-band region using the proposed C-band stacked antenna as a transceiver. The objects under examination and their respective captured images are depicted in Figure 7.27 (irregularly shaped objects) and Figure 7.28 (real-life objects). As elucidated in Section 7.6.2, the spatial resolution depends upon the operating wavelength. This accounts for the fact that in the C-band region, the images acquired under the same conditions as those in the X-band case and with

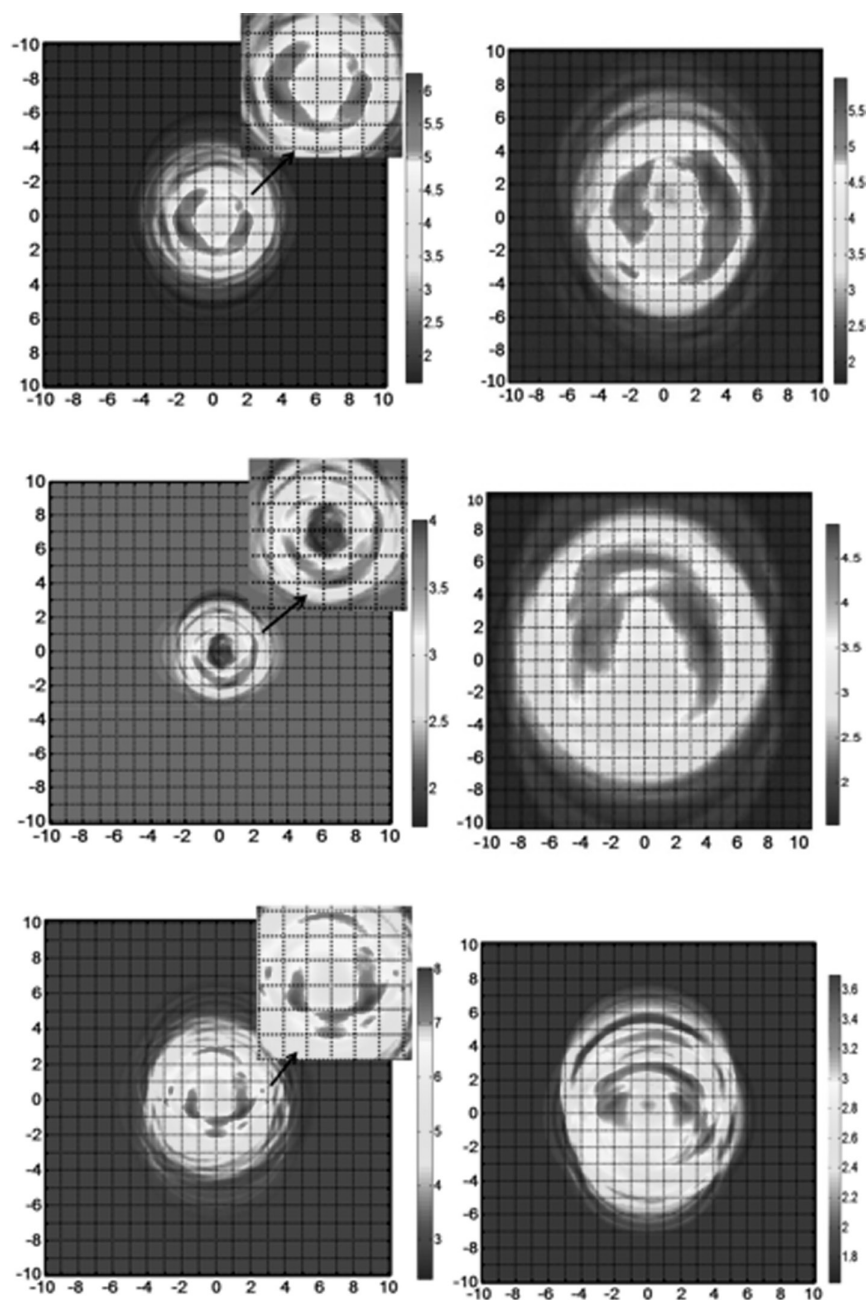


Figure 7.26 Images of targets obtained for the case of targets hidden behind the dielectric medium. Reproduced with permission from IEEE [27].

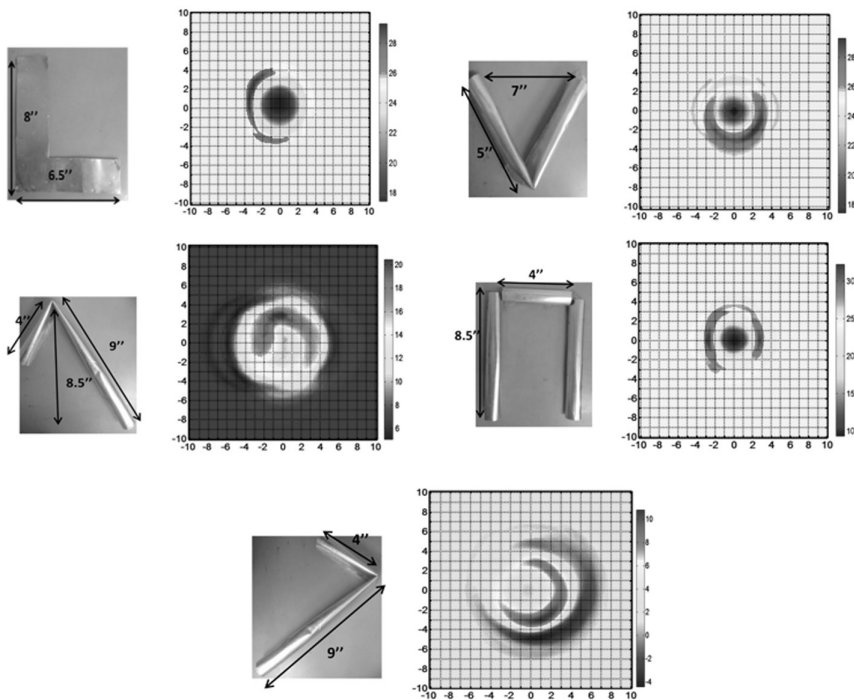


Figure 7.27 Irregularly shaped targets at 75 cm and their respective images (1 unit = 2.54 cm = 1 inch).

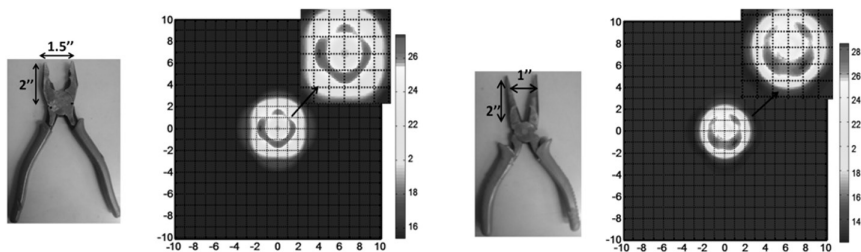


Figure 7.28 Real-life objects used as targets at 75 cm and their respective images (1 unit = 2.54 cm = 1 inch).

the same matrix formation will appear larger. This is ascribed to the fact that the same bandwidth in the C-band region will correspond to a broader response in the time domain as opposed to the X-band region. Thus, in this scenario, each unit cell must be proportionally adjusted as per Equation (7.13), which is derived from the cross-range resolution (Equation 7.12). By applying this scaling, the image matrix for this case can be readily juxtaposed with that obtained in the X-band region.

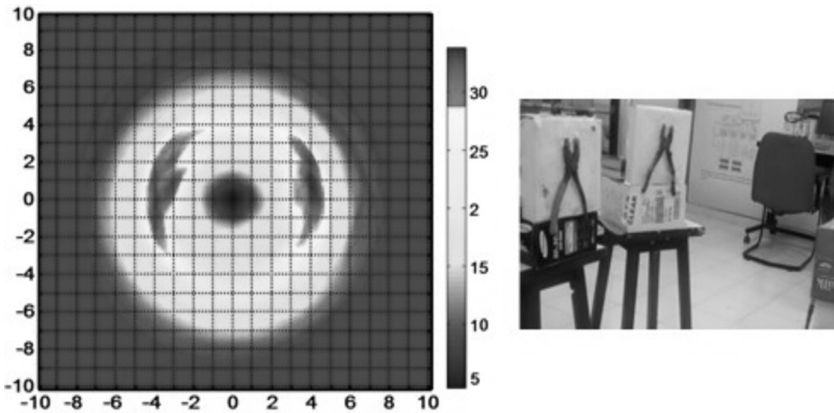


Figure 7.29 Two pliers in investigation domain separated in cross-range (1 unit = 2.54 cm = 1 inch).

$$\Delta x' = \Delta x * \frac{\lambda_2}{\lambda_1} \quad (7.13)$$

Here Δx is the spatial resolution for X-band, λ_2 is the operating wavelength of the C-band antenna at the centre frequency of the band of operation, while λ_1 is the operating wavelength of the X-band antenna. Similarly for targets at different distances, spatial resolution will change and has to be scaled according to Equation (7.12). The equation states that for larger distances, spatial resolution will be greater. The colour-bar amplitudes are scaled by 10^{-3} . Further, resolution and image reconstruction in the case of two objects in cross-range has been evaluated. Two pliers separated by 25 cm in cross-range and at a distance of 110 cm from the T/R module are shown in Figure 7.29 along with a reconstructed image. Further, the image reconstruction of a pair of pliers and vertical rod separated both in range and cross-range (as in previous case) in C-band is shown in Figure 7.30. The range separation of the target is $(d_2 - d_1)$ 25 cm while the cross-range separation is 30.5 cm. The range of the pliers is 85 cm and that of the rod is 110 cm from the T/R module.

The results obtained for the C-band frequency region, for the case when targets are kept in free-space, show that the resolution achieved is less than that in the X-band region (as was expected). However, images of larger objects are satisfactory as their size is comparable with the operating wavelength, whereas the images of smaller objects (pliers and nose-pliers) have been distorted. However the observation also highlights that the images of smaller objects are still distinguishable and can lead to shape estimation if some prior information about the target is available. Similarly, for the case of two pliers in the investigation domain, the shape of pliers is not enhanced;

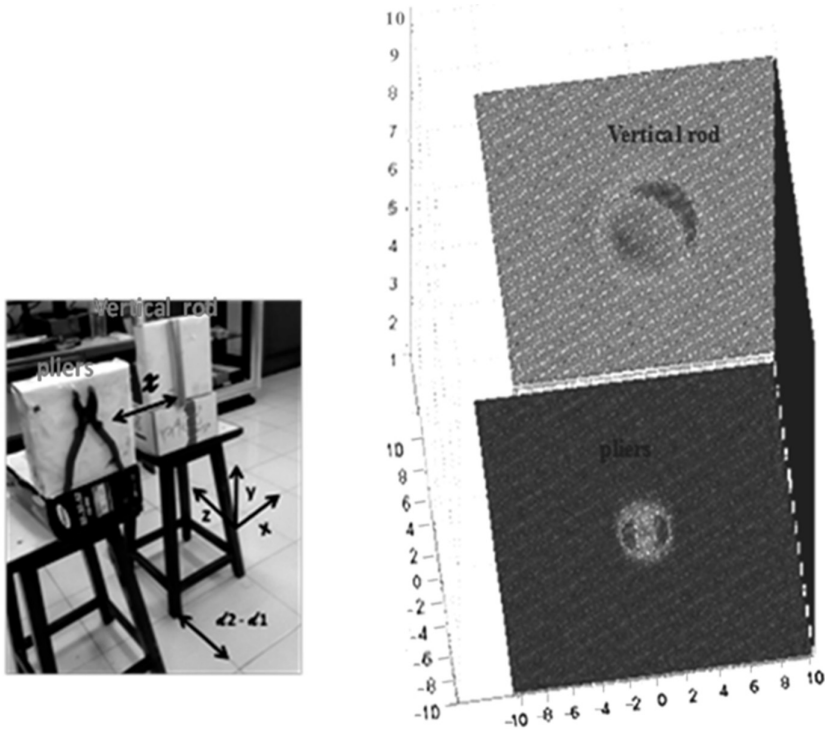


Figure 7.30 A pair of pliers and vertical rod in investigation domain separated both in range and cross-range.

however, the resolution among the two pliers is achieved. Moreover, the vertical rod and pair of pliers separated in range and cross-range show that resolution between the targets both in range and cross-range is achievable, but the individual image shows slight distortion.

7.8.4 Reconstructed images of targets hidden behind dielectric medium using C-band stacked antenna

Further, the imaging of targets concealed behind various dielectric mediums within the C-band frequency range is carried out. The targets tested are a horizontal cylindrical bent rod and a U-shaped rod, kept behind the dielectric materials previously described. The accompanying figures (Figure 7.31 and Figure 7.32) display the targets and their respective images for the different dielectric mediums positioned in front of them.

The images obtained in this case show that due to the better penetration capability of waves in the C-band frequency region as compared to the

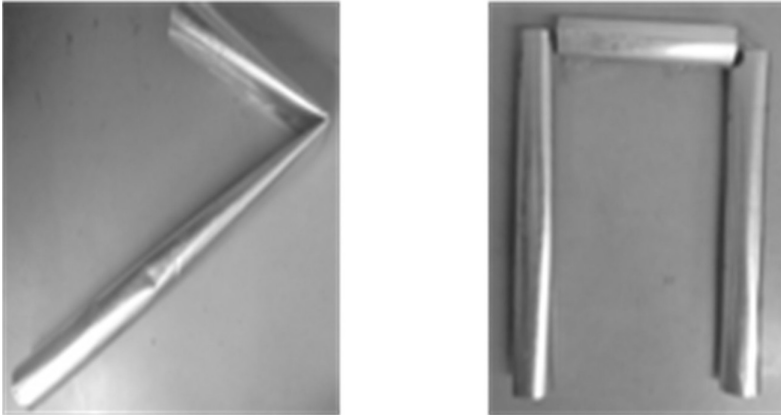


Figure 7.31 Objects under test for imaging with different dielectric mediums hiding the targets: horizontally lying bent rod and U-shaped bent rod.

X-band region, the images obtained are much clearer with minimum distortion even for the case of a dense medium like plywood. Hence compared to higher frequency antennas, lower frequency antennas can help achieve better shape estimation and target detection when targets are hidden behind a dielectric medium.

Comparing the reconstructed images in two operating bands for different cases, it is observed that using two/multiple frequency regions can provide more spectral information about the targets in different scenarios if the antenna is not a UWB antenna. This can be helpful in better target detection and shape reconstruction of targets in different conditions and for different target dimensions. Such a system can be better than a UWB imaging system, as it will avoid the noise present over such a wide band and allows the reduction of noise from back clutter too by employing stacked patch antennas with unidirectional radiation patterns (which is not the case with a UWB antenna). The next section will delve into the performance of a frequency-reconfigurable antenna for improved image reconstruction.

7.9 RECONFIGURABLE STACKED ANTENNA

A reconfigurable antenna, depicted in Figure 7.33 [29], operates in switched mode to enable the utilization of both X-band and C-band antennas in the imaging system as a single circuit. This configuration allows for the extraction of more spectral information from the target. Two diodes enable the antenna to operate in a switched mode, with one diode activating the corresponding antenna at a time. By illuminating the target using signals in X-band and C-band regions at different times while maintaining consistent

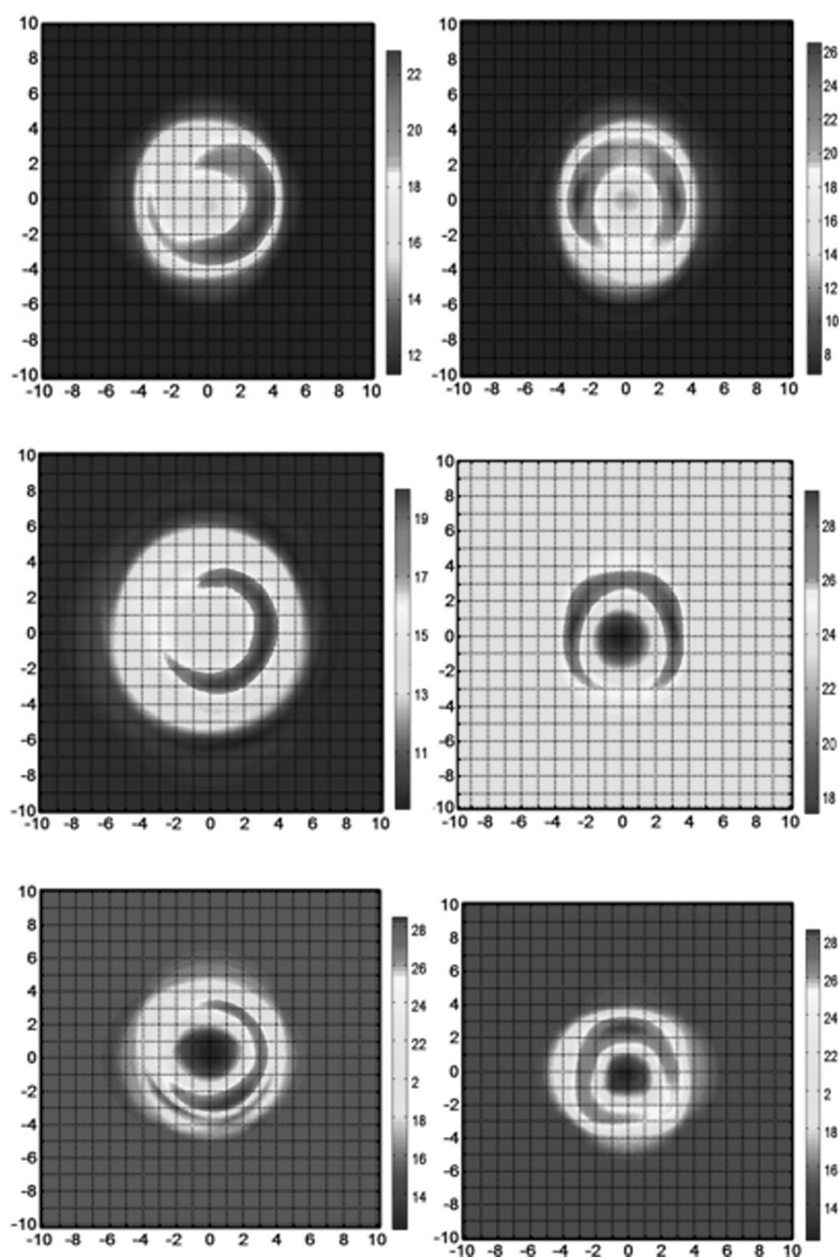


Figure 7.32 Reconstructed images of targets hidden behind different dielectric materials (1 unit = 2.54 cm = 1 inch).

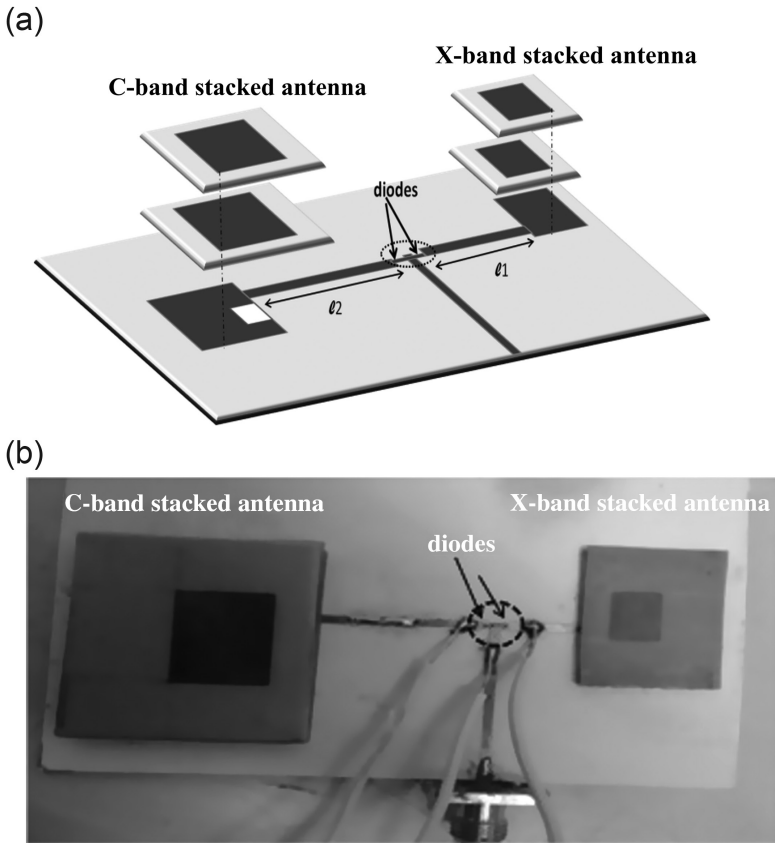


Figure 7.33 Reconfigurable stacked antenna, (a) 3D view, (b) fabricated antenna. Reproduced with permission from Cambridge University Press [29].

environmental conditions, the antenna captures the target's spectral information in two microwave bands. Combining this information provides a comprehensive view of the target's wideband spectral information under interrogation.

In the reconfigurable/switching antenna used here, the common 50-ohm feed line feeds both antennas through a switch (PIN diode). A regulated DC voltage supply is connected to each diode, with a positive terminal connected to the diode's anode and a negative terminal connected to the common feed line to make it a common ground. For practical implementation, the DC supply can be replaced by a potentiometer connected with DC batteries (to keep the antenna measurement set-up light and compact). The response of both antennas: the C-band and X-band stacked antennas, in the reconfigurable antenna design is given in Figure 7.34 and Figure 7.35 respectively.

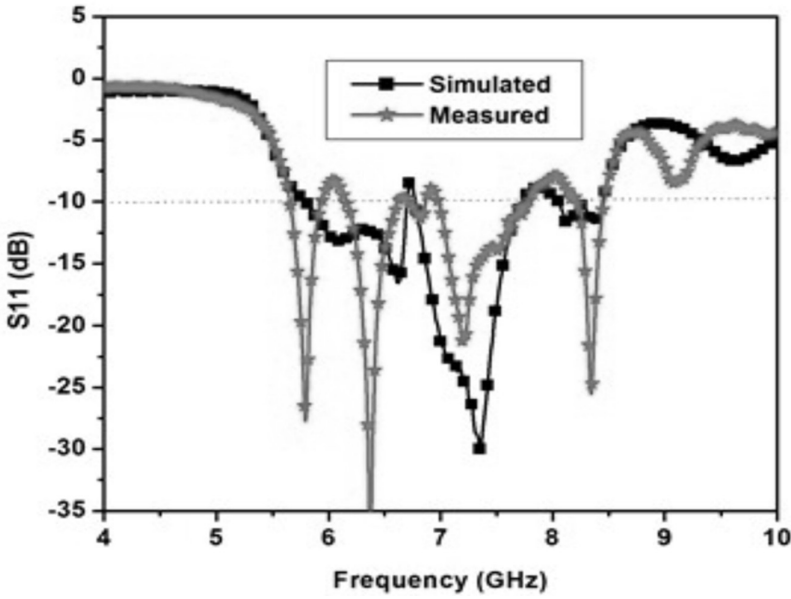


Figure 7.34 S_{11} response of reconfigurable stacked antenna for C-band antenna ON. Reproduced with permission from Cambridge University Press [29].

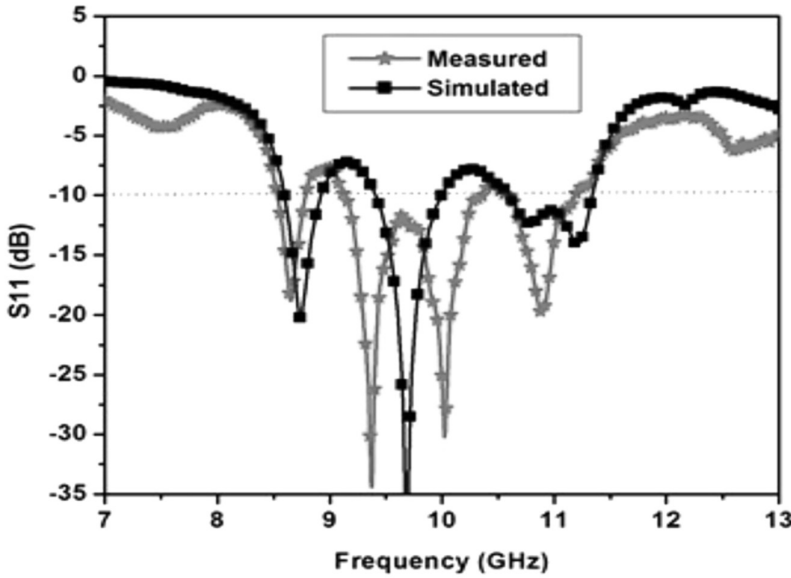


Figure 7.35 S_{11} response of reconfigurable stacked antenna for X-band antenna ON. Reproduced with permission from Cambridge University Press [29].

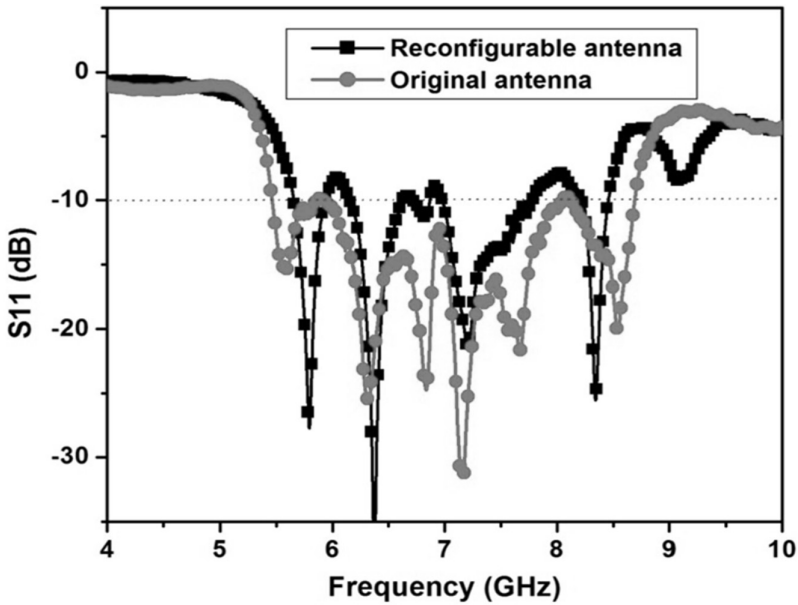


Figure 7.36 S11 response of reconfigurable stacked antenna, with C-band antenna ON vs original response of C-band stacked antenna. Reproduced with permission from Cambridge University Press [29].

However, integrating two antennas at a common ground causes slight distortion in their individual response due to some coupling between them as shown in Figure 7.36 and Figure 7.37 for C-band and X-band frequency regions respectively. This variation is quite negligible in both cases. The measured radiation patterns of reconfigurable stacked antenna are given in Figure 7.38 which show some deviation as compared to original patterns due to mutual coupling. Also, some drop in gain exists at higher frequencies in each case.

7.9.1 Measurement set-up employing reconfigurable stacked antenna

A microwave imaging measurement set-up, comprising of reconfigurable stacked antennas as transmitter and receiver (transceiver), is shown in Figure 7.39, with the target kept in the E-plane of both antenna elements of the reconfigurable antenna. The perpendicular distance between the target and the system's origin is " d ".

As can be seen from the set-up, the offset " s " in the origins of the two stacked antennas along the y -axis should be considered in the imaging algorithm. Further, as can be seen in Figure 7.33, the feed line is extended for the C-band antenna to avoid interference of its radiation pattern with the

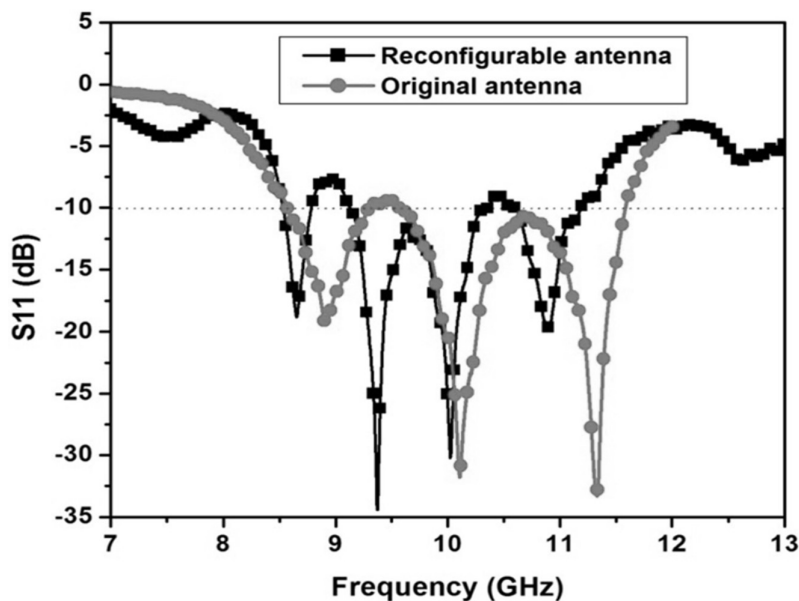


Figure 7.37 S11 response of reconfigurable stacked antenna, with X-band antenna ON vs original response of X-band stacked antenna. Reproduced with permission from Cambridge University Press [29].

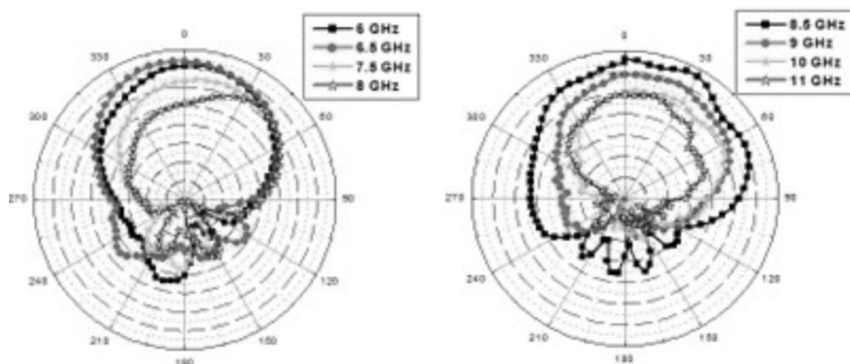


Figure 7.38 Measured H-plane radiation patterns of reconfigurable stacked microstrip antenna at different frequencies, (a) C-band antenna ON, (b) X-band antenna ON. Reproduced with permission from Cambridge University Press [29].

X-band antenna. This causes a delay in the time-domain signal received at the C-band receiver, such that

$$\Delta t = 2 \Delta l / c, \text{ where } \Delta l = l_2 - l_1 \tag{7.14}$$

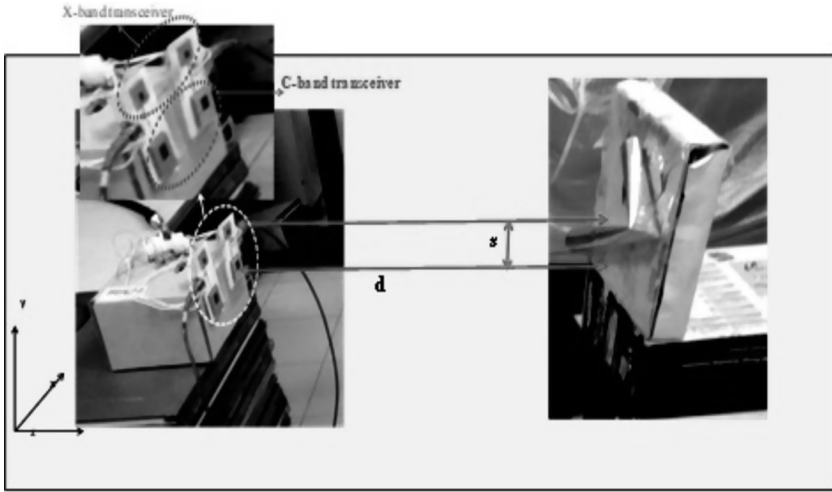


Figure 7.39 Measurement set-up employing reconfigurable stacked antenna as transceiver. Reproduced with permission from Cambridge University Press [29].

The factor of two exists to account for the delay at both the transmitter and the receiver. This should be incorporated while applying time-gating at the received time-domain signal for the C-band stacked antenna.

7.9.2 Image reconstruction using reconfigurable stacked antenna by matrix addition method

The target information is extracted in two frequency bands by scanning the targets using two stacked antennas, switching on one at a time. This process involves scanning the targets twice. Image matrices are created in each frequency band to estimate the shape of the target. The final image is obtained by combining the two image matrices using Equation (7.15). This results in an image containing more spectral information on the target and leads to an improved image. Before adding the matrices, the image matrix in the C-band frequency region is scaled according to Equation (7.16). This equalizes the image resolution in both matrices, making matrix addition possible.

$$P = I' * M_x + M_c \quad (7.15)$$

$$\text{where } I' = \frac{I_c}{I_x} \quad (7.16)$$

Using the above equation, image matrices obtained in the C-band and X-band regions can be combined. Here, in Equation (7.15), M_x and M_c are

the image matrices in the X-band and C-band frequency regions respectively, while I' is the intensity ratio given by Equation (7.16). I' represents the ratio of the intensity of the echo signal received from the target in the C-band frequency region to that received in the X-band frequency region if the received signal intensities differ in time domain for two different frequency antennas. This difference may exist due to the difference in gains of the two antennas (if any).

It is advantageous to use a reconfigurable stacked antenna for target scanning, as it maintains a consistent target scanning system and environment. This approach also reduces calibration errors, as the cables are fixed and remain stationary. Additionally, a reconfigurable antenna enables target illumination at various angles and ensures uniform reception of scattered waves from the target by both antennas.

7.9.3 Image reconstruction using reconfigurable stacked antenna by combining signals in the frequency domain

In the preceding section, we discussed target imaging using reconfigurable stacked antennas through method I. The target information extracted in individual frequency bands can be aggregated to produce an improved image. In this section, we will explore a second method for combining target information in two frequency bands. This involves combining the target's spectral information in the frequency domain, providing the target's information across a broad frequency spectrum, from C-band to X-band. This effectively simulates a very wideband antenna response, which should yield more precise target information [29]. The combined frequency domain information is then converted to its time-domain form and processed as detailed in Section 7.6. This approach helps avoid the noise that would normally be present in a broad frequency spectrum of a UWB antenna or an antenna with a very wideband response, while also enabling the extraction of more spectral information.

X-band and C-band antenna responses in the frequency domain are given in Figure 7.40 and Figure 7.41 respectively. The combined frequency domain response is given in Figure 7.42 and Figure 7.43 (in linear scale). The S21 responses show some noise that is mostly due to calibration errors. The time-domain response of this broad frequency spectrum (combined response in C-band and X-band regions) is given in Figure 7.44. The time-domain response also shows some distortion as compared to previous responses in individual bands due to calibration errors over the wide frequency spectrum. The C-band antenna's response is considered up to 8.5 GHz, after the 8.5 GHz X-band antenna's response is taken into account. This makes the given reconfigurable stacked antenna design response equivalent to an ultra-wideband response from 5.5 to 11.5 GHz.

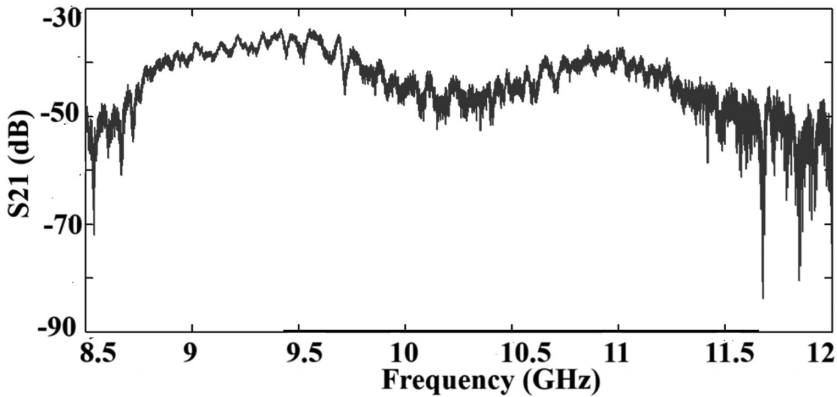


Figure 7.40 S21 response of C-band stacked antenna for pliers as target at 28 inches. Reproduced with permission from Cambridge University Press [29].

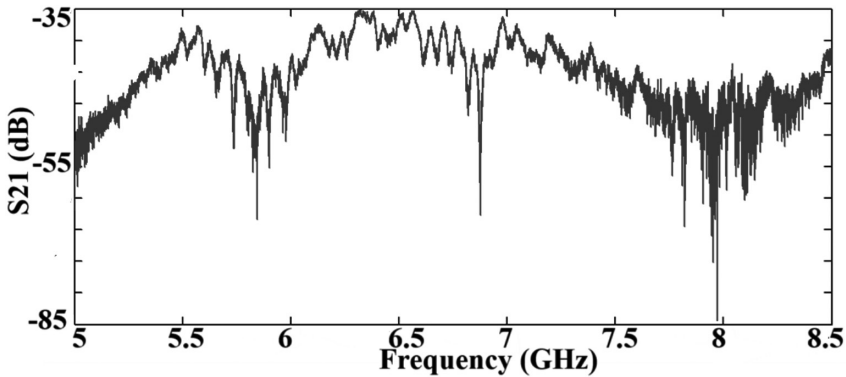


Figure 7.41 S21 response of X-band stacked antenna for pliers as target at 28 inches. Reproduced with permission from Cambridge University Press [29].

7.9.4 Reconstructed images using reconfigurable stacked antenna

Applying the earlier described image reconstruction algorithm in Section 7.6, an improvement in the obtained image is observed, as both methods combine additional target information to get the final image. The various irregularly shaped targets used are shown in Figure 7.45, while their imaging results are shown in Figures 7.46, 7.47, and 7.48. The images that have been reconstructed display the individual X and C-band images, each obtained with the respective antenna element switched ON in the reconfigurable antenna. Following these images is the combined image obtained

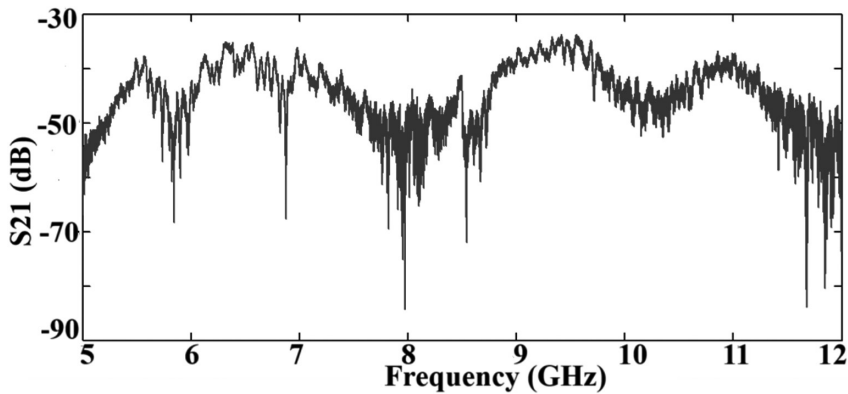


Figure 7.42 S21 response of C-band and X-band stacked antennas combined for pliers as target at 28 inches. Reproduced with permission from Cambridge University Press [29].

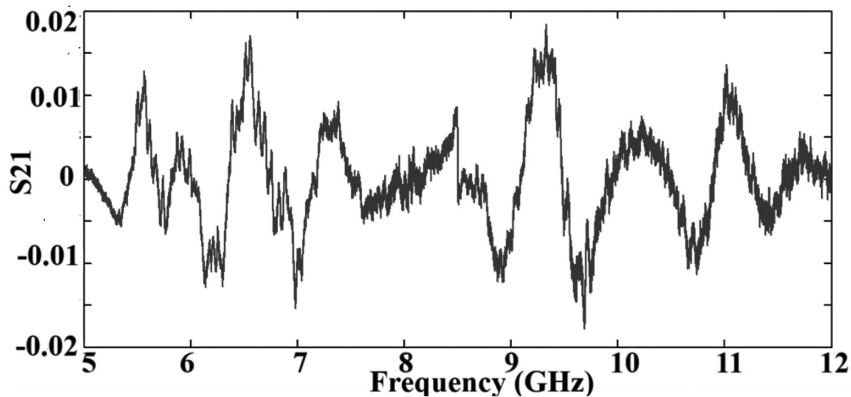


Figure 7.43 S21 response of C-band and X-band stacked antennas combined (linear) for pliers as target at 28 inches. Reproduced with permission from Cambridge University Press [29].

using image matrix addition (method I), and the spectral data combined at the pre-processing stage (method II). Both methods can be utilized based on the transceiver parameters and the specific application. In either case, there is a possibility of introducing additional spectral noise due to the wide-band data used, if the system calibration is not performed correctly. The second method may outperform the first as it effectively provides ultra-wideband data for processing in the time domain. However, the use of the second method (method II) is viable only if the two operating bands of the reconfigurable antenna can be merged into a single continuous wide-band. Otherwise, method I can be employed for any such configuration of a reconfigurable stacked antenna.

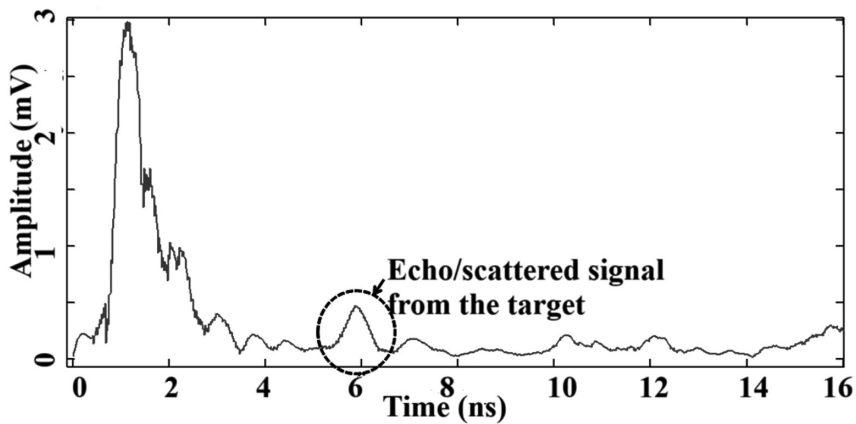


Figure 7.44 Time-domain response corresponding to combined frequency-domain responses of C-band and X-band antennas, for pliers as target at 28 inches. Reproduced with permission from Cambridge University Press [29].

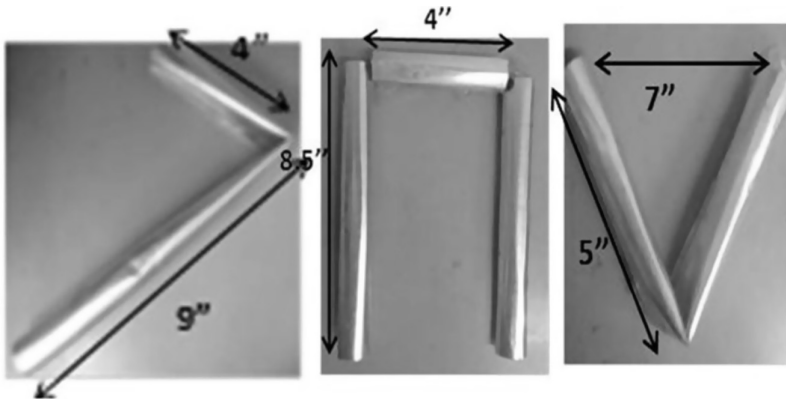


Figure 7.45 Objects used as targets with reconfigurable stacked antenna as transceiver. Reproduced with permission from Cambridge University Press [29].

7.10 BIOMEDICAL IMAGING USING STACKED MICROSTRIP ANTENNAS

Apart from metallic target detection, microwave imaging can be a useful non-destructive tool for the imaging of non-metallic targets as well. More importantly, microwave and mm-wave imaging are used in biomedical imaging applications nowadays owing to their non-ionizing property. In this case, rather than a reflected signal, the signals diffracted from or transmitted through the medium are taken into consideration. This maps the dielectric profile of the medium and helps in identifying any medium

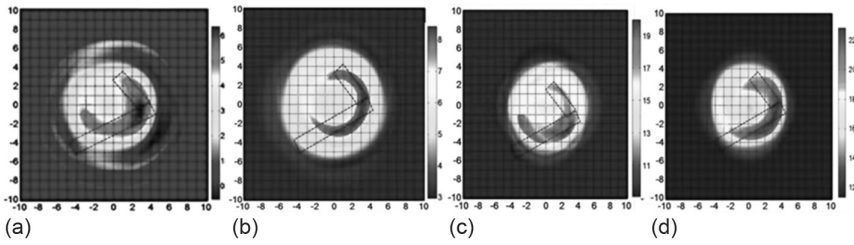


Figure 7.46 Reconstructed images of bent aluminium rod (a) in X-band, (b) in C-band, (c) X- and C-band data combined using image matrix addition (method I), and (d) X- and C-band data combined in the spectral domain (method II). Reproduced with permission from Cambridge University Press [29].

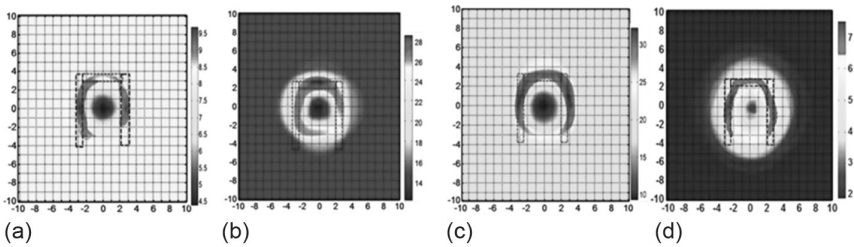


Figure 7.47 Reconstructed images of U-shaped aluminium rod (a) in X-band, (b) in C-band, (c) X- and C-band data combined using image matrix addition (method I), and (d) X- and C-band data combined in the spectral domain (method II). Reproduced with permission from Cambridge University Press [29].

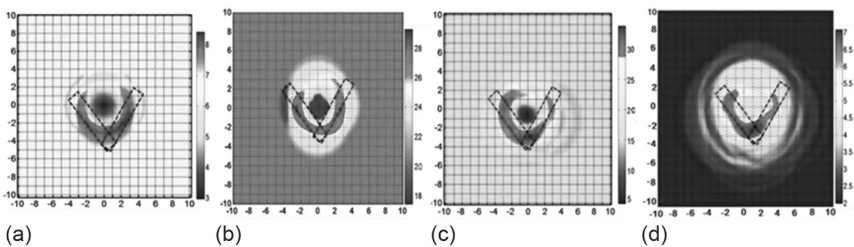


Figure 7.48 Reconstructed images of V-shaped aluminium rod (a) in X-band, (b) in C-band, (c) X- and C-band data combined using image matrix addition (method I), and (d) X- and C-band data combined in the spectral domain (method II). Reproduced with permission from Cambridge University Press [29].

changes that occurred while the wave propagated through the dielectric medium under test. In the case of biomedical imaging, the change in medium exists when there is any unknown variation in any body part at the tissue or molecular level. This variation in the dielectric profile of any tissue or area under scan exists due to some underlying cause. For example, in the case of breast cancer, the dielectric properties of the cancerous cell/tissue will

be different than the dielectric profile of the skin. This scenario will cause wave diffraction at the location of this cancerous tissue owing to changes in the medium through which the wave propagated. Thus, by subtracting the signal received when the cancerous tissue was not present or was not grown much, we can determine the presence and location of the cancerous tissue within the breast [30]. The microwave imaging set-up deployed for breast cancer imaging using stacked microstrip antennas is depicted in Chapter 6. Similarly, microwave imaging of head tumour is carried out in [31] using a folded stacked microstrip antenna.

7.11 SUMMARY

This chapter is focused on microwave imaging as a potential application of stacked microstrip antennas. The chapter introduced the basics of microwave imaging, system requirements, measurement and scanning set-up, and details of the SAR imaging algorithm. It further explored the utility of stacked microstrip antennas in the microwave imaging system and discussed different stacked antennas deployed in the set-up along with the imaging results. Additionally, it delved into microwave imaging using reconfigurable stacked antennas and examined two possible ways to enhance image quality. Finally, the chapter briefly discusses the biomedical imaging application of stacked microstrip antennas.

REFERENCES

1. Ananjan Basu Ankita, “Microwave Imaging Using Distributed Sensors”, IEEE MTT-S International Microwave and RF Conference, December 2013.
2. M. Pastorino, “*Microwave Imaging*”, Wiley, 2010.
3. R. K. Amineh, M. Ravan, A. Trehan, and N. K. Nikolova, “Near-field microwave imaging based on aperture raster scanning with TEM horn antennas”, *IEEE Trans. Antennas Propag.*, Vol. 59, No. 3, pp: 928–940, March 2011.
4. S. A. Rezaeieh, A. Zamani, and A. M. Abbosh, “3-D wideband antenna for head-imaging system with performance verification in brain tumor detection”, *IEEE Antennas Wireless Propag. Lett.*, Vol. 14, pp:910–914, April 2015.
5. T. F. Zanoon, and M. Z. Abdullah, “Quantitative imaging in the time domain featuring gradient based minimization and broyden updating”, *IEEE Microw. Wireless Comp. Lett.*, Vol. 21, No. 11, pp:628–630, November 2011.
6. A. Elboushi, and A. Sebak, “MMW sensor for hidden targets detection and warning based on reflection/scattering approach”, *IEEE Trans. Antennas Propag.*, Vol. 62, No. 9, pp:4890–4894, September 2014.
7. Z. Akhter, B. K. Buaman, and M. J. Akhtar, “Two-dimensional Microwave Imaging Scheme to Detect Concealed Objects”, IEEE MTT-S International RF and Microwave Conference, pp:1–4, December 2013.

8. O. Malyuskin, and V. Fusco, "Near field enhancement and sub-wavelength imaging using resonantly loaded apertures", *IEEE Trans. Antennas Propag.*, Vol. 62, No. 6, pp:3130–3140, June 2014.
9. M. R. Eskandari, M. Dehmollaian, and R. Safian, "Experimental investigation of factorization method as a qualitative approach for near-field microwave imaging", *IEEE Antennas Wireless Propag. Lett.*, Vol. 13, pp:289–292, February 2014.
10. R. Salman, I. Willms, L. Reichaedt, T. Zwick, and W. Wiesbeck, "On Polarization Diversity Gain in Short Range UWB-Radar Object Imaging", International Conference on Ultra-Wideband, pp:402–406, September 2012.
11. M. T. Bevacqua, L. Crocco, L. D. Donato, and T. Isernia, "Microwave imaging of nonweak targets via compressive sensing and virtual experiments", *IEEE Antennas Wireless Propag. Lett.*, Vol. 14, pp:1035–1038, May 2015.
12. R. K. Amineh, J. McCombe, and N. K. Nikolova, "Microwave holographic imaging using the antenna phaseless radiation pattern", *IEEE Antennas Wireless Propag. Lett.*, Vol. 11, pp:1529–1532, December 2012.
13. S. Y. Semenov, A. E. Bulyshev, A. Abubakar, et al., "Microwave tomographic imaging of the high dielectric contrast objects using different image reconstruction approaches", *IEEE Trans. Microw. Theory Techn.*, Vol. 53, No. 7, pp:2284–2294, July 2005.
14. J. M. Geffrin, C. Eyraud, and A. Litman, "3-D imaging of a microwave absorber sample from microwave scattered field measurements", *IEEE Antennas Wireless Propag. Lett.*, Vol. 25, No. 7, pp:472–474, July 2015.
15. C. Gilmore, P. Mojabi, et al., "On super-resolution with an experimental microwave tomography system", *IEEE Antennas Wireless Propag. Lett.*, Vol. 9, pp:393–396, May 2010.
16. M. Ostadrahimi, A. Zakaria, J. L. Vetri, and L. Shafai, "A near-field dual polarized (TE–TM) microwave imaging system", *IEEE Trans. Microw. Theory Tech.*, Vol. 61, No. 3, pp:1376–1384, March 2013.
17. M. N. Akinci, T. Caglayan, S. Ozgur, et al., "Qualitative microwave imaging with scattering parameters measurements", *IEEE Trans. Microw. Theory Tech.*, Vol. 63, No. 9, pp:2730–2740, September 2015.
18. M. Asefi, M. OstadRahimi, A. Zakaria, and J. LoVetri, "A 3-D dual-polarised near-field microwave imaging system", *IEEE Trans. Microw. Theory Tech.*, Vol. 62, No. 8, pp:1790–1797, August 2014.
19. Y. Wang, and A. E. Fathy, "Advanced system level simulation for three-dimensional UWB through-wall imaging SAR using time-domain approach", *IEEE Trans. Geosc. Remote Sens.*, Vol. 50, No. 5, pp:1986–2000, May 2012.
20. N. Ghavami, G. Tiberi, D. J. Edwards, and A. Monorchio, "UWB microwave imaging of objects with canonical shape", *IEEE Trans. Antennas Propag.*, Vol. 60, No. 1, pp:231–239, January 2012.
21. S. S. Ahmed, A. Schiessl, and L. P. Schmidt, "A novel fully electronic active real-time imager based on a planar multistatic sparse array", *IEEE Trans. Microw. Theory Techn.*, Vol. 59, No. 12, pp:3567–3576, December 2011.
22. G. Charvat, A. Temme, M. Feigin, and R. Raskar, "Time of flight microwave camera", *Nat. Sci. Rep.*, Vol. 5, Article no. 14709, October 2015.
23. R. W. Schafer, "What is Savitzky-Golay filter?" *IEEE Signal Process. Magazine*, pp:111–117, July 2011.

24. S. R. Krishnan, and C. S. Seelamantula, "On the selection of optimum savitzky-golay filters", *IEEE Trans. Image Process.*, Vol. 61, No. 2, pp:380–391, January 2013.
25. M. Soumekh, "A system model and inversion for synthetic aperture radar imaging", *IEEE Trans. Image Process.*, Vol. 1, No. 1, pp. 64–76, January 1992.
26. Ananjan Basu Ankita, "Ananlysis and optimization of broadband stacked microstrip antenna using transmission-line model", *IET Microw. Antennas Propag.*, Vol. 11, pp:81–91, 2017.
27. Ankita Malhotra, and Ananjan Basu, "Miniaturised Distributed Transceivers for Far-Field Microwave Imaging", *IEEE MTT-S International Microwave and R F Conference*, pp:1–4, December 2018.
28. Ankita Malhotra, "Broadband miniaturized c-band stacked antenna design and analysis using TLM", *IETE J. Res.*, pp:1–8, November 2023.
29. Ankita Malhotra, and Ananjan Basu, "Broadband frequency reconfigurable printed transceivers for microwave imaging systems", *Int. J. Microw. Wirel. Technol.*, Vol. 15, No. 7, pp:1130–1138, September 2023.
30. Mehdi Mehranpour, Saughar Jarchi, Asghar Keshtkari, Ayaz Ghorbani, Ali Araghi, Okan Yurduseven, and Mohsen Khalily, "Robust breast cancer imaging based on a hybrid artifact suppression method for early-stage tumor detection", *IEEE Access*, Vol. 8, pp:206790–206805, 2020.
31. Md. Rokunuzzaman, Md. Samsuzzaman, and Mohammad Tariqul Islam, "Unidirectional wideband 3-D antenna for human head-imaging application," *IEEE Antennas Wirel. Propag. Lett.*, Vol. 16, pp:169–172, 2017.



Taylor & Francis

Taylor & Francis Group

<http://taylorandfrancis.com>

Index

- Adaptive beamforming, 98
- Advantages, stacked microstrip antennas, 137–138
- Annular ring microstrip stacked antenna, 51–52
 - axial ratio bandwidths, 53, 55
 - current distribution, 53, 54
 - design parameters, 53
 - geometry, 52
 - input impedance variation, 53
 - measured and simulated radiation patterns, 53, 54
 - measured and simulated S11 parameter, 55, 56
- Antenna arrays
 - applications, 130–133
 - element-to-element spacing, 117
 - feeding networks, 117
 - sequential, 118–119
 - slot-coupled, 119
 - traditional, 118
 - phase difference, 117
 - planar stacked microstrip antenna array, *see* Planar stacked microstrip antenna array
 - shared aperture stacked antenna array, *see* Shared aperture stacked antenna array
 - stacked antenna array fed vertically, *see* Stacked antenna array fed vertically
- Antenna losses, 12
- Aperture-coupled microstrip antenna
 - bandwidth, 2
 - circularly polarized, 2
 - geometry of, 3
 - impedance bandwidth response, 3, 4
 - multiple resonances, 5
- TLM
 - circuit-level equivalent model, 70, 71
 - compensation length (L_c), 72
 - electromagnetic coupling, 70
 - induced electric field, 71
 - mutual coupling, 75
 - tilted slot, 69, 70
 - transformer coil turn ratio, 69, 70
- Aperture coupling, 1
- Applications, stacked microstrip antennas, 139–140
 - direction finding and localization, 147–148
 - in 4G/5G/6G communication, *see* 4G/5G/6G communication
 - in IoT, 141
 - in microwave/mm-wave imaging, *see* Microwave imaging system; mm-wave imaging
 - in remote sensing, 143–145
 - in RF energy harvesting, 145
 - in satellite communication, 141–143
 - in wearable electronics, 145–147
- Bandwidth, 9, 18–19, 131–133, 147–148
 - aperture-coupled stacked antennas, 4
 - E-shaped patch antenna, 41–44
 - F-probe-fed antenna, 44–47

- H-shaped antenna, 36, 37, 40
 - microwave imaging system, 159
 - multiple resonances, 16
- Beam shaping antennas, 98
- Beam steering antennas, 98
- Biomedical imaging, 195–197
- Broadband antenna response, 6, 8, 9, 17
- Broadband applications, 12–13
- Cavity-backed aperture-coupled stacked antennas, 152, 153
- Cavity model analysis, stacked ring patch antenna, 86–90
- C-band stacked antennas, microwave imaging, 169
 - vs.* C-band waveguide adaptor antenna, 171, 174
 - design parameters, 171, 174
 - geometry, 170, 173
 - H-plane radiation patterns, 171, 174
 - image reconstruction
 - targets hidden behind dielectric medium, 184–185
 - targets in free-space, 180–184
 - measured and simulated S11 response, 170
 - S21 response, 171, 176
 - simulated and measured gain, 171, 175
- Characteristics, stacked microstrip antennas
 - bandwidth, 9
 - directivity, 11
 - efficiency, 12
 - gain, 10–11
 - polarization, 9–10
 - radiation pattern, 10
- Conformal mapping
 - characteristic admittance, 66
 - characteristic impedance, 63–65
 - collinear coordinates on w -plane, 60, 61
 - effective dielectric constant, 62, 66
 - effective line width, 63
 - effect of fringing, 66
 - filling factors, 63
 - flux-potential coordinates on z' -plane, 60, 61
 - input admittance of antenna, 65–66
 - orthogonal transformation, 53
 - quasi-TEM wave propagation, 60
 - relative permittivity, z -plane, 66
 - space coordinates on z -plane, 60, 61
 - three-layer microstrip line, 62, 64
 - transmission line of two parallel strips, 60, 61
- Cross-polar radiation, 27
- Cross-range resolution, 168, 182
- Current distributions, 9, 59
 - annular ring microstrip stacked antenna, 53, 54
 - e-shaped stacked patch antenna, 41, 42
 - polarization reconfigurable antennas, 98
 - three-layered stacked microstrip antenna, 84, 86
- Design parameters and methodology
 - annular ring microstrip stacked antenna, *see* Annular ring microstrip stacked antenna
 - broadband antenna response, 6
 - broadband multi-layered stacked antenna structures, 19, 20
 - coaxial fed patch antenna, 19
 - design consideration, 1–2
 - effective permittivity, 21
 - E-shaped stacked patch antenna, *see* E-shaped stacked patch antenna
 - F-probe-fed stacked patch antenna, *see* F-probe-fed stacked patch antenna
 - H-shaped stacked antenna, *see* H-shaped stacked antenna
 - magneto-dielectric material, 47–49
 - number of stacked layers, 8
 - patch shapes and dimensions, 8, 19
 - rectangular microstrip-fed stacked antenna, *see* Rectangular microstrip-fed stacked antenna
 - relative placement of stacked patches, 8–9
 - resonant frequency, 19–22
 - selection of substrates, 6–7, 18–19
 - simulation and measurement, 55–56
 - total voltage across stacked antenna, 19–20
- Dielectric constant, 7, 17, 22, 25
 - cavity model, 86–89
 - effective, 20, 62, 66, 87, 89
 - material, 19

- Directivity, 11
- Dispersion effect, 87
- Effective permittivity, 12, 21, 89
- Efficiency, antenna, 12
- Electromagnetic coupling, *x*, 11, 101
 - aperture-coupled microstrip antenna, 70–72
 - microstrip and probe-fed stacked patch antennas, 3
 - multiple resonances, 16–17
 - placement of stacked patches, 8–9
 - polarization reconfigurability, 94
 - proximity-coupled stacked antenna, 5
 - rectangular microstrip-fed stacked antenna, 22, 24
 - textile-based stacked antennas, 13
 - three-layered stacked microstrip antenna with the patch offset, *see* Three-layered stacked microstrip antenna
 - transmission-line model (TLM) with, 76–78
 - two-layered stacked microstrip antenna, *see* Two-layered stacked microstrip antenna
- Electronic reconfigurability, 95–96
- E-shaped stacked patch antenna
 - current distributions, 42
 - design parameters, 44
 - measured and simulated return loss, 44
 - probe-fed stacked antenna structure, 41
 - simulated return loss response, 43
 - slots insertion in patch, 41
 - U-shaped slot, 41
- Field distribution, 9
- Finite-difference time domain (FDTD) approach, 59
- 4G/5G/6G communication
 - dual-polarized mm-wave antenna-in-package layout of 4×4 array of, 149, 150
 - S-parameters of, 149, 151
 - 3D layout of, 149
 - dual port stacked MIMO antenna, 3D layout of, 140, 144
 - high-gain stacked antenna arrays, 140
 - measured SAR and power density values, 141, 144
 - MIMO antenna arrays, 140
 - mm-wave stacked antenna array, 140, 141
 - orthogonal T-shaped feed lines, 148–149
 - 3D radiation patterns, 140–144
 - X- and Ku-band patches, 145
- F-probe-fed stacked patch antenna
 - design parameters, 46, 47
 - dual polarization, 45, 46
 - geometry, 45
 - L-shaped probes, 45
 - measured and simulated radiation patterns, 47–49
 - measured and simulated VSWR, 47, 48
 - stages of, 47
 - VSWR response, 47, 48
 - Wilkinson power divider, 44–45
- Frequency reconfigurable antennas, 97
- Frequency reconfigurable stacked microstrip antennas
 - with broadband frequency shift, 103–106
 - with continuous narrowband frequency shift, 101–103
- Fringing field effect, 87
- Full-wave analysis, 59
- Gain, 10–11
- Horn antenna, 97
- H-shaped stacked antenna, 36–37
 - approximate TLM equivalent, 40
 - equivalent circuit, 37, 38
 - geometry of, 36, 37
 - measure return loss, 40
 - miniaturization, 37–39
 - resonant frequency, 37
- Image reconstruction, *xi*, 158
 - amplitude vector and time vector, 164
 - fundamental principle, 164
 - illumination of target, 167
 - matrix cells, 164–165
 - matrix formation, 166, 167
 - using C-band antenna targets hidden behind dielectric medium, 176–180
 - targets in free-space, 180–184
 - using X-band antenna targets hidden behind dielectric medium, 176–180
 - targets in free-space, 180–184

- Impedance matching, 8, 22, 24, 25, 101
 - broadband, 18–19, 39
 - F-probes, 46–47
 - L-shaped probes, 45
 - multiband, 18
 - in probe-fed stacked antenna, 43–47
- Internet-of-Things (IoT), 141, 145
- Limitations, stacked microstrip antennas, 138–139
- Magneto-dielectric (MD) materials, inset-fed microstrip antenna
 - design of, 50
 - design parameters, 50
 - fabricated prototype, 50
 - high-frequency applications, 48
 - measured and simulated return loss, 48, 49
 - radiation patterns, 49, 51
 - SRR array structure, 49–51
- Mechanical reconfiguration technique, 97
- Meta-surface-based polarization reconfigurable antenna, 99
- Micro-electromechanical system (MEMS)-based switches, 96
- Microstrip and probe-fed stacked patch antennas, 3–5
- Microwave imaging system, xi; *see also* mm-wave imaging
 - applications, 157
 - bandwidth, 159
 - biomedical imaging, 195–197
 - block diagram, 157, 158
 - cavity-backed aperture-coupled stacked antennas
 - fabricated prototype, 152
 - imaging results, 152, 153
 - definition, 150–151
 - far-field imaging system, 159
 - hidden target detection, 150, 158
 - image reconstruction, *see* Image reconstruction
 - measurement set-up, 160
 - 3D scanning measurement set-up, 160–161
 - 2D scanning measurement set-up, *see* 2D scanning measurement set-up
 - multiband stacked microstrip antennas as transceivers, 168–169
 - C-band stacked antennas, *see* C-band stacked antennas, microwave imaging
 - X-band stacked antennas, 169–170
 - near-field imaging system, 159
 - polarization diversity, 158
 - qualitative and qualitative imaging, 157–158
 - radiation pattern, 159
 - reconfigurable stacked antenna, *see* Reconfigurable stacked antenna
 - stacked antennas as transceiver units, 159–160
 - surface and volume scattering, 157
 - through-wall imaging, 158
 - transmitter and receiver properties, 159
- mm-wave imaging
 - cavity-backed aperture-coupled stacked antennas, 152, 153
 - definition, 150–151
 - hidden target detection, 150
 - scattered/reflected/diffracted waves, 150
 - signal's penetration depth, 151
 - transceiver unit, 151, 152
- Multiband applications, stacked microstrip antennas, 12–13
- Multiple resonances, 16–17, 137, 138
 - aperture-coupled stacked antennas, 2
 - proximity-coupled stacked antenna, 5
- Optical reconfigurability, 96–97
- Pattern reconfigurable antennas, 98
- Pattern reconfigurable stacked microstrip antenna
 - array structure, 107, 109
 - driven patch layer, 106–107
 - feeding network layer, 106–108
 - parasitic patch layer, 106–107
 - radiation patterns, 107, 110
 - S11 response and gain response, 106, 107
- Phased array antennas, 98
- PIN diodes, 99
- Planar stacked microstrip antenna array
 - circularly polarized, 120

- design parameters, 120
- using meta-surface
 - design parameters, 122, 123
 - fabricated four element array structure, 124
 - geometry, 122
 - hybrid couplers, 124
 - leaf-shaped meta-surface-based antenna elements, 120
 - response at different design stages, 123
 - response of four element antenna array, 124, 125
 - stages of evolution, 121–122
- Polarization, 9–10, 94
 - circular, 112, 119
 - circularly polarized antenna, 120, 122
 - cross-polarization, 27, 28, 44
 - diversity, 158
 - dual, 44–46, 147
 - horizontal, 147
 - LHCP and RHCP, 108, 112
 - orthogonal, 131, 143
 - vertical, 147
- Polarization reconfigurable antennas, 98–99
- Polarization reconfigurable stacked antenna
 - array structure, 109
 - different states of operation, 110, 112
 - feeding layer, 112
 - geometry, 111
 - LHCP and RHCP, 108, 112
 - radiation pattern, 112–113
 - return loss and gain, 113, 114
 - SIW structure, 110
- Printed monopole antennas, 12
- Proximity-coupled stacked antennas, 5
- Q factor, 10
- Q value, 10, 11, 86
- Radiated power, 10, 11, 19, 118
- Radiation efficiency, 12, 117
- Radiation patterns, 10, 117
 - 4G/5G/6G communication, 140–141
 - annular ring microstrip stacked antenna, 44–47
 - directive, 117
 - F-probe-fed stacked patch antenna, 46–47
 - magneto-dielectric (MD) materials, 47, 48
 - microwave imaging, 157
 - C-band stacked antennas, 170–173
 - X-band stacked antennas, 169, 172
 - pattern reconfigurable array antenna, 110, 111
 - pattern reconfigurable stacked microstrip antenna, 106, 108
 - polarization reconfigurable stacked antenna, 112–114
 - of proposed modified stacked antenna, 34, 35
 - reconfigurable stacked antennas, 185, 189
 - rectangular microstrip-fed stacked antenna, 28, 30, 32, 33
 - stacked antenna array fed vertically, 126, 127
 - surface waves affecting, 16
- Radiation resistance, 11, 67–68
- Range resolution, 168, 175
- Realized gain, 11
- Reconfigurable antennas
 - frequency, 97
 - pattern, 98
 - polarization, 98–99
- Reconfigurable stacked antennas, x–xi
 - fabricated antenna, 187, 188
 - frequency reconfigurable design
 - with broadband frequency shift, 103–106
 - with continuous narrowband frequency shift, 101–103
 - image reconstruction
 - of bent aluminium rod, 180, 196
 - by combining signals in frequency domain, 192–193
 - by matrix addition method, 191–192, 194
 - objects used as targets, 195
 - pre-processing stage, 194
 - of U-shaped aluminium rod, 196, 197
 - of V-shaped aluminium rod, 196, 197
 - measurement set-up employing, 189–191
 - meta-materials, 101
 - overview, 94, 99–100

- pattern reconfigurable design, *see* Pattern reconfigurable stacked microstrip antenna
- polarization reconfigurable design, *see* Polarization reconfigurable stacked antenna
- reconfigurable feeding network, 101
- S11 response
 - C-band antenna, 189
 - measured H-plane radiation patterns, 189, 190
 - X-band antenna, 189, 190
- 3D view, 187, 189
- Reconfiguration techniques, 94
 - electronic reconfigurability, 95–96
 - mechanical reconfiguration technique, 97
 - optical reconfigurability, 96–97
 - through smart materials, 97
- Rectangular microstrip-fed stacked antenna
 - modified design
 - fabricated antenna, 34
 - layout, 34
 - radiation patterns, 34, 36
 - S11 response, 30, 32
 - simulated and measured gain, 32–34
 - overview, 22
 - parasitic substrate and patch parameters effect, 22–23
 - placement of parasitic patch and feed parasitic effects, 22–25
 - properties
 - cross-polar power ratio, 28, 30
 - electric field distribution, 28, 32
 - improved/proposed stacked antenna geometry, 29
 - measured H-plane co-polar and cross-polar radiation patterns, 27, 31
 - measured *vs.* simulated gain and efficiency graph, 30, 31
 - S11 response of improved/proposed stacked, 29, 30
 - S11 response of proposed stacked antenna, 29, 30
 - simulated S21 of proposed stacked antenna, 30, 32
 - second parasitic patch and substrate parameters effect, 25–26
 - slot at the driven patch effect, 27–28
- Remote sensing, 143–145
- RF energy harvesting, 145
- Satellite communication, 141–143
- Savitzky–Golay filter, 163–165
- Sequential feeding networks, 118–119
- Series-parallel curved transmission-line-based feed line, 119
- Shared aperture stacked antenna array
 - combining two different operating band antennas, 124
 - design parameters, 125, 128
 - dual-band stacked antenna array, 126
 - 8 × 16 E-band antenna elements, 126, 131
 - fabricated prototype, 126, 130
 - feeding network of E-band array elements, 128
 - with Ka-band and E-band patches, 124
 - S₁₁ response at E-band, 129
 - S₁₁ response at Ka-band, 128, 129
 - slot-coupling mechanism, 125, 126
 - 3D geometry of, 125
 - 2 × 4 Ka-band antenna elements, 126, 131
 - view inside metal cavity, 126, 130
- Slot-coupled feeding networks, 119
- Slot-line, 119
- Smart materials, reconfiguration techniques, 97
- Split-ring resonator (SRR) array, 47–49
- Stacked antenna array fed vertically
 - design parameters, 129, 135
 - directivity mode, 127–129
 - diversity mode, 127–129
 - simulated and measured radiation patterns, 126, 135
 - simulated S₁₁ response, 128, 133
 - with straight and curved feeding lines, 131, 134
- Stacked ring patch antenna, 86–90
- Static analysis models, *x*
 - cavity model analysis, stacked ring patch antenna, 86–90
 - conformal mapping, *see* Conformal mapping
 - overview, 59–60
 - transmission-line model analysis approach, *see* Transmission-line model (TLM)

- Substrate integrated waveguide (SIW)
 - structure, 110
 - Surface currents, 17
 - distribution of stacked antenna
 - design, 26, 28
 - electronic reconfigurability, 95
 - microwave imaging system, 157
 - polarization reconfigurability, 98
 - total radiated power of antenna
 - array, 118
 - Surface waves, 12, 118
 - affecting radiation pattern, 17
 - propagation, 7
 - substrate thickness, 17
 - Synthetic aperture radar (SAR)
 - approach, 164
 - Textile-based printed stacked
 - antennas, 13
 - Three-layered stacked microstrip
 - antenna
 - with patch offset, 62
 - TLM implementation
 - circuit-level equivalent, 87
 - circuit-level model, 80–81
 - CST simulation and circuit
 - simulation, 88
 - current distribution, 84, 86
 - design of proposed
 - antenna, 78–79
 - design parameters, 88
 - discontinuity, 86
 - fringing admittance, 82–83
 - geometry of shifted-fed patch,
 - 80, 81
 - shifted-fed driven patch, 81, 82
 - step-transition and equivalent
 - circuit parameters, 80
 - Time-gating phenomenon, 163
 - TM_{mn} mode, 18
 - Traditional feeding networks, 118
 - Transmission-line model (TLM), 21, 56
 - antenna with inter-layer coupling
 - modelled through mutual
 - capacitance
 - admittances, 76
 - computed input impedance, 75
 - edge admittance
 - parameters, 74–75
 - geometry of, 72, 73
 - modified coupling
 - capacitance, 75
 - resonant frequency, 73, 74
 - via-hole connection, 72–73
 - aperture-coupled microstrip
 - antenna analysis
 - circuit-level equivalent model,
 - 70, 71
 - compensation length (L_c), 72
 - electromagnetic coupling, 69–70
 - induced electric field, 71
 - mutual coupling, 68, 69
 - tilted slot, 68, 70
 - transformer coil turn ratio,
 - 68, 69
 - characteristic impedance
 - (Z_0), 66–67
 - coupling admittance, 68
 - with EM coupling modelled using
 - fringing admittance
 - fringing fields, 76
 - three-layered stacked microstrip
 - antenna with the patch offset,
 - see* Three-layered stacked microstrip antenna
 - two-layered stacked microstrip
 - antenna, *see* Two-layered stacked microstrip antenna
 - fringing capacitance (C_f), 66–67
 - H-shaped antenna, 37, 38
 - radiation resistance (R_r), 66–67
 - of rectangular microstrip patch
 - antenna, 66–67
- Travelling waves, 118
- T/R module, 183
- 2D scanning measurement set-up
 - bistatic system, 162
 - multi-static system, 162
- SAR algorithm
 - data processing, 164, 165
 - filter length, 163
 - image reconstruction, 164–168
 - incident electric field, 162
 - resolution, 168
 - scattered electric field, 162
 - signal-to-noise ratio of signal,
 - 163–164
 - synthetic focusing technique, 162
 - time-gating phenomenon, 163
 - total electric field, 162
 - vector network analyzer
 - (VNA), 162
 - types of, 161
- Two-layered stacked microstrip
 - antenna
 - circuit-level equivalent, 85

- circuit model, 82
- fringing admittance, 81–83
- geometry with parasitic patch at offset, 78
- input impedance, 83
- and its equivalent, 77, 78
- simulated and measured response, 83–84
- Varactor diodes, 95–96
- Vector network analyzer (VNA), 56, 162
- Vivaldi antennas, 12
- Wearable electronics, 145, 147
- X-band reconfigurable antenna, 105
- X-band stacked antennas, microwave imaging
 - bistatic microwave imaging set-up, 169
 - gain graph, 170, 171
 - image reconstruction
 - targets hidden behind dielectric medium, 176–179
 - targets in free-space, 173–176
 - proposed bistatic microwave imaging set-up, 169
 - radiation pattern, 170, 171
 - S11 response, 170
 - S21 response, 170, 172
 - set-up employed as transceiver, 170, 172
 - waveguide adaptor, 170